TYROSYL-DNA PHOSPHODIESTERASE 1 (TDP1): FROM SPINOCEREBELLAR ATAXIA TO ROLES IN MITOCHONDRIAL DNA REPAIR AND CANCER THERAPY

by

Hok Khim Fam

B.Sc., The University of British Columbia, 2010

A THESIS SUBMITTED IN PARTIAL FULFILLMENT OF
THE REQUIREMENTS FOR THE DEGREE OF

DOCTOR OF PHILOSOPHY
in
THE FACULTY OF GRADUATE AND POSTDOCTORAL STUDIES
(Medical Genetics)

THE UNIVERSITY OF BRITISH COLUMBIA
(Vancouver)

March 2017

Abstract

Tyrosyl-DNA phosphodiesterase 1 (Tdp1) is a 3'-DNA phosphodiesterase that resolves a variety of physiological and drug-induced 3'DNA-blocking lesions. This activity makes Tdp1 an important component of the base-excision repair pathway. While the biochemical activity of Tdp1 has been extensively studied, little is known about its role in cellular homeostasis. Nonetheless, the importance of Tdp1 in humans is exemplified by the observation that its dysfunction and dysregulation is associated with disorders such as neurodegeneration and cancer. My research attempts to broaden our understanding of Tdp1 as a DNA repair protein by providing a cell-physiological context within which the associations to these malignancies may be explored. I begin by characterizing Tdp1 expression in human tissue and exploring the significance of nuclear vs. mitochondrial Tdp1 localization in a subset of tissues. I observed that oxidative stress causes Tdp1 translocation from the nucleus into mitochondria, and identified through the use of human, yeast and mouse models a mechanism by which Tdp1 enters the mitochondria, as well as the mitochondrial DNA damage and respiratory impairment that occurs in the absence of Tdp1. The latter half of my work explores synthetic lethal approaches that may be used to target elevated Tdp1 expression in rhabdomyosarcoma. I found the combination of Tdp1 knockdown and PARP-inhibitor treatment to be effective in attenuating the growth of cultured rhabdomyosarcoma cells. Further validating my findings, I show through the identification of a Tdp1 inhibitor from small molecule libraries that the use of dual Tdp1 and PARP1 inhibition is a potent means of inhibiting the growth of Tdp1-expressing breast cancer cells. Taken together, my studies provide the foundation for further investigation into Tdp1-associated mitochondrial pathologies and the of targeting Tdp1 in cancer therapy.

Preface

Parts of Chapter 1 were previously published as a book chapter: **Hok Khim Fam**, Miraj K. Chowdhury and Cornelius F. Boerkoel (2012). **Spinocerebellar Ataxia with Axonal Neuropathy (SCAN1): A Disorder of Nuclear and Mitochondrial DNA Repair, Spinocerebellar Ataxia,** Dr. José Gazulla (Ed.), InTech, DOI: 10.5772/28279. Available from: http://www.intechopen.com/books/spinocerebellar-ataxia/spinocerebellar-ataxia-with-axonal-neuropathy-dissecting-dna-repair-mechanisms-in-neurodegeneration.

A version of Chapter 2 was previously published as a research article: **Hok Khim Fam**, Miraj K. Chowdhury, Cheryl Walton, Kunho Choi, Cornelius F. Boerkoel, and Glenda Hendson (2013). **Expression profile and mitochondrial colocalization of Tdp1 in peripheral human tissues**. *Journal of Molecular Histology* 44, no. 4: 481-494.
I performed all of the experiments excepting the immunofluorescent staining of human dermal fibroblasts and mitochondrial isolation. I generated all of the figures and tables and designed the experiments, performed data analyses, and wrote and edited the manuscript under the guidance of Dr. Cornelius F. Boerkoel
Contributions of co-authors:

- Miraj K. Chowdhury and Cheryl Walton performed immunofluorescent staining of human dermal fibroblasts to indicate the co-localization of Tdp1 with mitochondria
- Kunho Choi cultured human dermal fibroblasts and assisted in the isolation of mitochondria from these cells
- Dr. Glenda Hendson provided human autopsy tissue and assisted in the interpretation of Tdp1 staining of various tissue structures
- Dr. Cornelius F. Boerkoel designed the study and supervised the research

A version of Chapter 3 is currently under preparation: **Hok Khim Fam**, Kunho Choi, Lauren Fougner, Chinten James Lim, Cornelius F. Boerkoel (2016**). Reactive oxygen species stress causes the translocation of tyrosyl-DNA phosphodiesterase 1 into mitochondria.** *Manuscript in submission.*

I performed all of the experiments excepting the generation of Tdp1 deletion constructs and Tdp1 co-immunoprecipitation. I generated all of the figures and tables and designed the experiments, performed data analyses, and wrote and edited the manuscript under the guidance of Dr. Cornelius F. Boerkoel.

Contributions of co-authors:

- Lauren Fougner generated Tdp1 constructs for the identification of a mitochondrial localization signal
- Kunho Choi performed the co-immunoprecipitation of Tdp1 interacting proteins from cultured cells
- Dr. Chinten James Lim assisted in the live-cell imaging of human dermal fibroblasts
- Dr. Cornelius F. Boerkoel designed the study and supervised the research

A version of Chapter 4 was previously published as a research article: **Hok Khim Fam**, Cheryl Walton, Sheetal A. Mitra, Miraj Chowdhury, Nichola Osborne, Kunho Choi, Guobin Sun, Patrick C.W. Wong, Maureen J. O'Sullivan, Gulisa Turashvili, Samuel Aparicio, Timothy Triche, Mason Bond, Catherine J. Pallen, Cornelius F. Boerkoel (2013). **TDP1 and PARP1 deficiency are cytotoxic to rhabdomyosarcoma cells**. *Molecular Cancer Research* 11, no. 10 (2013): 1179-1192.

I performed all of the experiments excepting those outlined in the contributions described below; I generated all of the figures and tables; and I designed the experiments, performed data analyses, and wrote and edited the manuscript with Dr. Cornelius F. Boerkoel.

Contributions of co-authors:

- Cheryl Walton performed immunofluorescent staining of RMS cells
- Miraj Chowdhury analyzed the pediatric tumor microarray
- Sheetal Mitra collected analyzed Tdp1 expression in RMS patient tumors
- Dr. Nichola Osborne performed preliminary studies correlating Tdp1 expression in cultured cancer cells
- Kunho Choi maintained the cultured RMS cells and human skeletal muscle cells
- Dr. Guobin Sun performed preliminary PARP-1 siRNA knockdown in RMS cells
- Dr. Patrick C.W. Wong constructed the pediatric tumor microarray

- Dr. Maureen O'Sullivan performed tumor pathology analysis and provided the pediatric tumor samples for the array
- Dr. Gulisa Turashvili performed preliminary studies correlating Tdp1 expression and survival of cultured breast cancer cells
- Dr. Samuel Aparicio supervised Dr. Turashvili's experiments
- Dr. Timothy Triche provided the RMS patient tumor samples
- Dr. Mason Bond co-wrote the grant that provided the tumor microarray samples
- Dr. Catherine Pallen co-wrote the grant that provided the tumor microarray samples and supervised treearch by Drs. Sun and Wong
- Dr. Cornelius F. Boerkoel designed the study and supervised the research

A version of Chapter 5 was previously published as a research article: Dean, Richard A., **Hok Khim Fam**, Jianghong An, Kunho Choi, Yoko Shimizu, Steven JM Jones, Cornelius F. Boerkoel, Heidrun Interthal, and Tom A. Pfeifer (2014). **Identification of a putative Tdp1 inhibitor (CD00509) by in vitro and cell-based assays**. *Journal of Biomolecular Screening* 19, no. 10 (2014): 1372-1382.

I performed all of the experiments excepting those outlined below. I generated all of the figures and tables; Dr. Richard A. Dean, Dr. Tom A. Pfeifer, Dr. Cornelius F. Boerkoel and I designed the experiments and performed data analysis. I wrote and edited the manuscript with Dr. Cornelius F. Boerkoel.

Contributions of co-authors:

- Dr. Richard A. Dean performed the primary screen for inhibitors
- Dr. Jianghong An and Dr. Steven JM Jones performed in silico modeling of Tdp1 inhibitors
- Kunho Choi maintained the breast cancer cell culture
- Dr. Tom A. Pfeifer co-designed the study and co-supervised the research
- Dr. Cornelius F. Boerkoel co-designed the study and co-supervised the research

Table of Contents

List of Tables

List of Figures

List of Abbreviations

ANOVA	Analysis of variance
AP	Apurinic/apyrimidinic
APE1	AP endonuclease 1
aRMS	Alveolar rhabdomyosarcoma
ATP	Adenosine triphosphate
BER	Base excision repair
BRCA1	Breast cancer type 1 susceptibility protein
BRCA2	Breast cancer type 2 susceptibility protein
BSA	Bovine serum albumin
cDNA	Complementary DNA
CPT	Camptothecin
DMSO	Dimethyl sulfoxide
DNA	Deoxyribonucleic acid
DSBR	Double-stranded break repair
EDTA	Ethylene diamine tetraacetic acid
ERK1	Extracellular signal-regulated kinase 1
eRMS	Embryonal rhabdomyosarcoma
FUS3	Cell fusion protein type 3
GAPDH	Glyceraldehyde 3-phosphate dehydrogenase
GFP	Green fluorescent protein
H2AX	Histone 2A family member X
HF	Human fibroblast
HOG1	High osmolarity glycerol response protein 1
HSM	Human skeletal muscle
JNK1	Jun N-terminal kinase 1
K_m	Michaelis constant
LC_{50}	Median lethal concentration
LD_{50}	Median lethal dose
LIG3	DNA Ligase 3

MAPK	Mitogen-activated protein kinase
MEF	Mouse embryonic fibroblast
MIA40	Mitohondrial intermembrane space import and assembly protein 40
MMR	Mismatch repair
mRNA	Messenger RNA
MSBS	Menadione sodium bisulfite
mtDNA	Mitochondrial DNA
NAD	Nicotinamide adenine dinucleotide
NADP	Nicotinamide adenine dinucleotide phosphate
nDNA	Nuclear DNA
NER	Nucleotide excision repair
NHEJ	Non-homologous end-joining
P38	P38 mitogen-activated protein kinase
PARP	Poly-ADP ribose polymerase
PBS	Phosphate-buffered saline
PCR	Polymerase chain reaction
PFA	Paraformaldehyde
PFA	Paraformaldehyde
PVDF	Polyvinylidene diflouride
qRT-PCR	Quantitative reverse-transcriptase PCR
RMS	Rhabdomyosaroma
RNA	Ribonucleic acid
ROS	Reactive oxygen species
SCA	Spinocerebellar ataxia
SCAN1	Spinocerebellar ataxia with axonal neuropathy 1
SDS-PAGE	Sodium dodecyl sulfate- polyacrylamide gel electrophoresis
shRNA	Short hairpin RNA
siRNA	Small interfering RNA
SSBR	Single-stranded break repair
TDP1	Tyrosyl-DNA phosphodiesterase 1
TIM	Translocase of the inner membrane

TOM	Translocase of the outer membrane
Topo I	Topoisomerase I
TP53BP1	Tumor-suppressor p53 binding protein 1
TUNEL	Terminal deoxynucleotidyl transferase nick end labeling
V_{max}	Maximum rate at saturating substrate concentration
XRCC1	X-ray cross complementing protein 1

Acknowledgements

I would like to thank my supervisor Dr. Neal Boerkoel for his guidance and support. I would like to thank my committee members Dr. Catherine Pallen, Dr. Gregg Morin and Dr. Phil Hieter for their critique and constructive feedback. I would like to thank Kunho Choi for his assistance in the planning and execution of experiments, as well as Miraj Chowdhury and Cheryl Walton who laid the groundwork for my study. I thank Dr. Marie Morimoto for her kind help in proofreading my work and critiquing my manuscripts. Marie and many past members of the Boerkoel Lab constantly remind me of the importance of hard work and diligence in producing any work of significance. I am also thankful for the community at the Child and Family Research Institute, who have contributed to my personal and professional growth. Last but not least, I would like to thank my parents, my aunts and my wife, Alex, for supporting my scientific pursuit and for being there with me through thick and thin.

To all who devote their lives to solving the puzzles of life.

Chapter 1: Introduction

1.1 Spinocerebellar ataxia

Spinocerebellar ataxias (SCAs) are a group of progressive and irreversible neurological diseases affecting gait and movement coordination. Many result from cerebellar degeneration or the impairment of a portion of the neuroaxis that contributes to cerebellar inflow or outflow (Embirucu et al., 2009). In the cerebellum, the dysfunction and death of Purkinje cells, granule cells or interneurons can cause SCA. Molecular mechanisms for this pathology include polyglutamine tract expansion (SCA1, SCA2, SCA3), flawed basal transcription (SCA17) and defective DNA repair (ataxia telangiectasia, spinocerebellar ataxia with axonal neuropathy (SCAN1) and ataxia with oculomotor apraxia type 1) (Hire et al., 2011).

The mechanism by which defective DNA repair causes neuronal dysfunction and death is not yet fully understood, but damage to the nuclear and mitochondrial genomes underlie each potential explanation. Dysfunction of nuclear DNA repair enzymes results in nuclear DNA damage that impedes transcription and also induces programmed neuronal death (Fishel et al., 2007). Dysfunction of mitochondrial DNA repair enzymes leads to mitochondrial DNA damage that impairs mitochondrial gene expression causing mitochondrial dysfunction, oxidative stress and subsequently programmed neuronal death (Bender et al., 2006). Accumulation of DNA breaks within the neuronal nuclear genome has also been proposed to initiate expression of cell-cycle activators as a cellular response to repair genomic damage through replication-dependent mechanisms; however, these neurons are frequently unable to establish a new G0 quiescent state and this in turn activates neuronal death mechanisms (Kruman et al., 2004). Lastly, besides direct affects on the neurons, defective DNA repair also indirectly induces neuronal death by causing dysfunction of glia, which have trophic interactions with neurons and modulate neurotransmitter levels at synapses (Barzilai, 2011; Lobsiger and Cleveland, 2007)

1.1.1 Spinocerebellar ataxia with axonal neuropathy 1 (SCAN1)

SCAN1 is an autosomal recessive DNA repair disorder caused by the p.His493Arg active site mutation in tyrosyl-DNA phosphodiesterase1 (Tdp1), an enzyme that enables DNA repair by processing blocked 3' DNA termini. This mutation impairs this activity and also predisposes to the formation of Tdp1-DNA adducts. The only reported SCAN1 patients are from an extended

Saudi Arabian family having nine affected individuals (Takashima et al., 2002). SCAN1 is characterized by normal intelligence and a late-childhood onset progressive cerebellar ataxia and peripheral neuropathy. Initial features include ataxic gait, gaze nystagmus and cerebellar dysarthria. As the disease advances, the affected individuals develop impaired pain, vibration and touch sensation in the hands and legs and eventually a steppage gait and pes cavus. With further progression of their cerebellar, motor and sensory symptoms, affected individuals become wheelchair-dependent in early adulthood (Hirano et al., 2007). Magnetic resonance imaging studies show cerebellar atrophy, especially of the vermis (Takashima et al., 2002). Nerve conduction studies show decreased amplitudes characteristic of axonal neuropathy. These clinical findings suggest a disease of large, terminally differentiated, post-mitotic neurons, especially those of the cerebellum, dentate nuclei, anterior spinal horn and dorsal root ganglia.

Currently, there are only symptomatic treatments for SCAN1. Physical therapy is recommended for maintaining activity. Prostheses, walking aids and wheelchairs are recommended for improving mobility. In addition, based on studies of cells from SCAN1 patients and animal models, SCAN1 patients should avoid exposure to genotoxic agents such as camptothecin, irinotecan, topotecan, bleomycin and radiation (Hirano et al., 2007). Clinically, SCAN1 can be considered in the differential diagnosis for individuals who have 1) a slowly progressive cerebellar ataxia with onset in late-childhood or adolescence, 2) peripheral axonal neuropathy, 3) no signs of oculomotor apraxia and 4) no evidence of extraneurologic features such as telangiectasias, cancers or immunodeficiency. Supportive findings include increased serum cholesterol and decreased serum albumin (Takashima et al., 2002). The only known genetic defect causing SCAN1 is the c.1478A>G mutation in *TDP1*. This missense mutation, which encodes the p.His493Arg amino acid alteration, can be detected by DNA sequencing or by digestion of the PCR product with *Bsa*AI (Hirano et al., 2007; Takashima et al., 2002).

1.2 DNA repair

DNA repair is a ubiquitous cellular process that protects DNA from mutation by endogeneous and exogeneous genotoxic agents. The maintenance of genomic integrity is paramount in ensuring faithful transmission of genetic material from parental cell to daughter cell and in enabling the survival of organisms across generations. Most DNA damage occurs endogeneously. DNA bases are susceptible to reactive oxygen species (ROS), alkylating and

deaminating agents produced from cellular metabolism. DNA is also damaged by spontaneous alterations caused by errors in the maintenance of DNA such as misincorporation of nucleotides during DNA replication.

As exemplified by SCAN1, many DNA repair defects cause progressive neurodegenerative disease (Table 1-1) (Barekati et al., 2010; Sahin and Depinho, 2010). Neurons are particularly vulnerable to the accumulation of unrepaired DNA lesions because they are long-lived, post-mitotic and not readily replaced. DNA lesions arise as a consequence of endogenous or exogenous genotoxic insults. However, the seclusion of central neurons, which are frequently more severely affected than peripheral neurons, by the blood-brain barrier suggests that the DNA lesions arise predominantly from endogenous genotoxic insults, particularly the oxidative damage arising from mitochondrial dysfunction (Harman, 1972, 1981).

Since differing genotoxic agents produce varying genetic lesions, cells have evolved specific mechanisms capable of repairing DNA damage to prevent the propagation of deleterious changes in DNA. These DNA damage response (DDR) mechanisms can be broadly distinguished by four major DNA repair pathways: double-strand break repair (DSBR), mismatch repair (MMR), nucleotide excision repair (NER), and base excision repair (BER). DSBR corrects double-strand breaks (DSB) in the DNA backbone; MMR corrects mismatches of normal bases; NER repairs bulky helix distorting DNA lesions, and BER repairs damage to a single nucleotide and handles single-strand DNA breaks (SSB). Dysfunction of each of these DNA repair processes causes or has been associated with progressive neurodegenerative disease (Table 1-1) (Jeppesen et al., 2011).

Gene(s)	DNA Repair Defect	Clinical Syndrome	Main Symptoms
SETX	Defective DSBR	Ataxia with oculomotor apraxia type 2	• Cerebellar atrophy • Axonal sensorimotor neuropathy • Oculomotor apraxia • Elevated serum concentration of alpha-fetoprotein
ATM	Defective DSBR	Ataxia telangiectasia	• Progressive ataxia • Defective muscle coordination • Dilation of blood vessels in skin and eyes Immune deficiency • Predisposition to cancer
MRE11	Defective DSBR	Ataxia telangiectasia-like	• Slowly progressive cerebellar ataxia Ionizing radiation hypersensitivity
XPA, XPF, XPG, POLH, ERCC1-4, DDB2	Defective NER	Xeroderma pigmentosum	• Sensitivity to sunlight • Slow neurodegeneration • Skin cancer
ERCC6, ERCC8	Defective NER and TC-NER	Cockayne's Syndrome	• Sensitivity to sunlight • Growth retardation • Neurological impairment • Progeria
ERCC2, ERCC3, GTF2H5	Defective NER	Trichothiodystrophy	• Sensitivity to sunlight • Dystrophy • Short brittle hair with low sulfur content, Neurological and psychomotoric defects
TDP1	Defective BER	Spinocerebellar ataxia with axonal neuropathy 1	• Progressive degeneration of post-mitotic neurons
APTX	Defective BER	Ataxia with oculomotor apraxia type 1	• Slowly progressive cerebellar ataxia, followed by oculomotor apraxia • Severe primary motor peripheral axonal motor neuropathy
ALS2, SETX, SOD1, VAPB	Defective BER	Amyotrophic lateral sclerosis	• Progressive degeneration of motor neurons Muscle weakness and atrophy
C10orf2	Defective mitochon-drial DNA repair	Infantile-onset spinocerebellar ataxia	• Muscle hypotonia • Loss of deep-tendon reflexes • Athetosis

Table 1-1: DNA repair enzymes with mutations causing neurodegenerative disease.

NER:Nucleotide excision repair, TC-NER: Transcription-coupled nucleotide excision repair, MMR: Mismatch repair, BER: Base excision repair, DSBR: Double-strand break repair, (Embirucu et al., 2009; Katyal and McKinnon, 2007; Subba Rao, 2007).

1.2.1 Double-strand break repair

DSBR corrects DNA double-strand breaks (DSBs) induced by exogenous sources such as ionizing radiation and genotoxic compounds or by endogenous sources such as reactive oxygen species, replication fork collapse, and errors of meiotic recombination (Ciccia and Elledge, 2010). The two major DSBR pathways in mammalian cells are homologous recombination (HR) and non-homologous end-joining (NHEJ). HR allows high fidelity repair of DSBs during DNA replication by using the intact sister chromatid as a template, whereas NHEJ allows for the error-prone repair of DSBs by modifying and ligating the two DNA termini of a DSB without using an undamaged template. HR is restricted to the late S to G2/M phase of the cell cycle when a sister chromatid is available in proliferating cells, whereas NHEJ operates throughout the cell cycle and can repair DSBs in differentiated cells. Therefore, since the mature nervous system is predominately post-mitotic cells, NHEJ is the major DSBR pathway in the postnatal brain.

Two NHEJ disorders with progressive neurodegeneration of the postnatal brain are ataxia telangiectasia and ataxia telangiectasia-like disorder. The neurological symptoms of ataxia telangiectasia are an early childhood onset of ataxia that generally leads to wheel chair dependence before adolescence. The neurological symptoms of ataxia telangiectasia-like disorder are similar to those of ataxia telangiectasia but of later onset and slower progression. For both disorders, the neurodegeneration is characterized by the loss of cerebellar granule and Purkinje cells.

1.2.2 Mismatch repair

MMR removes base–base mismatches and insertion-deletion loops that arise during DNA replication and recombination. Base–base mismatches are created when errors escape DNA polymerase proofreading, and insertion-deletion loops arise when the primer and template strand in a microsatellite or repetitive sequence dissociate and re-anneal incorrectly causing the number of microsatellite-repeat units in the template and in the newly synthesized strand to differ. Interestingly, expression of MMR components is not limited to replicating cells but is also observed in non-replicating postnatal neurons suggesting that this pathway also plays a role in maintaining the genomic integrity of differentiated cells too (Ciccia and Elledge, 2010).

Consistent with a function in differentiated cells, studies of the Huntington trinucleotide repeat (CAG) in mice have shown somatic age-dependent repeat expansion that is suppressed by deficiency of some MMR components and is triggered by DNA glycosylases of the BER pathway (Kovtun et al., 2007; Owen et al., 2005). However, the relevance of the MMR pathway to trinucleotide repeat expansions of the human neurological disorders remains undefined.

1.2.3 Nucleotide excision repair

In human cells, recognition of bulky helix distorting DNA lesions leads to the removal of a short single-stranded DNA segment surrounding and including the lesion. This creates a single-strand gap in the DNA that is subsequently filled during repair synthesis by a DNA polymerase using the undamaged strand as a template. NER can be divided into two sub-pathways, global genomic NER (GG-NER) and transcription-coupled NER (TC-NER). GGNER and TC-NER differ in the recognition of the DNA lesion but subsequently use the same excision mechanism. GG-NER recognizes and repairs DNA lesions anywhere in the genome, whereas TC-NER only resolves lesions in the actively transcribed DNA strand (de Laat et al., 1999).

Two NER-associated disorders, xeroderma pigmentosum and Cockayne syndrome, feature progressive neurodegeneration (Kraemer et al., 1987). About 30% of xeroderma pigmentosum patients have neurological symptoms that include abnormal motor control, ataxia, peripheral neuropathy, dementia, brain and spinal cord atrophy, microcephaly and sensorineural deafness. In contrast, nearly all Cockayne syndrome patients have progressive neurological disease characterized by demyelination in the cerebral and cerebellar cortex, calcification in the basal ganglia and cerebral cortex, neuronal loss, sensorineural hearing loss and decreased nerve conduction (Nance and Berry, 1992). The progressive neurodegeneration in both xeroderma pigmentosum and Cockayne syndrome are attributable to apoptotic cell death (Lehmann, 2003).

1.2.4 Base excision repair

BER corrects the most common forms of DNA damage by recognizing, excising and replacing a broad spectrum of specific forms of DNA modifications including those arising from deamination, oxidation and alkylation. It is initiated by a distinct lesion-specific mono- or bi-functional DNA glycosylase and completed by either of two sub-pathways: short-patch BER

(SP-BER) that replaces one nucleotide or long-patch BER (LP-BER) that replaces 2–13 nucleotides (Frosina et al., 1996).

The BER proteins are also responsible for repairing DNA SSBs. SSBs are some of the most common lesions found in chromosomal DNA and arise via enzymatic cleavage of the phosphodiester backbone or from oxidative damage or ionizing radiation. Examples of enzymatic cleavage causing SSBs include those arising during BER (Connelly and Leach, 2004) and during DNA topoisomerase I (Topo I) activity (Pommier et al., 2003).

Ataxia with oculomotor apraxia type 1 and SCAN1 are both associated with defects in the repair of SSBs, specifically the processing of obstructive termini (Table 1). The neurodegenerative features of ataxia with oculomotor apraxia type 1 include progressive cerebellar atrophy, late axonal peripheral motor neuropathy, ataxia and oculomotor apraxia. The features of SCAN1, which is caused by a mutation of *TDP1*, have been described above.

1.3 Tdp1 function

TDP1 encodes tyrosyl-DNA phosphodiesterase 1 (Tdp1), a 608 amino acid enzyme that contains a bipartite nuclear localization sequence and two conserved HxKx4Dx6G (G/S) HKD (histidine-lysine-arginine) signature motifs. The two HKD motifs form a single symmetrical active site characteristic of the phospholipase D superfamily and catalyze a phosphoryl transfer that is common to enzymes in this superfamily (Interthal et al., 2001). The HKD motifs are very important for the catalytic function of Tdp1. Tdp1 enables SSBR and DSBR by removing obstructing compounds linked by a phosphodiester bond to DNA 3' termini and complements the 5'-phosphodiesterase function of TTRAP (Tdp2) (Cortes Ledesma et al., 2009; el-Khamisy and Caldecott, 2007; Zhou et al., 2009). Tdp1 endogenous substrates include 3' tyrosine-DNA phosphodiester moieties, phosphoglycolates, mononulceosides and tetrahydrofurans, and exogenous substrates include 4-methylphenol, 4-nitrophenol and 4-methylumbelliferone (Dexheimer et al., 2008; Interthal et al., 2005a). Tdp1 has the highest affinity for the 3' tyrosine-DNA phosphodiester moieties, which are characteristic of Topo I-DNA intermediates (Dexheimer et al., 2010).

During repair, replication, transcription, recombination and chromatin remodeling, Topo I relaxes superhelical tension by nicking DNA to allow controlled rotation of the broken DNA strand around the intact strand. After DNA relaxation has occurred, a nucleophilic attack by the

DNA 5’ hydroxyl group on the phosphotyrosyl linkage between Topo I and the 3’ end of the DNA at the nick usually religates the DNA, and the Topo I dissociates. However, DNA damage such as abasic sites, nicks, and mismatched base pairs frequently impede removal of Topo I from the DNA by causing a misalignment of the 5’ hydroxyl end of the DNA that prevents it from acting as a nucleophile (Pommier et al., 1998; Pommier et al., 2003; Pourquier and Pommier, 2001). Additionally, the 3’-Topo I-DNA intermediate can become unduly long-lived if Topo I binds oxidative base lesions (Interthal et al., 2005b). These trapped or long-lived Topo I-DNA covalent intermediates can then be converted to irreversible DNA breaks when the DNA replication machinery or RNA polymerase collides with the Topo I-DNA complex (Hsiang et al., 1989; Tsao et al., 1993; Wu and Liu, 1997).

Clearance of the trapped or stalled 3’-Topo I-DNA intermediates occurs via SSBR or DSBR if the SSB is converted to a DSB by collision of the DNA replication machinery with the trapped or stalled 3’-Topo I-DNA intermediate. Following recognition of the break, the trapped or stalled Topo I is proteolytically cleaved leaving a peptide bound to the 3’ end of the DNA by the phosphodiester bond formed between the DNA and the Topo I active site tyrosine (Tyr723). Tdp1 then acts on the phosphodiester bond and removes the obstructing Topo I peptide from the 3’ terminus (Debethune et al., 2002; Liu et al., 2002). The Tdp1 reaction removes the peptide from the DNA by an SN2 nucleophilic attack of His263, which resides in the first HKD motif, on the phosphodiester bond; Tdp1 is then released from the DNA by the catalytic activity of His493, which resides in the second HKD motif (Figure 1-1).

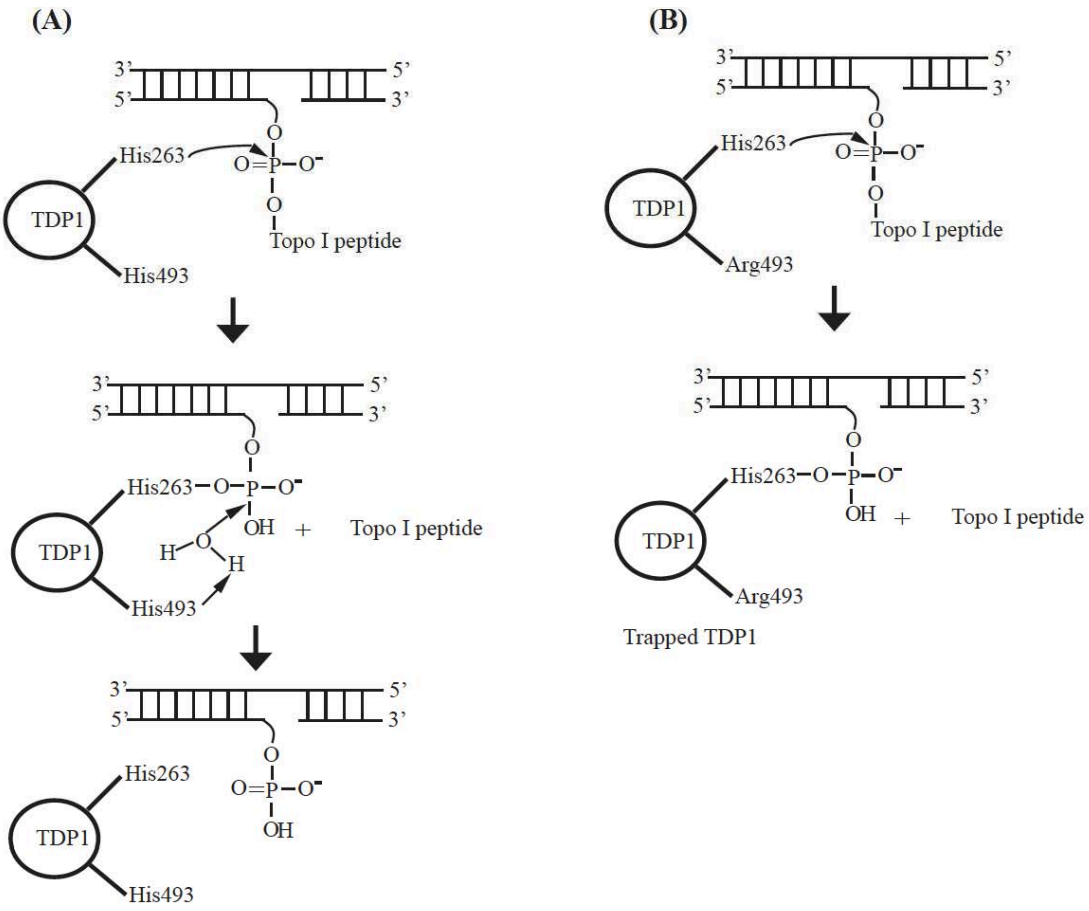

Figure 1-1: Mechanism of Tdp1 catalytic activity.

(A) Wild type Tdp1 removes proteolysed Topo I and forms a covalent intermediate with DNA before His493 of the second HKD motif excises Tdp1 from DNA through a nucleophilic substitution. (B) In SCAN1, the mutated Tdp1 (p.His493Arg) removes proteolysed Topo I but remains trapped on DNA and leads to accumulation of Tdp1-DNA adducts.

1.3.1 Tdp1 and nuclear DNA repair

Within the nucleus, Tdp1 is a component of the SSB multi-protein repair complex containing PARP1, LIG3, XRCC1 and PNKP (Das et al., 2009). This repair complex is activated after proteasomal degradation of stalled Topo I (Zhang et al., 2004). PARP1 is an important regulator of the SSBR/BER pathway as it enhances the recruitment of DNA repair proteins. PARP1 hydrolyzes NAD+ to catalyze the synthesis of ADP-ribose units onto glutamate molecules of acceptor proteins. The addition of poly-ADP ribosyl (PAR) polymers onto histones promotes the relaxation of chromatin, while SSBR proteins such as XRCC1 and Lig3a are

electrostatically attracted to PAR and are thus recruited to the site of DNA damage (El-Khamisy et al., 2003; Krishnakumar and Kraus, 2010). It is thought that XRCC1 acts as a molecular scaffold for the binding of Tdp1 and Lig3a and stabilizes the enzyme complex in the processing of Topo I derived SSBs. Processing of the 3' tyrosine-DNA phosphodiester moieties by Tdp1 leaves a 3'-P terminus that is converted to 3'-OH by the phosphatase action of PNKP. The kinase activity of PNKP phosphorylates the 5'-OH terminus, allowing gap filling by DNA polymerase (Polß), and finally the DNA nick is sealed by lig3a with the aid of the XRCC1 scaffold (Figure 1-2).

How Tdp1 processes obstructing 3' overhangs on DNA DSBs has not been fully defined. The dependence of Tdp1 processing of DSB termini on the autophosphorylation activity of the NHEJ component DNA-PK suggests that Tdp1 contributes within the NHEJ pathway and that DNA-PK modulates the accessibility of DNA ends enabling Tdp1 to accomplish the processing necessary for eventual end-joining (Zhou et al., 2009). One redundant DNA repair activity for Tdp1 is the nucleolytic removal of several DNA bases beginning upstream of the stalled Topo I. This is mediated by 3'-flap endonuclease complexes in the nucleus such as Mus81-MMS4 and XPF-ERCC1 that cleave at the 3'-flap created by stalled Topo I to enable short-patch gap filling. In comparison to Tdp1 processing, however, this mechanism is error-prone and less efficient.

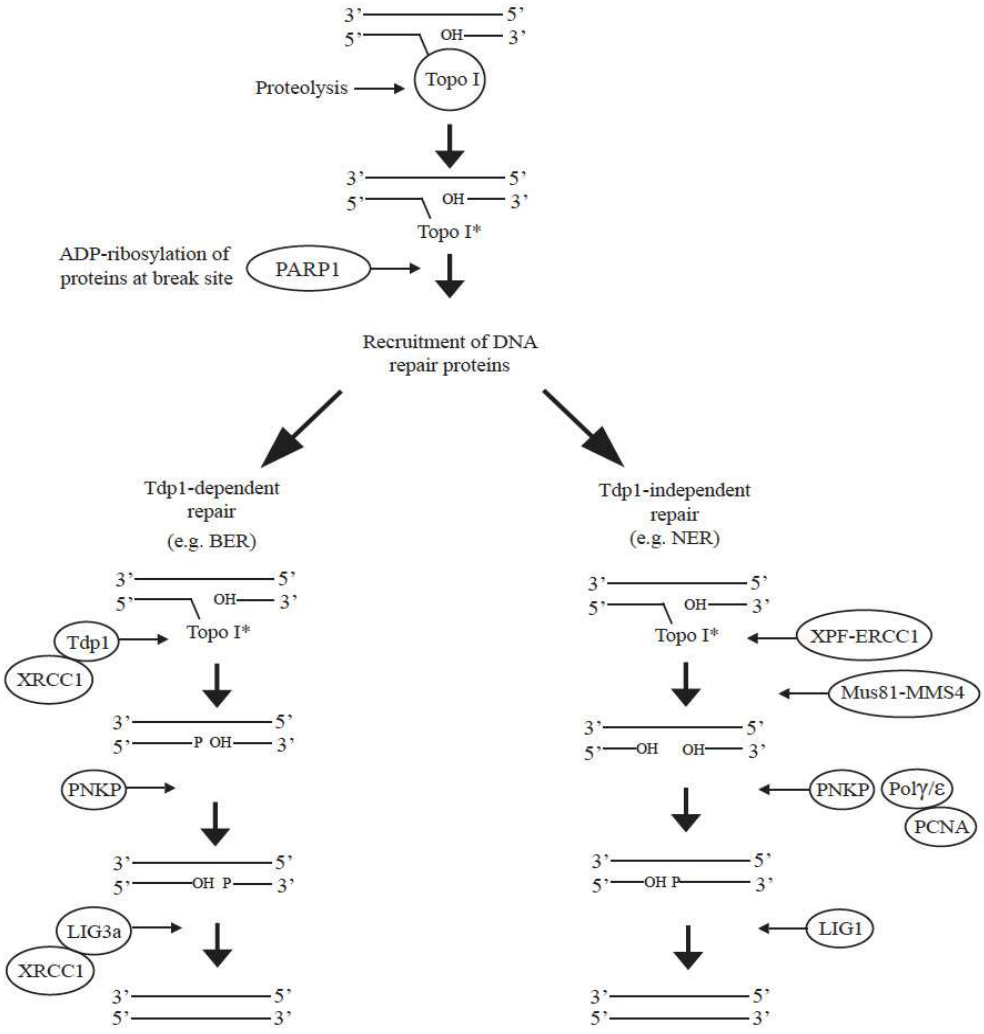

Figure 1-2: Tdp1-dependent and Tdp1-independent pathways for the removal of Topo I-DNA covalent complexes.

Topo I* = Topo I peptide

1.3.2 Tdp1 and mitochondrial DNA repair

Mitochondria are membrane-enclosed organelles that generate most of the ATP via the electron transport chain at the inner mitochondrial membrane. This process leads to the generation of reactive oxygen species, and while mitochondria have various antioxidant enzymes to deactivate these highly reactive molecules, they do not constitute a perfect defense. This inevitably exposes the mtDNA to high levels of oxidative stress, particularly since the mtDNA is located in close proximity to the inner mitochondrial membrane and lacks protective histones

(Ames et al., 1993). Consequently, the levels of oxidative base damage in mitochondrial DNA are 2–3 fold higher compared to nuclear DNA (Hudson et al., 1998), and the damage is more extensive and persistent than in nuclear DNA (Yakes and Van Houten, 1997).

Several DNA repair activities and pathways that function in the nucleus have also been identified and characterized in mammalian mitochondria. These include BER, MMR, and some components of DSBR (Larsen et al., 2005). Given the prevalence of small lesions generated by oxidative stress in the mitochondria, BER is the predominant mtDNA repair pathway. Mitochondrial BER proteins are not encoded by the mitochondrial genome; rather they are mitochondrial versions of nuclear-encoded proteins (Larsen et al., 2005). Among these is Tdp1, which could resolve 3'-phosphotyrosyl and phosphoglycolate obstructive termini. Indeed, besides its role in the repair of nuclear DNA, Tdp1 also plays a role in mitochondrial DNA (mtDNA) repair, as it is present in the mitochondria of cultured cells and repairs 3'-phosphotyrosyl and phosphoglycolate ends in the presence of Lig3a (Das et al., 2010). Cells devoid of Tdp1 are prone to accumulating mtDNA lesions in the presence of H_2O_2 (Das et al., 2010). Besides Tdp1, studies have also shown that the localization of APE1, another BER protein in the mitochondria is responsible for the repair of apurinic/apyrimidinic (AP) sites arising from the DNA glycosylase removal of DNA lesions in the mitochondria (Shokolenko et al., 2009). Similar to the absence of Tdp1, cells lacking APE1 are also prone to accumulating mtDNA lesions in the presence of H_2O_2 (Barchiesi et al., 2015).

1.3.3 Protein import into the mitochondria

The mitochondrion is a double membrane-bound organelle. Since the human mitochondrial genome encodes only13 protein-coding genes, almost all of the thousands of proteins that exist within the mitochondrial milieu are transported through one or both of its membranes (Taanman, 1999). Most incoming precursor proteins are folded as it is threaded through the mitochondrial outer membrane into the intermembrane space (Stojanovski et al., 2012). Mitochondria-bound proteins often contain one or more signal sequences that act as "barcodes" to allow recognition and guidance by appropriate intermembrane chaperones (Omura, 1998). The series of interactions between chaperones and the target protein allow efficient sorting to its final destination (Harbauer et al., 2014). Protein complexes known as translocases of the inner and outer mitochondrial membrane (TIM/TOM) facilitate this process by allowing the passage of

proteins between the cytoplasm and mitochondrial matrix. Taken together, the TIM/TOM complexes and mitochondrial chaperones form the backbone of a classic pathway form mitochondrial protein import (Wiedemann et al., 2004). Although little work has been done to elucidate the mechanism(s) of transport for proteins involved in the mitochondrial DNA damage response, it is plausible that the canonical TIM/TOM pathway proteins facilitate this process.

1.3.4 Tdp1 and cancer

The study of SCAN1 defined Tdp1 as a drug target for other diseases, particularly cancer. The absence of neurological disease in Tdp1-deficient mice and the adolescent-onset of SCAN1 in humans suggest that Tdp1 inhibition or deficiency can be tolerated for a period by normal mammalian tissues (Brangi et al., 1999). Since Tdp1 resolves topoisomerase I-DNA complexes, it promotes resistance to topoisomerase I poisons, which are used as anticancer agents. This suggests that a combination therapy of Topoisomerase I poisons with Tdp1 inhibitors might enhance the efficacy of the Topoisomerase I poisons as anticancer drugs (Marchand et al., 2009).

Similar to the mechanism of Topo I inhibitors, PARP inhibitors trap PARP-DNA complexes at the site of damage and are especially toxic to cells highly expressing PARP-1 (Murai et al., 2012b). Several studies have shown that the inhibition of PARP-1 can be harnessed to kill tumors with defects in DNA-repair pathways complementary to PARP-1, a concept known as ‘synthetic lethality’ (Drew et al., 2016; Farmer et al., 2005; Rottenberg et al., 2008). The participation of PARP-1 and Tdp1 in the same DNA repair pathway makes the combination of Tdp1, PARP1 and Topo 1 poisons a potential drug combination for the treatment of cancers expressing Tdp1. The effective use of Tdp1 inhibition as a means for precision cancer therapy, however, requires the identification of conserved synthetic lethal interactions in the cell (Srivas et al., 2016). This will allow the filtering of functionally redundant proteins and pathways that may dampen the effect of Tdp1 inhibition (Mosesso et al., 2005; Vance and Wilson, 2002).

1.4 Rationale, hypothesis and objectives

It has been established that Tdp1 has a role in nuclear DNA repair. To further characterize the role of Tdp1 as a DNA repair protein in the mitochondria, I screened and annotated the expression of Tdp1 protein in human autopsy tissue. I hypothesized that Tdp1 is transported into mitochondria during times of mtDNA stress, and that the localization of Tdp1

within the mitochondria has several important consequences for the maintenance of mitochondrial DNA, preservation of mitochondrial function and overall well-being of the organism.

In Chapter 2, I show that Tdp1 was expressed exclusively within the mitochondria of human and mouse skeletal muscle, and that oxidative stress caused the localization of Tdp1 in the mitochondria of human fibroblasts.

In Chapter 3, I further characterize the conditions that cause mitochondrial localization of Tdp1 and show that the transport of Tdp1 occurred between the nucleus and mitochondria in the presence of oxidative stress and that the absence of Tdp1 was detrimental to mtDNA and mitochondrial function.

In Chapter 4, I switched gears and explored the relationship between Tdp1 and its classical function as a nuclear protein involved in the resolution of 3'-DNA adducts. Given that several studies have shown the ineffectiveness of camptothecin in cancer therapy, I explored the role of Tdp1 overexpression in rhabdomyosarcoma and uncovered synthetic lethal interactions and conditions that drove the growth of several rhabdomyosarcoma cell lines.

In Chapter 5, I explored through a series of chemical and biological screens, the feasibility of small molecule inhibitors of Tdp1 as a potential treatment in Tdp1-overexpressing cancer cells. Taken together, the studies presented in my thesis provide a preliminary understanding of one mechanism of Tdp1-mediated DNA repair in the mitochondria and a role of Tdp1 as a target in cancer therapy.

Chapter 2: Analysis of Tdp1 Expression in Human Tissue

2.1 Introduction

In contrast to humans, mice lacking functional *Tdp1* fail to develop ataxia (Hawkins et al., 2009; Hirano et al., 2007; Katyal et al., 2007). Interestingly, mouse Tdp1 is expressed mainly in the nucleus of neurons analogous to those presumably affected in SCAN1 (Purkinje, dentate nuclei, anterior horn and dorsal root ganglia cells), whereas human Tdp1 is expressed predominantly in the cytoplasm of those neurons (Hirano et al., 2007). These observations suggested to us that the sub-cellular localization of Tdp1 could define a function underlying the pathology of SCAN1 (Hirano et al., 2007), particularly since Tdp1 colocalizes with mitochondria in cultured breast cancer cells (Das et al., 2010; Walton C, 2009).

As a first step in defining the relevance of cytoplasmic Tdp1 and its relationship to the mitochondria, I profiled the expression and sub-cellular localization of Tdp1 in human and mouse tissues. Tdp1 was present in the nucleus and cytoplasm of most tissues and its subcellular localization did not change notably between neonatal and adolescent human tissue. In human skeletal muscle and mouse tissues some cytoplasmic Tdp1 colocalized with mitochondrial markers and in cultured human dermal fibroblasts, Tdp1 colocalized with mitochondria following exposure to oxidative stress. I hypothesize that the localization of Tdp1 in the mitochondria is both dynamic and functional in human tissues.

2.2 Methods

2.2.1 Human samples

Anonymized normal human postmortem tissues from a 6-week old female infant, a 39-week gestation male fetus and a 16-year old female were obtained in accordance with institutional policies approved by the Clinical Research Ethics Board (H09-03301) at the University of British Columbia.

2.2.2 Animal samples

Mice used in the study were bred, housed and sacrificed according to institutional policies approved by the Animal Care Committee of the University of British Columbia (A06-0257). Briefly, *Tdp1*$^{-/-}$ mice were generated by injection of a gene trap embryonic stem cell line into

albino C57 mice, which were then bred to 129/SvEv mice to generate the founder population (Hirano et al., 2007).

2.2.3 Immunohistochemistry of human tissue

Human tissues, listed in Supplementary Table A-2, were fixed in formalin. 5 µm sections were cut from paraffin embedded tissue. After deparaffinization in xylene and rehydration through ethanol to water, antigen was retrieved in 10 mM citrate, 0.05% Tween 20, pH 6 at 95°C for 20 min. Endogenous peroxidase activity was blocked with 3% H_2O_2 before preincubation in blocking solution (10% casein (Vector Laboratories), Tris buffered saline (TBS, 10 mM Tris–HCl pH 7.0, 150 mM NaCl), 0.2% Triton X-100) for 1 hour at room temperature. The tissue sections were incubated with rabbit anti-human Tdp1(1:100) diluted with blocking solution overnight at 4°C, washed five times with TBS, and then incubated for one hour in biotinylated anti-rabbit secondary antibody (1:100) (Vector Laboratories) diluted with blocking solution. The Tdp1 antibody was custom-generated in rabbits against amino acids 1-152 of human Tdp1 as previously described (Hirano et al., 2007). After washing the tissue sections three times with TBS, immune complexes were visualized using peroxidase-conjugated streptavidin (VECTASTAIN Elite ABC standard kit, Vector Laboratories) and 3, 3´-diaminobenzidine (Dako) according to the manufacturers' instructions. Tissue sections were counterstained with Mayer's hematoxylin. The degree of Tdp1 expression in each individual was independently judged by H.K. Fam, M.K. Chowdhury, C. Walton and G. Hendson and given a score ranging from no expression to high expression. G. Hendson resolved discrepancies in scoring. Images were acquired using a Zeiss Axiovert 200 microscope, a Zeiss AxiocamHR camera and the Zeiss Axiovision imaging system.

2.2.4 Hematoxylin and eosin staining of frozen mouse tissue

Cryosectioned mouse tissue was allowed to air dry for thirty minutes in room temperature and then fixed in ice-cold acetone for ten minutes. Tissues were air dried and then briefly washed in PBS and stained in Harris hematoxylin for eight minutes and washed in running water for five minutes. The tissues were then differentiated in 1% acid alcohol for thirty seconds and washed in running water again before bluing in 0.2% ammonia water for thirty seconds. This was followed by another five-minute wash in running water and then immersion in 95% ethanol for one

minute, counterstained in eosin B for one minute and put through two five-minute 95% ethanol, before washing in two five minute changes of xylene and coverslipping.

2.2.5 Cell culture and oxidative stress treatment

Normal human dermal fibroblast cells were cultured using Dulbecco's modified eagle medium (Gibco BRL) supplemented with 15% fetal bovine serum (Gibco BRL) and 1% antibiotic-antimycotic (Invitrogen). Fibroblasts were cultured at 37ºC with 5% CO_2. For oxidative stress assays, 2000 cells were seeded per well of a 96 well plate incubated for 48 hours, and then treated with 12µM menadione sodium bisulfite (Sigma) or 200 nM hydrogen peroxide (Sigma) for 24 hours. Each treatment was done in triplicate.

2.2.6 Immunofluorescence microscopy

Immunofluorescence microscopy was performed as described (Hirano et al., 2007). Briefly, approximately 5 X 10^5 cells were grown on a cover slip. The cells were washed with phosphate buffered saline (PBS, 137 mM NaCl, 2.7 mM KCl, 10 mM Na_2HPO_4, 2 mM KH_2PO_4, pH 7.4) and fixed with 4% paraformaldehyde (PFA) in phosphate buffer (PB, 22.46 mM NaH_2PO_4, 77.54 mM Na_2HPO_4, pH 7.4) for 15 minutes. For tissue sections, 5 µm cryosections of mouse and human tissue were air-dried, post fixed with acetone at –20º C for 15 minutes and air-dried again for 30 minutes. Then the cells or tissue sections were permeablized with 0.5% Triton X-100 in PBS for 15 minutes and blocked overnight at 4ºC with blocking buffer (20% horse serum, 1% casein in PBS). Human tissues were incubated overnight at 4º C with custom-generated rabbit anti-human Tdp1 (1:100) and mouse tissues were incubated overnight at 4º C with custom-generated guinea-pig anti- mouse Tdp1 (1:100). Both anti-human and anti-mouse Tdp1 antibodies were generated as previously described (Hirano et al., 2007). Both mouse and human tissues were concurrently incubated with mouse anti-cytochrome C (1:250, 6H2.B4, BD Biosciences) diluted in blocking buffer. After washing with PBS, human tissues were incubated with Alexa 488 conjugated goat anti-rabbit IgG (1:500, A-11008, Invitrogen) and Alexa 647 conjugated goat anti-mouse IgG (1:500, A-21236, Invitrogen) diluted in blocking buffer for 45 minutes at room temperature. Mouse samples were incubated with Alexa 488 conjugated goat anti-guinea pig IgG (1:500, A-11073, Invitrogen) and Alexa 647 conjugated goat anti-mouse IgG (1:500, A-21236, Invitrogen) diluted in blocking buffer for 45 minutes at room temperature.

After washing, samples were mounted in Vectashield containing DAPI (Vector Laboratories). With the exception of mouse tissue processed for immunofluorescent analysis, all images were acquired using a Zeiss Axiovert 200 microscope, a Zeiss Axiocam MR camera and the Zeiss AxioVision imaging system. Immunofluorescent images of mouse tissue were acquired using a Leica TCS SP5 II confocal microscope.

2.2.7 Colocalization analysis

Deconvolution and colocalization analysis of photomicrographs for human tissue and cells was performed using the Zeiss AxioVision software. The relative amount of Tdp1 signal colocalizing with cytochrome C and vice-versa was determined by dividing the percent colocalized area by the percent area occupied by either the Tdp1 or the cytochrome C signal. Colocalization analysis for mouse tissue was determined by the Leica Application Suite software under the following conditions and calculations: threshold 30%, background 20%, colocalization rate [%] = colocalization area/area foreground, and area foreground = area of image − area of background.

2.2.8 RT-PCR analysis

RNA was isolated from each cell-line using Qiagen RNeasy mini kit (Qiagen) and 3 μg were reverse transcribed with qScript cDNA supermix (Quanta Biosciences). Quantitative PCR (qPCR) was performed using the PerfeCTa Sybergreen mix (Quanta Biosciences) and a 7500 Applied Biosystems qPCR system. Data was analyzed using the manufacturer's software (v2.0.1) accompanying the 7500 Applied Biosystems qPCR system. RT-PCR primers*: TDP1*- forward AGGCTAAGGCTCACCTCCAT; *TDP1*- reverse TTCCTGGAGTCTTGCTTTCC; *GAPDH*- forward TTAGCACCCCTGGCCAAGG; *GAPDH*- reverse CTTACTCCTTGGAGGCCATG.

2.2.9 Purification of mitochondria and cytoplasm

Mitochondria and cytoplasm were isolated from skeletal muscle as described previously (Rebrin et al., 2003; Zhou et al., 2001). To purify mitochondria and cytoplasm, snap-frozen skeletal muscle was chopped with fine scissors and treated with 100 ¥ g/ml Nagarase in ionic medium (100 mM sucrose, 10 mM EDTA, 100 mM Tris-HCl, 46 mM KCl pH 7.4) for 5

minutes. The lysate was homogenized using a loose-fitting Dounce-homogenizer with 20 strokes and centrifuged at 100 x g to remove nuclei and tissue debris. The supernatant was removed and centrifuged at 14,000 x g to obtain a crude pellet containing mitochondria and supernatant containing cytoplasmic proteins without contaminating mitochondria. The mitochondria were purified from this crude fraction by ultracentrifugation at 80,000 x g for 4 hours using a step gradient of Optiprep^{TM} (60% iodixanol, AXIS-SHIELD). The step gradient was prepared using 40% (w/v), 30% (w/v) and 10% (w/v)iodixanol and the crude mitochondrial pellet was loaded as the bottom layer. Mitochondria were collected from the 30%-10% iodixanol interface and diluted 1:5 with mitochondria isolation buffer (0.25 M sucrose, 1 mM EDTA, 20 mM HEPES-NaOH, pH 7.4). This preparation was centrifuged at 14,000 x g for 10 minutes to obtain a mitochondrial pellet to use for immunoblotting. All steps were done at 4ºC and all solutions and buffers contained 1X protease inhibitor cocktail (Roche).

2.2.10 Purification of nuclei

Nuclei were purified from skeletal muscle using Optiprep^{TM}(60% iodixanol, AXIS-SHIELD) with minor modifications as described (Graham et al., 1994). Briefly, snap-frozen samples of muscle were homogenized in homogenization medium (0.25 M sucrose, 25 mM KCl, 5 mM $MgCl_2$, 20 mM Tricine-KOH, pH 7.8) using a loose-fitting Dounce-homogenizer with 20 strokes on ice. The homogenate was cleared through a 100 µm cell strainer and centrifuged at 1000 x g for 10 minutes to prepare a crude nuclear pellet. Nuclei were purified from this crude fraction by centrifuging at 12,000 x g for 2 hours using a step gradient of Optiprep^{TM}. The step gradient was prepared using 35% (w/v), 30% (w/v) and 25% (w/v) iodixanol. Crude nuclei were suspended in 25% iodixanol and used as the top layer. Purified nuclei were collected from the 30%-35% iodixanol interface, washed once with homogenization buffer and used for immunoblotting. All steps were done at 4ºC and all solutions and buffers contained 1X protease inhibitor cocktail (Roche).

2.2.11 Immunoblotting

Immunoblotting was performed as described (Hirano et al., 2007). Briefly, cells, tissue or organelle fractions were lysed in SDS-sample buffer (63 mM Tris HCl, 10% glycerol, 2% SDS, 0.0025% bromophenol blue, pH 6.8) and denatured by boiling for 5 minutes. Then the proteins

were fractionated on a 10% or 15% gel by sodium dodecyl sulfate polyacrylamide gel electrophoresis (SDS-PAGE) and transferred to a polyvinylidene fluoride (PVDF) membrane. The membrane was blocked with blocking solution (0.2% I-Block (Applied Biosystems) and 0.1% Tween 20 in PBS) overnight at 4°C with gentle agitation. The membrane was next incubated overnight at 4ºC with each of the following primary antibodies diluted in blocking buffer: anti-mouse Tdp1 or rabbit anti-human Tdp1, which we generated in a previous study, (1:1000, Hirano et al., 2007), mouse anti-glyceraldehyde 3-phosphate dehydrogenase (GAPDH) (1:5,000, 6C5, Advanced ImmunoChemical Inc.), mouse anti-complex IV subunit I (1:1000, 1D6E1A8, MitoSciences.), mouse anti-tubulin (1:1000, E7, Developmental studies hybridoma bank, Iowa city, IA, USA) and rabbit anti-histone H2B (1:1000, 07-371, Millipore.). After washing, the membranes were incubated with either alkaline phosphatase conjugated anti-rabbit IgG (1:10000, A9919, Sigma) or anti-mouse IgG (1:10000, A3562, Sigma.) for 1 hour at room temperature. The signal was detected with the CDP-Star^{TM} chemiluminescent system (Applied Biosystems).

2.3 Results

2.3.1 Immunohistochemical analysis shows cytoplasmic and nuclear expression of human Tdp1 protein in most peripheral tissues

To clarify whether Tdp1 is expressed in the cytoplasm of tissues other than the neurons reported by Hirano *et al.* (Hirano et al., 2007), we profiled human Tdp1 protein expression by immunohistochemistry in postmortem tissues from a 6-week old female infant, a 39-week gestation male fetus and a 16-year-old woman (Figures. 2-1 to 2-5, Supplementary Figures A-6 to A-10 and Supplementary Table A-1). Comparison of the expression profiles found no significant changes overall in the subcellular localization of Tdp1 with age or sex. Similar to its expression in neural tissue (Hirano et al., 2007), cytoplasmic Tdp1, when expressed, had a punctate cytoplasmic subcellular distribution within all cell types analyzed. Processing of these tissues with pre-immune serum in place of immune serum did not show significant non-specific staining (Supplementary Figures A-1 to A-5, A-11 to A-13).

2.3.2 Endocrine system

In the adrenal cortical and medullary cells, Tdp1 was expressed in both the nucleus and cytoplasm (Figure 2-1A-E). Among cells of the adrenal cortex, Tdp1 was most highly expressed in the cytoplasm of cells within the zona glomerulosa (Figure 2-1B). To a lesser degree, Tdp1 was expressed in the cells of the zona fasciculata and zona reticularis (Figure 2-1C-D). In the adrenal medulla Tdp1 was expressed in both the nucleus and cytoplasm (Figure 2-1E). In the follicular cells of the thyroid, Tdp1 was also expressed in both the cytoplasm and nucleus (Figure 2-1F-G), whereas Tdp1 expression in the parafollicular cells was mostly nuclear. Tdp1 was expressed in both the nucleus and cytoplasm of parathyroid cells (Figure 2-1H-I).

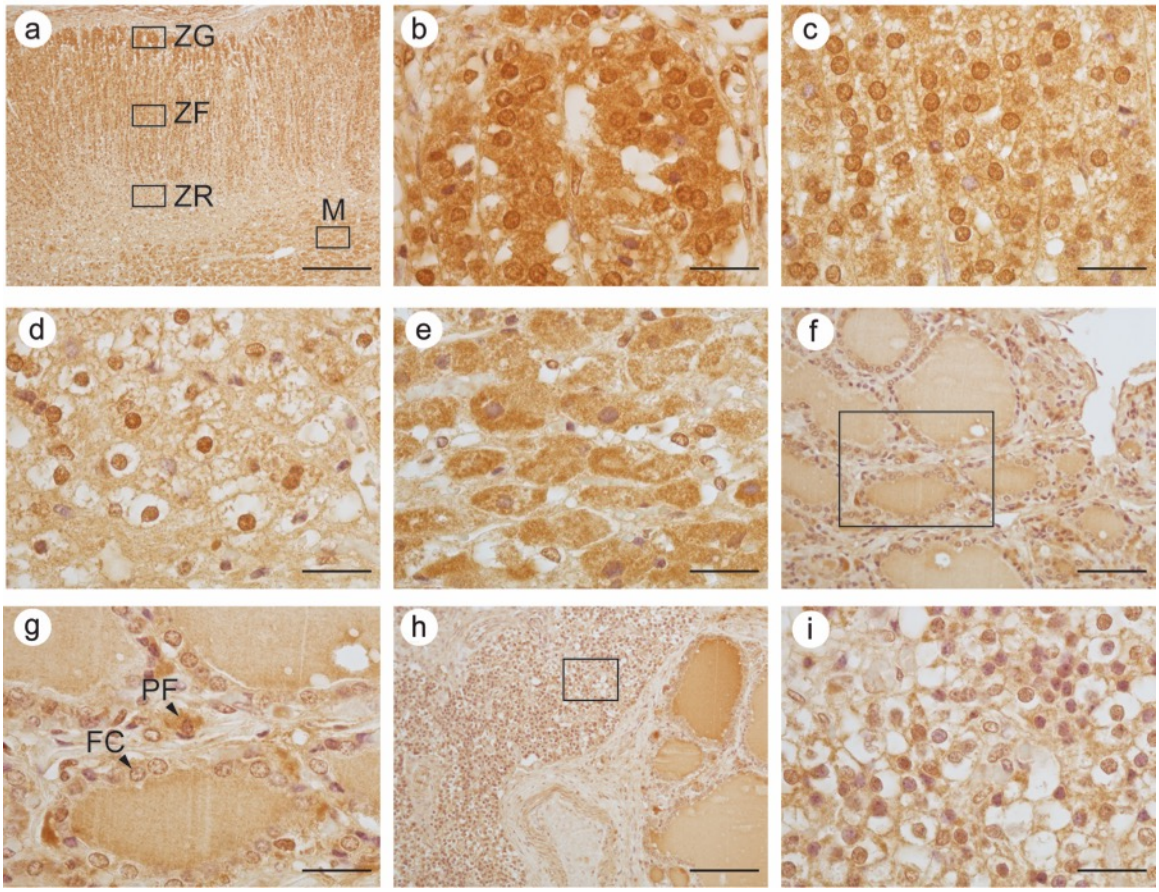

Figure 2-1: Photomicrographs of immunohistochemical analysis of human Tdp1 expression in the endocrine system.

A Overview of the adrenal gland **B** cells of the zona glomerulosa **C** zona fasciculata **D** zona reticularis **e** adrenal medulla **F-G** thyroid **H-I** parathyroid. ZG = zona glomerulosa; ZF = zona fasciculata; ZR = zona reticularis; M =

medulla; PF = parafollicular cell; FC = follicular cell. Boxed regions correspond to higher magnification images. Arrowheads indicate cells of interest. Scale bars: **A**= 1000 ¼m; **B**, **C**, **D**, **E**, **G**, **I** = 100 µm; **F** = 250 µm; **H** = 500µm.

2.3.3 Gastrointestinal system

Tdp1 was also expressed in the cytoplasm and nucleus of cells in the esophagus. Tdp1 expression was highest in the cells of the luminal epithelium (Figure 2-2A-B).

In the mucosal cells throughout the remainder of the gastrointestinal tract, Tdp1 expression was predominantly cytoplasmic (Supplementary Table A-2). In the stomach, Tdp1 was detected in the cytoplasm of the gastric pit cells (Figure 2-2C). In the small intestine, Tdp1 was expressed most highly in villi, specifically in the enterocytes within the villi (Figure 2-2D-E). In the colon, Tdp1 was expressed most highly in the nucleus and cytoplasm of the glandular epithelium (Figure 2-2F-G).

In the liver, Tdp1 was expressed in the cytoplasm and nuclei of hepatocytes and in bile duct cells (Figure 2-2I-J). In the exocrine pancreas, Tdp1 was predominantly in the cytoplasm of the acinar cells (Figure 2-2J-K). This contrasted with the islets of Langerhans, where Tdp1 was expressed almost exclusively in the nucleus (Figure 2-2L).

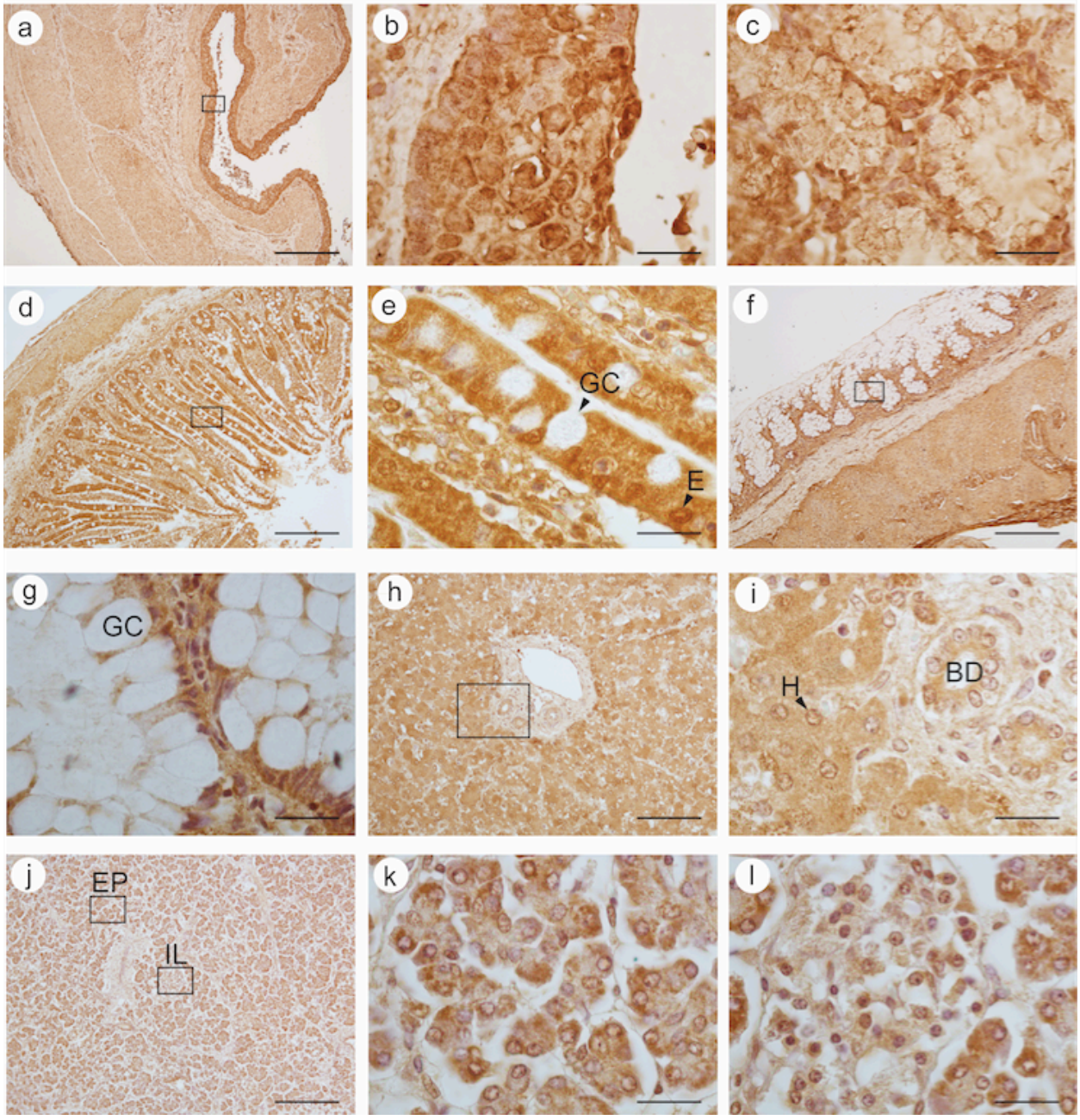

Figure 2-2: Photomicrographs of immunohistochemical analysis of human Tdp1 expression in the gastrointestinal system.

A-B esophagus **C** stomach gastric pit **D-E** intestinal villi **F-G** colon **H-I** liver **J** overview of pancreas **K** pancreatic acinar cells L islets of Langerhans. Boxed regions correspond to higher magnification images. Arrowheads indicate cells of interest. GC = goblet cell; E = enterocyte;BD = bile duct; H = hepatocyte; EP = endocrine pancreas; IL = islets of Langerhans. Scale bars: **A** = 2000 µm; **B**, **C**, **E**, **G**, **I**, **K**, **L** = 100µm**; D, F, J** = 1000µm; **H** = 500µm.

2.3.4 Genitourinary system

Tdp1 staining in the kidney showed prominent nuclear localization in the glomeruli (Figure 2-3A-B), whereas Tdp1 expression was comparable between the cytoplasm and nucleus of collecting ducts, tubules and the loop of Henle (Figure 2-3C-D). In the urinary bladder, the transitional epithelium and underlying connective tissue had both cytoplasmic and nuclear staining (Figure 2-3E-F). Within the seminiferous tubules of the testis, Tdp1 was detectable in the nuclei and cytoplasm of Sertoli cells, whereas the Leydig cells between the tubules had no Tdp1 staining (Figure 2-3G). In the epididymis, Tdp1 nuclear and cytoplasmic expression was highest in the epithelium and lowest in the surrounding smooth muscle (Figure 2-3H). Within the prostate, Tdp1 was most highly expressed in the cytoplasm and nuclei of the glandular epithelium (Figure 2-3G-H).

In the ovary, Tdp1 was expressed in the primary oocyte cytoplasm but nearly undetectable in the nucleus (Figure 2-3K=L). In contrast, follicular cells surrounding the primary oocyte expressed more Tdp1 in the nucleus than in the cytoplasm (Figure 2-3L). Tdp1 was also expressed in the zona granulosa and the follicular antrum. In the fallopian tube, Tdp1 was expressed both in the nucleus and cytoplasm of the columnar epithelial cells and cells within the lamina propria (Figure 2-3N-O).

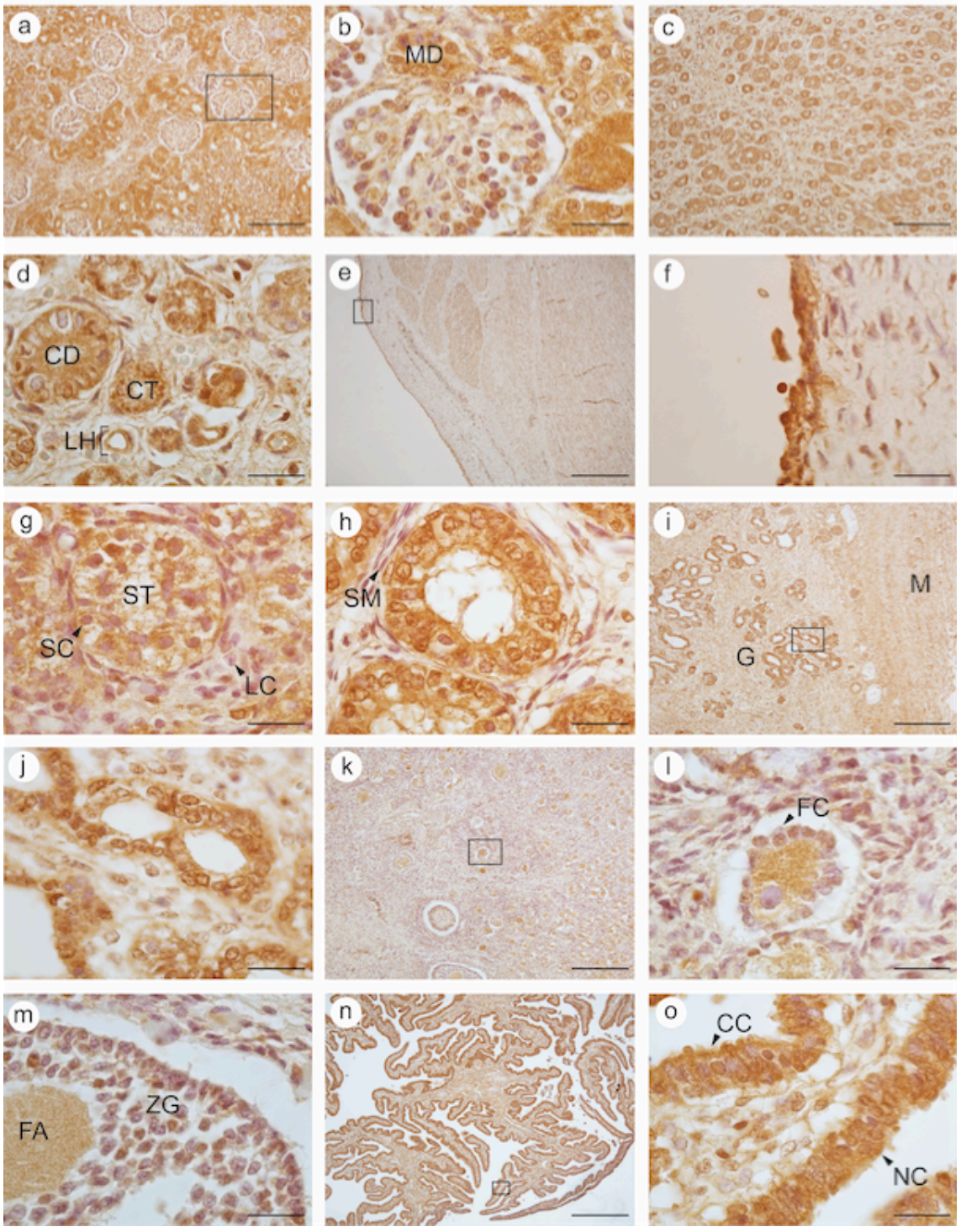

Figure 2-3: Photomicrographs of immunohistochemical analysis of human Tdp1 expression in the genitourinary system.

A-B glomeruli **C-D** renal tubules **E-F** urinary bladder **G** seminiferous tubule **H** epididymis **I-J** prostate **K-M** ovary **N-O** fallopian tube. Boxed regions correspond to higher magnification images. Arrowheads indicate cells of interest.

MD = macula densa; CD = collecting duct; LH = loop of Henle; ST = seminiferous tubule; SC = Sertoli cell; LC = Leydig cell; SM = smooth muscle; M = muscle; G = Glands; FC = follicular cell; FA = follicular antrum; ZG = zona granulosa; CC = ciliated columnar cell; NC = non-ciliated columnar cell. Scale bars: **A**, C=500 μm; **B**, **D**, **F**, **G**, **H**, **J**, **L**, **M**, **O** = 100 μm; **E**, **N** = 2000 μm; **I**, **K** = 1000 μm.

2.3.5 Pulmonary and cardiovascular systems

In the heart, Tdp1 was highly expressed in the myocardium and endocardium (Figure 2-4A-D). Within the myocardium, Tdp1 expression was high and comparable between the nucleus and cytoplasm (Figure 2-4A and B), whereas in the endocardium cytoplasmic expression predominated (Figure 2-4C and D).

Within the lung, Tdp1 localized predominantly to the cytoplasm of type I pneumocytes, whereas expression in type II pneumocytes was mostly nuclear (Figure 2-4F). Tdp1 was also detected in alveolar macrophages (Figure 2-4G). In the intrapulmonary bronchus, it was expressed in the cytoplasm and nucleus of the luminal epithelium (Figure 2-4H). In the blood vessel, Tdp1 was expressed in the nucleus and cytoplasm, albeit slightly more in the nuclei of cells within the tunica media (Figure 2-4I).

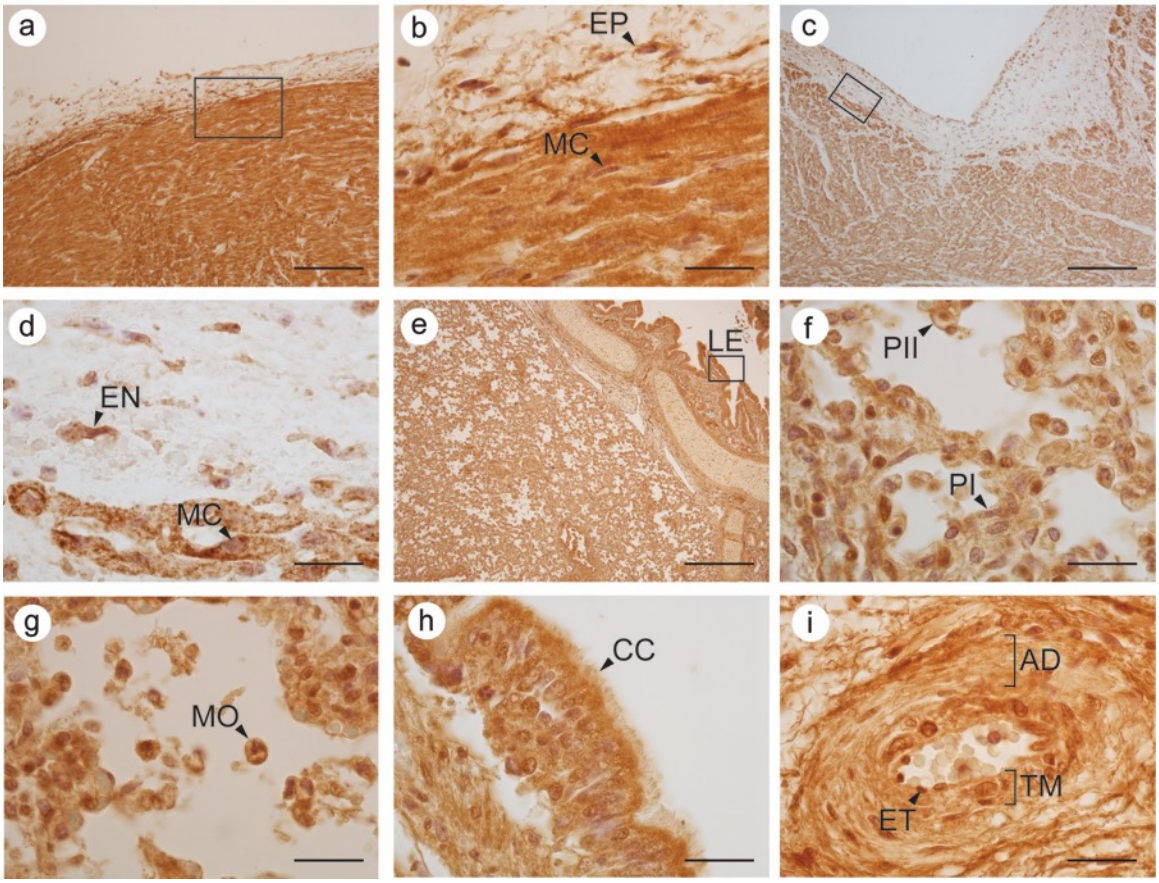

Figure 2-4: Photomicrographs of immunohistochemical analysis of human Tdp1 expression in the cardiovascular and pulmonary system.

A-B myocardium **C-D** endocardium **E** overview of lung **F-G** alveoli **H** bronchial epithelium I blood vessel. Boxed regions correspond to higher magnification images. Arrowheads indicate cells of interest. EP = epicardial cell; MC = myocardial cell; EN = endocardial cell; LE = luminal epithelium; PI = type I pneumocyte; PII = type II pneumocyte. MO = macrophage CC = ciliated epithelium. ET = endothelial cell; AD = adventitia; TM = tunica media. Scale bars: **A** = 500 µm; **C**, **D**, **F**, **H**, **H**, **I** = 100µm; **C** = 1000 µm; **E** = 2000 µm.

2.3.6 Immune system and bone

In the spleen (Figure 2-5A), Tdp1 was expressed in the cytoplasm and nuclei of cells within the white pulp (Figure 2-5B) and red pulp (Figure 2-5C). In the thymus (Figure 2-5D), Tdp1 was expressed predominantly in nuclei of lymphocytes in the thymic cortex and medulla (Figure 2-5E-F). Within bone marrow, Tdp1 expression was predominant in the nucleus of megakaryocytes, white blood cells and erythrocyte precursor cells (Figure 2-5G). Tdp1 was

expressed in the cytoplasm and nuclei of chondrocytes within the bone growth plate (Figure 2-5H-I).

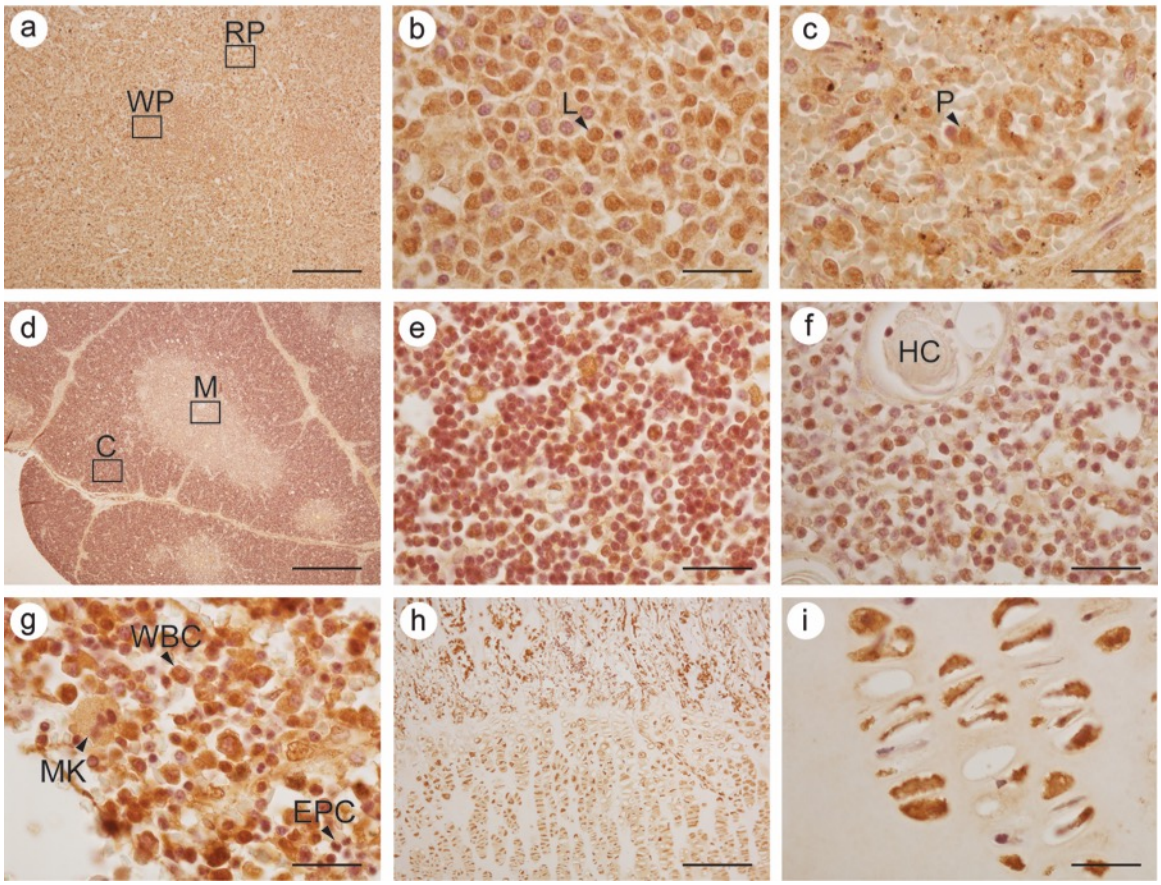

Figure 2-5: Photomicrographs of immunohistochemical analysis of human Tdp1 expression in the immune system and bone.

A overview of spleen **B** white pulp of spleen **C** red pulp of spleen **D** overview of thymus **E** cortex of thymus **F** medulla of thymus **G** bone marrow **H** bone growth plate **I** growth plate chondrocytes. Boxed regions correspond to the higher magnification images. Arrowheads indicate cells of interest. WP = white pulp; RP = red pulp; L = lymphocytes; P = phagocytic cells; M = medulla; C = cortex; HC = Hassal's corpuscle; MK = megakaryocyte; WBC = white blood cell; EPC = erythrocyte precursor cell. Scale bars: **A**, **H** = 1000 μm; **B**, **C**, **E**, **F**, **G**, **I** = 100 μm; **D** = 2000 μm.

2.3.7 Muscular system

Within skeletal muscle, Tdp1 was expressed in the cytoplasm and had undetectable expression in the nucleus (Figure 2-6A-D). Transverse sections showed that Tdp1 expression varied among muscle fibers (Figure 2-6C), and longitudinal sections showed Tdp1 expression along the Z-line (Figure 2-6D), which is where most mitochondria reside (Ogata and Yamasaki, 1997).

2.3.8 Cytoplasmic Tdp1 colocalizes with mitochondria *in vivo*

Given the localization of Tdp1 along the Z-line of skeletal muscle (Figure 2-6D) and prior reports that Tdp1 colocalized with the mitochondria in cultured breast cancer cells (Das et al., 2010; Walton et al., 2009), I hypothesized that cytoplasmic Tdp1 colocalized with mitochondria and selected skeletal muscle as a representative tissue for study. Indeed, immunofluorescence microscopy showed that cytoplasmic Tdp1 partially colocalized with the mitochondria and was hardy detectable in the nuclei of skeletal muscle cells (Figure 2-6E-G). Colocalization analysis of the image revealed that over 60% of skeletal muscle mitochondria contained Tdp1, and that this constitutes 95% of the total Tdp1 signal (Figure 2-6I). Confirming this distribution of Tdp1, immunoblotting of mitochondrial and nuclear subcellular fractions from skeletal muscle detected Tdp1 expression only in the mitochondrial fraction (Figure 2-6J).

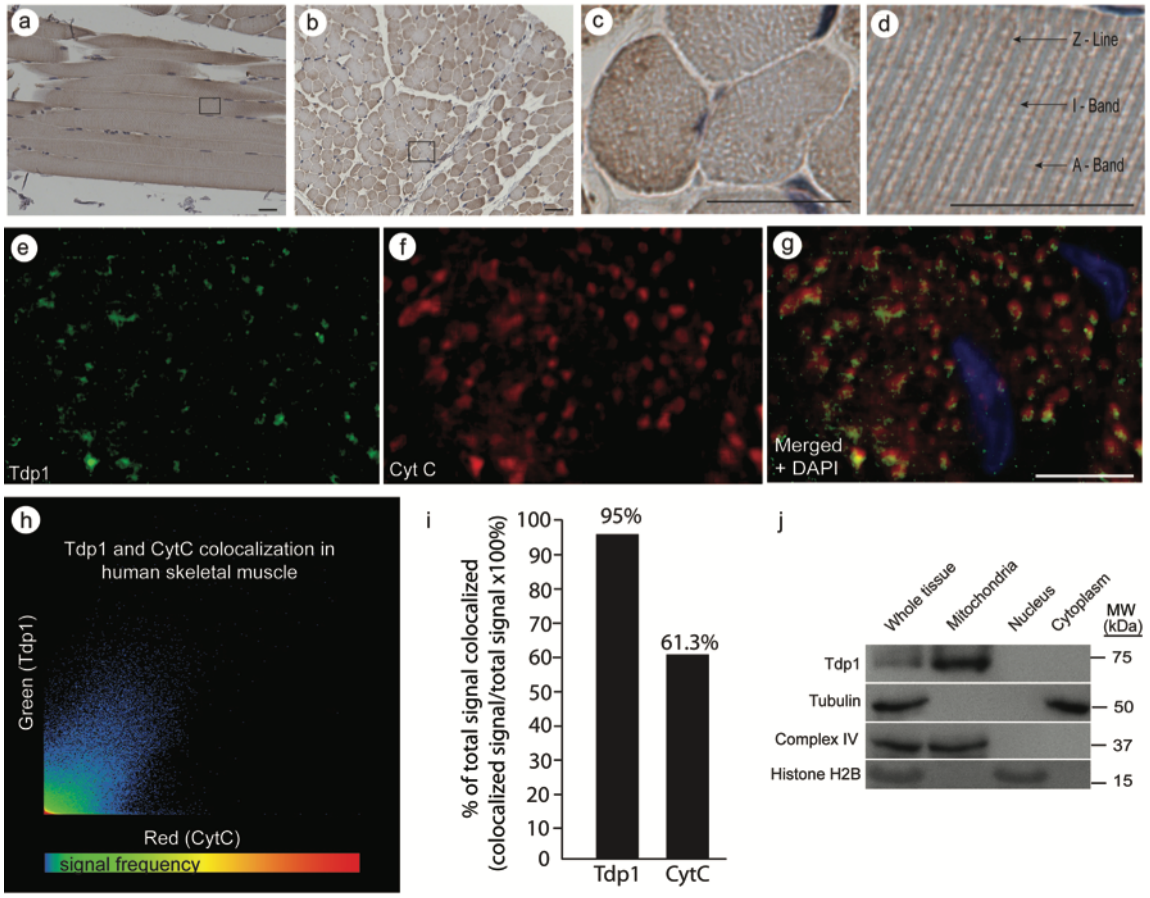

Figure 2-6: Tdp1 expression in human skeletal muscle.

A-D skeletal muscle. Note that Tdp1 staining is predominantly cytoplasmic and lies along the Z-line of muscle fiber. **E-G** Photomicrographs of immunofluorescent colocalization of human Tdp1 with the mitochondrial protein cytochrome C (Cyt C) in a transverse section of skeletal muscle. **H** scatterplot of Tdp1 and cytochrome C signal frequency and intensity, showing a high amount of colocalizing signals **I** graph showing degree of colocalization in Tdp1 and cytochrome C signals **J** photograph of an immunoblot of skeletal muscle subcellular fractions showing co-purification of Tdp1 protein with mitochondria but not nuclei. The boxed regions correspond to higher magnification images. Scale bars = 10 µm.

2.3.9 Tdp1 is primarily in the mouse cytoplasm and colocalizes with mitochondria

To test whether the cytoplasmic localization of Tdp1 in human tissue might arise from diffusion out of the nucleus secondary to rapid tissue degradation, I assessed Tdp1 subcellular distribution in tissues harvested from mice perfused with 4% paraformaldehyde while alive and sedated. These tissues, which were immediately harvested for cryosectioning, had cytoplasmic

Tdp1 and partial colocalization of Tdp1 with cytochrome C (Supplementary Figures A-14 to A-19). Similar to human tissue, therefore, mouse Tdp1 colocalized with mitochondrial markers in many tissues (Supplementary Figures A-14 to A-19).

2.3.10 Tdp1 relocates to the mitochondria during oxidative stress

Having observed colocalization and co-purification of Tdp1 with mitochondria, I questioned what stimuli might regulate the differential distribution between the mitochondria and nucleus. Since the mitochondrial DNA is highly susceptible to oxidative damage (Mecocci et al., 1993), I hypothesized that Tdp1 protects mitochondrial DNA from such damage (Ames et al., 1993). To assess this in cultured human dermal fibroblasts, we determined the 24 hour LD_{50} for H_2O_2 (200 nM) and menadione sodium bisulphite on human fibroblasts and chose doses below the LD_{50} to assess Tdp1 distribution (Supplementary Figure A-20). As shown at doses of 200 nM for H_2O_2 and 12 μM for menadione sodium bisulphite, immunofluorescence colocalization and immunoblotting showed that treatment with oxidants increased expression of Tdp1 in the cytoplasm (Figure 2-7A-I). Treatment with MSBS caused Tdp1 to colocalize with 30% of mitochondria, and H_2O_2 treatment led to colocalization with >75% of mitochondria (Figure 2-7J-O). Immunoblotting of subcellular fractions from fibroblasts in the presence and absence of H_2O_2 treatment also confirmed the colocalization of Tdp1 with mitochondria (Figure 2-7P). Lastly, to investigate whether the oxidant treatment induced increased expression of *TDP1* mRNA and the Tdp1 protein, we performed qRT-PCR analysis and immunoblotting of Tdp1 and found reduced mRNA levels and steady protein levels (Figure 2-7Q-R). This suggested that oxidant stress caused the relocalization of existing Tdp1 into the mitochondria.

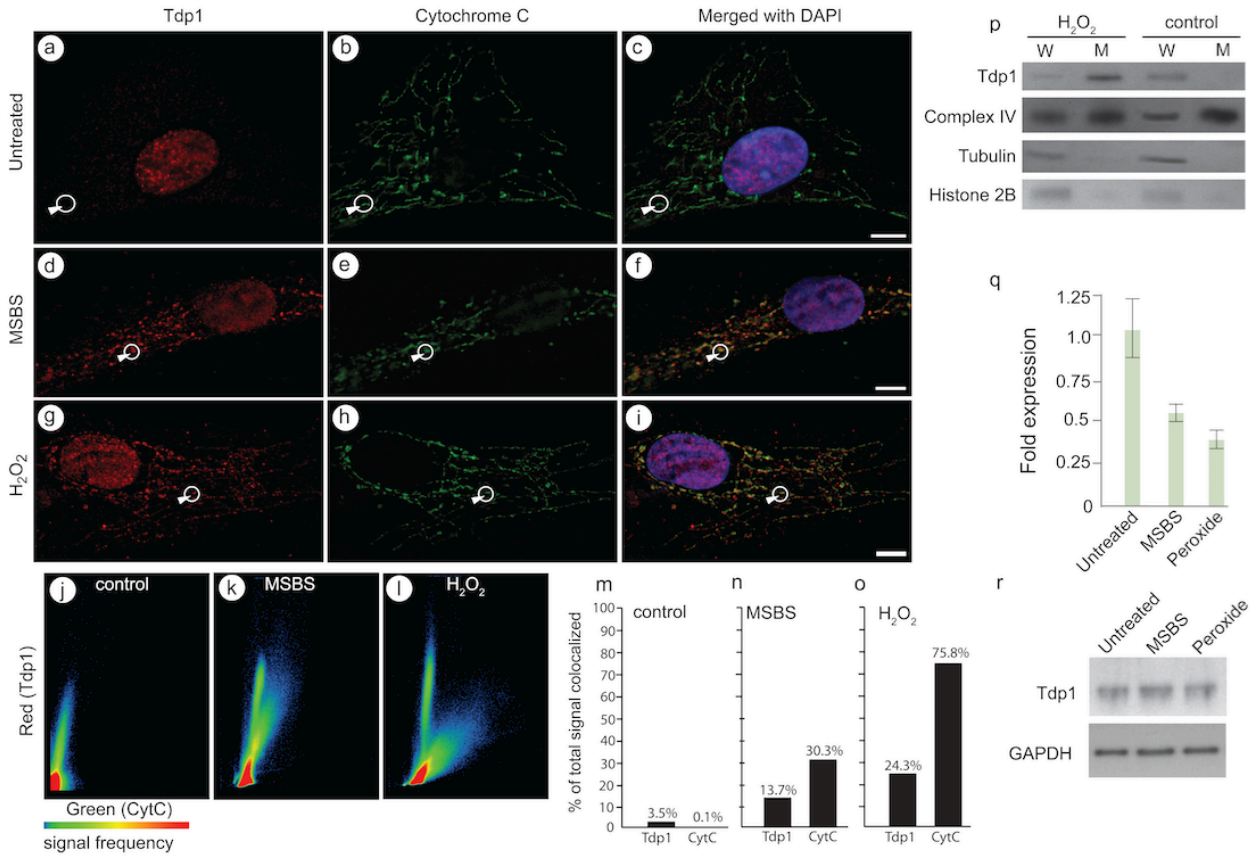

Figure 2-7: Tdp1 expression in cultured human dermal fibroblasts in the presence and absence of oxidative stress.

A-C Photomicrographs of immunofluorescent colocalization of human Tdp1 with the mitochondrial protein cytochrome C (Cyt C) in untreated dermal fibroblasts. **D-I** photomicrographs of immunofluorescent colocalization of human Tdp1 with the mitochondrial protein cytochrome C (Cyt C) in dermal fibroblasts treated with 12 µM menadione sodium bisulphite (MSBS) or 200 nM hydrogen peroxide (H_2O_2) for 24 hours **J-L** scatterplot of Tdp1 and cytochrome C signals showing increased colocalization of Tdp1 with cytochrome C after oxidative stress **M-O** graphs showing the degree of colocalization of Tdp1 and cytochrome C signals **P** immunoblot of mitochondrial fraction in human fibroblasts post-treatment with and without hydrogen peroxide treatment for 24 hours **Q** RT-PCR analysis of Tdp1 gene expression in human fibroblast cell lines with and without oxidant treatment for 24 hours **R** immunoblot of whole-cell extracts showing Tdp1 protein levels with and without oxidant treatment for 24-hours. W = whole cell extract. M = mitochondrial extract. Scale bars = 10 µm.

2.4 Discussion

I showed for the first time Tdp1 protein expression in peripheral human tissue. Tdp1 was expressed in all non-central nervous system tissues studied. Similar to the neurons presumably affected in SCAN1 (Hirano et al., 2007), it was expressed in the cytoplasm of peripheral tissues

obtained from three unrelated individuals, and exhibited no notable sex or age-dependent differences in expression among tissues from the three individuals. Comparison of expression between human and mouse tissues showed more prominent cytoplasmic expression of Tdp1 in most mouse tissues but no other marked differences. In both species, Tdp1 was rarely expressed exclusively in either the nucleus or the cytoplasm suggesting that it has a function in both locations. In human skeletal muscle, which had undetectable nuclear Tdp1, the cytoplasmic Tdp1 localized near or with mitochondria and co-purified with mitochondria, and similar colocalization with mitochondria was observed in the mouse tissues. Because this subcellular distribution of Tdp1 was observed in tissues from three different humans and from perfused mice, I conclude that the cytoplasmic Tdp1 does not arise from postmortem diffusion of Tdp1 out of the nucleus.

This then raised the question of what a DNA repair enzyme is doing in the cytoplasm. I chose to test whether oxidative stress could alter the localization of Tdp1 because it is a known mutagen of mitochondrial DNA and because Tdp1 deficient cells are hypersensitive to oxidative stress (El-Khamisy et al., 2005). Cultured human dermal fibroblasts were the perfect model for this test since they have nearly undetectable cytoplasmic Tdp1, and indeed oxidative stress markedly increased expression of cytoplasmic Tdp1 and caused its partial colocalization with mitochondria. Based on these observations, I hypothesize therefore that, in addition to its nuclear role, Tdp1 is also likely a mitochondrial DNA repair enzyme (Das et al., 2010; Walton et al., 2009) and that one stimulus for its traffic to mitochondria is oxidative stress.

The generation of ATP via the electron transport chain at the inner mitochondrial membrane generates reactive oxygen species. This inevitably exposes the mitochondrial DNA (mtDNA) to high levels of oxidative stress, particularly since the mtDNA is located in close proximity to the inner mitochondrial membrane and lacks protective histones (Ames et al., 1993). Consequently, the levels, extent and persistence of oxidative base damage in mtDNA are higher than in nuclear DNA, and this damage could predispose mitochondrial Topo I (mtTopo I) to form long lived complexes with mtDNA (Hudson et al., 1998; Takashima et al., 2002; Yakes and Van Houten, 1997; Zhang et al., 2001), a substrate of Tdp1. Indeed, the presence of reactive oxygen species sensitizes $Tdp1^{-/-}$ cells to DNA strand breaks (El-Khamisy et al., 2005).

DNA repair activities identified and characterized in mammalian mitochondria include base excision repair (BER), mismatch repair and double-stranded break repair (Kamenisch et al.,

2010; Lakshmipathy and Campbell, 1999; Larsen et al., 2005). BER is the predominant mechanism for repair of the oxidative base damage and DNA single strand breaks in the mitochondria. As a mitochondrial BER protein (Das et al., 2010), Tdp1 might participate in the repair of oxidative mtDNA damage via processing of 3′-phosphoglycolate obstructive termini, apurinic/apyrimidinic sites and mtTopo I-mtDNA complexes (Fam et al., 2012).

This raised the question of whether SCAN1 is a mitochondrial disorder (Fam et al., 2012). Mitochondrial disorders are classically progressive multisystem disorders; however, mitochondrial dysfunction also causes isolated optic atrophy, sensorineural deafness, cardiomyopathy, diabetes, pseudo-obstruction, neuropathy, myopathy, liver disease, early strokes, or seizures (Johns, 1995; Koene and Smeitink, 2011). Mitochondrial disorders arise throughout life, can be tissue specific and are modified by gene-gene interactions (Dimauro, 2011; Thorburn et al., 2004). Mitochondrial dysfunction has been associated with cancer, infertility, diabetes, heart diseases, blindness, deafness, kidney disease, liver disease, stroke, migraine, dwarfism, medication toxicity, aging and age-related neurodegenerative diseases such as Parkinsonism and Alzheimer disease (Abou-Sleiman et al., 2006; Koene and Smeitink, 2011; Moreira et al., 2006). In this context, therefore, SCAN1 could well be a mitochondrial disorder, although proof of that requires more study.

Regardless of whether SCAN1 is a mitochondrial disorder, the abundance of Tdp1 in human and mouse cytoplasm is intriguing. It is unknown whether Tdp1 is stored in a cytoplasmic reservoir for dynamic transport between the nucleus and mitochondria, or whether it has an undescribed cytoplasmic function. Additionally, there has been almost no study of the mechanism of its relocalization within the cell. Post-translational modification is one mechanism by which the localization of proteins is regulated (Silhavy et al., 1983). Tdp1 undergoes two post-translational modifications (Chiang et al., 2010; Hudson et al., 2012). It is phosphorylated at serine 81 and SUMOylated at lysine 111; however, in Chapter 3, I show that phosphorylation of serine 81 is not required for Tdp1 subcellular localization. SUMOylation of lysine 111 has only been studied in the context of Tdp1 enzymatic activity and affinity for its substrate, not in the context of Tdp1 subcellular localization.

In contrast to a prior comparison of the mouse and human central nervous systems (Hirano et al., 2007), I did not find a notable difference of Tdp1 localization between mouse and human peripheral tissues. Defining the basis of the differences in the expression pattern in the brain

might provide an explanation for why Tdp1 deficient mice do not develop ataxia reminiscent of humans with SCAN1 (Hirano et al., 2007). However, other possible explanations include the finding that the affected humans have a point mutation in *TDP1* which confers neomorphic properties on the Tdp1 enzyme, whereas the mutant mice have a simple deficiency of the Tdp1 enzyme (El-Khamisy et al., 2009; Hawkins et al., 2009; Hirano et al., 2007; Interthal et al., 2005b). Lastly, as has been observed with several mouse models of neurological disease, mice may not be a good model system for the study of this particular disease because they have more robust redundant DNA repair mechanisms, because they have shorter lifespans or because their neurons have a reduced stress against which Tdp1 is protective (Hafezparast et al., 2002).

In summary, I conclude that Tdp1 is expressed in most, if not all, peripheral human and mouse tissues and that nearly all of the studied tissues express cytoplasmic Tdp1. By comparing male and female as well as neonatal and adolescent tissues, I see no notable differences in Tdp1 localization over time. Importantly, we find that in both mice and human tissues, some cytoplasmic Tdp1 colocalizes with mitochondria. However, more studies are necessary to define fully the function of cytoplasmic and mitochondrial Tdp1 as well as the mechanism regulating its distribution among subcellular compartments.

Chapter 3: Reactive Oxygen Stress Mediates Tdp1 Translocation from the Nucleus to Mitochondria

3.1 Introduction

Tyrosyl-DNA phosphodiesterase 1 (Tdp1) is a 3′-DNA phosphodiesterase that participates in DNA repair. It resolves stalled topoisomerase I-DNA complexes by cleavage of the 3′-phosphotyrosine bond. Less characterized functions of Tdp1 include the processing of endogenous 3′-DNA lesions such as alkylated bases, phosphoamides and chain-terminating nucleosides (Alagoz et al., 2014; Huang et al., 2013; Lebedeva et al., 2013; Pommier et al., 2014).

Tdp1 colocalizes with mitochondria in human and mouse tissue and in cultured human and mouse cells following exposure to hydrogen peroxide (Fam et al., 2013b). These findings suggest that Tdp1 enters the mitochondria in response to mitochondrial DNA (mtDNA) stress to repair mtDNA (Das et al., 2010; Fam et al., 2013b).

Compared to nuclear DNA, maintenance of mtDNA has several challenges. First, 95% of mtDNA is gene coding, whereas approximately 1-2% of nuclear DNA is (Alexeyev et al., 2013). Second, unlike nuclear DNA, mtDNA is not packaged into chromatin, which increases its exposure to mutagens as it lacks protective histones and DNA compaction (Taanman, 1999). Third, mtDNA is in close proximity to the reactive oxygen species (ROS) generated by mitochondrial respiration (Wei, 1998). Fourth, mitochondria lack some DNA repair pathways comparable to those in the nucleus (Larsen et al., 2005). Unlike the nuclear genome, which maintains two copies of each gene, these vulnerabilities in mtDNA maintenance are partially compensated by the existence of several hundred copies of mtDNA genome in a cell. This allows more robust tolerance of mutagens.

Mitochondria produce oxidative agents as a by-product of electron transport chain activity. The generation of volatile oxidants during respiration causes polymerase-blocking oxidative lesions in mtDNA such as thymine glycols and 8-oxoguanine (Shokolenko et al., 2009; Yakes and Van Houten, 1997). The 8-oxoguanine lesions cause guanine to thymine transversions (Ohno et al., 2014) and mitochondrial dysfunction by mutation of mtDNA-encoded proteins, tRNAs and rRNAs. Mitochondrial lysates from breast cancer cells demonstrate base-excision repair (BER) activity (Das et al., 2010), a repair mechanism for oxidative lesions. Because Tdp1

participates in nuclear BER and colocalizes with mitochondria, I hypothesized that it also functions in mitochondrial BER (Fam et al., 2013b; Murai et al., 2012a).

H_2O_2-induced ROS activates stress-activated protein kinase (SAPK) signaling for import of proteins into the mitochondria. The activation of P38 MAP kinase mediates translocation of Bax to mitochondria where it oligomerizes with Bak and forms a pore on the mitochondrial outer membrane, allowing the release of cytochrome C and other pro-apoptotic proteins (Van Laethem et al., 2004). H_2O_2 also mediates crosstalk between mitochondria and neighboring organelles and, by peroxidation of mitochondrial membrane lipids, regulates secondary redox signaling in the cytoplasm (Ayala et al., 2014; Barbosa et al., 2013).

Herein I show that within *S. cerevisiae,* mouse and human cells, ROS induces Tdp1 entry into the mitochondrial matrix and that this is independent of new protein synthesis and mtDNA. I also find that intramitochondrial ROS is a signal for translocation of Tdp1 out of the nucleus and acts through P38 and ERK1. Within mitochondria, Tdp1 interacts with BER proteins ligase III and XRCC1. Consistent with a role for Tdp1 in mtDNA repair, embryonic fibroblasts and myoblasts derived from *Tdp1*$^{-/-}$ mice have more mtDNA lesions and impaired mitochondrial respiration compared to *wt* tissues.

3.2 Materials and methods

3.2.1 Cell culture

Human dermal fibroblasts and mouse embryonic fibroblasts were cultured in DMEM (Gibco BRL Life Technologies) supplemented with 10% heat-inactivated FBS (Hyclone) and 1% antibiotic-antimycotic (Gibco BRL Life Technologies). All cells were grown at 37º C with 5% CO_2 in a humidified environment.

3.2.2 MTT assay

Cell proliferation and viability were measured by MTT assay as previously described (Fam et al., 2013c). Briefly, 5 x 10^3 cells were plated in each well of a 96-well plate and cultured in phenol red-free media. MTT solution was prepared by dissolving 5 mg of MTT in 1 mL of 1X PBS. Following treatment of cultured cells with H_2O_2, the culture media was supplemented with 10% MTT and incubated for 3 hours. This was followed by a 30-minute incubation in 100%

DMSO. Spectrophotometry was done at 565 nm using the Wallac VICTOR2 Multilabel Plate Reader (Beckman-Coulter).

3.2.3 Immunoblotting

Immunoblotting was performed as described (Hirano et al., 2007). Briefly, cells were lysed in SDS-sample buffer (63 mM Tris HCl, 10% glycerol, 2% SDS, 0.0025% bromophenol blue, pH 6.8) and denatured by boiling for 5 minutes. The lysate was fractionated on a 10% or 15% gel by SDS-PAGE and transferred to a PVDF membrane. The membrane was incubated overnight at 4°C with blocking solution (0.2% I-Block (Applied Biosystems) and 0.1% Tween 20 in 1X PBS) and gentle agitation. The membrane was then incubated overnight at 4º C with primary antibodies diluted in blocking buffer. After washing, the membranes were incubated with secondary antibodies for 1 hour at room temperature. The signal was detected with the CDP-Star™ chemiluminescent system (Applied Biosystems). The antibodies used for immunoblotting are listed in Supplementary Table B-1.

3.2.4 Quantitative immunoblotting

Quantitative fluorescent immunoblotting was performed as previously described (Eaton et al., 2014). Briefly, 20 µg of total protein was separated by SDS-PAGE on a 10% gel and then transferred to a PVDF membrane. Subsequently, the membrane was rocked with a blocking solution (1:1 mixture of LI-COR Odyssey blocking buffer and 1X phosphate buffered saline (PBS, 137 mM NaCl, 2.7 mM KCl, 10 mM Na_2HPO_4, 2 mM KH_2PO_4, pH 7.4)) for 1 hour at room temperature. The membrane was then incubated for 1 hour at room temperature with primary antibodies diluted in blocking solution and 0.01% Tween 20 (Supplementary Table B-1). The membrane was then washed four times for 5 minutes in washing solution (1X PBS, 0.01% Tween 20). The membrane was then incubated for 1 hour at room temperature with secondary antibodies diluted in blocking solution plus 0.01% Tween 20. The membrane was then washed four times for 5 minutes in washing solution. A final 5-minute wash was with 1X PBS. A laser intensity of 5 for the appropriate channels was used as default when the membrane was scanned. The IRDye® 800 CW Goat anti-Mouse IgG and IRDye® 800 CW Goat anti-Rabbit IgG antibodies were used at a dilution of 1:10,000.

3.2.5 Immunofluorescence microscopy

Immunofluorescence microscopy was performed as described (Hirano et al., 2007). Briefly, approximately 5 x 10^5 cells were grown on a cover slip. Human or mouse cells were washed with 1X PBS and fixed with 4% paraformaldehyde (PFA) in phosphate buffer (PB, 22.46 mM NaH_2PO_4, 77.54 mM Na_2HPO_4, pH 7.4) for 15 minutes. Cells were permeablized with 0.5% Triton X-100 in 1X PBS for 15 minutes, blocked for 1 hour at room temperature with blocking buffer (20% horse serum, 1% casein in 1X PBS), and then incubated overnight at 4º C with the primary antibodies (Supplementary Table B-1). All images were acquired using the Leica TCS SP5 II confocal microscope.

3.2.6 Subcellular fractionation of human and mouse cells

To purify mitochondria, confluent cultured cells from five 10 cm dishes were released using trypsin and pooled. The cells were lysed in lysis buffer A (Mitochondria Isolation Kit for Cultured Cells, Abcam) and centrifuged at 14,000 x *g* to obtain a crude mitochondrial pellet and supernatant containing cytoplasmic proteins without contaminating mitochondria. The mitochondria were purified from this crude pellet by ultracentrifugation at 80,000 × *g* for 4 hours using a step gradient of Optiprep™ (60% iodixanol, AXIS-SHIELD). The step gradient was prepared using 40% (w/v), 30% (w/v) and 10% (w/v) iodixanol and the crude mitochondrial pellet was dispersed in the bottom 40% layer. Mitochondria were collected from the 30%-10% iodixanol interface and diluted 1:5 with mitochondria isolation buffer (0.25 M sucrose, 1 mM EDTA, 20 mM HEPES-NaOH, pH 7.4). This preparation was centrifuged at 14,000 × *g* for 10 minutes to obtain a mitochondrial pellet for immunoblotting. All steps were done at 4º C, and all solutions and buffers contained 1X protease inhibitor cocktail (Roche).

3.2.7 Immunoprecipitation of Tdp1

Briefly, I used the Pierce™ Pull-Down PolyHis Protein:Protein Interaction Kit (Thermo Scientific) to immunoprecipitate Tdp1-interacting proteins in the mitochondria of cultured MEFs. Preparation of mitochondrial lysate was as described above. Preparation and immobilization of the polyhistidine-tagged Tdp1 protein, as well as capture and elution of prey protein was performed as per the manufacturer's protocol. The presence of Tdp1-interacting proteins in the eluate was determined by SDS-PAGE and immunoblotting.

3.2.8 Yeast strains

Yeast strains were cultured as described in their source publications. Single gene mutants were obtained from the yeast deletion collection (Winzeler et al., 1999). The TDP1-GFP strain was obtained from the Yeast GFP collection (Huh et al., 2003). Temperature-sensitive knockout strains of essential genes TIM23 and MIA40 were obtained from the temperature sensitive mutant repository (Ben-Aroya et al., 2008).

3.2.9 Subcellular fractionation of yeast cells

The fractionation of yeast cells was adapted from a previous study (Rieder and Emr, 2001). Briefly, yeast cells were grown to mid-exponential phase in YPD and harvested by centrifugation at 3,000 × *g*. The cells were then resuspended in 100 mM tris-sulphate buffer (pH 9.4) and 10 mM DTT; the yeast cells were then treated with Zymolase 100T at a concentration of 5 μg/OD_{600} unit of cells at 30°C. Spheroplasts were then harvested by centrifugation at 1,500 × *g* at room temperature and washed twice in homogenization medium (HM; 250 mM sucrose, 10 mM HEPES (pH 7.4), 1 mM EDTA (pH 8.0) and 1 mM DTT) supplemented with complete protease inhibitor (Roche). Spheroplasts were lysed with 20 strokes of a tight-fitting Dounce homogenizer, and then the cell homogenate was centrifuged at 10,000 × *g* for 15 minutes at 4°C. The pellet was suspended in 2 mL 250 mM sucrose, 10 mM HEPES (pH 7.4) and 1 mM EDTA (pH 8.0) buffer, and layered on top of a 10 mM HEPES-buffered sucrose step gradient (2 mL, 15%; 3 mL, 25%; 3 mL, 40%; and 2 mL, 60%, respectively) and centrifuged for 1 hour at 4°C at 32,000 rpm in a SW32Ti rotor (Beckman). The visible reddish-brown mitochondria-enriched layer was collected into a 2 mL centrifuge tube.

3.2.10 Generation of Rho-zero MEFs

Mouse embryonic fibroblasts were treated with 100 ng/mL of ethidium bromide in DMEM (Gibco BRL Life Technologies) supplemented with 10% heat-inactivated FBS (Hyclone) and 1% antibiotic-antimycotic (Gibco BRL Life Technologies), 2.5 mM sodium pyruvate and 50 μg/mL uridine for 2 weeks. Cells were considered Rho-zero when expression of mitochondrial genes was undetectable by PCR and mtDNA was undetectable by PicoGreen staining, which was performed as previously described (Ashley et al., 2005). To determine the

expression of mitochondrial (i.e., cytochrome oxidase II) and nuclear (i.e., S6 ribosomal subunit) genes, total RNA was isolated using the Qiagen RNeasy mini kit (Qiagen). 3 µg of RNA was reverse transcribed with qScript cDNA Supermix using a proprietary blend of random and oligo (dT) primers (Quanta Biosciences). Quantitative PCR of the cDNA was performed with the PerfeCTa SYBR Green SuperMix mix (Quanta Biosciences) using the Applied Biosystems 7500 Real-Time PCR System. Data was analyzed using the Applied Biosystems 7500 software. Primer sequences are listed in Supplementary Table B-2.

3.2.11 Transfection of cultured cells with siRNA

Human dermal fibroblasts were transfected with ERK1 siRNA (Thermo Scientific/Dharmacon; L-003592-00-0005), p38 siRNA (Cell Signaling; 6562S) or Tim23 siRNA (Thermo Scientific/Dharmacon; L-190121-00-0005). Rho-zero MEFs were transfected with ERK1 siRNA (Thermo Scientific/Dharmacon; L-040126-00-0005) or p38 siRNA (Cell Signaling; 6417S). All siRNAs were transfected using Lipofectamine 3000 (Thermo Fisher Scientific) according to the manufacturer's protocol and incubated in appropriate culture media for 48 hours prior to experimentation. Cells were transfected with non-targeting siRNA as control (Thermo Scientific/Dharmacon; D-001810-01-05).

3.2.12 Isolation of mouse skeletal muscle myoblasts

Mouse skeletal myoblast isolation was performed as described (Rando and Blau, 1994). Briefly, the limbs of 3 mice were rinsed with 70% ethanol. The muscle tissue was dissected away from the skin and bone and placed into a tissue culture dish. The tissue was kept submerged in PBS and finely cut up with a razor blade and then triturated several times to break up larger clumps. The cells were centrifuged at 4°C, 350 × *g* for 5 minutes. Two mL of collagenase solution per gram of tissue was added to the minced tissue and incubated at 37°C for 20 minutes. The tissue mixture was triturated every 5 minutes to mix collagenase thoroughly with the tissue. This slurry was then filtered through an 80-micron filter and the eluted cells were centrifuged for 5 minutes at 400 × *g*. The pellet was suspended in 4 mL of F-10 myoblast growth medium and plated into a 35 mm collagen-coated tissue culture plate. To enrich for myoblasts, the cells were incubated at 37°C, 5% CO_2 for several days. The F-10 culture medium was changed every 2 days. When 80% confluent, the F-10 culture medium was removed and the cells were incubated

in 1X PBS for 2 minutes at 37°C. Following aspiration of the PBS, the myoblasts were selected by hitting the side of the dish firmly with the palm of the hand to allow the myoblasts to come off the bottom of the plate and leave the fibroblasts behind. The myoblasts were then plated on a collagen-coated dish for 15 minutes to allow residual fibroblasts to stick to the dish. The cells remaining in suspension after 15 minutes were transferred into a new dish; passaging was repeated until fibroblasts were removed.

3.2.13 Respiration analysis of cultured cells and myoblasts

Seahorse analysis was performed as described (Nicholls et al., 2010). Briefly, the plates were put in a Seahorse XF24 extracellular flux analyzer at 37°C (Agilent Technologies) for a 10-minute calibration and 3 measurement cycles to record basal cellular respiration. Oligomycin (5 μg/mL), FCCP (5 μM), and a mixture of rotenone (1 μM) plus antimycin A (2 μM) were then added sequentially to inhibit the ATP synthase, to uncouple oxidative phosphorylation, and to gauge non-mitochondrial respiration, respectively.

3.2.14 Measurement of ATP production in cultured cells

ATP production in cultured cells was measured using the CellTiter-Glo® Assay kit (Promega). Briefly, 1 x 10^4 cells were seeded in 100 μL of culture media, in an opaque-walled 96-well plate and placed in an incubator overnight at 37°C, 5% CO_2. The following day, 100 μL of CellTiter-Glo® reagent was added to each well. The 96-well plate was then put onto an orbital shaker for 2 minutes to lyse the cells and incubated for 10 minutes at room temperature. Luminescence was measured at 520 nm using the Wallac VICTOR2 Multilabel Plate Reader (Beckman-Coulter).

3.2.15 Mitochondrial random mutation assay

Mutations in the mouse mitochondrial genome were quantified as previously described (Vermulst et al., 2008). Briefly, mtDNA was digested with *TaqI* for 5 hours, with the addition of 100 units of *TaqI* every hour. The mtDNA was then aliquoted at 5 ng/μL per well of a 96-well plate. PCR amplification of mtDNA regions encompassing *TaqI* restriction sites was performed using the primers listed in Supplementary Table B-2. Primers that did not flank a *TaqI* restriction site were used to quantify the mtDNA genomes. PCR amplification was performed as follows:

step 1, 37°C for 10 minutes; step 2, 95°C for 10 minutes; step 3, 95°C for 30 seconds; step 4, 58/60°C for 1 minute; step 5, 72°C for 1.5 minutes; step 6, go to step three 44 times; step 7, 72°C for 4 minutes; step 8, melting curve from 65°C to 95°C; step 9, hold at 4°C indefinitely. PCR reactions were carried out in 25 μL reactions using the Brilliant SYBR-green real-time PCR master mix (Thermo Fisher Scientific), 10 pM of forward and reverse primers, and 1 unit of uracil DNA glycosylase.

3.2.16 Mitochondrial lesion assay

Mitochondrial lesions were quantified by long-amplicon quantitative PCR as described (Gonzalez-Hunt et al., 2016). Primers amplifying the short and long mtDNA regions of interest are listed in Supplementary Table B-2. Briefly, the LongAMP Hot Start Taq 2x (New England Biolabs) was used to amplify mtDNA by quantitative PCR. The PCR master mix consisted of the following: nuclease-free water, LongAmp Master Mix, 10 μM primers, and 15 ng total cellular DNA template per 50 μL reaction. PCR amplification was performed as follows: step 1, 94°C for 2 minutes; step 2, 94°C for 15 seconds; step 3, 64°C for 12 minutes; step 4, go back to step two 20 times; step 5, 72°C for 10 minutes; step 6, melting curve from 65°C to 95°C; step 7, hold at 4°C indefinitely. The short 117-bp mtDNA fragment was normalized to the 84-bp GAPDH fragment to derive relative mtDNA copy number. The frequency of DNA lesions was calculated as previously described (Rothfuss et al., 2010).

3.2.17 mtDNA deletion assay

The amplification of mtDNA deletion products was performed as previously described (Tanhauser and Laipis, 1995). Primers used to amplify the deletion junction are listed in Supplementary Table B-2. The thermal cycling protocol used was 95°C for 20 seconds, 55°C for 45 seconds, 72°C for 90 seconds for 35 cycles. A 3′-5′ DNA proofreading-deficient MEF cell line generated by a D181A point mutation in the mtDNA polymerase (PolG) was used as a positive control for mtDNA deletions. This PolG MEF cell line was a gift from Dr. David Chan at the California Institute of Technology.

3.2.18 Time-lapse photography of Tdp1 transport

For live-cell imaging, 3 x 10^5 human fibroblasts expressing Tdp1-cGFP and a mitochondria-targeted mCherry were seeded into an opaque-walled 35 mm glass-bottom cell culture dish (Willco Wells) and placed in a 37°C and 5% CO_2 environmental chamber (Precision Control Systems). Images were taken using a 96X objective with the MetaMorph 7.5 software (Molecular Devices) on an Olympus IX81 epifluorescent microscope. Images were taken once every 100 seconds and stitched together using MetaMorph (Molecular Devices).

3.2.19 Oligonucleotide assay for Tdp1 activity

Tdp1 enzymatic activity was determined by cleavage of an artificial substrate as described (Dean et al., 2014). Briefly, the assay was run at room temperature in a 96-well plate with a final volume of 100 µL per well. A final concentration of 50 nM DNA was used (5′-/56-TAMN/AGG ATC TAA AAG ACT T/3BHQ_1/-3′). Kinetic analysis was performed using a Varioskan plate reader (Thermo Fisher Scientific) at Ex557/Em582 for the TAMRA fluorophore. To establish Tdp1 cleavage activity, 20 reads were recorded at a kinetic interval of 45 seconds per read.

3.2.20 Homogeneous caspase assay for apoptotic cells

The activity of caspases 3 and 7, which play key effector roles in mammalian cell apoptosis, was measured using the Apo-ONE Homogeneous Caspase-3/7 kit according to the manufacturer's protocol (Promega). Briefly, 5 x 10^3 cells were plated per well of a 96-well plate, cultured for 24 hours and treated as described. Fluorescence of the cleaved caspase 3 and 7 substrate was measured at 520 nm using the Wallac VICTOR2 Multilabel Plate Reader (Beckman-Coulter).

3.2.21 Site-directed mutagenesis of Tdp1

The p.S81A mutation was introduced into *pcDNA3.1(-)•TDP1*^{WT} by site-directed mutagenesis according to the manufacturer's protocol using the QuikChange II XL site-directed mutagenesis kit (Agilent Technologies). *Tdp1*$^{-/-}$ MEFs were transfected with recombinant WT or mutant Tdp1 using Lipofectamine 3000 (Invitrogen). The sequences of the oligonucleotides used

are listed in Supplementary Table B-2. The mutant vector was validated by Sanger sequencing (Macrogen).

3.3 Results

3.3.1 H_2O_2 treatment of cells causes Tdp1 to enter the mitochondria

In a previous study, I found that Tdp1 colocalizes with mitochondria in MEFs and human dermal fibroblasts treated with H_2O_2 (Fam et al., 2013b). I treated both human dermal fibroblasts and MEFs with varying concentrations of H_2O_2 and found that a non-lethal dose of 1 μM H_2O_2 for 24 hours causes colocalization of Tdp1 and mitochondria (Supplementary Figure B-1(A and B)). To determine whether Tdp1 was associating with mitochondria or entering the mitochondrial matrix, I treated mitochondria purified from H_2O_2-exposed human dermal fibroblasts with proteinase K in the presence and absence of Triton X-100. Tdp1 was only digested by proteinase K following permeabilization of the mitochondrial membrane with Triton X-100 (Figure 3-1A), suggesting that H_2O_2 treatment causes Tdp1 to enter the mitochondria.

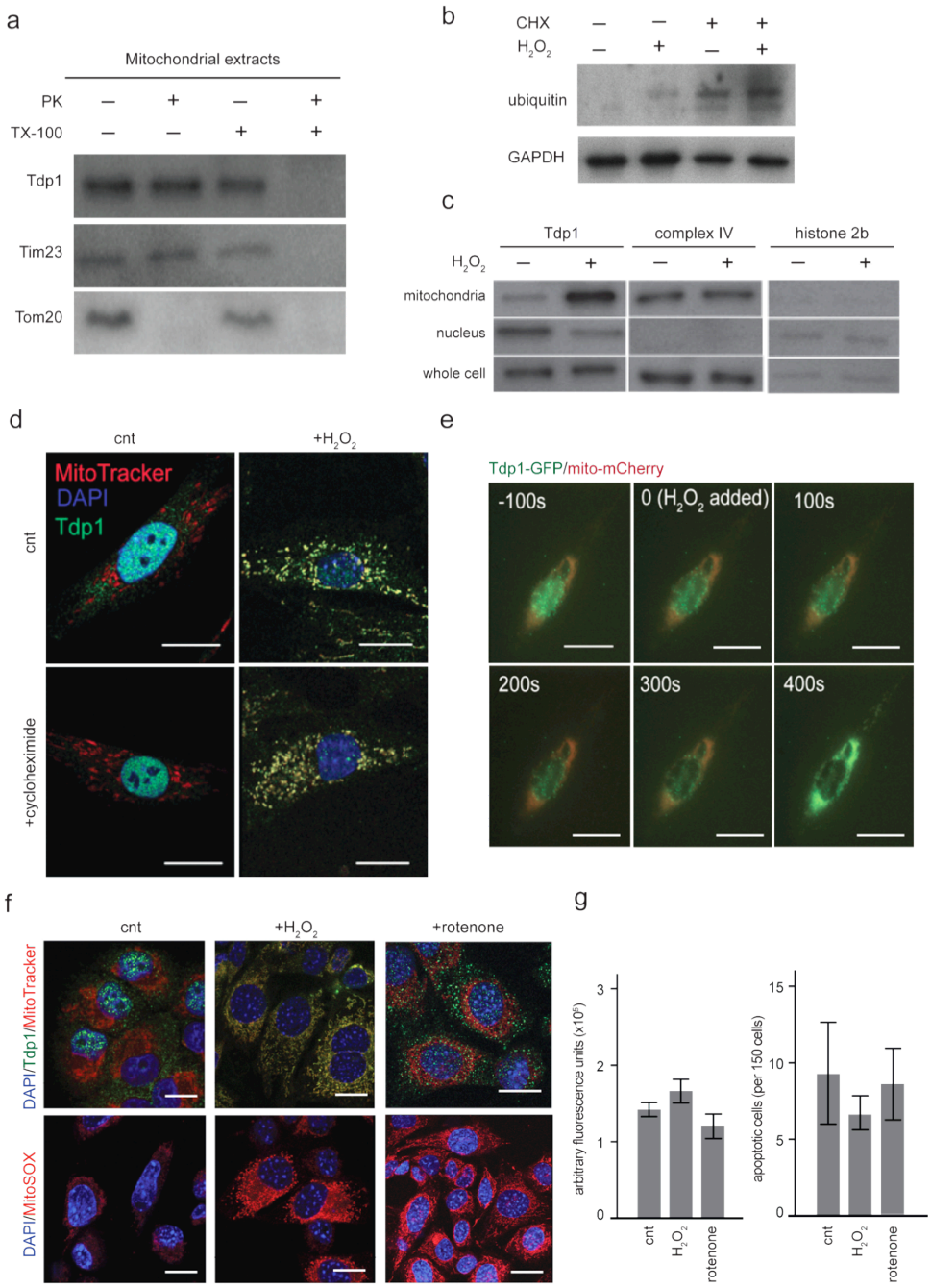

Figure 3-1: Tdp1 translocates from the nucleus into the mitochondria following H_2O_2 stress. (A) Photograph of an immunoblot showing susceptibility of mitochondrial Tdp1 to proteinase K digestion in the presence and absence of the detergent Triton X-100 (TX-100). Human fibroblasts were treated with 1 µM H_2O_2 for 1 hour and fractionated to collect mitochondria. Mitochondrial fractions were subsequently treated with 5 µg/mL proteinase K and/or 0.25% Triton X-100. Tim23 and Tom20 are components of the inner and outer mitochondrial membranes, respectively. (B) Photograph of an immunoblot of cytoplasmic extracts of cultured human fibroblasts in the absence or presence of treatment with 10 µM cycloheximide (CHX) and/or 1 µM H_2O_2 for 1 hour. GAPDH is a loading control. Indicative

of inhibition of protein synthesis, the treatment with CHX caused accumulation of ubiquitylated proteins. (C) Photograph of an immunoblot of subcellular lysates showing movement of Tdp1 within cultured human fibroblasts from the nucleus to the mitochondria in response to an hour treatment with 1 μM H_2O_2. Complex IV and Histone 2b are loading controls for the mitochondria and the nucleus. (D) Representative immunofluorescent images showing distribution of Tdp1 within human fibroblasts in the absence or presence of 10 μM cycloheximide and/or 1 μM H_2O_2 treatment for 1 hour. (E) Live cell imaging of the distribution of Tdp1-GFP and mitochondria-targeted mCherry within cultured human fibroblasts during treatment with 1 μM H_2O_2. Cells were photographed every 100 seconds. (F) Representative immunofluorescent images showing distribution of Tdp1 and mitochondrial superoxide levels within human fibroblasts in the presence or absence of 1 μM H_2O_2 or 200 nM rotenone treatment for 1 hour. (G) Graphs showing levels of caspase-3/7 activity (left) and DNA fragmentation (right, TUNEL assay) detected in three independent experiments with human fibroblasts cultured in the absence or presence of 1 μM H_2O_2 or 200 nM rotenone for 1 hour. Error bars represent one standard deviation. Scale bar = 10μm

3.3.2 Entry of Tdp1 into the mitochondria is not dependent on *de novo* protein synthesis

To determine whether Tdp1 entry into the mitochondria required *de novo* protein synthesis, I treated H_2O_2-treated human dermal fibroblasts with 10 μM cycloheximide, a ribosome translocation inhibitor. Indicating blocked protein synthesis at this concentration, ubiquitylated proteins accumulated in human fibroblasts (Figure 3-1B). As detected by immunoblotting and immunofluorescence, Tdp1 translocated to the mitochondria in the presence of 10 μM cycloheximide (Figure 3-1C and D). Consistent with translocation of Tdp1 from the nucleus to the mitochondria, live-cell imaging of H_2O_2-treated human dermal fibroblasts showed loss of Tdp1 from the nucleus and subsequent localization to the mitochondria (Figure 3-1E).

3.3.3 Increased intramitochondrial ROS is sufficient to cause translocation of Tdp1 into the mitochondria

To determine whether translocation of Tdp1 into the mitochondria correlated with elevated mitochondrial superoxide levels, I stained H_2O_2-treated human dermal fibroblasts with the superoxide indicator mitoSOX and observed elevated levels of mitochondrial superoxide compared to untreated cells (Figure 3-1F). To determine whether intramitochondrial oxidative stress was sufficient to cause translocation, I treated human dermal fibroblasts with 10 μM rotenone, a mitochondrial complex I inhibitor that increases levels of intramitochondrial oxidants (Li et al., 2003). This elevated intramitochondrial ROS to levels comparable to those observed with H_2O_2 treatment and caused translocation of Tdp1 into the cytoplasm (Figure 3-1F). Entry of

Tdp1 into the mitochondria likely did not occur because loss of mitochondrial protein import is a known consequence of rotenone administration. Rotenone dissipates the proton motive force needed for transfer of proteins into the intermembrane space and occludes the mitochondrial outer membrane import channel (Di Maio et al., 2016; Jastroch et al., 2010).

3.3.4 Tdp1 translocation is not associated with activation of caspases 3 and 7

Although ROS stress can initiate mitochondria-dependent apoptosis (Qiu et al., 2015; Simon et al., 2000), neither rotenone nor H_2O_2 treatments caused an elevation in cellular caspase-3/7 activity or DNA fragmentation (Figure 1G). This minimizes the likelihood that Tdp1 translocation is a response to apoptotic mitochondrial signaling.

3.3.5 Mitochondrial Tdp1 interacts with BER constituents and maintains mtDNA integrity

I hypothesized that Tdp1 interacts with mtDNA repair proteins to maintain mtDNA integrity. To test for interaction with DNA repair proteins, Kunho Choi expressed FLAG-HA-tagged Tdp1 in human dermal fibroblasts and immunoprecipitated the tagged Tdp1 from purified mitochondria following treatment of the cells with H_2O_2. By immunoblotting, Kunho detected ligase III and XRCC1 that co-precipitated with Tdp1 (Figure 3-2A), consistent with Tdp1 being a component of the mitochondrial BER complex (Chiang et al., 2010; Plo et al., 2003).

To determine if Tdp1 deficiency compromised mtDNA integrity, I harvested MEFs from *Tdp1*$^{-/-}$ mice and assessed the level of polymerase-impeding lesions, random mutations, and deletions within the mtDNA. As assessed by interference with *Taq* polymerase extension, both *wt* and *Tdp1*$^{-/-}$ cells had comparable amounts of baseline lesions (Figure 3-2B, left panel). After 4 weeks of culture, *Tdp1*$^{-/-}$ MEFs harbored approximately 30% more mtDNA lesions than *wt* MEFs (Figure 3-2B, left panel), and after culture in the presence of 1 μM H_2O_2 for a month, *Tdp1*$^{-/-}$ MEFs had 200% more mtDNA lesions than *wt* MEFs (Figure 3-2B, left panel). To assess accumulation of mtDNA point mutations, I digested the mtDNA with *Taq1* and amplified the mtDNA using primers hybridizing to sequences flanking the Taq1 recognition sites. Because mutations of the *Taq1* recognition sites block *Taq1* digestion, the amount of PCR product is proportional to the abundance of *Taq1* site mutations. This showed that *Tdp1*$^{-/-}$ and *wt* MEFs harbored similar quantities of mtDNA mutations at baseline. However, after culturing in the

presence of 1 μM H_2O_2 for 4 weeks, *Tdp*$^{-/-}$ cells had 40% more mtDNA point mutations than *wt* cells (Figure 3-2B, right panel).

Because dysfunctional mtDNA repair and incomplete resolution of DNA breaks during mtDNA replication are thought to cause the formation of deleted mtDNA products and give rise to mitochondrial dysfunction (Fukui and Moraes, 2009; Krishnan et al., 2008; Shoffner et al., 1989), I checked if the absence of Tdp1 favors the accumulation of mtDNA deletions. Using mtDNA extracted from *wt, Tdp1*$^{-/-}$, and *PolG* null MEFs cultured in the presence or absence of 1 μM H_2O_2, I quantified a common mitochondrial deletion product and found no relative increase in the level of this mtDNA deletion among *Tdp1*$^{-/-}$ MEFs, whereas there was in the *PolG* null MEFs (Figure 3-2B, bottom panel). This suggests that, unlike the repair of DNA lesions and point mutations, the repair mechanisms preventing mtDNA deletions is independent of Tdp1.

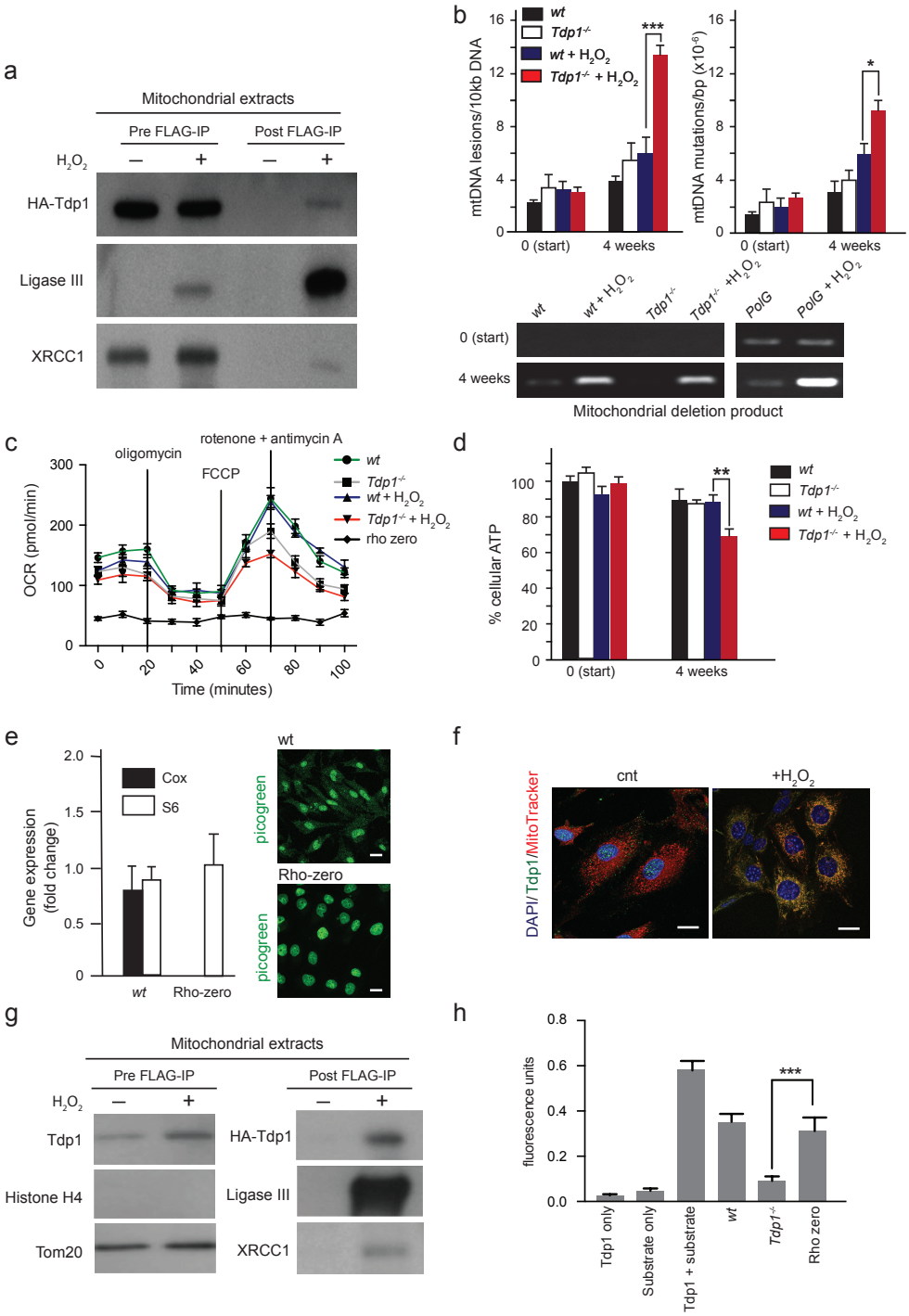

Figure 3-2: Tdp1 interacts with DNA repair proteins in the mitochondria and maintains mtDNA integrity. (A) Photograph of an immunoblot of FLAG-HA-tagged Tdp1 immunoprecipitates from mitochondrial extracts of human fibroblasts showing co-precipitation of ligase III and XRCC1. Human fibroblasts were treated with 1 μM H_2O_2 for 1 hour prior to immunoprecipitation (IP) with anti-FLAG. (B) Top panel: Graphs showing levels of mtDNA lesions (left) and mtDNA *Taq1* recognition site mutations (right) before and following culture of *wt* and *Tdp1*$^{-/-}$ MEFs with 1 μM H_2O_2 for 4 weeks. Lesions and mtDNA *Taq1* recognition site mutations were quantified by

qPCR. Bottom panel: Agarose gel photographs showing the accumulation of a common mtDNA deletion product before and following culture of *wt* and *Tdp1*$^{-/-}$ MEFs with 1 μM H_2O_2 for 4 weeks. Untreated *wt* and *Tdp1*$^{-/-}$ MEFs do not have detectable levels of the mtDNA deletion, whereas MEFs treated with 1 μM H_2O_2 for 4 weeks have comparable levels. Proofreading-deficient PolG mutant MEFs have detectable levels of the mtDNA deletion at baseline and these increase following culture for 4 weeks in 1 μM H_2O_2. (C) Graph representing three independent Seahorse measurements of oxygen consumption rate in mitochondria isolated from *wt* and *Tdp1*$^{-/-}$ MEFs after 4 weeks of culture with 1 μM H_2O_2. The mtDNA-depleted Rho-zero cell line was used as a negative control for mitochondrial respiration. 2 μM oligomycin was used to inhibit ATP production. 2 μM of the ionophore FCCP was used to uncouple the electron transport chain, allowing maximal respiration. Finally, 500 nM rotenone and antimycin A were used to inhibit ATP synthesis. Error bars represent one standard deviation. (D) Graphs showing level of ATP production before and following culture of *wt* and *Tdp1*$^{-/-}$ MEFs with 1 μM H_2O_2 for 4 weeks. (E) Left panel: Graph showing normalized mitochondria-encoded cytochrome c oxidase II (Cox) and nuclear-encoded S6 ribosomal (S6) RNA levels as measured by qRT-PCR in MEFs untreated (*wt*) or treated (Rho-zero) with ethidium bromide for 14 days. Cox RNA levels were normalized to S6 RNA levels. The expression of Cox (mitochondria-encoded) and S6 (nuclear-encoded) were used to determine the presence of transcribed mitochondrial and nuclear DNA in *wt* and Rho-zero MEFs. Right panel: Photographs of picogreen staining of MEFs untreated (*wt*) or treated (Rho-zero) with ethidium bromide for 14 days. Note the absence of cytoplasmic staining in Rho-zero MEFs indicating the absence of mtDNA. (F) Representative immunofluorescent images showing distribution of Tdp1 in Rho-zero MEFs in the absence or presence of treatment with 1 μM H_2O_2 for 1 hour. (G) Photograph of an immunoblot of FLAG-HA-tagged Tdp1 immunoprecipitates from mitochondrial extracts of Rho-zero MEFs showing co-precipitation of ligase III and XRCC1. Human fibroblasts were treated with 1 μM H_2O_2 for 1 hour prior to immunoprecipitation (IP) with anti-FLAG. (H) Graph showing Tdp1 enzymatic activity in mitochondrial lysates of *wt*, *Tdp1*$^{-/-}$ and Rho-zero MEFs after treatment with 1 μM H_2O_2 for 1 hour. Tdp1 enzymatic activity in three independent experiments was measured by fluorescence following cleavage of a quencher off an oligonucleotide substrate. *, $P<0.05$, **, $P<0.01$; ***, $P<0.001$. Scale bar = 10μm

3.3.6 Tdp1 deficiency impairs mitochondrial respiration

To test whether the increase in mtDNA lesions and mutations correlated with mitochondrial respiratory dysfunction, I performed a Seahorse assay on mitochondria isolated from *wt* and *Tdp1*$^{-/-}$ MEFs. At baseline, the *wt* and *Tdp1*$^{-/-}$ MEF mitochondria had no significant difference in oxygen consumption rate, whereas following 4 weeks of treatment with 1 μM H_2O_2, *Tdp1*$^{-/-}$ MEF mitochondria consumed 20% less oxygen than *wt* MEF mitochondria (Figure 2C). Similarly, despite being comparable at baseline, ATP production from *Tdp1*$^{-/-}$ MEF mitochondria was 25% less than from *wt* MEF mitochondria after 4 weeks of treatment with 1 μM H_2O_2 (Figure 3-2D).

3.3.7 Tdp1 translocates into mitochondria devoid of mtDNA

The above data define a role for Tdp1 in maintenance of mtDNA and suggest that mtDNA stress is a possible signal for Tdp1 translocation into the mitochondria. To test this, I generated Rho-zero MEFs, cells devoid of mtDNA, by treatment with ethidium bromide and validated the absence of mtDNA by loss of expression of the mtDNA-encoded complex IV subunit by qRT-PCR and by loss of mtDNA staining with picogreen (Figure 3-2E). H_2O_2 treatment of the Rho-zero MEFs caused translocation of Tdp1 to the mitochondria similar to that observed in *wt* MEFs (Figure 3-2F). In the mitochondria of Rho-zero cells, FLAG-HA-tagged Tdp1 formed a complex with ligase III and XRCC1 (Figure 3-2G), and the intramitochondrial Tdp1 was enzymatically active as judged by cleavage of a 3′-quencher from a fluorescent oligonucleotide (Dean et al., 2014) (Figure 3-2H). Thus Tdp1 translocation into the mitochondria is not mediated by mtDNA.

3.3.8 *S. cerevisiae* screen identifies P38, ERK, JNK, the TIM/TOM complex and Mia40 as contributors to H_2O_2-dependent translocation of Tdp1 into the mitochondria

To determine if intramitochondrial ROS is the origin of the signal for translocation of Tdp1, I used *S. cerevisiae* to screen for factors participating in the H_2O_2-dependent translocation of Tdp1 to the mitochondrial matrix. After 5 μM H_2O_2 treatment, I observed Tdp1 expression in the cytoplasm of yeast by immunofluorescence and in the mitochondrial fraction by immunoblotting (Figure 3-3A and B). Studies have shown that H_2O_2 exposure is a known activator of Rho5, mitogen-activated protein (MAP) kinase P38, ERK1 and JNK1 (Johnson and Lapadat, 2002). *P38* and *ERK1* are respectively orthologs of yeast *HOG1* and *FUS3*. Knocking out each of these 3 MAP kinases showed that loss of *HOG1* and *FUS3*, but not *JNK1*, reduced Tdp1 translocation into the mitochondria by 70-80% at 1 hour following exposure to 5 μM H_2O_2 (Figure 3-3C). Indicative of HOG1 and FUS3 redundantly regulating Tdp1 translocation, the double-knockout of *HOG1* and *FUS3* inhibited Tdp1 translocation more than the individual knockouts (95% vs. 70-80%, Figure 3-3D). Suggesting that Rho5 mediates this activation of HOG1 and FUS3, as knockout of *Rho5* alone and double-knockout of *RHO5* and *HOG1* reduced Tdp1 translocation into the mitochondria by 95% at 1 hour following exposure to 5 μM H_2O_2 (Figure 3-3E).

Knockout of the mitochondrial intermembrane transporter *MIA40*, a redox-responsive protein (Barchiesi et al., 2015), reduced H_2O_2-dependent translocation of Tdp1 by 85% (Figure 3-3F). Knockout of *TIM23*, a subunit of the inner membrane translocase of the canonical mitochondrial protein import complex completely abrogated Tdp1 import (Figure 3-3F). These results indicate that Tdp1 transport proceeds through the canonical TIM-TOM complexes and is chaperoned through the intermembrane space by Mia40 (Figure 3-3G).

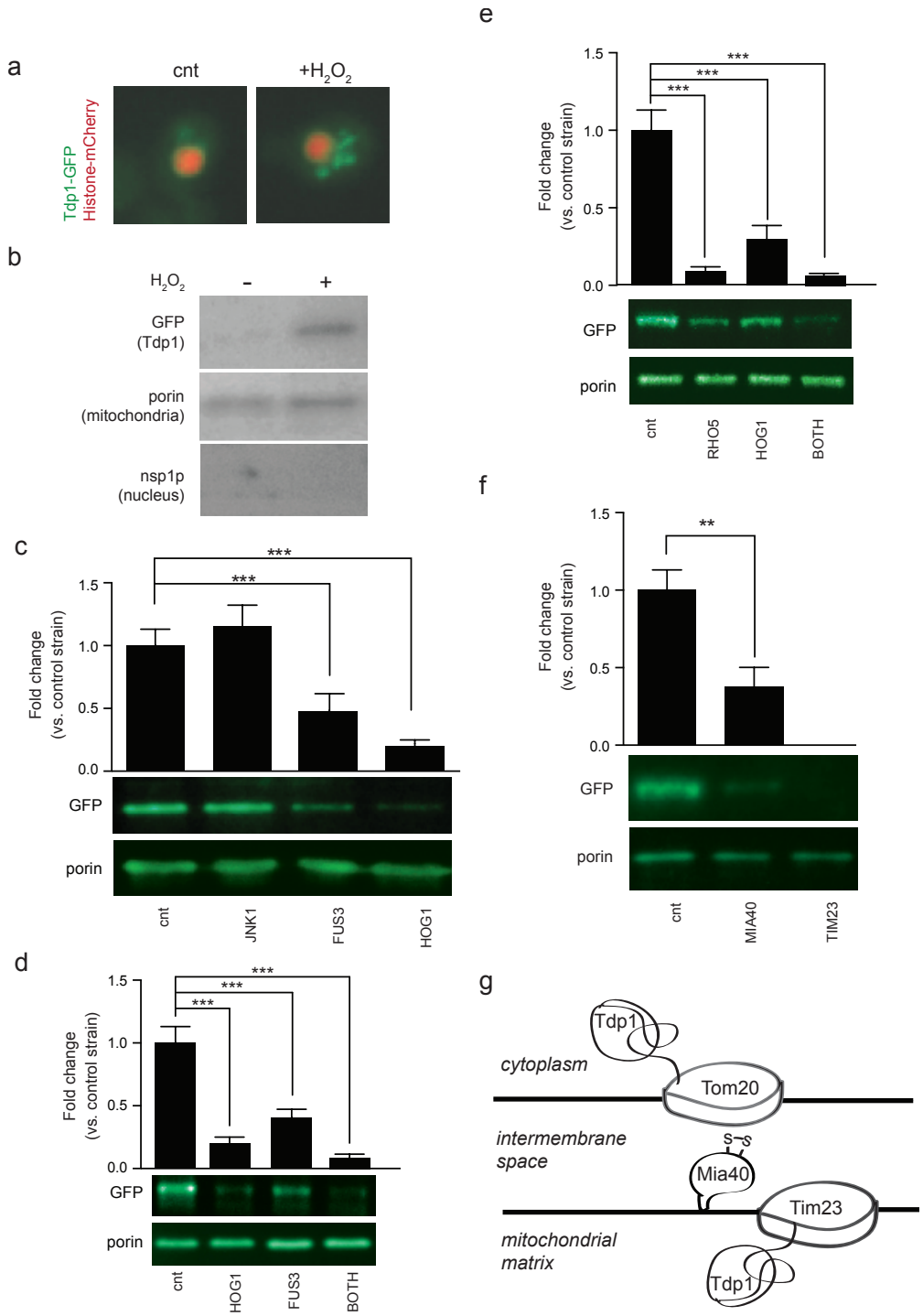

Figure 3-3: Tdp1 entry into *S. cerevisiae* mitochondria under H_2O_2 stress is facilitated by MAP kinases and the canonical mitochondrial import pathway. (A) Representative fluorescent images of yeast expressing Tdp1-GFP and Histone-mCherry and showing cytoplasmic accumulation of Tdp1-GFP following H_2O_2 treatment. The images were taken with or without treatment with 5 μM H_2O_2 for 1 hour. (B) Photograph of an immunoblot showing

accumulation of Tdp1-GFP in lysates from purified mitochondria after treatment of yeast with 5 μM H_2O_2 for 1 hour. Porin is a mitochondrial protein and nsp1p is a nuclear protein. (C) FUS3- and HOG1-dependent Tdp1-GFP accumulation in the mitochondria following H_2O_2 treatment. Upper panel: Quantification of mitochondrial Tdp1-GFP following treatment of yeast (control (cnt) and yeast knockouts JNK1, FUS3 and HOG1) with 5 μM H_2O_2 for 1 hour. Tdp1-GFP levels were normalized to porin levels. JNK1, FUS3 and HOG1 are yeast orthologs of human JNK, ERK1 and P38. Error bars represent one standard deviation for three independent experiments. Lower panel: Photograph of an immunoblot of lysates from purified mitochondria of control (cnt) and yeast knockouts JNK1, FUS3 and HOG1 probed for GFP and porin. (D) HOG1 and FUS3 signaling co-mediate Tdp1-GFP mitochondrial entry following H_2O_2 treatment. Upper panel: Quantification of mitochondrial Tdp1-GFP following treatment of yeast (control (cnt) and yeast knockouts FUS3, HOG1 and FUS3 + HOG1 (Both)) with 5μM H_2O_2 for 1 hour. Tdp1-GFP levels were normalized to porin levels. Error bars represent one standard deviation for three independent experiments. Lower panel: Picture of an immunoblot of lysates from purified mitochondria of control (cnt) and yeast knockouts FUS3, HOG1 and FUS3 + HOG1 (Both) probed for GFP and porin. (E) RHO5 and HOG1 signaling mediate Tdp1-GFP mitochondrial entry following H_2O_2 treatment. Upper panel: Quantification of mitochondrial Tdp1-GFP following treatment of yeast (control (cnt) and yeast knockouts RHO5, HOG1 and RHO5 + HOG1 (Both)) with 5 μM H_2O_2 for 1 hour. Tdp1-GFP levels were normalized to porin levels. Error bars represent one standard deviation for three independent experiments. Lower panel: Photograph of an immunoblot of lysates from purified mitochondria of control (cnt) and yeast knockouts RHO5, HOG1 and RHO5 + HOG1 (Both) probed for Tdp1-GFP and porin. RHO5 is the yeast ortholog of human RAS. (F) MIA40 and TIM23 facilitate import of Tdp1-GFP into the mitochondria following H_2O_2 treatment. Upper panel: Quantification of mitochondrial Tdp1-GFP following treatment of yeast (control (cnt) and yeast knockouts MIA40 and TIM23) with 5 μM H_2O_2 for 1 hour. Tdp1-GFP levels were normalized to porin levels. Error bars represent one standard deviation for three independent experiments. Lower panel: Photograph of an immunoblot of lysates from purified mitochondria of control (cnt) and yeast knockouts MIA40 and TIM23 probed for Tdp1-GFP and porin. (G) Schematic drawing illustrating a possible mechanism for Tdp1 transport across the mitochondrial double-membrane. $P<0.05$; **, $P<0.01$; ***, $P<0.001$.

3.3.9 siRNA knockdown of P38, ERK1, and TIM23 impedes H_2O_2-dependent translocation of Tdp1 into the mitochondria of human dermal fibroblasts

Similar to *S. cerevisiae*, exposure of cultured human dermal fibroblasts to H_2O_2 activates mitogen-activated protein (MAP) kinases P38, ERK1 and JNK (the respective human orthologs of *HOG1, FUS3, JNK1*) (Smith et al., 2010). I found that exposure of human dermal fibroblasts to 1 μM H_2O_2 for 1 hour promoted the maximal phosphorylation of P38 and ERK1 while minimally affecting the phosphorylation of JNK (Supplementary Figure B-1C). Given that Tdp1 translocated into the mitochondria within 6-7 minutes at 1 μM H_2O_2 (Figure 3-1E), I focused on P38 and ERK1 as mediators of H_2O_2-dependent mitochondrial Tdp1 translocation. Using siRNA,

an 80% knockdown of P38 resulted in a 50% reduction in H_2O_2-mediated mitochondrial Tdp1 translocation, and a 70% knockdown of ERK1 resulted in a 20% reduction in H_2O_2-dependent mitochondrial Tdp1 translocation (Figure 3-4A and Supplementary Figure B-1D). Knockdown of P38 or ERK1 in Rho-zero MEFs also impaired H_2O_2-dependent transport of Tdp1 into the mitochondria (Figure 3-4B). Concurrent 80% knockdown of P38 and ERK1 resulted in an 80% reduction in H_2O_2-dependent mitochondrial Tdp1 translocation (Figure 3-4C). The decrease in mitochondrial Tdp1 after P38 and ERK1 knockdown is due to retention of nuclear Tdp1 (Supplementary Figure B-2 (A and B)). Confirming that intramitochondrial ROS generated by addition of 1 μM rotenone activated the same pathways, 80% knockdown of P38 or 75% knockdown of ERK1 increased the retention of Tdp1 in the nucleus (Supplementary Figure B-2(C and D)).

P38 and ERK1 translocate from the cytoplasm into the nucleus upon phosphorylation and activate nuclear substrates (Aplin et al., 2001; Gong et al., 2010). Within 5 minutes of adding 1 μM H_2O_2 and 1 μM rotenone to human dermal fibroblasts, I detected increased nuclear P38 and ERK1 (Figure 3-4D). This timing is consistent with Tdp1 translocation out of the nucleus and into the mitochondria (Figure 3-1E) and suggests that P38 and ERK1 activate nuclear targets facilitating Tdp1 translocation from the nucleus to the mitochondria.

Consistent with the yeast studies, siRNA knockdown of TIM23 in human dermal fibroblasts reduced Tdp1 translocation into the mitochondria; Tdp1 aggregated in the cytoplasm (Figure 3-4D). This illustrates the conservation between human and yeast cells of Tdp1 mitochondrial import via the canonical TIM-TOM pathway.

Tdp1 does not contain a canonical mitochondria-targeting presequence identifiable by mitochondrial targeting sequence predictors TargetP, MitoProt and MitoFates (data not shown). Additionally, serial truncations performed by Lauren Fougner from either the N- or C-terminus of Tdp1 did not identify a distinct mitochondrial-targeting signal; rather it identified contributions from multiple regions of the Tdp1 protein to Tdp1 mitochondrial entry (data not shown). In addition, site-directed mutagenesis of Ser81, a phosphorylation site in Tdp1, showed that changing serine 81 to alanine was insufficient to block H_2O_2-dependent translocation of Tdp1 into the mitochondria (Figure 3-4E).

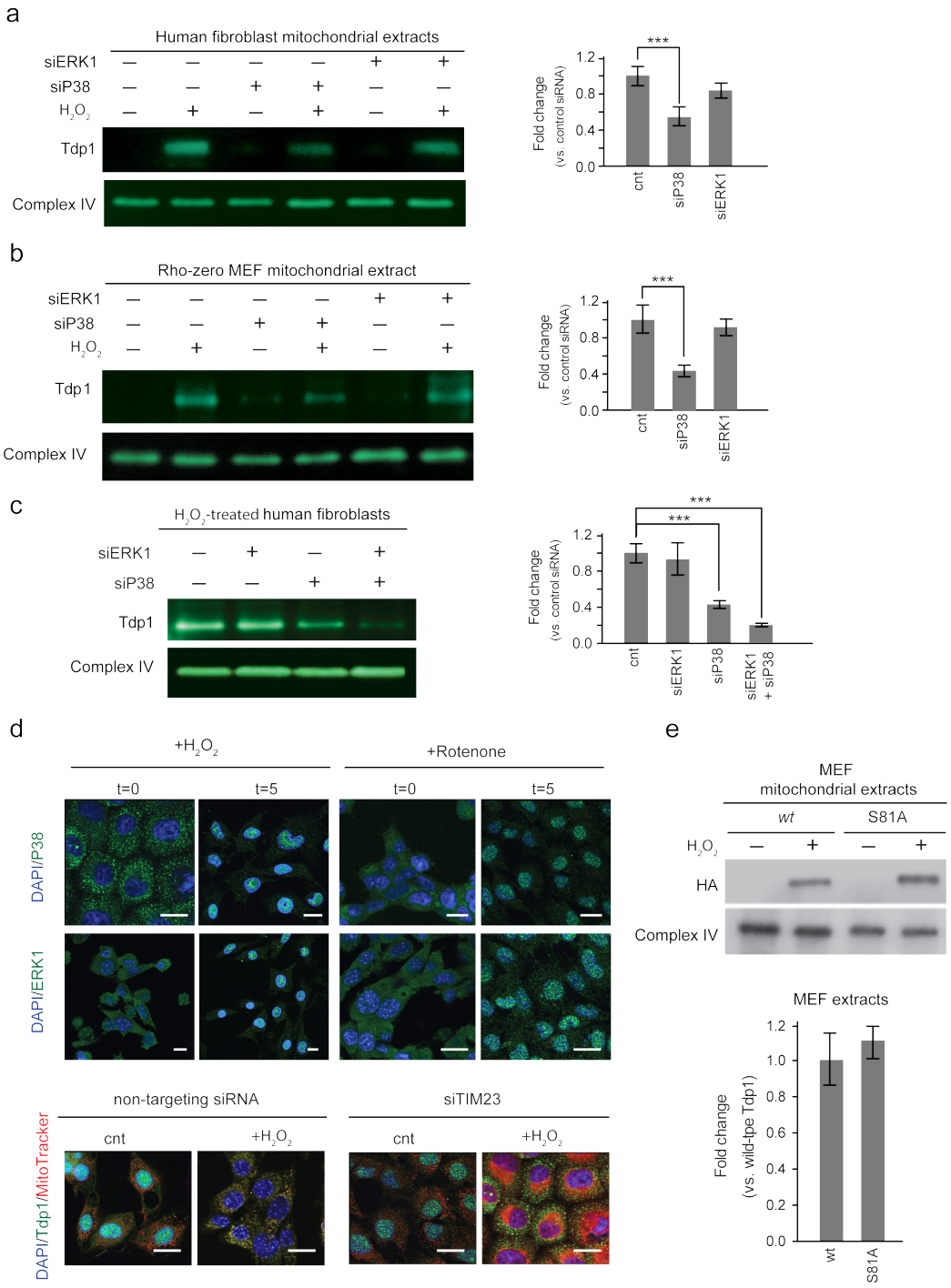

Figure 3-4: MAP kinases and the canonical mitochondrial import pathway facilitate Tdp1 entry into human and mouse fibroblast mitochondria following H_2O_2 stress. (A) Dependence of Tdp1 accumulation in the mitochondria on ERK1 and P38 following H_2O_2 treatment of cultured human fibroblasts. Left panel: Phoptograph of a representative immunoblot of lysates from purified mitochondria of cultured human fibroblasts without or with knockdown of ERK1 and P38 and in the absence or presence of H_2O_2 treatment. Mitochondrial complex IV was

used as a loading control. Right panel: Graph showing fold change in mitochondrial Tdp1 across three independent experiments following treatment with 1 μM H_2O_2 for 1 hour. Tdp1 levels were normalized to complex IV levels and then fold changes are shown relative to levels in cells treated with nontargeting siRNA. Error bars represent one standard deviation. (B) Dependence of Tdp1 accumulation in the mitochondria on ERK1 and P38 following H_2O_2 treatment of cultured Rho-zero MEFs. Left panel: Photograph of a representative immunoblot of lysates from purified mitochondria of cultured Rho-zero MEFs without or with knockdown of ERK1 and P38 and in the absence or presence of H_2O_2 treatment. Mitochondrial complex IV was used as a loading control. Right panel: Graph showing fold change in mitochondrial Tdp1 across three independent experiments following treatment with 1 μM H_2O_2 for 1 hour. Tdp1 levels were normalized to complex IV levels and then fold changes are shown relative to levels in cells treated with nontargeting siRNA. Error bars represent one standard deviation. (C) Additive dependence of Tdp1 accumulation in the mitochondria on ERK1 and P38 following H_2O_2 treatment of cultured human fibroblasts. Left panel: Photograph of a representative immunoblot of lysates from purified mitochondria of cultured human fibroblasts without or with knockdown of ERK1 and P38 and in the presence of H_2O_2 treatment. Mitochondrial complex IV was used as a loading control. Right panel: Graph showing fold change in mitochondrial Tdp1 across three independent experiments following treatment with 1 μM H_2O_2 for 1 hour. Tdp1 levels were normalized to complex IV levels and then fold changes are shown relative to levels in cells treated with nontargeting siRNA. Error bars represent one standard deviation. (D) Dependence of mitochondrial import of Tdp1 on the TIM/TOM complex. Upper panel: Representative immunofluorescent images showing distribution of P38 and ERK1 in human dermal fibroblasts before and after 5 minutes with 1 μM H_2O_2 or 200 nM rotenone treatment. Lower panel: Representative immunofluorescent images showing distribution of Tdp1 in human dermal fibroblasts treated with non-targeting siRNA or Tim23 siRNA and 1 μM H_2O_2 for 1 hour. (E) Mitochondrial import of Tdp1 is independent of phosphorylation of S81. Upper panel: Picture of a representative immunoblot of lysates from purified mitochondria of cultured MEFs expressing *wt* or S81A HA-tagged Tdp1 cDNA in the presence or absence of treatment with 1 μM H_2O_2 for 1 hour. Mitochondrial complex IV was used as a loading control. Lower panel: Graph showing fold change in mitochondrial Tdp1 across three independent experiments following treatment with 1 μM H_2O_2 for 1 hour. Tdp1 levels were normalized to complex IV levels. Error bars represent one standard deviation. *, $P<0.05$; **, $P<0.01$; ***, $P<0.001$. Scale bar = 10μm

3.3.10 *Tdp1*$^{-/-}$ mice accumulate mutations in mtDNA and have impaired mitochondrial respiration

Given that long-term culture of *Tdp1*$^{-/-}$ MEFs in low dose H_2O_2 is detrimental to cultured cells, I examined the mtDNA integrity and the mitochondrial respiratory function of skeletal muscle 1 to 6 month old *Tdp1*$^{-/-}$ mice. Analysis of polymerase-interrupting lesions in mtDNA showed a 70% to 400% increase in these lesions in 4-, 5- and 6-month old *Tdp1*$^{-/-}$ mice (Figure 3-5A). Quantification of mutations that inhibited *Taq1* digestion showed that myoblast mtDNA from 1-month-old *Tdp1*$^{-/-}$ mice and *wt* mice had a comparable mutation burden (Figure 3-5A),

whereas myoblast mtDNA from 2-, 3-, 4-, 5- and 6-month-old *Tdp1*$^{-/-}$ mice had mtDNA mutation loads 20%-120% higher than did *wt* mice myoblast mtDNA (Figure 3-5B).

Since mutations in mtDNA-encoded genes can alter mitochondrial function, I examined mitochondrial respiration using myoblasts isolated from skeletal muscle. Comparative Seahorse analysis of myoblast cultures from *wt* and *Tdp1*$^{-/-}$ mice showed that *Tdp1*$^{-/-}$ myoblasts isolated from 3-, 4-, 5-, and 6-month-old mice were unable to achieve full respiratory potential; that is, uncoupling of the electron transport chain by FCCP treatment detected a 30-60% reduction in oxygen consumption rate in *Tdp1*$^{-/-}$ myoblasts compared to *wt* myoblasts (Figure 3-5C).

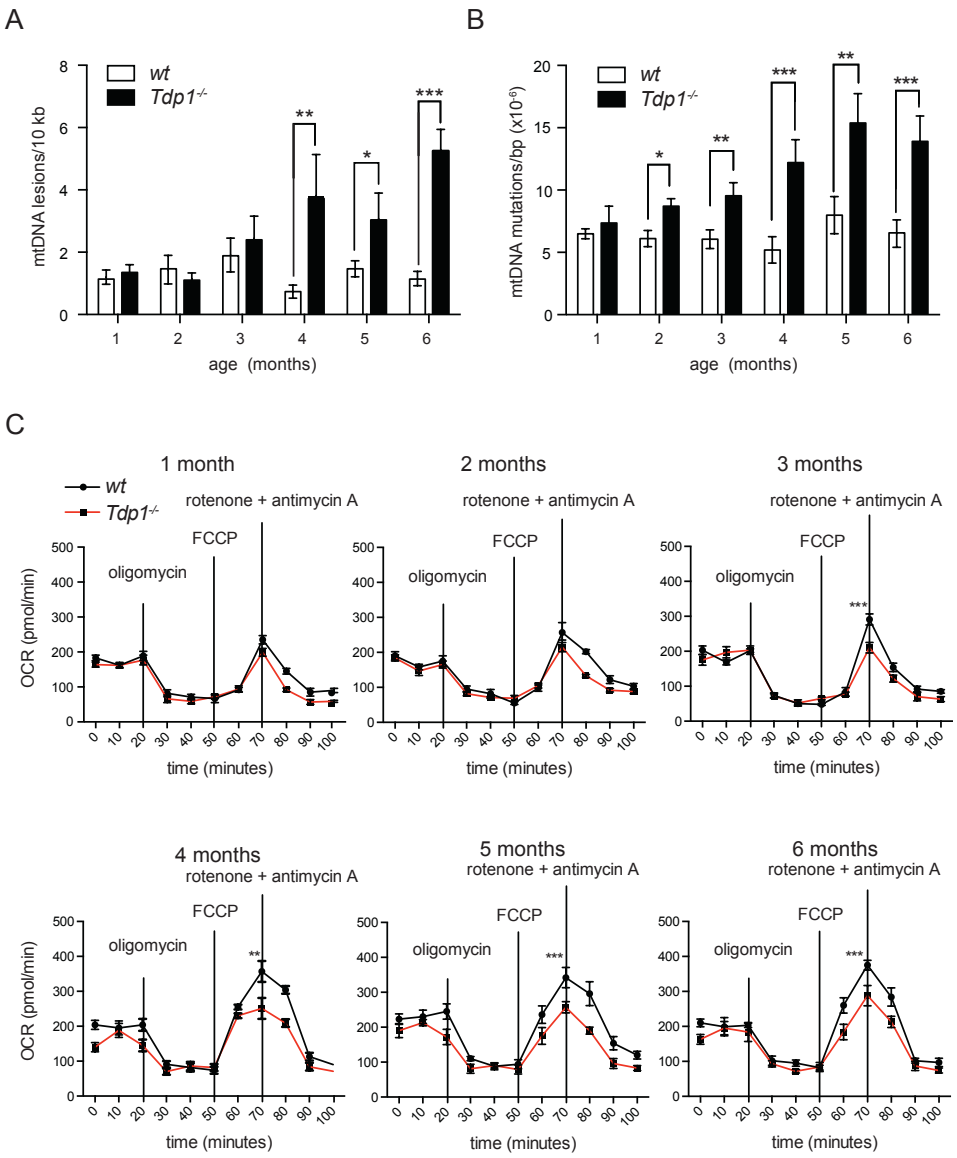

Figure 3-5: Tdp1 maintains mtDNA integrity and respiratory function in mouse mitochondria. (A) Graph showing quantity of mtDNA lesions detected by qPCR in isolated skeletal muscle mitochondria of 8 *wt* and 8 *Tdp1*$^{-/-}$ mice at ages 1 through 6 months. Each bar is the mean of three independent experiments, and error bars represent one standard deviation. (B) Graph showing quantity of *Taq1* cut site mutations detected by qPCR in pooled mtDNA isolated skeletal muscle mitochondria of 8 *wt* and 8 *Tdp1*$^{-/-}$ mice at ages 1 through 6 months. Each bar is the mean of three independent experiments, and error bars represent one standard deviation. (C) Graph showing the mitochondrial oxygen consumption rate in cultured *wt* and *Tdp1*$^{-/-}$ primary myoblasts harvested and pooled from 8 mice at the age of 1 through 6 months. 2 µM oligomycin was used to inhibit ATP production. 2 µM of the ionophore FCCP was used to uncouple the electron transport chain, allowing maximal respiration. 500 nM rotenone and

antimycin A was used to inhibit ATP synthesis. Each bar is the mean of three independent experiments, and error bars represent one standard deviation. *, $P<0.05$, **; $P<0.01$; ***, $P<0.001$.

3.4 Discussion

An objective of cell biology is to determine the catalytic function of proteins and provide a subcellular context for their function. Since the discovery of Tdp1 as the first 3'-DNA phosphodiesterase, the biochemical activity of Tdp1 has been well characterized (El-Khamisy et al., 2007; Huang et al., 2013; Interthal et al., 2005a; Murai et al., 2012a; Pouliot et al., 1999). I herein report the first delineation of Tdp1 transport into the mitochondria and its significance for mitochondrial function. Within *S. cerevisiae,* mouse and human cells, intramitochondrial ROS induces Tdp1 translocation from the nucleus to the mitochondria via P38- and ERK1-dependent mechanisms. This translocation is independent of new protein synthesis and of mtDNA. My findings also show that Tdp1 interacts with BER proteins ligase III and XRCC1 within mitochondria and that cultured cells and tissues deficient for Tdp1 have more mtDNA lesions, accumulate mtDNA mutations, and have impaired mitochondrial respiration.

Given that exogenous rotenone stimulated the transport of Tdp1 out of the nucleus via the P38 and ERK1 signaling cascades, intramitochondrial ROS appears sufficient for Tdp1 translocation from the nucleus to the mitochondria. Unlike H_2O_2, however, rotenone treatment did not result in entry of Tdp1 into the mitochondrial matrix. Two factors account for this failure. First, inhibition of complex I by rotenone blocks electron transfer between complex I and co-enzyme Q and prevents the concurrent transfer of hydrogen ions out of the matrix into the intermembrane space; thereby decreasing the proton motive force driving transfer of proteins into the intermembrane space (Jastroch et al., 2010). Second, rotenone impedes mitochondrial import by occluding the mitochondrial outer membrane import channel (Di Maio et al., 2016).

Although intramitochondrial ROS likely signals translocation of Tdp1 from the nucleus to the mitochondrial matrix, the mediating MAP kinase P38 and ERK1 reside in the cytoplasm. This implies that either the intramitochondrial ROS or a signal from the intramitochondrial ROS crosses the mitochondrial membranes to activate these signaling cascades. A possible mediator is H_2O_2, a cell-permeable signaling molecule produced by NADPH oxidases (NOX), cyclooxygenases and lipooxygenases (Lennicke et al., 2015). H_2O_2 might therefore be the

messenger activating the extra-mitochondrial pathways of stress-activated protein kinases; it also inhibits phosphatases that attenuate signaling of cell survival pathways, and in the nucleus it activates transcription factors by oxidation of cysteine residues (Gough and Cotter, 2011). Further studies are required to determine if H_2O_2 is the mitochondrial to cytoplasmic messenger mediating Tdp1 translocation.

The mechanisms by which the P38 and ERK1 signaling cascades trigger Tdp1 translocation from the nucleus to the mitochondrial matrix are unknown. The rapid translocation of P38 and ERK1 from the cytoplasm to the nucleus following generation of intramitochondrial ROS suggests that Tdp1 or a nuclear chaperone of Tdp1 is the target of P38 and ERK1. Phosphorylation of Tdp1 serine 81 activates repair of topoisomerase-I mediated DNA damage, promotes Tdp1 interaction with ligase III and enhances the stability of Tdp1 *in vitro* (Chiang et al., 2010) but is not required for translocation of Tdp1. This suggests that if Tdp1 is a direct target of P38 and ERK1, then other serines or threonines are phosphorylated.

A surprising observation was that mtDNA was unnecessary for translocation of Tdp1 into the mitochondria or its incorporation into the BER complex. These findings are however, consistent with a prior study showing that components of the BER complex reside in the mitochondria of Rho-zero cells (Stuart et al., 2004). The insufficiency of mtDNA stress suggests that Tdp1 is recruited by conditions predisposing to DNA damage and not by the DNA damage itself.

Maintenance of mtDNA is crucial because the mitochondrial genome consists almost entirely of open reading frames encoding essential proteins, rRNAs or tRNAs. Despite the importance of mtDNA repair, little detail is known about mtDNA repair mechanisms or the transport of DNA repair proteins into the mitochondria. Approximately 1,500 nuclear-encoded proteins are transported to the human mitochondria (Reja et al., 2009). Most of these proteins thread through mitochondrial membrane translocases coincident with protein synthesis (Wiedemann et al., 2004). Many proteins destined for the matrix contain matrix-targeting pre-sequences recognized by the outer and inner membrane translocase (TOM/TIM) subunits (Pfanner, 2000), which form a channel to the matrix (Wiedemann et al., 2004). In the intermembrane space, chaperones guide proteins with these signal sequences (Wiedemann et al., 2006). Once in the matrix, the pre-sequence is cleaved by Matrix Processing Peptidase (MPP) (Schneider et al., 1990). However, Tdp1 does not have an identifiable targeting pre-sequence;

therefore it classifies as a mitochondrial matrix protein without an identifiable targeting pre-sequence (Rada et al., 2015; Spadafora et al., 2016)

In the absence of a targeting pre-sequence, Tdp1 mitochondrial translocation might rely on cryptic mitochondrial targeting residues. The presence of such residues usually results in truncated isoforms of the protein within the mitochondria following post-translational endoprotease processing of the protein into a translocation-active form (Boopathi et al., 2008; Kazak et al., 2013). This is unlikely for Tdp1 because truncated isoforms of Tdp1 were not detected by immunoblotting of mitochondrial extracts.

The H493R mutation in Tdp1 causes Spinocerebellar Ataxia with Axonal Neuropathy 1 (SCAN1), a neurodegenerative disease (Takashima et al., 2002). This mutation reduces the enzymatic activity of Tdp1 by 25-fold and causes accumulation of Tdp1-DNA reaction intermediates (Hirano et al., 2007; Interthal et al., 2005b). My findings that skeletal muscle isolated from *Tdp1*$^{-/-}$ mice have an increased mtDNA mutation load and that myoblast mitochondria isolated from *Tdp1*$^{-/-}$ mice have significantly reduced respiratory capacity suggest that mitochondrial dysfunction contributes to the pathogenesis of SCAN1.

I show that cytoplasmic or mitochondrial ROS promotes the translocation of Tdp1 from the nucleus to the mitochondria of yeast, mouse and human cells and that translocation occurs independently of protein synthesis and the presence of mtDNA. Transport of nuclear Tdp1 to the mitochondria is mediated by P38 and ERK1 MAP kinase activation, and Tdp1 entry into the mitochondrial matrix is through the TIM/TOM complexes. Within the mitochondria, Tdp1 associates with the BER complex, and consistent with a role for Tdp1 in mtDNA repair, mtDNA from *Tdp1*$^{-/-}$ mouse tissue has increased mutations and lesions. Functionally, this translates into *Tdp1*$^{-/-}$ mouse myoblasts having impaired mitochondrial respiration.

In summary, my findings define a mitochondrial role for Tdp1 and suggest that the neuropathology observed in SCAN1 patients might in part be due to mitochondrial dysfunction. Additionally, given that several cancers have elevated Tdp1 expression (Fam et al., 2013c; Liu et al., 2007; Meisenberg et al., 2015) and that evasion of apoptotic cell death increases tumorigenesis (Lowe and Lin, 2000), one might also hypothesize that the mitochondrial localization of Tdp1 favors the survival of cancer cells.

Chapter 4: A Role for Tdp1 in Rhabdomyosarcoma

4.1 Introduction

Conventional chemotherapeutic agents have targeted general cellular processes such as nucleotide synthesis, DNA replication, and cell division. Because each of these processes is required for homeostasis of normal tissues, these treatments cause significant morbidity and limit the doses of drugs that can be given for a cure. Despite these shortcomings, combinations of cytotoxic agents have improved cure rates for many malignancies such as pediatric acute lymphoblastic leukemia (Stanulla and Schrappe, 2009).

Pediatric sarcomas and other cancers have not responded as well to these conventional therapies (Hingorani and Kolb, 2010). Improvement in cancer-free survival therefore requires a better understanding of cancer biology and the identification of cancer-specific targets (Stegmeier et al., 2010). During the evolution of human cancers, cancer cells accumulate genetic alterations such that each tumor contains multiple genetic and epigenetic abnormalities (Cahill et al., 1999). As illustrated by Imatinib inhibition of *BCR-ABL* in chronic myelogenous leukemia (Pinilla-Ibarz and Quintas-Cardama, 2009), the inhibition of a single oncogene is sufficient to block cancer cell growth in some cancers . In other cancers, DNA maintenance pathways mutate during the evolution of the cancer (Bartek et al., 2007), and inhibition of remaining DNA repair pathways causes cancer cell death. This is illustrated by the synthetic lethal interaction of PARP-1 inhibitors with deficits of homologous recombination such as those arising from mutations of *BRCA1* and *BRCA2* (Fong et al., 2009). Sparing normal tissues, these two approaches demonstrate the potential for preferential targeting of malignant cells.

The question then arises as to whether such targets might be identifiable for the high-risk pediatric sarcomas (Hingorani and Kolb, 2010). Rhabdomyosarcoma (RMS) is one of the most common soft tissue sarcomas of childhood. Each year approximately 300 children in the United States are diagnosed with this disease, and two thirds are younger than 10 years old (Dagher and Helman, 1999). The two major subtypes are embryonal (eRMS) and the more aggresive alveolar (aRMS) rhabdomyosarcoma (Dagher and Helman, 1999). Although the overall cure increased from 25 to 70% between the 1970s and the 1990s (Arndt et al., 2009; Dagher and Helman, 1999), the 5-year failure-free survival rate is only 65% for children with non-metastatic aRMS or

eRMS at unfavorable sites (Arndt et al., 2009). Survival is even less for the ~30% of children presenting with metastatic RMS (Ellison et al., 2007).

The genetic alterations associated with RMS include chromosomal translocations and deletions and these correlate with outcome. Many eRMS tumors have loss of heterozygosity at the 11p15.5 locus (Zhan et al., 1994), and 70-80% of aRMS have chromosomal translocation t(2;13)(q35;q14) or t(1;13)(p36;q14) resulting in expression of PAX3/7-FOXO1 chimeric proteins that function as transcription factors (Barr et al., 1993; Davis et al., 1994). The PAX3-FOXO1 transcription factor increases expression of the insulin growth factor 1 receptor (IGF-1R) (Ayalon et al., 2001), and inhibition of IGF-1R signaling shows promise in impeding RMS tumor growth (Kolb et al., 2008).

Unlike recent studies implicating a role for the EWS-FLI fusion protein in maintaining the PARP-1-mediated DNA damage response in Ewing sarcoma, defects of DNA repair have not been reported in RMS despite the genomic rearrangements identified in these tumors (Brenner et al., 2012; Garnett et al., 2012). Of particular interest is whether the recent failure of the irinotecan trials for metastatic or recurrent RMS is attributable to compensatory increased expression of Tdp1; resistance of some cancers to topoisomerase-I inhibitors has been attributed to overexpression of Tdp1 (Liu et al., 2007; Mascarenhas et al., 2010; Pappo et al., 2007; Walterhouse et al., 2004). Such overexpression might also suggest that RMS tumors have defective DNA double strand break repair since expression of the Tdp1-PARP-1 complex is increased in other cancers with such deficits (Domagala et al., 2011; Goncalves et al., 2011; Nosho et al., 2006). To assess whether Tdp1 and PARP-1 might be targets for treatment of RMS, I profiled the expression of Tdp1 in human pediatric tumors and analyzed the effect of topoisomerase-I inhibition, *TDP1* knockdown, PARP-1 inhibition and nutrient restriction on RMS cell lines.

4.2 Methods

4.2.1 Human subjects

Human tissue and material use for this study was approved by the Institutional Review Board of the University of British Columbia (H09-03301).

4.2.2 TMA construction

Dr. Catherine Pallen assembled pediatric tumor samples from cases referred to BC Children's Hospital into four tissue microarray (TMA) blocks. The tumors that were readable (vs. total number of tumor samples) included aRMS (n=18/21), eRMS (n=24/25), ganglioneuroma (n=12/14), neuroblastoma (n=23/30), Ewing's sarcoma (n=10/22), medulloblastoma (n=9/14), and Wilms tumor (n=24/24). Of the 46 RMS tumors, 14 were metastatic. Molecular diagnosis performed on 31 of 46 RMS tumors identified 18 fusion-positive and 13 fusion-negative tumors. Hematoxylin-eosin images of all cores are provided online at http://www.cfri.ca/pallenlab/ .

Additional TMAs were obtained from the Childrens Oncology Group (COG). These included 34 eRMS and 39 aRMS tumors derived from individuals enrolled in protocols 9602, 9150, D9902, D9802 and D9803.

4.2.3 Immunohistochemistry

The TMAs were screened for Tdp1 expression according to standard immunohistochemistry protocols. Briefly, 4 μm thick sections were cut from each block and immunostained on a Ventana Discovery XT staining system (Ventana Medical Systems). Sections were deparaffinized in xylene, dehydrated through three alcohol changes and transferred to Ventana Wash solution. Endogenous peroxidase activity was blocked in 3% hydrogen peroxide. Antigen retrieval was performed in Ventana CC1 buffer. Slides were incubated with anti-Tdp1 rabbit antibody (dilution 1:200) for 32 min and developed in DAB for 10 min. Tissue sections were then counterstained with hematoxylin and mounted. Pre-immune serum was used as a negative control in place of immune serum.

Miraj Chowdhury, Dr. Cornelius Boerkoel and I scored Tdp1 expression. Any discrepancies between the three scores were resolved by Dr. Boerkoel. Images of each tumor were acquired using a Zeiss Axiovert 200 microscope, a Zeiss AxiocamHR camera, and the Zeiss Axiovision imaging system.

4.2.4 Gene expression arrays

Transcriptome profiling data on primary RMS tumors and seven normal skeletal muscle specimens generated using Human Genome U133A arrays (Affymetrix) were obtained from the

NCI caArray (trich-00099) and GEO (GSE873, GSE1462) databases. From the available 185 samples in the caArray database, expression data on 147 primary RMS were selected for analysis after confirmation of their diagnosis and PAX-FOXO1 translocation status. Additionally, expression data on five randomly selected samples each of non-RMS soft tissue sarcoma (NRSTS), osteosarcoma and Ewing sarcoma were obtained from GEO (GSE16088, GSE37372) and NCI caArray (trich-00099) databases. Tdp1 expression was compared among specimens using Partek Genomics Suite software (Partek) after quantile normalization by robust multichip averaging and median summarization of raw data using one-way ANOVA.

4.2.5 Cell culture

RH30 (aRMS, PAX3-FOXO1) and CW9019 (aRMS, PAX7-FOXO1) cells were cultured in DMEM (Gibco BRL Life Technologies) supplemented with 10% heat-inactivated FBS (Hyclone) and 1% antibiotic-antimycotic (Gibco BRL Life Technologies). RD (eRMS) cells were grown in DMEM supplemented with 10% heat inactivated FBS, 1% antibiotic-antimycotic, 4ml/L L-glutamine (Gibco BRL Life Technologies), 4.5g/L glucose and 1.5 g/L $NaHCO_3$. Human skeletal myoblast cells were cultured using skBM-2 (Lonza) supplemented with 15% FBS, 1% antibiotic-antimycotic and 9 g/L D-glucose (final concentration 10g/L glucose). A204 (eRMS) and Birch (eRMS) cells were grown in RPMI 1640 media (Gibco BRL Life Technologies) supplemented with 10% FBS and 1% antibiotic-antimycotic. RMS cell lines were procured from the Leibniz Institute DSMZ-German Collection of Microorganisms and Cell Cultures or the American Type Culture Collection (ATCC). The human skeletal muscle cell line was obtained from Lonza (XM13A1). All cells were grown at 37º C with 5% CO_2 in a humidified environment. Human skeletal muscle cells under nutrient-restricted conditions were cultured in skBM-2 supplemented with 1% heat inactivated FBS and containing 1 g/L D-glucose. RH30 and CW9019 cells under nutrient-restricted conditions were cultured in glucose-free DMEM supplemented with 1% heat inactivated FBS and 1.0g/L glucose. A204 and Birch cells under nutrient-restricted conditions were cultured in glucose-free RPMI supplemented with 1% heat inactivated FBS and 1.0g/L glucose.

4.2.6 Anti-Tdp1 serum production

An anti-human Tdp1 serum was generated in rabbits against amino acids 1-152 of the human Tdp1 protein as previously described (Hirano et al., 2007). The specificity of the antiserum was confirmed by immunofluorescent comparison of *Tdp1*$^{+/+}$ and *Tdp1*$^{-/-}$ mouse skeletal muscle (Supplementary Figure C-1).

4.2.7 Immunofluorescence

Immunofluorescence was performed as described by Hirano *et al.* (Hirano et al., 2007). Rabbit anti-Tdp1 and mouse anti-α-tubulin (DM1A, Sigma) were diluted 1:100 and 1:400, respectively. Images were acquired using a Zeiss Axiovert 200 microscope, a Zeiss AxiocamMR camera, and the Zeiss Axiovision imaging system.

4.2.8 Immunoblot analysis

Immunoblotting was performed as previously described (Hirano et al., 2007). Antibodies used were anti-human TDP1 (1:1000), mouse anti-GAPDH monoclonal antibody (1:5000; Chemicon), mouse anti-α-tubulin (1:1000; Abcam), rabbit anti-histone H2B (1:1000; Upstate), rabbit anti-PARP-1 (1:400, Abcam) and rabbit anti-caspase-3 (1:1000, Cell Signaling).

4.2.9 qRT-PCR

RNA was isolated from each cell-line using Qiagen RNeasy mini kit (Qiagen) and 3 µg were reverse transcribed with qScript cDNA supermix (Quanta Biosciences). Quantitative PCR was then done using PerfeCTa Sybergreen mix (Quanta Biosciences) and the 7500 Applied Biosystem qPCR machine. Data was analysed using the 7500 software (v2.0.1). The sequences of the primers used for qRT-PCR are listed in Supplementary Table C-1.

4.2.10 MTT assay

Cell proliferation and viability were measured by MTT assay as previously described (Mosmann, 1983). Briefly, $5x10^3$ cells were plated in each well of a 96-well plate and cultured in phenol red-free media. MTT solution was prepared by dissolving 5mg of MTT in 1 mL of 1X PBS. Following the described treatments, the culture media was supplemented with 10% MTT and incubated for 3 hours. This was followed by a 30-minute incubation in 100% DMSO.

Spectrophotometry was done at 565nm using the Wallac VICTOR2 Multilabel Plate Reader (Beckman-Coulter).

4.2.11 TUNEL assay

Briefly, $5x10^3$ cells were seeded per well in 6-well plates, and following the described treatments, apoptotic cells were visualized by colorimetric labeling of free 3'OH DNA termini using the Apoptag Plus Peroxidase *In Situ* Apoptosis Detection Kit according to the manufacturer's protocol (EMD Millipore). The number of stained nuclei per 100 total cells was determined for three independent replicates to quantify apoptosis.

4.2.12 Homogeneous caspase-3/7 assay

The activity of caspases 3 and 7, which play key effector roles in mammalian cell apoptosis, was measured using the Apo-ONE Homogeneous Caspase-3/7 kit according to the manufacturer's protocol (Promega). Briefly, $5x10^3$ cells were plated in each well of a 96-well plate and cultured for 24 hours and following the described treatments, fluorescence of the cleaved caspase 3 and 7 substrate was measured at 520nm using the Wallac VICTOR2 Multilabel Plate Reader (Beckman-Coulter).

4.2.13 Comet Assay

DNA damage was assessed by the comet assay as previously described (Hirano et al., 2007). While the assay is unable to distinguish between single stranded versus double stranded breaks, the alkaline conditions used also detect single-stranded break sites and promote conversion of alkali-labile apurinic and apyrimidinic (AP) sites to DNA breaks. Since Tdp1 also participates in the repair of AP sites (Murai et al., 2012a), the alkaline conversion of these sites to single stranded breaks allows a greater appreciation of the function of Tdp1. Briefly, RMS cell lines were seeded at a density of $3x10^5$ cells in a 6-well (9.6 cm^2) plate. After 24 hours, the cells were treated for 2 hours (37˚C, 5%CO_2) with 4μM, 8μM and 16μM camptothecin (CPT) (Sigma), harvested by trypsinization, resuspended in 80μL of 0.5% low melting point agarose and pipetted onto microscope slides pre-coated with 1% agarose. After addition of a second layer of 1% normal melting point agarose, the cells were immersed in lysis solution (2.5M NaCl, 100mM EDTA, 10mM Trizma base, 1% Triton X-100, 10% DMSO) for 2 hours. The DNA was then

denatured by incubation at 4˚C in alkaline buffer (50mM NaOH, 1mM EDTA, 1% DMSO, pH>13) for 25 minutes. Following electrophoresis at 25V and 4˚C for 25 minutes, the slides were neutralized in 0.4M Tris-HCl and stained with SYBR®-Green (Invitrogen). Images were acquired using a Zeiss Axiovert 200 microscope, a Zeiss AxiocamMR camera, and the Zeiss Axiovision imaging system. A total of 100 comets were scored for each sample using the Comet Assay IV software (Perceptive Instruments).

4.2.14 *TDP1* knockdown

TDP1 was knocked down transiently by transfecting $8x10^4$ cells with 100nM of pooled siRNAs (Dharmacon) in a 24-well plate using Lipofectamine 2000 (Invitrogen). Knockdown was confirmed by immunoblotting and qRT-PCR. The sequences of the siRNAs are listed in Supplementary Table C-1.

For stable knockdown of *TDP1*, $1\text{-}2x10^4$ cells were plated in each well of a 96-well plate and cultured overnight (37˚C, 5%CO_2). The culture medium was replaced for 4 to 18 hours with serum-free culture medium, 3µg/mL polybrene and lentivirus carrying the SMARTvector 2.0 shRNA (Dharmacon). The infection was carried out at a multiplicity of infection (MOI) of 0.3, 1, 2 or 5. Stably infected cells were selected with 0.5µg/mL puromycin, and ultimately the MOI that gave the best knockdown was used for each cell line. Knockdown of *TDP1* was verified by immunoblotting and qRT-PCR. The sequences of the shRNAs are listed in Supplementary Table C-2.

4.2.15 PARP inhibition

PARP inhibitors AG-014699 (Rucaparib), AZD-2281 (Olaparib) and ABT-888 (Veliparib) were obtained from Selleck Chemicals. The LD_{50} for each inhibitor was determined by seeding each wild-type RMS cell line at $5x10^3$ cells per well in 96-well microtiter plates. After 24 hours, the PARP inhibitors were added to the culture medium to a final concentration of 0.1µM, 0.5µM, 1µM or 10µM. Cell viability and proliferation was measured in triplicate every 24 hours for 96 hours by the MTT assay.

4.2.16 Tdp1 cleavage assay

Cells were lysed and their nuclear contents extracted as previously described (Jensen et al., 2013). Briefly, cells were pelleted and lysed in 1mL of lysis buffer. The cells were placed on ice for 10 minutes and vortexed every 2 minutes to allow complete lysis. The nuclei were pelleted for 4 minutes at 2000 rpm. Following removal of the supernatant, 3X the volume of the pellet of nuclear extraction buffer was added. The pellet was resuspended and incubated at 4°C for one hour to isolate nuclear proteins. The lysate was clarified for 10 minutes at 11000 rpm to obtain nuclear extracts. The supernatant containing nuclear proteins were diluted 1:10 in reaction buffer (10 mM Tris-HCl, 50 mM KCl, 1 mM EDTA, 1mM DTT, 0.01% Brij-35, pH 7.5).

Tdp1 enzymatic activity was determined by cleavage of an artificial substrate as described (Dean, 2013). Briefly, the assay was run at room temperature, in 96-well format with a final volume of 100µL per well. A final concentration of 50nM DNA substrate was used (5'-/56-TAMN/AGG ATC TAA AAG ACT T/3BHQ_1/-3'). Kinetic analysis was performed using a Varioskan plate reader (Thermo Scientific) at Ex557/Em582 for the TAMRA fluorophore. To establish Tdp1 cleavage activity, 20 reads were recorded at a kinetic interval of 45 seconds per read. 2.5nM of purified Tdp1 was used in the control samples. Purified Tdp1 was isolated as previously described (Dean, 2013).

4.2.17 Statistical analysis

Microsoft Excel was used to compute the group means and standard deviations for all treatment and control groups from cell viability data derived from the MTT, caspase and apoptosis assays. The GraphPad Prism software was used for two-way ANOVA to compare the differences in growth and viability under varying treatment conditions over time. The F-ratio was used to test the validity of interactions between treatment groups over the course of the experiment. Statistical significance between individual groups was established by the t-test, and a p-value of <0.05 was judged significant. The Bonferroni correction was applied to all comparisons of replicate means for the duration of the experiments.

4.2.18 Sequencing of *TDP1*, *BRCA1* and *BRCA2*

Genomic DNA was isolated from RMS cell lines using the Gentra Puregene Blood kit (Qiagen). RNA was extracted from RMS cells using the Qiagen RNeasy kit (Qiagen) and cDNA

synthesized using the qScript cDNA SuperMix. PCR amplification of the *TDP1* coding exons was performed as previously described (Boerkoel et al., 2002). PCR amplification of the *BRCA1* cDNA and of *BRCA2* exons was performed using the primers listed (Supplementary Table C-4) and HotStar Taq Plus (Qiagen) with the following conditions: Denaturation stage: 95°C for 5 minutes, Cycling stage (40 cycles): 95°C for 30 seconds, 57°C for 30 seconds, 72°C for 1 minute. End stage: 72°C, 10 minutes, hold at 4°C. All amplicons were sequenced at Macrogen and the sequences were aligned and analyzed using Sequencher 4.3 (Gene Codes).

4.3 Results

4.3.1 Tdp1 is highly expressed in RMS tumors

To determine if Tdp1 is expressed in RMS and other pediatric solid tumors, Miraj Chowdhury immunohistochemically screened a pediatric tumor microarray consisting of 24 eRMS, 18 aRMS, 12 ganglioneuroma, 23 neuroblastoma, 10 Ewing's sarcoma, 9 medulloblastoma, and 24 Wilms tumour readable tissue cores. This showed that Tdp1 was expressed with the highest frequency in RMS tumors (Supplementary Figure C-2). To confirm this expression in RMS tumors, Dr. Catherine Pallen obtained 34 eRMS and 39 aRMS tumors from the Children's Oncology Group and observed Tdp1 expression respectively in 97% and 100% of the tumors. By comparison to adjacent non-cancerous tissue, Tdp1 also appeared to have increased expression in the cancer cells (Fig. 4-1A-C).

To confirm *TDP1* mRNA expression in RMS tumors, Sheetal Mitra screened an independent soft tissue sarcoma cohort that included 20 RMS (specifically, 10 PAX-FKHR-positive alveolar RMS, 5 PAX-FKHR-negative alveolar RMS, and 5 embryonal RMS), 5 NRSTS, 5 osteosarcomas and 5 Ewing sarcomas by Affymetrix expression arrays. This analysis revealed that *TDP1* mRNA was expressed in all soft tissue sarcomas (Fig. 4-1D). The mean (± standard deviation) normalized microarray expression levels for these soft tissue sarcomas were 189.6 (±31.9), 161.5 (±32.2), 164.9 (±38.1) and 148.7 (±16.0), respectively. *TDP1* expression levels in RMS were significantly higher compared to the other sarcomas in the group (ANOVA $p=0.041$).

To further investigate the specific pattern of *TDP1* expression in RMS, transcriptome profiling data on 147 primary tumors was compared to that of normal skeletal muscle. This analysis indicated that Tdp1 was significantly overexpressed in all primary RMS samples

compared to normal skeletal muscle (Supplementary Table C-2, Fig. 4-1E). In addition, the mean expression level in fusion-positive RMS tumors was significantly greater than in fusion-negative tumors (233.1 versus 192.2; Mann-Whitney $p<0.001$, data not shown). Thus, although *TDP1* is highly expressed in RMS in general ($p<0.001$), it is most significantly over-expressed in fusion-positive RMS ($p<0.001$) when compared to normal skeletal muscle, suggesting a correlation between RMS subtypes and *TDP1* expression.

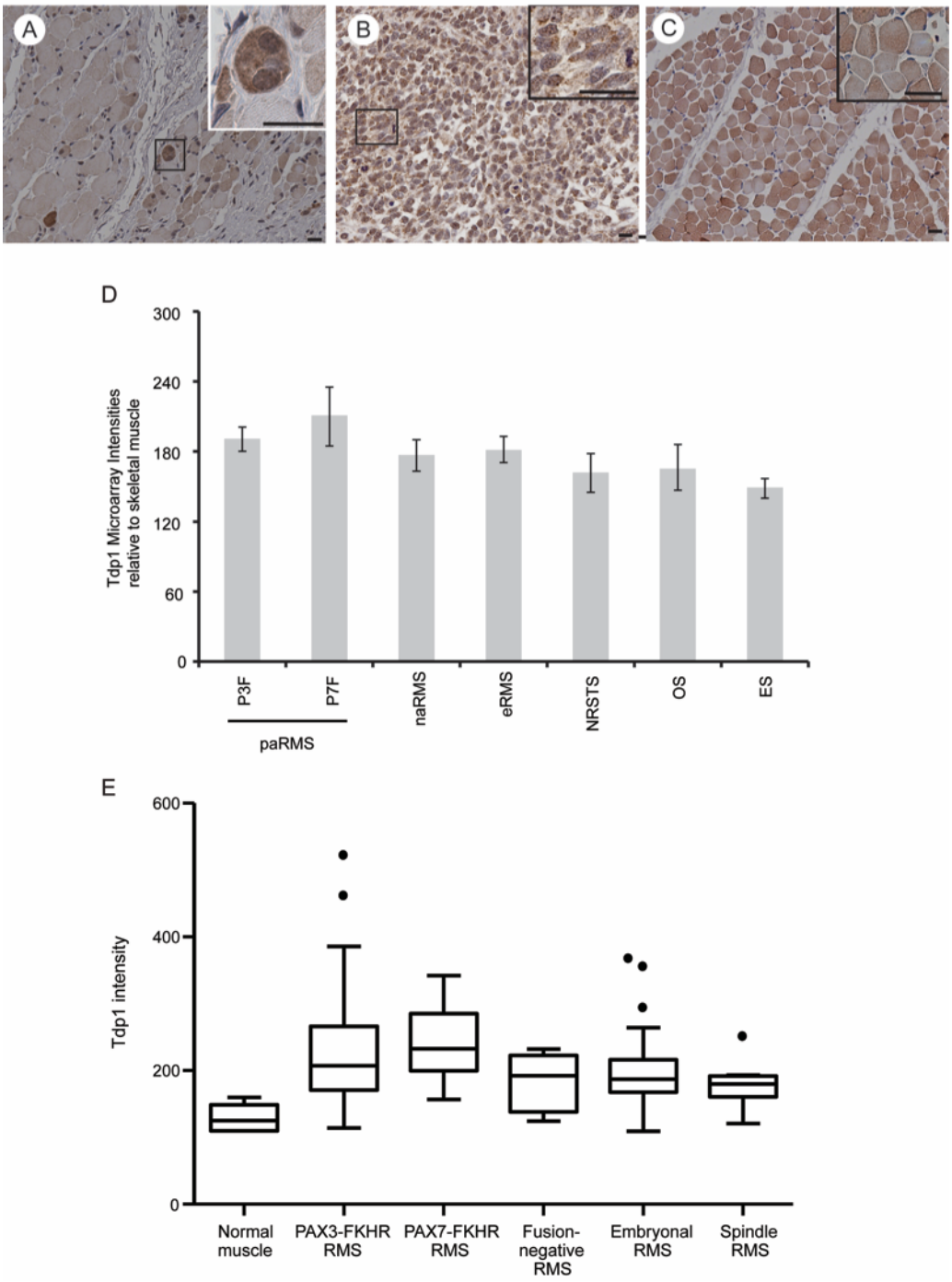

Figure 4-1: Tdp1 expression in RMS tumors.

Photomicrographs showing immunohistochemical detection of Tdp1 in (A) alveolar RMS (B) embryonal RMS and (C) unaffected human skeletal muscle tissue. Scale bar = 10 µm. (D) Graph of the *TDP1* transcript intensity in soft tissue sarcomas as measured by Affymetrix array. NRSTS = Non-Rhabdomyosarcoma Soft Tissue Sarcoma. OS = Osteosarcoma. ES = Ewing Sarcoma. (E) Tukey box plots representing Tdp1 expression intensities across 7 normal

skeletal muscle samples, 44 PAX3-FKHR RMS, 17 PAX7-FKHR RMS, 9 fusion-negative RMS, 69 embryonal RMS, and 8 spindle RMS. The boxes represent median with interquartile range; whiskers extend 1.5 times the interquartile distance or to the highest or lowest point, whichever is shorter. Dots represent outliers.

4.3.2 Tdp1 is highly expressed in RMS cell lines

To further validate expression of Tdp1 in RMS cells, I studied RMS cell lines RD, A204, Birch, RH30 and CW9019. Immunoblotting and qRT-PCR indicated increased expression of *TDP1* mRNA and protein (Fig. 4-2A-B) in RMS cell lines relative to skeletal muscle. Immunoblotting for Tdp1 protein confirmed that Tdp1 was most abundant in the cell lines that most highly express *TDP1* mRNA (CW9019 and RH30). For each cell line, immunofluorescence staining of Tdp1 showed both nuclear and cytoplasmic expression (Fig. 4-2C), and sequencing of all *TDP1* exons detected no mutations within the exons or canonical splice sites (data not shown)**.**

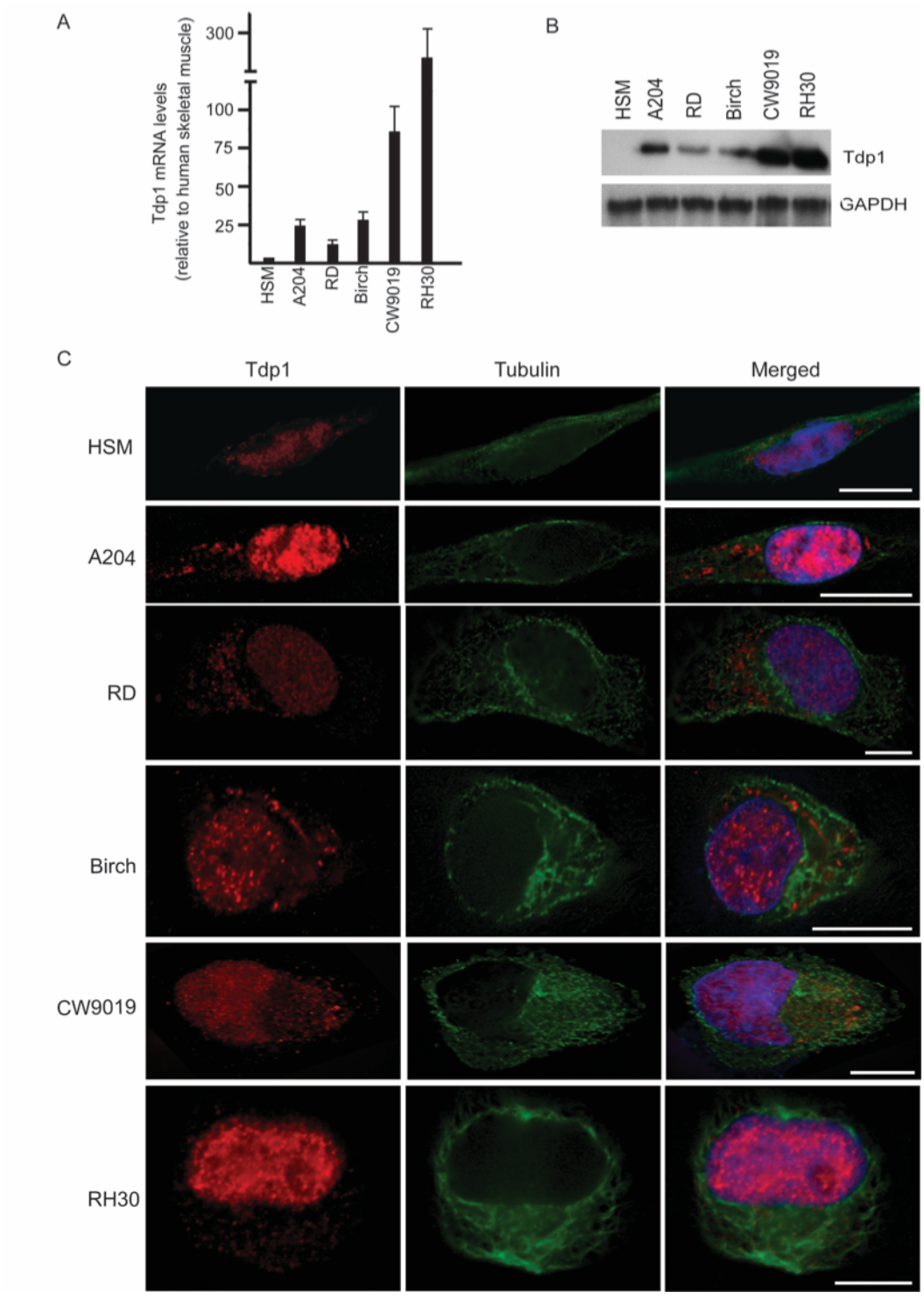

Figure 4-2: Tdp1 expression in alveolar and embryonal RMS cell lines.

(A) Graph showing the level of *TDP1* mRNA in RMS cell lines relative to unaffected skeletal muscle and standardized to GAPDH mRNA levels (n=3) (B) Immunoblot showing Tdp1 protein expression in RMS cell extracts. GAPDH was used as a loading control. (C) Photomicrographs showing immunofluorescent detection of

Tdp1 expression in the nucleus and cytoplasm of cultured embryonal (A204, RD and Birch) and alveolar (CW9019 and RH30) RMS cells. n, number of replicates. Scale bar = 10 μm.

4.3.3 *TDP1* knockdown preferentially increases CPT sensitivity of RMS cell lines compared to control skeletal myoblasts

Since Tdp1 expression is elevated in RMS cells relative to skeletal muscle, this might explain the unresponsiveness of RMS to treatment with the irinotecan, an analogue of camptothecin (CPT) (Mascarenhas et al., 2010). Consistent with this, siRNA knockdown of *TDP1* by 70 to 85 % decreased the viability of all CPT-treated RMS cell lines except RD (Supplementary Figure C-3A and Figure 4-3A). In contrast, *siRNA TDP1* knockdown of nearly 90 % (Supplementary Figure C-3A) did not significantly decrease the viability of CPT-treated control skeletal myoblasts. Since complete loss of functional Tdp1 dramatically increased the sensitivity of mouse embryonic fibroblasts to CPT (Supplementary Figure C-3B), I hypothesized that residual Tdp1 activity provided this resistance of skeletal myoblasts to CPT and indeed observed 50% residual activity among myoblasts with 85% knockdown of *TDP1* mRNA by expression of a *TDP1*-targeting shRNA (Supplementary Figure C-4).

To determine if the increased sensitivity of RMS cells to CPT arose from accumulation of DNA breaks, I used alkaline comet assays to compare 1μmol/L CPT treatment alone and 1μmol/L CPT treatment plus knockdown of *TDP1*. The combined treatment induced 5-fold more DNA strand breaks in A204, Birch and CW9019 cells and 15-fold more in RH30 cells over cells treated with CPT alone (Figure 4-3B). In contrast, combined treatment did not significantly increase the amount of DNA breaks over CPT treatment alone in control myoblasts.

To determine if this differential sensitivity of RMS cells versus control myoblasts was attributable to different proliferation rates that gave rise to differences in the likelihood of collision between the replication apparatus and DNA-TopoI complexes, I analyzed the consequences *of TDP1* knockdown on the breast cancer cell line MDA-231. The proliferation rate of MDA-231 cells was 16 hours (Supplementary Figure C-5A), comparable to that of CW9019 cells (Figure 4-3A) and approximately 3-fold faster than normal myoblasts (48 hours, Figure 4-3A). *TDP1* expression level of MDA-231 was comparable to that of the myoblasts (Supplementary Fig. C-4 and C-5B). 1μmol/L CPT treatment of MDA-231 cells after 75% *TDP1*

knockdown did not significantly increase the amount of DNA breaks compared to CPT treatment alone (Supplementary Figure C-5 (C and D)). This suggested that the increased CPT sensitivity of these cells was in proportion to elevated *TDP1* expression, but not due to an increased proliferation rate.

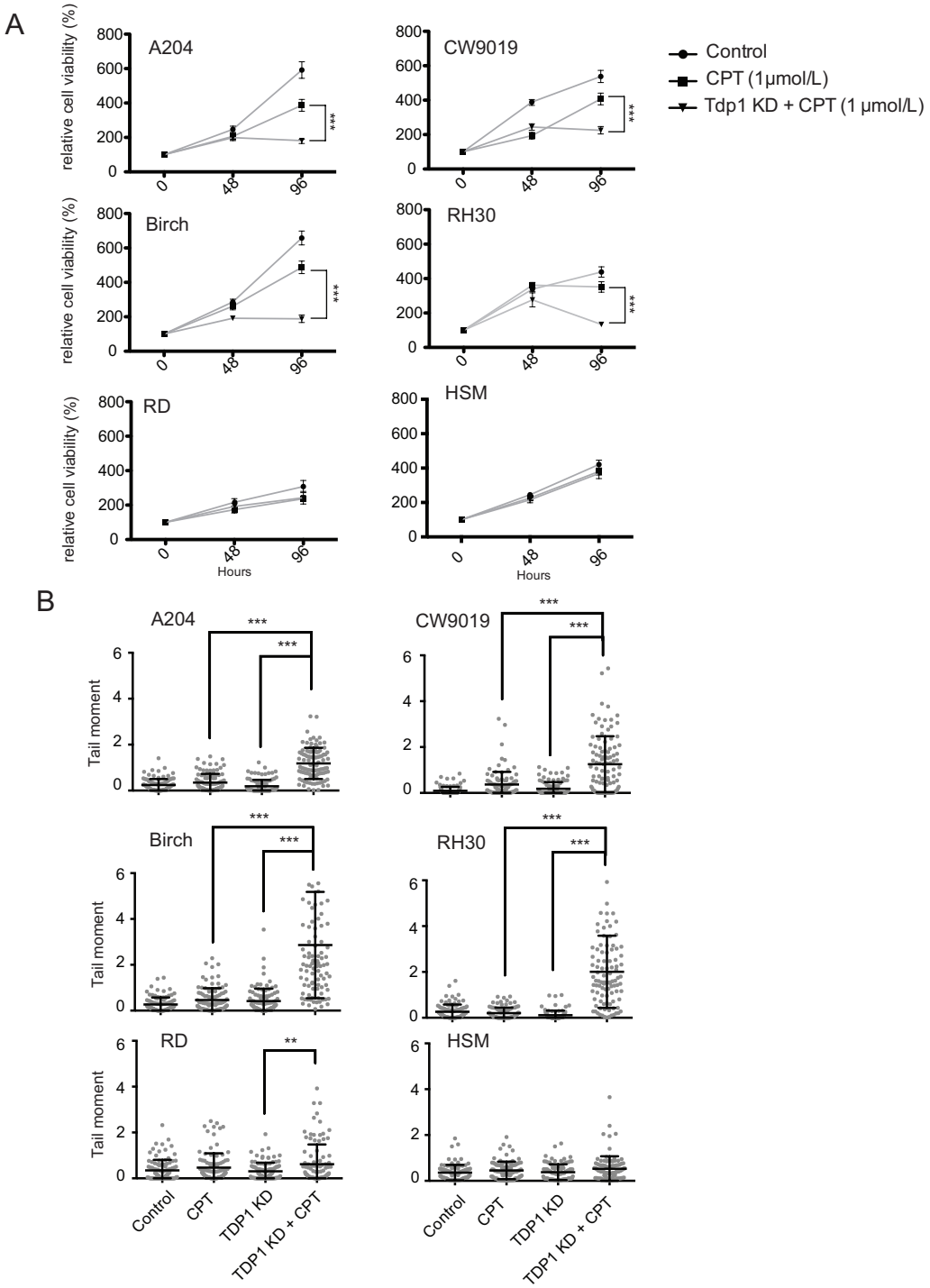

Figure 4-3: *TDP1* knockdown increases the sensitivity of RMS cell lines to CPT treatment.
(A) Graphs showing the percent proliferation of RMS cells and control myoblasts over a 96 hour period during which the cells 1) received no CPT, 2) were treated with 1μmol/L CPT or 3) were treated with 1μmol/L CPT after transient *TDP1* knockdown (n=4). (B) Graphs showing the results of an alkaline comet assay, which analyzes the number of DNA breaks (tail moment) in all cell lines after 2 hours of culture under the conditions stated above (n=4). n, number of replicates; error bars, mean ± s.d. **, $P<0.01$; ***, $P<0.001$.

4.3.4 PARP-1 expression is increased in RMS cell lines and its inhibition preferentially increases CPT sensitivity of RMS cell lines compared to control skeletal myoblasts

Since PARP-1 and Tdp1 are in the same DNA repair complex, I hypothesized that PARP-1 inhibition also sensitizes RMS cells to CPT. As observed for Tdp1, RMS cells expressed more *PARP-1* mRNA and protein than control skeletal myoblasts (Supplementary Figure C-6 (A and B)). The administration of the PARP-1 specific inhibitor AG-014699 (Rucaparib) reduced the amount of PARP-1 (poly-ADP ribosyl polymers, PAR) products in all cell lines (Figure 4-4, insets). As shown by comet assay (Supplementary Figure C-7), treatment with 10μmol/L Rucaparib increased the number of DNA breaks in all RMS cell lines exposed to 1μmol/L CPT by 4-5 fold compared to treatment with 1μmol/L CPT alone. In contrast, the same treatment on control myoblasts only increased the sensitivity to 1μmol/L CPT by 2 fold.

To ascertain whether inhibition of PARP-2 in conjunction with inhibition of PARP-1 would be more effective than inhibition of PARP-1 alone, I tested inhibitors targeting both PARP-1 and PARP-2. In contrast to Tdp1 and PARP-1, *PARP-2* mRNA and protein expression are unaltered or decreased in most RMS cells lines compared to control myoblasts (Supplementary Figure C-6 (A and C)). As measured by comet assay, AZD-2281 (Olaparib) and ABT-888 (Veliparib), which inhibit both PARP-1 and PARP-2, sensitized RMS cells less to CPT than did Rucaparib (Supplementary Figure C-7). Since Rucaparib (K_i = 1.4nM) is a more potent inhibitor of PARP-1 than are Olaparib (K_i = 5nM) and Veliparib (K_i = 5.2nM), I hypothesized that one cause of the difference in effectiveness of these three compounds is the differential inhibition of PARP-1.

4.3.5 *TDP1* knockdown and PARP-1 inhibition alone and together are more cytotoxic to RMS cells than to control skeletal myoblasts

I observed that either *TDP1* knockdown or PARP-1 inhibition impaired proliferation of the RMS cell lines (Figure 4-4A), as measured using the MTT assay. 70-90% siRNA knockdown of *TDP1* reduced proliferation of A204, Birch and RH30 by 30%, 50%, and 30% respectively but had no effect on control myoblasts (Figure 4-4A). Of the PARP-1 inhibitors tested, Rucaparib was most detrimental to the RMS cell proliferation (Supplementary Table C-3). Treatment with 10μmol/L Rucaparib for 96 hours led to a 50% or greater decrease in proliferation of four out of five RMS cell lines compared to untreated cells, but only a 10% decrease in the proliferation of control myoblasts (Supplementary Table C-3 and Figure 4-4A). Excepting Birch, this reduction in proliferation is 2-fold greater than that observed with *TDP1* knockdown alone (Figure 4-4A), suggesting that either PARP-1 inhibition is more effective than *TDP1* knockdown or that PARP-1 inhibition is affecting pathways essential for RMS cell survival other than those involving Tdp1.

To investigate whether *TDP1* knockdown and PARP-1 inhibition are additive, I found that the combination of 70-90% knockdown of *TDP1* and 10 μmol/L Rucaparib decreased A204, Birch, RH30, CW9019 cell proliferation more than either treatment alone; this treatment had no effect on control myoblasts (Figure 4-4A). Over the course of 96 hours, A204, Birch and RH30 cell numbers declined by 70-80%, and as measured by caspase-3/7 expression and TUNEL-positive staining, this toxicity correlated with induction of apoptosis (Figure 4-4B and C), implying that cytotoxicity was responsible for the decline in proliferation. Additionally, suggestive of an additive effect arising from *TDP1* knockdown and PARP-1 inhibition targeting the same pathway, constitutive *TDP1* knockdown (Supplementary Figure C-3 (C and D)) resulted in the selection of cells that were resistant to 10 μmol/L Rucaparib treatment, whereas cells constitutively expressing a non-targeting shRNA remained sensitive to PARP-1 inhibition (Supplementary Figure C-8A).

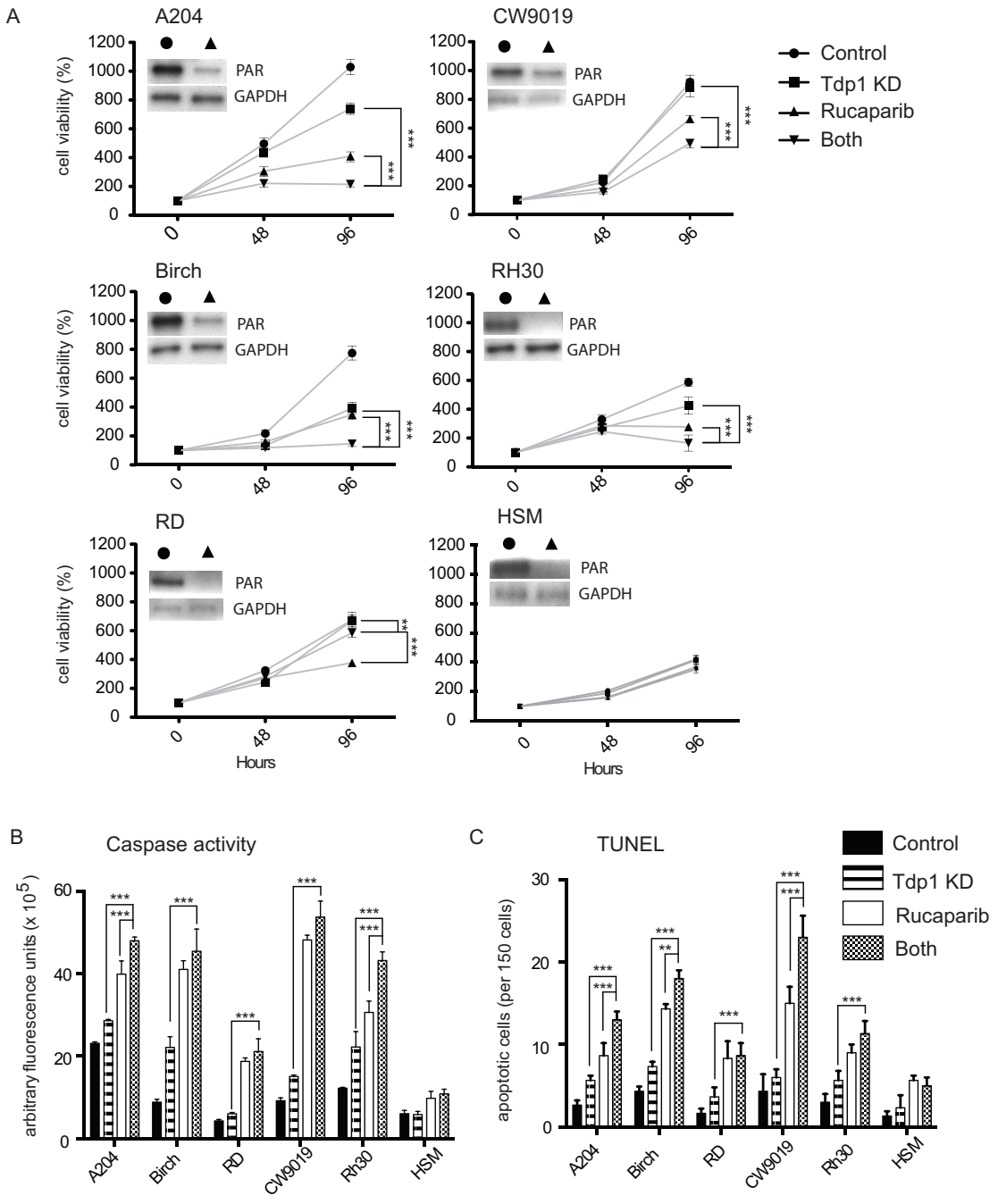

Figure 4-4: Combined *TDP1* knockdown and PARP-1 inhibition are more cytotoxic to RMS than either alone.

(A) Graph of the number of RMS cells and control myoblasts over a 96-hour period during which the cells were subjected to 1) non-targeting siRNA treatment 2) *TDP1* siRNA treatment 3) 10µmol/L PARP-1 inhibitor (Rucaparib) treatment or 4) combined Rucaparib and *TDP1* siRNA treatment (n=4). Inset within graphs are photographs of immunoblots showing poly-ADP ribosyl (PAR) polymer expression after 24 hour Rucaparib

treatment. GAPDH is used as a loading control. (B) Graph of a caspase-3/7 activation assay illustrating caspase-3/7 cleavage for all cell lines under conditions 1 through 4 above (n=3). (C) Graph of TUNEL assay showing the number of terminally apoptotic cells as measured by DNA strand breaks assay for all cell lines under conditions 1 through 4 above (n=3). n, number of replicates; error bars, mean ± s.d. among treatments 2, 3 and 4. **, $P<0.01$; ***, $P<0.001$.

4.3.6 RMS cell lines do not harbor pathogenic *BRCA1* or *BRCA2* mutations

Based on the effect of PARP-1 inhibitors on cancer cells with *BRCA1* or *BRCA2* mutations or other defects of DNA double-strand break repair (Fong et al., 2009; Tutt et al., 2010), the cytotoxicity of Tdp1 knockdown and PARP-1 inhibition on RMS cells could arise from loss of functional BRCA1 or BRCA2. However, qRT-PCR did not detect a significant loss of *BRCA1* or *BRCA2* mRNA and sequencing of the *BRCA1* cDNA and *BRCA2* exons detected no pathogenic mutations (Supplementary Tables C-4, C-5 and Supplementary Figure C-8B). Therefore, *BRCA1 and BRCA2* perturbations did not explain the sensitivity of RMS cells to PARP-1 inhibition.

In the absence of *BRCA1* and *BRCA2* mutations, reversions of such mutations do not explain the PARP-1 inhibitor resistance of RMS cells with constitutive *TDP1* knockdown. Also, since expression of *BRCA1* mRNA in RMS cells with constitutive Tdp1 knockdown declined or stayed the same relative to RMS cells expressing a non-targeting shRNA, increased *BRCA1* expression did not account for the PARP-1 inhibitor resistance (Supplementary Figure C-8C). However, since resistance to PARP-1 inhibitors is also correlated with a reduction in *TP53BP1* expression (Aly and Ganesan, 2011), I tested for this and found that A204, Birch, RD and RH30 cells surviving selection for constitutive *TDP1* knockdown had a 50% reduction in *TP53BP1* expression (Supplementary Figure C-8C).

4.3.7 Serum and glucose restriction is cytotoxic to Birch and CW9019 cell lines

Despite the absence of deleterious *BRCA1* and *BRCA2* mutations, the sensitivity of RMS cells to Tdp1 knockdown and PARP-1 inhibition suggests they harbor a defect of DNA repair. Therefore, as glucose and serum restriction increase cellular oxidative stress and error-prone DNA repair in mammalian cells (Siggens et al., 2012), I tested if this was cytotoxic to RMS cells. As measured by MTT, caspase-3/7 and TUNEL assays, glucose and serum restriction were

cytotoxic to Birch and CW9019 but not to other RMS cell lines or control skeletal myoblasts (Figure 4-5A-C).

4.3.8 Serum and glucose restriction sensitizes RMS cells to PARP-1 mediated cytotoxicity compared to control skeletal myoblasts

Although PARP-1 inhibition in normal tissues can protect tissues from serum starvation by maintaining cellular energy and activating survival pathways (Mathews and Berk, 2008), recent findings that serum and glucose restriction sensitizes cancer cells to genotoxic agents led me to hypothesize that such restriction increases sensitivity of RMS cells to PARP-1 inhibitors (Lee et al., 2012a). Indeed, serum and glucose restriction increased the cytotoxicity of 10 μmol/L Rucaparib on the aRMS cell lines RH30 and CW9019 but not the eRMS cell lines or control myoblasts (Figure 4-5A-C).

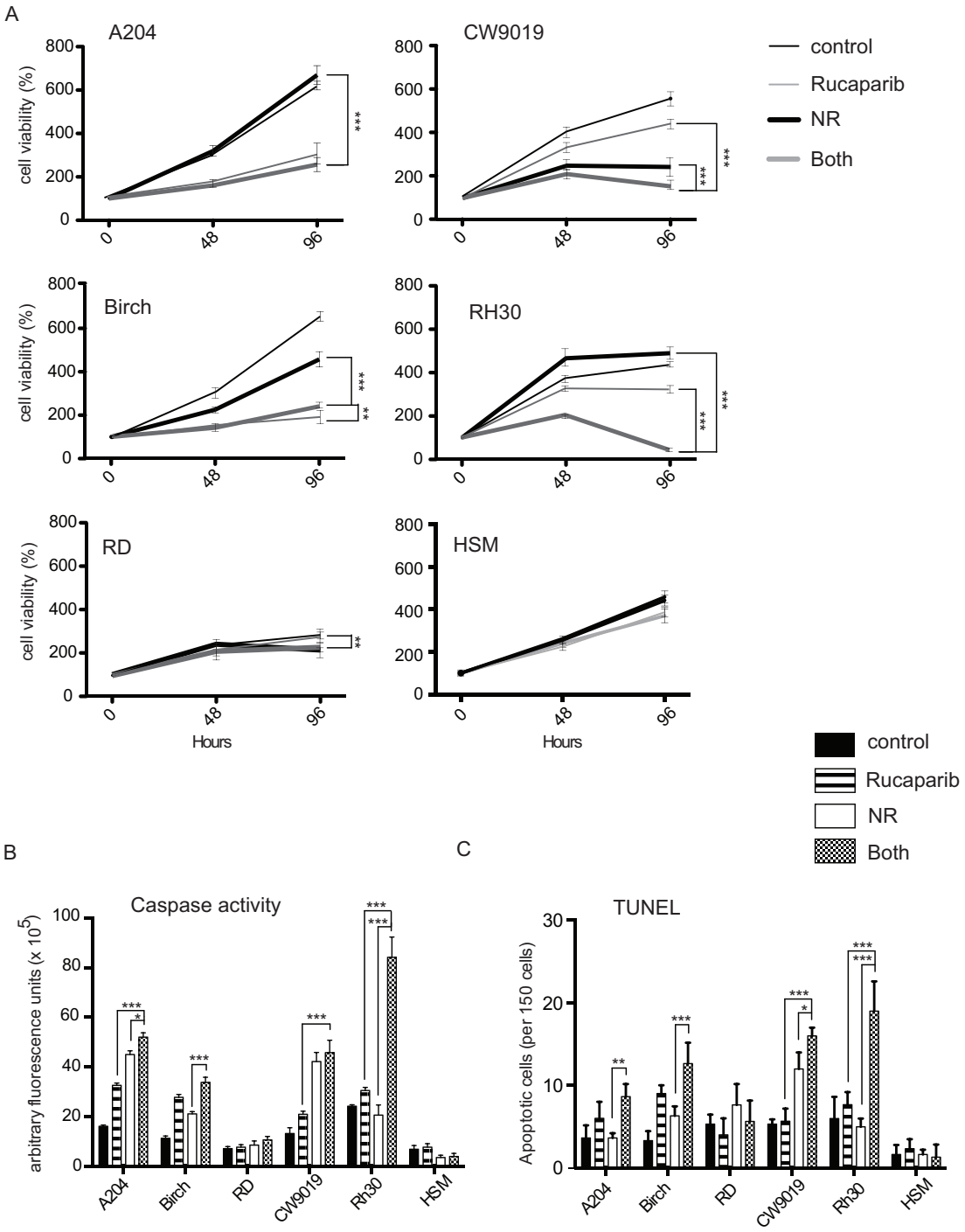

Figure 4-5: PARP-1 inhibition sensitizes RMS cells to nutrient restriction.

(A) Graphs showing the number of RMS cells and control myoblasts over a 96 hour period during which the cells were subjected to 1) normal cell culture media (4.5g/L glucose, 10% FBS) 2) 10µmol/L Rucaparib treatment 3) nutrient restriction (1g/L glucose, 1%FBS) (NR) 4) combination of 10µmol/L Rucaparib treatment and nutrient restriction (n=4). (B) Graph of caspase-3/7 cleavage for all cell lines under conditions 1 through 4 above (n=3). (C)

Graph of the number of terminally apoptotic cells as measured by DNA strand break assay for all cell lines under conditions 1 through 4 above (n=3). NR= nutrient restriction. n, number of replicates; error bars, mean ± s.d. among treatments 2, 3 and 4. **, $P<0.01$; ***,$P<0.001$.

4.3.9 RMS cells resistant to Tdp1 knockdown and PARP-1 inhibition are sensitive to serum and glucose restriction

To determine if nutrition restriction were a potential complementary therapy to *TDP1* knockdown and PARP-1 inhibition, I determined if serum and glucose restriction were cytotoxic to RMS cells resistant to 10 μmol/L PARP-1 inhibition and constitutive *TDP1* knockdown. I found that serum and glucose restriction did cause apoptosis of A204, Birch, RH30 and CW9019 cells resistant to PARP-1 inhibitors, whereas control myoblasts were minimally affected (Figure 4-6A-C).

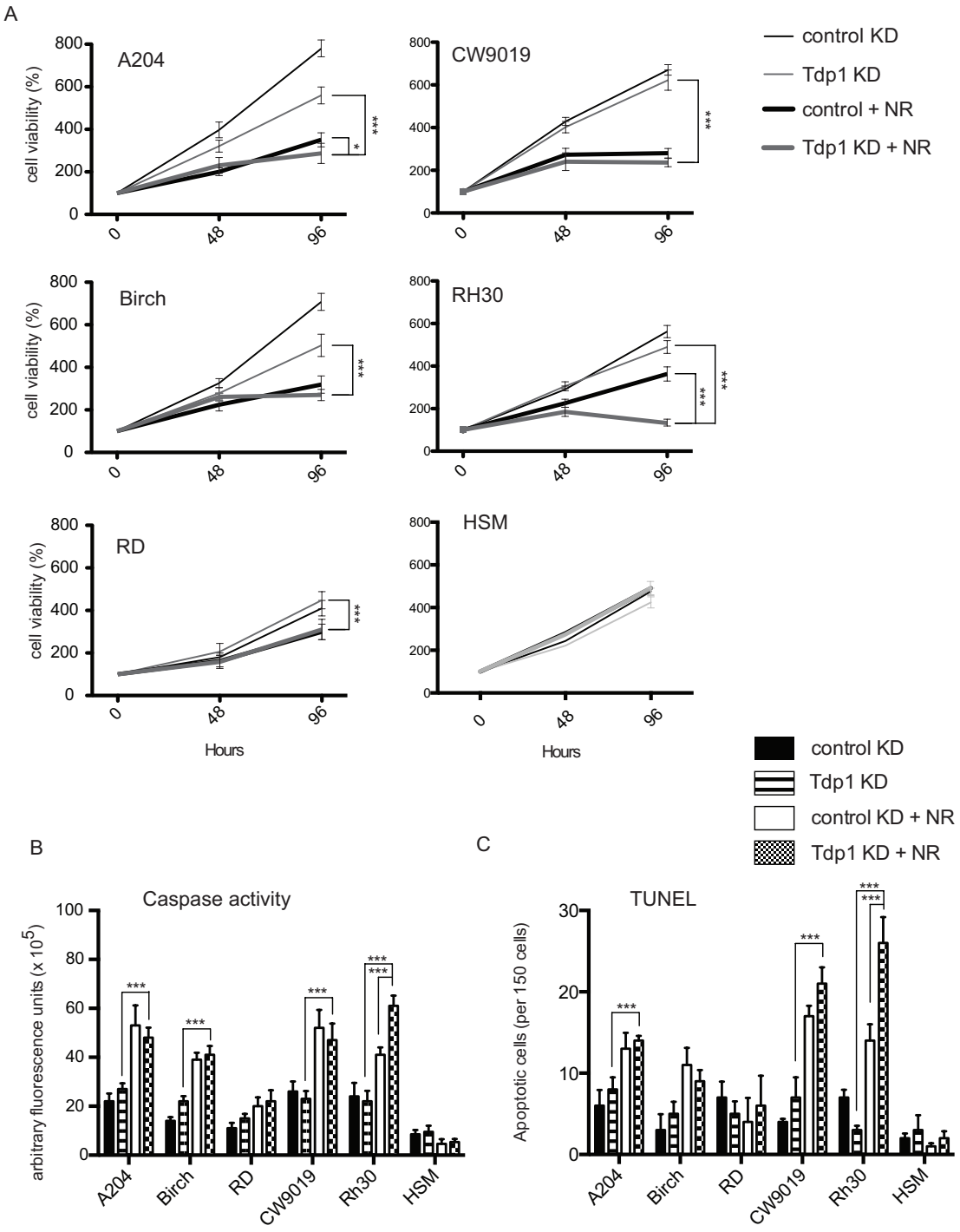

Figure 4-6: Nutrient restriction is an effective alternative for treating RMS cells resistant to *TDP1* knockdown and PARP-1 inhibition.

(A) Graphs showing the number of RMS cells and control myoblasts over a 96 hour period for 1) cells treated with non-targeting shRNA 2) cells treated with *TDP1* shRNA 3) non-targeting shRNA cells cultured under nutrient

restriction or 4) *TDP1* shRNA cells cultured under nutrient restriction (n=4). (B) Graph of caspase-3/7 cleavage for all cell lines under conditions 1 through 4 above (n=3). (C) Graph of the number of terminally apoptotic cells as measured by DNA strand break assay for all cell lines under conditions 1 through 4 above (n=3). n, number of replicates; error bars, mean ± s.d. among treatments 2, 3 and 4. *, $P<0.05$; ***, $P<0.001$.

4.4 Discussion

I have shown that Tdp1 and PARP-1 are highly expressed in RMS tumors, and that as predicted from the functions of Tdp1 and PARP-1 in DNA repair, knockdown of *TDP1* and inhibition of PARP-1 sensitized RMS cells to CPT treatment. Suggestive of an intrinsic defect of DNA repair in RMS cell lines, *TDP1* knockdown and PARP-1 inhibition alone or in combination also caused apoptosis of RMS cells. Additionally, stressing the DNA repair and replication system through glucose and serum restriction reduced viability of some RMS cells and enhanced sensitivity to PARP-1 inhibitors. Remarkably, each of these manipulations preferentially affected tumor cells compared to control skeletal myoblasts.

Tdp1 and PARP-1 are members of a DNA single-strand-break repair complex that also includes XRCC1, Ligase III and PNKP (El-Khamisy et al., 2005). Within this complex, Tdp1 processes topoisomerase-I-DNA complexes and blocked 3'-termini (Murai et al., 2012a). Tdp1 mutant cell lines and knockout mice have increased sensitivity to several anticancer agents (Hirano et al., 2007; Katyal et al., 2007). These observations have consequently led to the suggestion that Tdp1 overexpression in tumor cells confers resistance to anti-cancer agents, particularly the CPT analogues (Liu et al., 2007). The increased expression of Tdp1 in RMS compared to unaffected skeletal muscle and the increased sensitivity of RMS cells to CPT after *TDP1* knockdown or PARP-1 inhibition suggest a possible answer for the failure of irinotecan to show efficacy against of RMS (Mascarenhas et al., 2010).

For the RMS cell lines RD, A204, Birch, RH30, CW9019, this markedly elevated expression of Tdp1 is not explicable as a compensatory reaction to a *TDP1* hypomorphic allele or to aberrant Tdp1 subcellular localization. Since many cancers compensate for defects of DNA repair, which are permissive for rapid tumor evolution, by overexpression of other DNA repair pathways (Chiarugi, 2012; Messina et al., 2012), I had wondered if RMS cells might also have a defect of DNA repair and if the overexpression of Tdp1 was a compensatory survival mechanism. Finding that *TDP1* knockdown and PARP-1 inhibition preferentially decreased

RMS cell viability over that of control myoblasts, I hypothesize that RMS tumors have a damaged DNA repair process that is at least partially compensated for by processes in which Tdp1 and PARP-1 are involved.

Tdp1 and PARP-1 are involved in repairing both single and double strand DNA breaks (Katyal et al., 2007; Plo et al., 2003; Schultz et al., 2003). However, PARP-1 has additionally been shown to participate in the processes of DNA replication and transcription (Kim et al., 2004; Ray Chaudhuri et al., 2012). The role of PARP-1 in these latter functions might partially explain why PARP-1 inhibition had a more deleterious effect on RMS cells than did *TDP1* knockdown. Alternatively, PARP-1 inhibition might have reduced DNA repair activity more than *TDP1* knockdown since the knockdown alone left more than 10% expression of Tdp1. Supporting the last explanation, 85% knockdown of *TDP1* diminished Tdp1 cleavage activity by 50% in myoblasts and was insufficient to induce CPT hypersensitivity, a property of tissues and organisms fully deficient for Tdp1 (El-Khamisy et al., 2005; Hirano et al., 2007; Katyal et al., 2007).

Even though *TDP1* knockdown was insufficient to cause hypersensitivity of control myoblasts to CPT, it was sufficient to decrease the viability of RMS cells and to increase their sensitivity to CPT. These observations raise the possibility of selectively targeting Tdp1 and PARP-1 to sensitise cancer but not non-cancerous cells. Additionally, Tdp1 knockdown or PARP-1 inhibition alone were cytotoxic to a subset of cells in all RMS cell lines analysed. However, because some cells were resistant to these treatments, RMS cells have or rapidly develop resistance to *TDP1* knockdown and PARP-1 inhibition. In other cancers, resistance to PARP-1 inhibition occurs through partial correction of defects in homologous recombination-mediated DNA double-strand break repair and can include reversion of mutations in *BRCA1* or loss of *TP53BP1* expression (Aly and Ganesan, 2011). Two recent studies in mice showed that loss of *TP53BP1* in *BRCA1* mutant cells leads to PARP-1 inhibitor resistance and that *TP53BP1* loss did not alleviate sensitivity to PARP-1 inhibition without the accompanying *BRCA1* loss-of-function mutation (Bouwman et al., 2010; Bunting et al., 2010). Therefore, since I did not find mutations in *BRCA1*, I hypothesize that if the decreased *TP53BP1* expression is relevant to the resistance to PARP-1 inhibition, then there must be other mutations of DNA repair in the RMS cell lines to complement the reduced *TP53BP1* expression. Additionally, the presence or

development of cells resistant to *TDP1* knockdown and PARP-1 inhibition suggest that targeting Tdp1 and PARP-1 in RMS needs to be part of a multimodal therapy.

Targeting the altered energy metabolism common among solid tumors is a potential component of multimodal therapy (Marin-Valencia et al., 2012). Altered tumor metabolism arises because even though solid tumor cells require a high metabolic rate to support their rapid proliferation (Gatenby and Gillies, 2004), they come to rely on inefficient anaerobic metabolism as they outgrow their blood supply. In one study, glucose deprivation in glioblastoma cells triggered mitochondria-derived ROS production that caused ROS-mediated cell death (Graham et al., 2012). As Tdp1 and PARP-1 contribute to the base excision repair processes targeting oxidatively damaged nuclear and mitochondrial DNA (Das et al., 2010; Fam et al., 2013a; Luo and Kraus, 2012), the complementation between inhibition of Tdp1 or PARP-1 and glucose deprivation has a logical basis. Further studies are required however to test this hypothesis as was recently done for other cell lines (Luo and Kraus, 2012; Rodriguez-Vargas et al., 2012). Nonetheless, the observation does suggest that nutritional restriction is a consideration for treatment of RMS.

A final therapeutic consideration arising from this study is that none of the five RMS cell lines responded identically to any one therapy, let alone all therapies. This suggests that the genetic and epigenetic defects intrinsic to each RMS tumor are likely different. In the understanding of these differences resides the ability to target therapies to the tumor and minimally harm normal tissues. The three potential therapeutic approaches identified herein all preferentially affected RMS cell lines compared to control myoblasts, and thus provide direction for tumor stratification, analysis of genomic studies of RMS tumors and a basis for future preclinical trials.

In summary, I show that *TDP1* knockdown and PARP-1 inhibition increase the sensitivity of RMS cells to CPT analogues and have a direct toxic effect on some RMS cell types. I also find that glucose and serum restriction can be cytotoxic to RMS cells and sensitize them to PARP-1 inhibition. Although further study is needed to understand the molecular mechanisms underlying the effects of these therapies on RMS cells and to determine if they have relevance *in vivo*, these or similar therapies have the potential to improve outcomes for individuals with RMS.

Chapter 5: Identification of a Tdp1 Inhibitor

5.1 Introduction

Deficits of DNA repair contribute to the survival and proliferation of tumor tissue and hence are implicated in cancer progression (Helleday, 2008; Wei et al., 2000). Since the chemotherapeutic agents that target proliferative tumors are often harmful to normal cells and therefore carry significant adverse side effects, more specific targets that differentiate between tumorigenic and normal cells are needed.

The defects in DNA repair that many cancers have are an Achilles heel because these genetic deficits can have synthetic lethal interactions with inhibitors of other DNA repair processes. This is typified by the interaction between inhibitors of PARP-1/2 and BRCA1-deficient cancers (Fong et al., 2009). Based on these observations and the facts that Tdp1 is highly expressed in some cancers and that it processes stalled DNA- TopoI complexes, I hypothesized that Tdp1 function is essential for survival of those cancers and is therefore a potential anticancer target (Fam et al., 2013d; Liu et al., 2007). Supporting this reasoning, reducing Tdp1 expression in some rhabdomyosarcoma cell lines enhanced the cytotoxicity of PARP-1 inhibitors and was independently cytotoxic (Fam et al., 2013d).

Since Tdp1 repairs Topo I-DNA complexes such as those induced by CPT, inhibitors of Tdp1 may also enhance the sensitivity of cancer cells to the CPTs. Consistent with this thinking, increased Tdp1 expression counteracts the cytotoxicity of CPTs (Barthelmes et al., 2004) and is frequently observed in cancers resistant to CPT therapy (Fam et al., 2013d; Liu et al., 2007; Pappo et al., 2007). Also, reduction of Tdp1 expression in rhabdomyosarcoma cell lines sensitizes them to CPT (Fam et al., 2013d).

To identify an inhibitor that preferentially inhibits the growth of breast cancer cells but not noncancerous mammary epithelial cells, Dr. Richard Dean devised an *in vitro* activity assay for Tdp1 and screened approximately 80,000 chemical compounds. Putative inhibitors identified by this screen were then evaluated by me in breast cancer cells for their ability to induce lethality, increase CPT sensitivity and function additively with the PARP-1 inhibitor Rucaparib.

5.2 Methods

5.2.1 Expression and purification of Tdp1 proteins

N-terminally His-tagged Tdp1 protein was expressed as previously described (Interthal et al., 2001). Briefly, Tdp1 was expressed in *E.coli.* BL21 (DE3) cells using the pET expression system (Novagen) and after two hours induction with 1 mM isopropyl β-d-thiogalactoside, cells were harvested, and the dry pellets stored at −80°C.

For Tdp1 purification, cell pellets were thawed on ice, resuspended in breaking buffer (100 mM KCl, 30 mM KPO_4 pH 7.0, with protease inhibitors), and sonicated. After centrifugation at 20,000 x g (4°C), for 45 min, the supernatant was passed through a 22-gauge needle, filtered through a 0.22 μm filter and loaded onto a Whatman Cellulose Phosphate P11 column. The column was washed with wash buffer (400 mM KCl, 30 mM KPO_4 pH 7.0, with protease inhibitors) and eluted with wash buffer containing 800 mM KCl. The eluate was desalted using a PD-10 column (GE Healthcare) equilibrated with dialysis buffer (20 mM Tris, pH 7.9, 500 mM NaCl, 10 mM imidazole, 0.2 mM phenylmethanesulfonyl fluoride (PMSF)) prior to passing through a $NiSO_4$-charged HiTrap chelating column (GE Healthcare). The His-bind buffer kit (Novagen) supplemented with protease inhibitors was used to charge, bind, wash and elute the column. The eluate was dialyzed against storage buffer (50 mM Tris.HCl, pH7.5, 50 mM KCl, 1 mM EDTA, 2 mM DTT, and 50% glycerol) using a 10,000 MWCO Slide-A-Lyzer (Pierce). The protein was stored at -20 °C.

5.2.2 Tdp1 *in vitro* activity assay

The Tdp1 *in vitro* activity assay was designed as a linear quenched fluorescent substrate that negated interaction with DNA intercalators. A μFill microplate dispenser (Bio-Tek) was used to dispense 25 μL/well of a Tdp1 enzyme solution (0.02 μL purified Tdp1 (10 nM) in 10 mM Tris.HCl, pH 7.5, 50 mM KCl, 1mM EDTA, 1 mM DTT, 0.01% Brij-35) into wells of a black 384-well plate (Costar). Seventy (70) nL of each test compound (5 mM) was pinned into assay plates using an FP3-384 pin tool (VP Scientific) on a PlateMate™ Plus (Thermo Scientific) and incubated at room temperature for 30 min. During this time, the plates were read by a Varioskan® Flash multimode reader (Thermo) at Ex_{485}/Em_{510} nm to identify false positive compounds that had auto fluorescence. The μFill dispenser was used to add 25 μL/well of linear oligonucleotide substrate (35 nM, (5'-/6-FAM/AGGATCTAAAAGACTT/3BHQ_1/-3'))

(Integrated DNA Technologies) in dH_2O. The fluorophore 6-carboxyfluorescein (FAM) was coupled to the 5'terminus, whereas the Black Hole Quencher (BHQ)_1 was coupled to the 3' terminus. The whole plate was immediately read 5 times using a kinetic read on the Varioskan® (Ex_{485}/Em_{510} nm). Tdp1 % inhibition was calculated for each compound by comparing the rate of increase in fluorescence over time for the compound-treated wells to that of DMSO control wells. All compounds considered for follow-up were retested using the primary screening assay, and if confirmed, an IC_{50} was determined using an 8-point concentration response curve. Concurrently, a counter screen to identify false positives that quenched the fluorescence of the fluorophore was carried out using the substrate oligonucleotide without the quencher. Lastly, inhibitors were purchased and reconfirmed prior to the secondary cell-based assays.

Dr. Richard Dean screened a total of >80,000 compounds. These included the CCBN (Canadian Chemical Biology Network) collection consisting of 16,000 selected Maybridge compounds, 9989 selected Chembridge compounds, the Chembridge DIVERset (50,000 compounds), the KD2 library consisting of LOPAC (Sigma) library, the Prestwick library, and selected compounds from BIOMOL and Microsource.

5.2.3 Small molecule database and protein structures

The small molecule databases and the crystal structure data of Tdp1 were respectively downloaded from ZINC (Irwin and Shoichet, 2005) and PDB (Berman et al., 2000). Three crystal structures of Tdp1 were used for ligand screening (PDB accession numbers: 1jy1, 1qzq and 1nop).

5.2.4 Computational screening and molecular docking

ICM was licensed from Molsoft LLC for a Linux-based computer cluster of 400 CPUs. The binding pocket was identified by the PocketFinder program. The pocket was represented by a set of maps for van der Waals (carbon-based and hydrogen-based), electrostatic, hydrogen bonding and hydrophobic interactions. Each compound (ligand) of the database was docked to the pockets one-by-one and a score (ICM score) reflecting the quality of the docked complex was assigned to each compound (Totrov and Abagyan, 1997). The compound was fully flexible, and both the intramolecular ligand energy and the ligand-receptor interaction energy were optimized during the docking. The conformational sampling was based on the biased probability Monte

Carlo procedure in the internal coordinate space. Due to the nature of Monte Carlo based sampling, the database screening process was repeated five times. The results were combined and the best score for each compound was retained.

5.2.5 Tumor microarray

Three tumor microarrays of 17 common adult cancers were purchased from Imgenex, Inc. To assess Tdp1 protein expression, the microarrays were first de-paraffinized by baking at 62°C and stained for Tdp1 expression using anti-human Tdp1 serum as previously described (Fam et al., 2013d). Tumors were considered Tdp1 positive if Tdp1 expression was observed in the cytoplasm, nucleus, or in both locations.

5.2.6 Cell culture

MCF-7, MDA-MB-231, human dermal fibroblasts and murine embryonic fibroblasts were cultured in Dulbecco's Modified Eagle's Medium (Gibco) supplemented with 10% heat-inactivated FBS (Hyclone), 4 mL/L L-glutamine and 1% antibiotic-antimycotic (Gibco). HCC-1937 cells were cultured in RPMI-1640 (Gibco) with 10% heat-inactivated FBS (Hyclone), 4 mL/L L-glutamine and 1% antibiotic-antimycotic (Gibco). SUM-1315MO2 cells were cultured in Ham's F-12 media (Gibco), supplemented with 10 mM HEPES (Gibco), 5 µg/mL insulin (Gibco), 10 ng/mL EGF (Gibco) and 20% heat-inactivated FBS (Hyclone). Human mammary epithelial cells were cultured in Mammary Epithelial Cell Basal Medium (Lonza) and supplemented with MEGM SingleQuots (Lonza). All cells were grown at 37º C with 5% CO_2 in a humidified environment.

MCF7, MDA-MB-231, HCC-1937 and SUM-1315MO2 cells were a kind gift from Dr. Sam Aparicio's laboratory at the BC Cancer Agency. Human mammary epithelial cells (CC-2551) were purchased from Lonza. Wild-type and *Tdp1*$^{-/-}$ murine embryonic fibroblasts (MEF) were obtained as previously described (Hirano et al., 2007). *Tdp1*$^{-/-}$ mice were generated by insertion of a gene trap vector into intron 11 of *TDP1* (Hirano et al., 2007).

5.2.7 Tdp1 knockdown

Tdp1 was knocked down transiently by transfecting $8x10^4$ cells with 100 nM of pooled siRNAs (Dharmacon) in a 24-well plate using Lipofectamine 2000 (Invitrogen). Knockdown of

Tdp1 expression was confirmed by immunoblotting and qRT-PCR. The sequences of the siRNAs and PCR primers are listed in Supplementary Table D-1.

5.2.8 γH2AX assay

MCF-7 cells were seeded in MEM + 10% FBS, plated at 20,000 MCF-7 cells per well, of a 96-well black, clear bottom view plate and incubated at 37°C, 5% CO_2 overnight. The next day, cells were incubated for 1 hour at 37°C, 5% CO_2 with medium containing 4 μM CPT and the putative inhibitor at a final concentration of 30 μM. This medium was removed after one hour and replaced with medium containing only the putative inhibitor at a final concentration of 30 μM. Following incubation at 37°C, 5% CO_2 and removal of growth medium, the cells were fixed by adding 100 μL of 4% PFA to each well and incubating for 15 minutes at 37°C, 5% CO_2. Subsequently, the wells were washed with 150 μL PBS and stored at 4°C. For immunofluorescence, cells in each well were permeabilized by incubation at room temperature for 30 minutes with 100 μL of 0.3% TritonX-100 in PBS, washed 3X with 150 μL PBS and blocked with 100 μL of 3% BSA diluted in PBS for 20 minutes. The cells in each well were then incubated at room temperature for 1 hr with 50 μL of 0.5 μg/mL anti-H2A.X antibody (Millipore JBW301) diluted in 3% BSA, washed 3X with 150 μL PBS, incubated at room temperature for 45 minutes with 4 μg/mL secondary antibody (Alexa Fluor 488) diluted in 3% BSA, washed 3X with 150 μl PBS, stained with 1 ug/mL Hoechst (10 mg/mL stock) and immediately washed 3X with 150 μL PBS. Fluorescence was quantified using the Cellomics Arrayscan.

5.2.9 Comet assay

Comet assays were performed to assess DNA damage as previously described (Hirano et al., 2007). Briefly, MCF-7 cells were seeded at a density of $3x10^5$ cells. After 24 hours, the cells were treated for 2 hours with 4 μM of CPT and/or 10 μM of test compound at 37˚C, 5% CO_2. Then $1x10^4$ cells were harvested, resuspended in 80 μL of 0.5% low melting point agarose and pipetted onto microscope slides pre-coated with 1% normal melting agarose. After addition of a second layer of 1% normal melting point agarose, the cells were lysed by immersing the slides in lysis solution (2.5 M NaCl, 100 mM EDTA, 10 mM Trizma base, 1% Triton X-100, 10% DMSO) for 2 hours. DNA was then denatured by incubation of the slides at 4˚C in alkaline

buffer (50 mM NaOH, 1 mM EDTA, 1% DMSO, pH>13) for 25 minutes. Following electrophoresis at 25 V and 4˚C for 25 minutes, the slides were neutralized in 0.4 M Tris-HCl and stained with SYBR-Green (Invitrogen). Images were acquired using a Zeiss Axiovert 200 microscope, a Zeiss AxiocamMR camera, and the Zeiss Axiovision imaging system. Comet tail analysis was done using the Comet Assay IV software by Perceptive Instruments.

5.2.10 MTT assay

Cell proliferation and viability were measured by MTT assay as previously described (Mosmann, 1983). Briefly, $5x10^3$ cells were plated in each well of a 96-well plate and cultured in phenol red-free media. MTT solution was prepared by dissolving 5mg of MTT in 1 mL of 1X PBS. Following the described treatments, the culture media was supplemented with 10% MTT and incubated for 3 hours. Subsequently, culture media was replaced with 100 µL of 100% DMSO and cells were incubated for 30 minutes. All incubation steps were performed in the cell culture incubator (37º C with 5% CO_2 in a humidified environment). Spectrophotometry was done at 565nm using the Wallac VICTOR2 Multilabel Plate Reader (Beckman-Coulter).

5.2.11 Caspase-3/7 activity assay

Briefly, $5x10^3$ cells were plated in each well of a 96-well plate and allowed to incubate in the cell culture incubator (37º C with 5% CO_2 in a humidified environment). The cells were treated for 96 hours with CD00509 or Rucaparib or CPT or a combination of these as described. Caspase activity was measured using the Apo-ONE Homogeneous Caspase-3/7 kit according to the manufacturer's protocol (Promega). Fluorescence of the cleaved caspase-3 and 7 substrate was measured at 520nm using the Wallac VICTOR2 Multilabel Plate Reader (Beckman-Coulter).

5.2.12 TUNEL assay

Briefly, $5x10^3$ cells were seeded on a cover slip placed a 6-well plate and allowed to incubate in the cell culture incubator (37º C with 5% CO_2 in a humidified environment). The cells were treated for 96 hours with CD00509 or Rucaparib or CPT or a combination of these as described. Nuclei with DNA breaks were visualized by colorimetric labeling of free 3'OH DNA termini using the Apoptag Plus Peroxidase *In Situ* Apoptosis Detection Kit according to the

manufacturer's protocol (EMD Millipore). The number of stained nuclei per 100 cells was recorded as indicative of apoptosis.

5.2.13 PARP-1 inhibition

The PARP-1 inhibitor AG-014699 (Rucaparib) was obtained from Selleck Chemicals. The LD_{50} for the inhibitor was determined by seeding MCF-7 cells at $5x10^3$ cells per well in 96-well microtiter plates. After 24 hours, the PARP inhibitors were added to the culture medium to a final concentration of 10 μM. Cell viability and proliferation was measured in triplicate every 24 hours for 96 hours by the MTT assay.

5.2.14 Statistical analysis

Microsoft Excel was used to compute the group means and standard deviations for all treatment and control groups from cell viability data derived by the MTT and comet assays. GraphPad Prism was used to analyze data from the primary screen and γH2AX staining. Prism was also used to perform two-way ANOVA to compare the differences in growth and viability under varying treatment conditions over time. Tukey's test was used to assess statistical significance between individual groups. A p-value of <0.05 was judged significant.

5.3 Results

5.3.1 Tdp1 is expressed in many cancers

To test if Tdp1 was highly expressed in cancers besides rhabdomyosarcoma and non-small cell lung cancer (Fam et al., 2013d; Liu et al., 2007), I immunohistochemically assessed Tdp1 expression in 10 cores for each of 17 common adult cancers. I found that at least half of all the tumors assayed were Tdp1-positive, and that for 5 of the 17 cancers, ≥90% of the tumor samples were Tdp1-positive (Figure 5- 1A). The tissues of origin for these 5 cancers were thyroid, breast, liver, enodometrium and ovary.

5.3.2 Tdp1 has increased expression in breast cancer cell lines

Observing the expression of Tdp1 in many breast tumors, I hypothesized that Tdp1 expression is increased in breast cancer tissue. To test this, I compared Tdp1 mRNA and protein levels for the patient-derived breast cancer cell lines HCC-1937, MDA-MB-231, SUM-

1315MO2 and MCF-7 with non-cancerous mammary tissue and cultured mammary epithelial cells (Figure 5-1B-C). Indeed, Tdp1 expression was 4-10 fold higher in the breast cancer cell lines than in the controls.

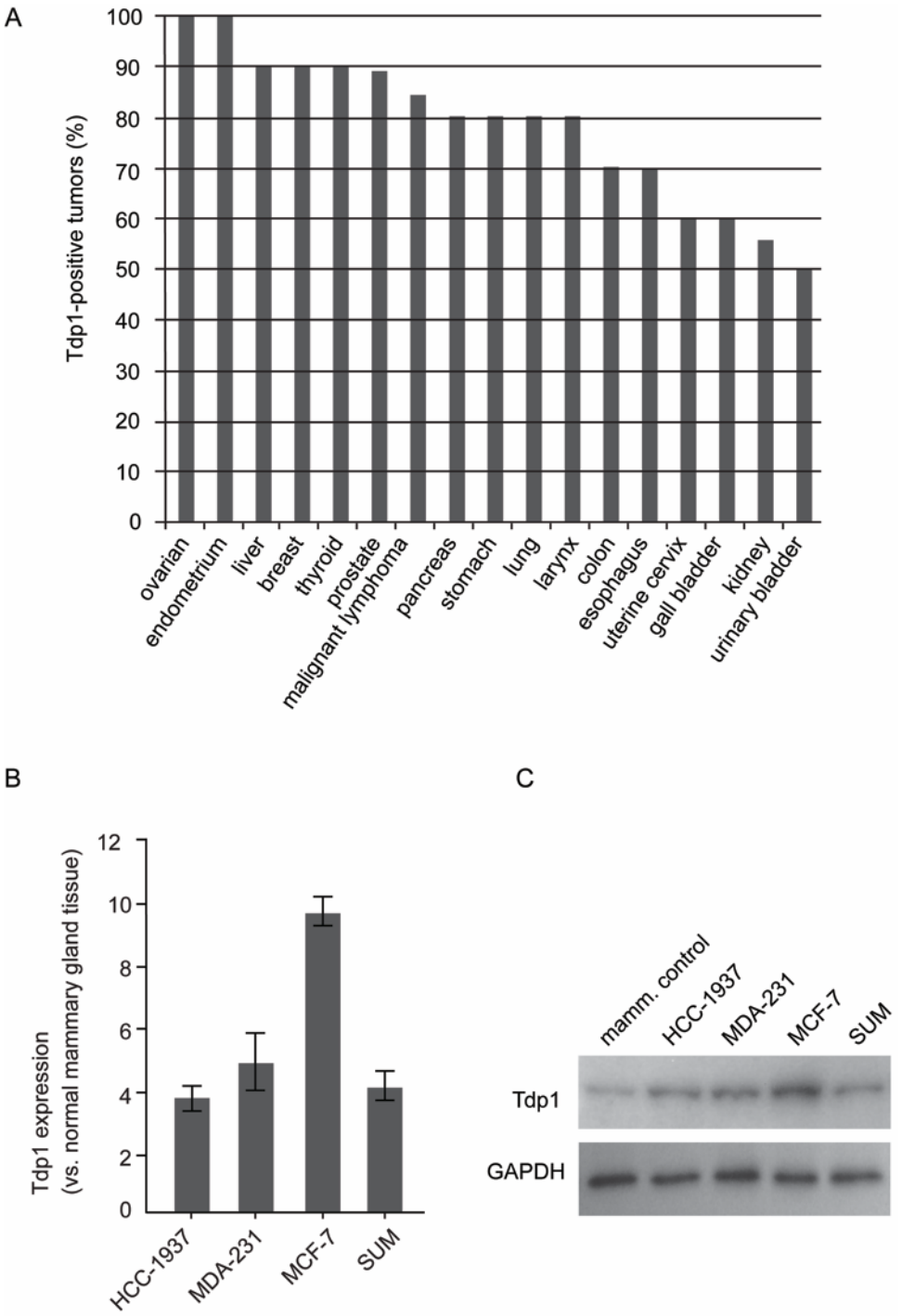

Figure 5-1: Tdp1 expression in cancer.

A. Tdp1 expression in a tumor microarray panel of common human cancers immunohistochemically stained for Tdp1 protein **B-C**. *TDP1* mRNA and protein expression in cultured breast cancer cell lines as measured by qRT-PCR (left panel) and immunoblotting (right panel). *TDP1* mRNA expression is relative to that of mammary gland tissue (left panel) and Tdp1 protein expression is relative to that of cultured mammary epithelial cells (right panel). Tdp1 expression in MCF-7 cells is significantly higher than in HCC-1937, MDA-MB-231 or SUM-1315MO2 cells ($P<0.001$). *TDP1* mRNA and Tdp1 protein levels were normalized to *GAPDH* mRNA and protein, respectively. (n=3) n, number of replicates. error bars, mean ± s.d.

5.3.3 Knockdown of Tdp1 expression reduces the proliferation of MCF-7 cells

Given this expression of Tdp1 in breast tumors and cell lines and the known interaction between Tdp1 and PARP-1 (Zhang et al., 2011), I hypothesized that like PARP-1 inhibition, the abrogation of Tdp1 processing of blocked 3' DNA termini is lethal to breast cancer cells. Using siRNA to achieve a 65-85% knockdown of Tdp1 expression I observed a 20% reduction in the proliferation of MCF-7 cells and no change in proliferation for HCC-1937, MDA-MB-231 and SUM-1315MO2 (Figure 5-2A-H).

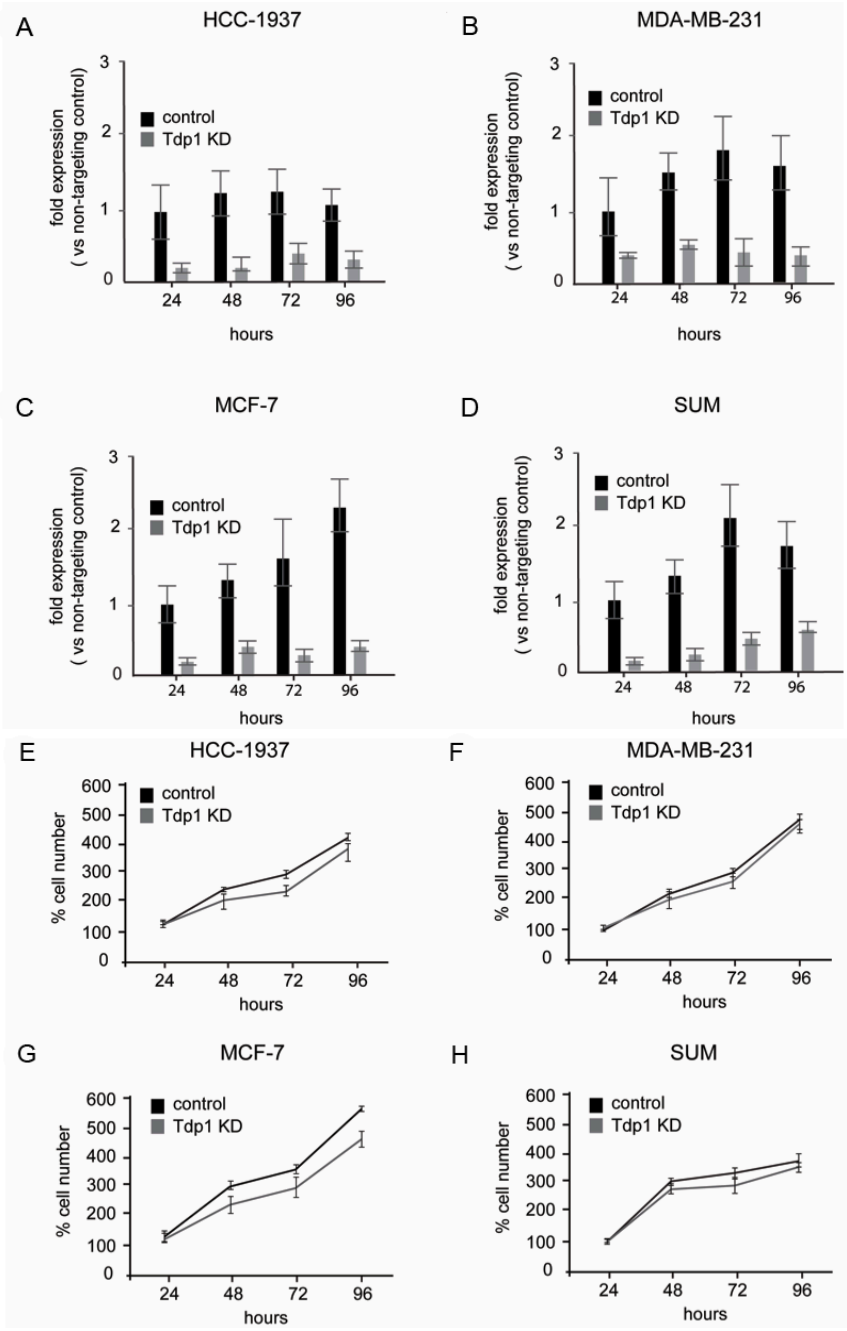

Figure 5-2: The effect of *TDP1* knockdown on proliferation of breast cancer cell lines.

A-D. qRT-PCR showing *TDP1* mRNA levels in breast cancer cell lines during Tdp1-targeting siRNA treatment relative to non-targeting siRNA treatment for 96 hours. *TDP1* mRNA levels were normalized to GAPDH mRNA levels. **E-H**. MTT assay showing proliferation of breast cancer cell lines during 96 hours of treatment with *TDP1*-targeting siRNAs or a scrambled non-targeting control siRNA. (n=3) n, number of replicates. error bars, mean ± s.d.

5.3.4 *In vitro* assay for Tdp1 inhibitors

Given these findings and my prior observations with rhabdomyosarcoma (Fam et al., 2013d), chemical inhibition of Tdp1 may be an effective adjuvant for anticancer treatment. To screen for inhibition of Tdp1 activity, the hydrolysis of the phosphodiester bond between the O-4 atom of tyrosine and the 3'-phosphate of DNA (Interthal et al., 2005a; Interthal et al., 2001), Dr. Richard Dean constructed a single-stranded oligonucleotide substrate with a BHQ quencher instead of a tyrosine moiety attached to the 3' end of the oligonucleotide via a phosphodiester bond and a 6- FAM fluorophore attached to the 5' end (Figure 5-3A). Basal fluorescence of this substrate is fully quenched. The recombinant Tdp1 enzyme had a K_m of 23.8 and a V_{max} of 0.0016 for cleavage of the phosphodiester bond between the quencher and the oligonucleotide.

The substrate and the purified Tdp1 were tested by conducting a pilot screen with the KD2 library of approximately 5000 compounds. To exclude false positives that intrinsically quenched the fluorophore, Dr. Dean screened all identified compounds using a single stranded oligonucleotide with a fluorophore bound to the 5' terminus but no quencher on the 3' terminus. All compounds that quenched the fluorophore also had an autofluorescence of >4-fold that of DMSO control when pre-measured at the same Ex_{485}/Em_{510} nm. Therefore, only compounds that had <4-fold autofluorescence compared to DMSO and that inhibited Tdp1 in the biochemcial assay >70% were selected for retesting. Of the 31 compounds restested, 14 confirmed and inhibited Tdp1 >60%.

5.3.5 Identification and characterization of putative Tdp1 inhibitors using the *in vitro* assay

Having validated the *in vitro* assay methodology, the CCBN collection (Canadian Chemical Biology Network) and the ChemBridge DIVERSet (ChemBridge Corporation, USA) libraries were screened for compounds that inhibited Tdp1 activity at low micromolar concentrations (Supplementary Figure D-1). The Z' was 0.69 for the primary screen and from a total of 80,750 compounds screened, 17 compounds gave >95% inhibition of Tdp1, and had concentration-dependent Tdp1 inhibition with an $IC_{50} < 1\mu M$ (Table 5-1). Structure activity relationship (SAR) was examined on these 17 compounds and three structural families were chosen for follow up (Figure 5- 3B-D). Family 1 was characterized by analogs derived from the Paal-Knorr synthesis

of pyrroles; family 2 was characterized by a rhodanine substructure, and family 3 was characterized by an alkylidene barbiturate moiety.

Compound Name and SAR family (F)	ID[1]	Plate IC_{50} (μM) [2]	Fresh stock IC_{50} (μM) [3]
Aurintricarboxylic acid (*F1*)	A1895	-	$0.023^{\pm}0.001$
5-(3-bromo-4-hydroxy-5-methoxybenzylidene)-3-(4-nitrophenyl)-2-thioxo-1,3-thiazolidin-4-one *(F2)*	5675056	$1.08^{\pm}0.07$	$0.28^{\pm}0.04$
4,4'-Diisothiocyanostilbene-2,2'-sufonic acid sodium salt *(F2)*	1505164	$0.08^{\pm}0.01$	$0.37^{\pm}0.07$
ethyl 3-[4-(2-ethoxy-2-oxoethyl)-2-(hydroxyiminomethyl)-1H-pyrrol-3-yl]propanoat *(F1)*	NRB 02765	$0.7^{\pm}0.03$	$0.52^{\pm}0.03$
4-(2,5-dimethyl-1H-pyrrol-1-yl)benzoic acid *(F1)*	5128772	$1.07^{\pm}0.05$	$0.71^{\pm}0.07$
5-(2-furylmethylidene)-2-thioxohexahydropyrimidine-4,6-dione *(F3)*	CD 00509	$0.71^{\pm}0.04$	$0.96^{\pm}0.04$
Chicago sky blue 6B *(F3)*	Prestw-425	$0.96^{\pm}0.04$	$1.03^{\pm}0.04$
SENNOSIDE A *(F2)*	68909	-	$1.07^{\pm}0.07$
(3Z,7E)-3,7-bis(furan-2-ylmethylidene)bicyclo[3.3.1]nonane-2,6-dione *(F3)*	5728647	$0.68^{\pm}0.05$	$1.1^{\pm}0.06$
5-amino-2-(4-aminoanilino)benzene-1-sulfonic acid *(F3)*	JFD 00257	$0.66^{\pm}0.06$	$2.06^{\pm}0.12$
2-[3-(dimethylamino)prop-2-enylidene]cyclopentan-1-one *(F1)*	BTB 11050	$0.74^{\pm}0.07$	$2.17^{\pm}0.21$
(5Z)-1-(3-chlorophenyl)-5-(furan-2-ylmethylidene)-2-sulfanylidene-1,3-diazinane *(F3)*	5673625	$0.62^{\pm}0.06$	$2.59^{\pm}0.16$
2-chloro-5-(2,5-dimethyl-1H-pyrrol-1-yl)benzoic acid *(F1)*	5952489	$0.11^{\pm}0.01$	$2.77^{\pm}0.07$
Chlorophyllide Cu complex Na salt *(F3)*	C6003	-	$3.71^{\pm}0.52$
6-Hydroxy-DL-DOPA *(F1)*	H 2380	$0.27^{\pm}0.01$	$4.83^{\pm}0.53$
Ellagic acid *(F3)*	E2250	-	$7.18^{\pm}0.66$
5-(3-bromo-4-hydroxy-5-methoxybenzylidene)-3-(3-chlorophenyl)-2-thioxo-1,3-thiazolidin-4-one *(F2)*	5584680	n/a	$7.41^{\pm}0.62$

Table 5-1: Top 17 Tdp1 inhibitory compounds carried forward to the secondary screen.

The criteria for selection of these compounds is an $IC_{50} \leq 1$uM and percent Tdp1 inhibition of over 95%.

[1] Chemical vendor catalogue number.

[2] IC_{50} (n=3) using compound from library cherry picking plates. SEM reported.

[3] IC_{50} (n=3) established from new powder stock of compound. SEM reported.

5.3.6 *In silico* screen and compound selection

In parallel with the *in vitro* screen, Dr. Jianghong An conducted a screen for compounds predicted to bind the Tdp1 catalytic site using molecular ligand docking. The molecular docking software ICM (MolSoft) was used for screening of approximately 140,000 and 500,000 compounds from the National Cancer Institute (NCI, USA) and the ChemBridge databases, respectively (Milne et al., 1994). Each compound (ligand) was docked to the small molecule-binding pocket in a flexible-ligand rigid-receptor docking approach. Protein flexibility was addressed by using multiple receptor conformations from experimental structures. A docking score reflecting the "fit quality" of the ligand to the receptor was calculated and used for compound selection, where low scores indicate a better fit. The best-scoring compounds were also inspected visually and evaluated according to their chemical and drug-like properties, as well as three-dimensional conformations of the docked ligand-receptor complex (Figure 5-3E-F). Forty compounds were selected and obtained for *in vitro* validation (Supplementary Figure D-2). One of these ((2,6-bis(2-(2-(hydroxymethyl)phenyl)ethyl)pyrrolo[3,4-f]isoindole-1,3,5,7(2H,6H)-tetrone)) confirmed as a possible Tdp1 inhibitor with an IC_{50} of 3.5μM (boxed compound, Supplementary Figure D-2). However, due to the weaker potency of this compound compared to others identified by the *in vitro* screen, it was not further characterized. One compound from each of the three main structural families identified by the *in vitro* screen was also docked using the *in silico* model, but each gave a high docking score, suggesting that either the model needs further optimization to define the binding pocket or that these compounds bind alternate sites on the enzyme.

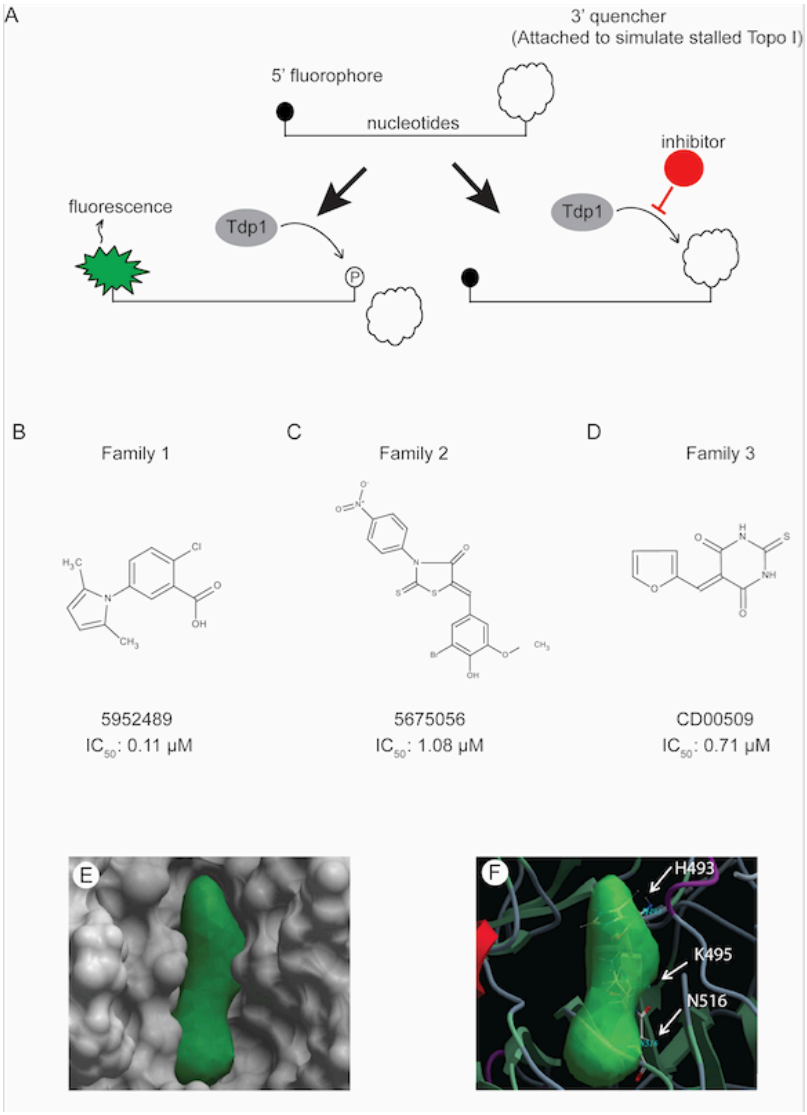

Figure 5-3: *In vitro* and *in silico* screens for inhibitors of Tdp1 activity.

A. A custom made oligonucleotide substrate containing a 3'-BHQ quencher and 5'-6-FAM substrate identified potential Tdp1 inhibitors by real-time detection of fluoresence gain after the addition of the compound to the substrate. A Varioskan plate reader (ThermoScientific) was used to detect the increase in fluorescence every 45 seconds for 10 minutes. **B-D** . Putative Tdp1 inhibitors were categorized into three families according to their structure-activity relationship (SAR). Three were amenable for medicinal chemistry followup. Family 1 members are characterized by analogs derived from the Paar-Knorr synthesis of pyrroles; family 2 members are characterized by a rhodanine substructure, and family 3 members are characterized by an alkylidene barbiturate moiety. **E**. Model of the surface topology of the small molecule binding pocket (green) used for the *in silico* screen for Tdp1 inhibitors. The Tdp1 enzyme active site is shown in grey. **F**. Transparent mode of the pocket showing three key active site residues of Tdp1: H493, K495 and N516.

5.3.7 CD00509 and 5675056 increase γ-H2AX foci in CPT-treated MCF-7 cells

Based on their sensitivity to Tdp1 knockdown (Figure 5-2C,G), MCF-7 cells were selected for cell-based studies of the putative Tdp1 inhibitors. Because Tdp1 deficiency increases the number of blocked DNA 3' termini arising from stalled Topo I and consequently the number of γ-H2AX foci following treatment with CPT (Katyal et al., 2007), Yoko Shimizu tested if any of the 17 compounds identified above caused greater than baseline (Supplementary Figure D-3) accumulation of γ-H2AX foci following a 1 hour treatment with CPT. Compounds CD00509 and 5675056 increased the number of γ-H2AX foci in MCF-7 cells (Figure 5-4A and B).

To determine if treatment with CD00509 and 5675056 not only acutely increased sensitivity to CPT but also impeded repair of the Topo I-DNA complex after CPT treatment, Yoko measured persistence of γ-H2AX foci after removal of CPT. This showed a statistically significant increase in the number of γ-H2AX foci until 6 hours after CPT treatment for CD00509 but not 5675056 (Figure 5-4A and B). The prolonged persistence of γ-H2AX observed in CD00509-treated MCF-7 cells is consistent with cellular toxicity and DNA repair by less efficient mechanisms (Ivashkevich et al., 2012).

5.3.8 CD00509 increases DNA breaks detectable by alkaline comet assay of CPT-treated MCF-7 cells

To correlate γ-H2AX foci number with DNA strand breaks, I measured DNA strand breaks by the alkaline comet assay as previously described (Fam et al., 2013d). MCF-7 cells were treated with 10 μM of candidate Tdp1 inhibitors and 4 μM CPT for 2 hours before analysis of DNA strand-breakage. Treatment with CD00509, but not 5675056, sensitized MCF-7 cells to CPT, as shown by an increase in DNA breaks by alkaline comet assay (Figure 5-4C and D).

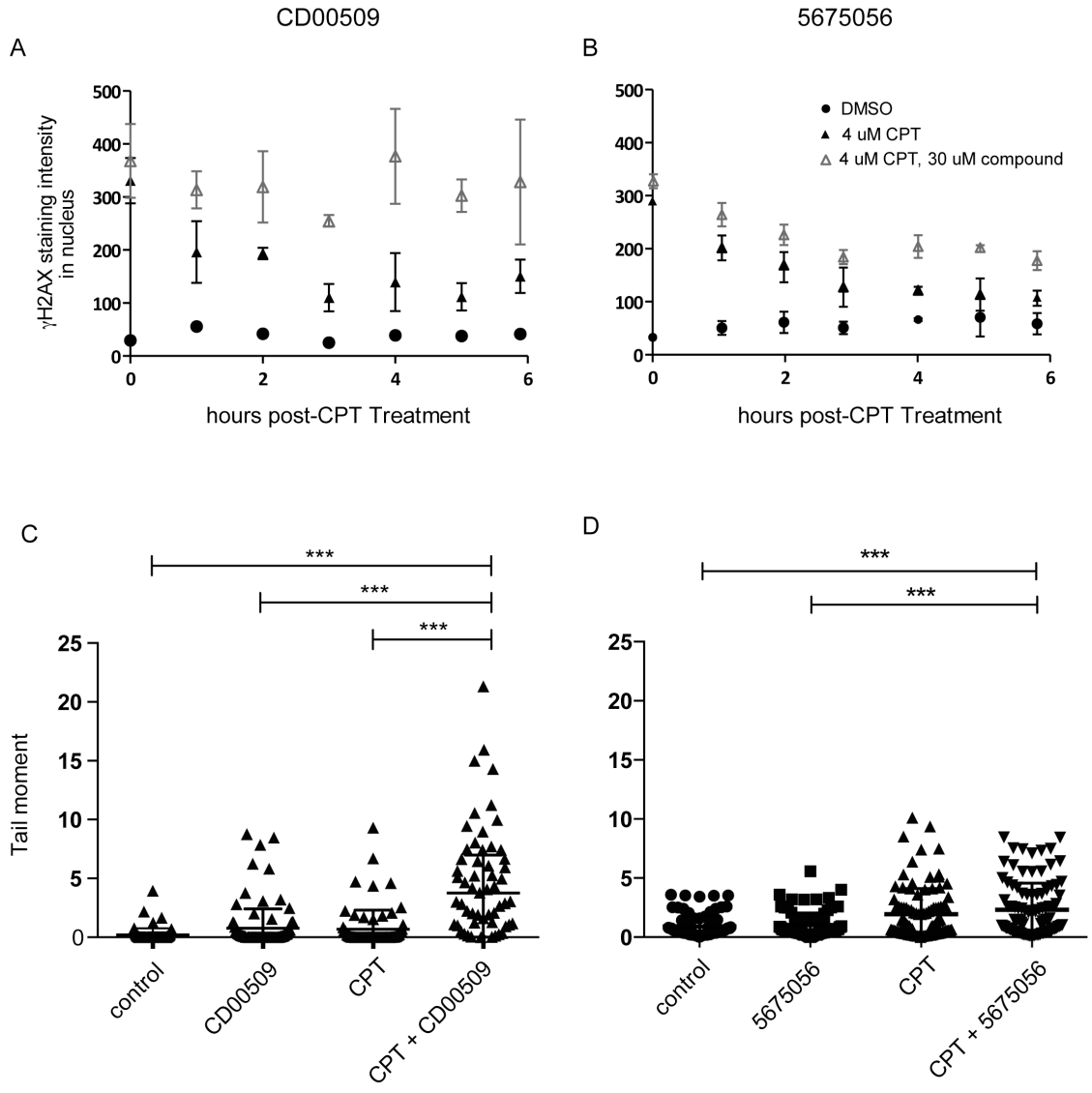

Figure 5-4: Tdp1 inhibitor CD00509, but not 5675056 is additive with CPT in inducing DNA damage.
A-B. γH2AX staining in MCF-7 cells after a 1 hour treatment with either 4μM CPT alone (black triangles) or CPT and 30μM Tdp1 inhibitor (diamonds). To test the efficacy of Tdp1 inhibitors, medium containing inhibitor and CPT were added simultaneously to MCF-7 cells for 1 hour; this medium was then removed and replaced with medium containing Tdp1 inhibitor only. A DMSO vehicle control is noted in black circles. **C-D**. DNA strand-breaks in MCF-7 cells 2 hours after treatment with CPT and Tdp1 inhibitor or either alone (n=3). n, number of replicates; error bars, mean ± s.d. ***, $P<0.001$. Control lane includes DMSO as a vehicle control.

5.3.9 CD00509 and 5675056 do not decrease the proliferation of wild type human mammary epithelial cells

To determine if the Tdp1 inhibitors CD00509 and 5675056 were toxic to noncancerous cells, I measured the LD50 for human mammary epithelial cells. By MTT assay, neither of the compounds decreased the viability of mammary epithelial cells up to 10 μM Tdp1 inhibitor (Supplementary Figure D-4(A-B)).

5.3.10 Combined Tdp1 and toposiomerase-I inhibition reduce MCF-7 cell number more than does either treatment alone

Since CD00509 treatment increased the number of DNA strand breaks in CPT-treated MCF-7 breast cancer cells, I determined the effect of CD00509 and CPT on cellular proliferation. Treatment with 10 μM CD00509 alone reduced the number of MCF-7 cells by 16%, but did not impede the proliferation of mammary epithelial cells (Figure 5-5A-D). Treatment with 1 μM CPT alone reduced the number of MCF-7 cells by 32% and mammary epithelial cells by 24% after 96 hours (Figure 5-5A-B). Co-treatment with CD00509 and CPT reduced the proliferation of MCF-7 cells by 50% (18% more than did CPT treatment alone), whereas combination treatment in mammary epithelial cells was not additionally detrimental over CPT treatment alone (Figure 5-5 A-B).

To ascertain whether CD00509 and CPT co-treatment reduced cell number by impairing cellular proliferation or apoptosis, I checked for activation of caspases-3 and 7 by a colorimetric assay and for DNA fragmentation by TUNEL assay. Both measures suggest that the combined treatment preferentially increased apoptosis in MCF-7 cells compared to control mammary epithelial cells (Supplementary Figure D-5 (A and C)).

5.3.11 CD00509 treated *Tdp1*$^{+/+}$ MEFs are comparably sensitive to CPT as *Tdp1*$^{-/-}$ MEFs

After establishing that CD00509 was not cytotoxic to *Tdp1*$^{+/+}$ and *Tdp1*$^{-/-}$ MEFs and that *Tdp1*$^{-/-}$ MEFs were more sensitive to CPT treatment than *Tdp1*$^{+/+}$ MEFs (Supplementary Figure D-4 (C and D)), I tested if treatment of *Tdp1*$^{+/+}$ MEFs with CD00509 sensitized them to CPT. Indeed, this increased sensitivity to a level comparable to that of *Tdp1*$^{-/-}$ MEFs (Supplementary Figure D-4E).

5.3.12 Inhibition of MCF-7 proliferation is more severe with combined CD00509 and PARP-1 inhibition than either treatment alone

As PARP-1 poly-ADP ribosylation of DNA-binding proteins at DNA breaks facilitates the recruitment of DNA repair proteins (Li and Yu, 2013), and cancers frequently have compromised DNA repair processes (Nowell, 1976) that poorly tolerate further impairment, I investigated the effect of the PARP-1 inhibitor Rucaparib (AG014699) on MCF-7 cells. Rucaparib treatment decreased MCF-7 cell number by 40% (Figure 5-5D), and the combination of Rucaparib with CD00509 decreased MCF-7 cell number by 56% (15% more than Rucaparib treatment alone) (Figure 5-5 D). Neither Rucaparib nor CD00509 treatments alone significantly impaired the proliferation of mammary epithelial cells (Figure 5-5 C), although the combination of Rucaparib and CD00509 decreased the number of mammary epithelial cells by 25% (Figure 5-5 C). Combined CD00509 and Rucaparib treatment also caused an increase in caspase-3/7 activation and TUNEL staining in MCF-7 cells but not mammary epithelial cells indicating that the decrease in cell number is likely due to apoptosis (Supplementary Figure D-5 (B and D)).

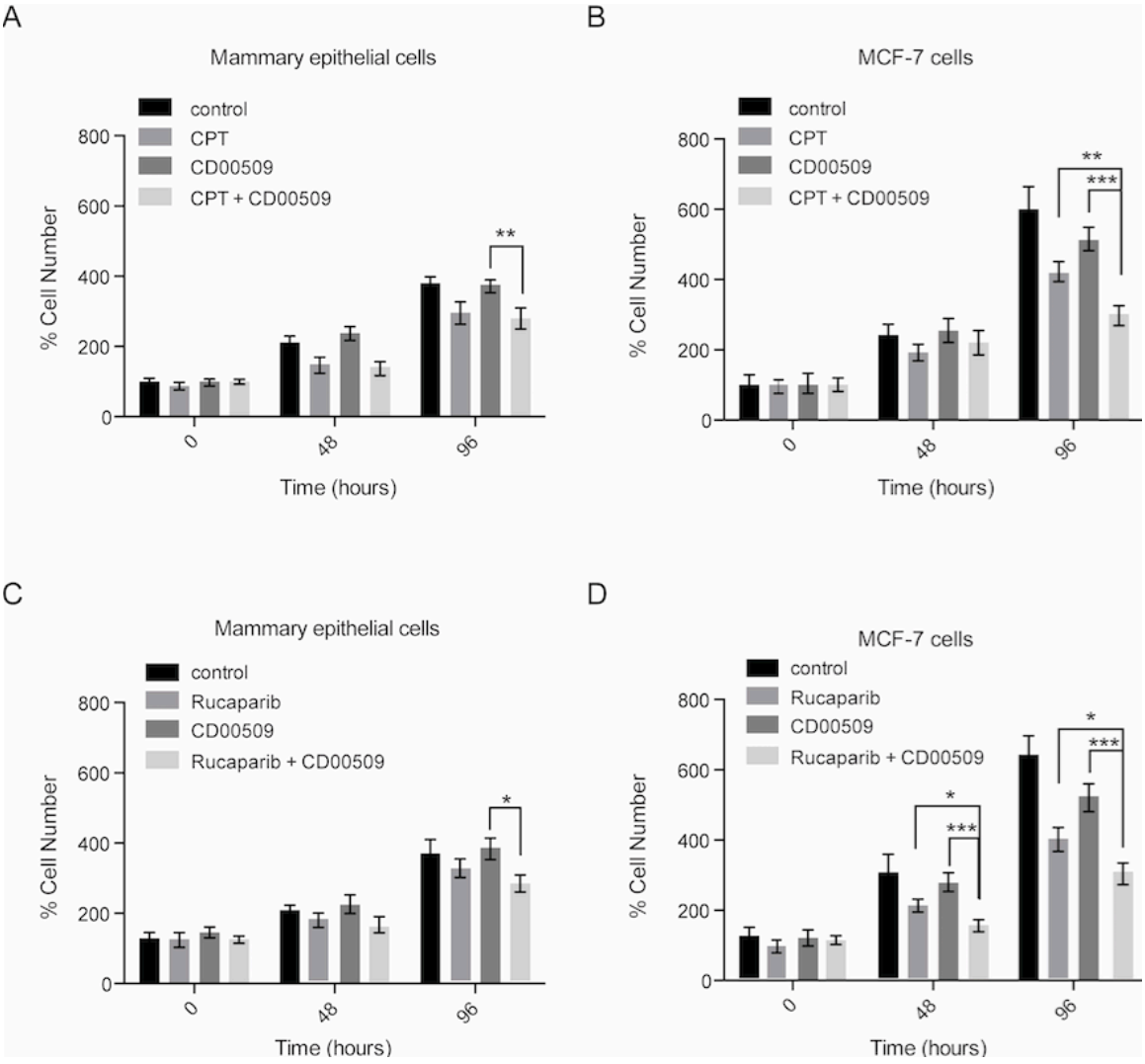

Figure 5-5: Co-treatment with CD00509 and CPT or CD00509 and Rucaparib is more lethal to MCF-7 cells than either treatment alone as measured by MTT assay.

A-B. Growth over a 96 hour period of mammary epithelial cells and breast cancer cell lines when treated with 1 μM CPT or 10 μM CD00509 or CPT and CD00509. **C-D**. Growth of mammary epithelial cells and breast cancer cell lines over a 96 hour period when treated with 10 μM Rucaparib or 10 μM CD00509, or Rucaparib and CD00509 treatment. (n=3) n, number of replicates; error bars, mean ± s.d. *, $P<0.05$, **, $P<0.01$. ***, $P<0.001$.

5.4 Discussion

I found that Tdp1 is highly expressed in many cancers and that its subcellular localization is variably nuclear and cytoplasmic. This data, taken together with my observation of Tdp1

localization in the mitochondria during oxidative stress suggests that further analysis of its subcellular localization might provide a basis for cancer stratification. Additionally, I found that Tdp1 inhibition may be an effective adjuvant in anticancer therapy when combined with the use of other DNA repair inhibitors such as Topo I poisons. Through the screening of chemical libraries using *in silico* and *in vitro* efforts, Dr. Richard Dean identified CD00509 as a potential Tdp1 inhibitor. Furthermore, consistent with such inhibition, I found that treatment with CD00509 increased MCF-7 sensitivity to CPT and additively suppressed cell proliferation when combined with the PARP-1 inhibitor Rucaparib.

The suppression of MCF-7 cell proliferation by CD00509 and Rucaparib occurs in the absence of identified *BRCA1* or *BRCA2* mutations (Barretina et al., 2012; Forbes et al., 2011). This suggests that Rucaparib and CD00509 have potential synthetic lethal interactions with other deleterious mutations carried by the MCF-7 cell line. For example, the mutation in *PIK3CA* (NP_006209.2:p.E545K) causes MCF-7 cells to proliferate more rapidly than other breast cancer cell lines (Figure 5-2A-D) (Kang et al., 2005); therefore, one might hypothesize that because Tdp1 and PARP-1 help maintain DNA replication forks (Huang et al., 2013; Sugimura et al., 2008), inhibition of these enzymes by CD00509 and Rucaparib causes replication fork collapse and cytotoxicity.

Induction of synthetic lethality to selectively kill cancer cells has been discussed for at least 20 years (Guarente, 1993). According to data annotated by the Cancer Cell Line Encyclopedia, Tdp1 is highly expressed in over 30 cancers (Barretina et al., 2012). Since Tdp1 is a member of the phospholipase D (PLD) family, known inhibitors of the PLD family such as vanadate, paromomycin, lividomycin and several teracyclines have been tested on Tdp1, but they are only weak inhibitors (Liao et al., 2006). A recent paper by Walker et al. describes the utility of fluorescence-based oligonucleotide assays in the determination of Tdp1 activity in whole cell extracts (Walker et al., 2014) and validates this independently developed sensitive and high throughput approach to Tdp1 inhibitor screening. Removing the extra Gyrasol assay sensor step used by Walker et al., the design of the quencher and fluorophore on the small substrate in this study permitted real-time kinetic monitoring of Tdp1 activity and decreased the background fluorescence to a signal to noise ratio >10.

Over 20 distinct diseases have been associated with defective DNA repair (O'Driscoll, 2012). This highlights the importance of DNA repair in disease including cancer, which has a

high turnover and heightened sensitivity to DNA repair inhibition. However, the relative contribution of closely related and potentially redundant DNA repair pathways needs better delineation to pave the way for effective targeted drug development.

In the context of such targeted drug development, there is a need for combination therapies that improve anticancer activity in cancers resistant to conventional therapies such as Topo I poisons. To the best of my knowledge, no such Tdp1 inhibitors are being developed in the pre-clinical or clinical stage, although a co-inhibitor of Tdp1 and Topo I has been described (Nguyen et al., 2012). Herein I confirm the potential efficacy of Tdp1 inhibition and the potential utility of combination therapies with PARP-1 inhibitors.

In summary, I provide further evidence that Tdp1 is a valid anticancer target and report a novel high-throughput method for identifying Tdp1 inhibitors using a single stranded oligonucleotide reporter capable of identifying compounds with significant specificity towards the killing of Tdp1-expressing cells. This study identified CD00509, a potent Tdp1 inhibitor, and show that it intrinsically restricts the growth of some patient-derived breast cancer cells and that, with or without PARP inhibition, further sensitizes patient-derived breast cancer cells to Topo I poisons.

Chapter 6: Conclusion

6.1 Tdp1 function through a pathobiological lens

Almost 20 years have elapsed since the discovery of Tdp1 as the first DNA repair protein with phosphodiesterase activity (Pouliot et al., 1999). The scientific community has since associated several other functions with Tdp1, including 3'-phosphoglycolate activity (Inamdar et al., 2002), 5'phosphotyrosyl activity (Nitiss et al., 2006), and apurinic/apyrimidinic (AP) site cleavage activity (Lebedeva et al., 2011). While the biochemical activities of Tdp1 have been studied extensively, less has been done to explore its relevance in human disease. My work explores the significance of Tdp1 in the mammalian cell and attempts to reconcile Tdp1 as a nuclear and mitochondrial DNA repair enzyme with the growing body of evidence connecting the failure of proper DNA repair with cellular stress and disease.

This dissertation addresses the above in four parts. The first is a thorough histopathological analysis of Tdp1 expression in human and mouse tissue and the discovery of Tdp1 in the mitochondria. The second is a study of the cellular factors underlying mitochondrial Tdp1 transport in stressed cells. The third is the use of synthetic-lethal approaches for the treatment of topoisomerase-inhibitor resistant rhabdomyosarcoma. The last is the screening, identification, and validation of a Tdp1 inhibitor. I discuss each point in the following sections as well as questions raised in my work.

6.2 mtDNA repair and disease

Mitochondrial dysfunction is a hallmark of ageing and is increasingly associated with cancer progression. Central to the maintenance of mitochondrial function is mtDNA. Of the different DNA repair mechanisms introduced in Chapter 1, the Base Excision Repair pathway proteins are known to repair oxidative DNA damage in the mitochondria. Oxidative damage of mtDNA predominates because the electron transport chain generates large quantities of oxidative molecules such as superoxide radicals and H_2O_2 (Murphy, 2009). The Mismatch Repair pathway repairs oxidatively damaged deoxyribonucleotide triphosphates. Homologous recombination and Non-Homologous End Joining repair double strand breaks and play important roles in the replication of mtDNA, although the specific mechanisms for the latter remain to be characterized (Alexeyev et al., 2013; Tadi et al., 2016). The Nucleotide Excision Repair pathway has not been detected in mitochondria (Alexeyev et al., 2013).

Since mtDNA codes for critical components of mitochondrial respiration, mtDNA mutations indirectly impinge upon a variety of cellular functions. Pathogenic mtDNA mutations are known causes of debilitating disease (Holt et al., 1988; Shoffner et al., 1990; Wallace et al., 1988). A single cell often contains mutant mtDNA and normal mtDNA, a condition known as heteroplasmy. The unequal segregation of heteroplasmic alleles during mitosis and meiosis gives rise to cell populations with high mutant mtDNA load (Wallace, 2005). Disease manifests when the bioenergetic ability of a cell falls below the minimum threshold required for its normal function. Consequently, because skeletal muscle and neurons have high bioenergetic requirements, they are frequently affected. This logic also suggests that mitochondrial dysfunction may be a factor in complex diseases.

Analysis of human tissue showed cytoplasmic staining of Tdp1 in Purkinje neurons (Hirano et al., 2007). My observation that Tdp1 localized to the mitochondria of mammalian skeletal muscle and fibroblast culture in Chapters 2 and 3 suggested a role for Tdp1 in mtDNA repair. Given that mutant Tdp1 is associated with SCAN1, I hypothesized that establishing functional relevance for Tdp1 in the mitochondria provides insight into the pathophysiology of SCAN1. Measuring well-characterized processes such as mitochondrial respiration, ATP production, apoptosis and mtDNA integrity, I showed that the presence of Tdp1 in mitochondria promotes maintenance of mtDNA integrity, and that a lack of Tdp1 in the mitochondria impedes mitochondrial respiration and ATP production.

The translocation of Tdp1 from the nucleus to the mitochondria under H_2O_2 stress suggests a protective role for Tdp1 in the mitochondria. A signal for Tdp1 translocation is intramitochondrial reactive oxygen. mtDNA stress is not a signal because Tdp1 translocation is unaltered in cells devoid of mtDNA. This raises the question of whether Tdp1 has mitochondrial functions besides DNA repair. Such a dual function is illustrated by TIN2, a nuclear protein in the mitochondria (Chen et al., 2012). Full-length TIN2 is a telomerase-regulating protein in the nucleus, where it interacts with TPP1. The TPP1-interacting domain on TIN2 overlaps with its mitochondria-targeting sequence; thus, interaction of TIN2 with TPP1 abolishes TIN2 import into the mitochondria and vice-versa. In the mitochondria, TIN2 regulates mitochondrial respiration and morphology (Chen et al., 2012). Determining whether Tdp1 plays roles in the mitochondria besides mtDNA repair requires further dissection. A starting point might be to assess post-translational modifications (PTMs) of mitochondrial Tdp1 as PTMs might confer a

different function upon mitochondrial Tdp1. Identified PTMs in Tdp1 include phosphorylation of Serine 81, which increases the enzymatic activity of Tdp1, and SUMOylation of Lysine 111, which causes the accumulation of Tdp1 at sites of DNA damage (Chiang et al., 2010; Hudson et al., 2012). Another starting point might be to use mitochondrial function as a surrogate for Tdp1 function and compare the mitochondrial function of *Tdp1*$^{-/-}$ rho zero cells to *wt* rho zero cells, although this approach might be compromised because rho-zero cells are metabolically weak.

Although research in mice and yeast has deciphered much about Tdp1 function, much remains to be discovered. Tdp1 orthologues have been described in 29 organisms. In the plants *Arabidopsis sp*. and *Medicago sp*., Tdp1 repair of Topo I-induced damage is consistent with its role in mammalian cells (Lee et al., 2010; Macovei et al., 2010). As the time and cost of DNA sequencing continues to decline and techniques for probing the genome become more accessible, the study of emerging model organisms will provide valuable insights into the evolutionary conservation of Tdp1. This approach would allow more detailed evaluation of Tdp1 from an evolutionary perspective and enhance our mechanistic understanding. For example, this might enlighten us as to why the *Drosophila melanogaster* homologue *glaikit* appears to have a function distinct from that of the mammalian and plant Tdp1 homologues (Dunlop et al., 2000; Dunlop et al., 2004)

6.3 A Mitochondrial role for Tdp1 and its implications for SCAN1

I showed that tissue from *Tdp1*$^{-/-}$ mice have increased mtDNA mutations and lesions, as well as impaired mitochondrial respiration compared to tissue from *wt* mice. This discovery of Tdp1 in mitochondria places the pathobiology of SCAN1 in a new light. If human postmortem or biopsy tissue from individuals with SCAN1 were available, characterization of the mitochondrial pathology could provide further insight into the relevance of mitochondrial dysfunction into the pathogenesis of SCAN1.

Despite the nuclear and mitochondrial defects identified in cultured cells and tissues derived from *Tdp1*$^{-/-}$ mice, *Tdp1*$^{-/-}$ mice neither exhibited deficiencies in physical activity as assessed by a homecaging study nor showed symptoms of ataxia with footprint analysis and hang tests. This absence of pathology might have arisen because the p.His493Arg mutation that causes SCAN1 results in a neomorphic protein with a lower K_d and greater tendency to form Tdp1-

DNA aggregates; therefore, the generation of *Tdp1*$^{p.His493Arg}$ mice is required to thoroughly investigate the contribution of this mutation to the physical and molecular characteristics of SCAN.

6.4 Tdp1 in cancer

The idea that cancer cells undergo dynamic rewiring of cellular circuits in response to endogeneous and exogeneous stresses has been widely explored (Creixell et al., 2015; Kolch et al., 2015; Oh et al., 2015). Elevated expression of Tdp1 in non-small cell lung cancer, colorectal cancer and rhabdomyosarcoma has been associated with an increased survival response to prolonged topoisomerase I cleavage complexes in actively replicating cancer cells. Supporting this, decreasing Tdp1 levels or inhibiting Tdp1 activity in cancer cells selectively enhances camptothecin and/or irinotecan killing of those cells that may be otherwise unresponsive (Fam et al., 2013c; Meisenberg et al., 2015). While the simultaneous attenuation of Tdp1 and camptothecin poisoning shows therapeutic promise possibly because the administration of camptothecin rewires cellular circuits in fast-growing cancer cells to increase tumor cell reliance on Tdp1-mediated DNA repair, such a process would leave the tumor acutely susceptible to Tdp1 attenuation, particularly after camptothecin therapy as opposed to concurrent treatment. Indeed, several studies have shown that staggering the timing of chemotherapeutic drug administration in combination therapy enhances tumor cell killing compared with concurrent administration (Koopman et al., 2007; Lee et al., 2012b; Morton et al., 2014). I hypothesize therefore that understanding the spatiotemporal effects of re-wiring tumor cell growth pathways under the selective pressures of topoisomerase I poisons and Tdp1 inhibitors can be harnessed to improve the efficacy of the anticancer properties of topoisomerase I poisons.

Tumors may promote growth through modulation of tumor-suppressor and oncogenic pathways. For example, c-Myc and mTOR promote mitochondrial biogenesis, mitochondrial respiration and cell-cycle progression (Li et al., 2005; Morita et al., 2015). Other tumors cheat death by downregulation of pro-apoptotic and/or upregulation of anti-apoptotic factors (Lopez and Tait, 2015). It is becoming increasingly clear that cancer cells employ a combination of methods for survival. However, there seems to be consensus that cancer cells, through successive generations of accumulating mutations required for tumorigenesis, acquire significant mutability through the degradation of DNA damage response components (Jackson and Bartek, 2009;

Negrini et al., 2010; Salk et al., 2010). Indeed, my observations that RMS cells that overexpress Tdp1 are more sensitive to Tdp1 knockdown, and that Tdp1 knockdown and PARP1 inhibition selectively kills RMS cells over control myoblasts, suggest a deficiency in the DNA damage response in RMS cells.

The pathophysiology of cancer can also be set in the context of mitochondrial function. Otto Warburg's observation that cancer cells undergo anaerobic glycolysis, fermenting glucose to lactate rather than the total oxidation of glucose via mitochondrial respiration called attention to the capacity for tumorigenesis in cancer cells with damaged mitochondria. Although this "Warburg Effect" is observed in subtypes of cancer cells, there are many exceptions to the rule (Hanahan and Weinberg, 2011). Among tumors that outgrow their blood supply, cell survival depends upon anaerobic glycolysis in lieu of mitochondrial respiration (Gatenby and Gillies, 2004). I showed for some cultured rhabdomyosarcoma cells that the use of PARP inhibition and serum and glucose starvation is a multimodal therapy selectively targeting cancer cells.

The characterization of individual tumors promised by next-generation cancer diagnostics will enable use of small-molecules as a means of targeting specific survival dependencies in tumor cells rather than the underlying driver mutations in them. The use of computational genomics for predicting cancer targets greatly benefits the screening of new small molecule inhibitors or repurposing of existing compounds. Efforts to generate comprehensive maps of key genetic changes in tumorigenesis such as The Cancer Genome Atlas (TCGA) and gene expression changes in cancer cell lines such as the Cancer Cell Line Encyclopedia (CCLE) allow predictive modeling of drug response in pre-clinical research (Barretina et al., 2012; Cancer Genome Atlas Research et al., 2013). The availability of comprehensive gene expression and synthetic lethal interaction datasets will greatly reduce the time needed to pinpoint cancer subtypes that may be responsive to Tdp1 inhibition. This would also broaden the scope of therapeutic targets for Tdp1 inhibitors beyond its combination with irinotecan and camptothecin.

The most effective Tdp1 inhibitors identified to date are two phosphotyrosine mimetics methyl-3.4-dephostatin and the steroid NSC88915 (Dexheimer et al., 2009; Marchand et al., 2009). Examination of the structure-activity relationship between these and CD00509 reveals no close structural similarities. CD00509 is an alkylidene barbiturate, a class of compounds notable for reactivity interference (Baell and Holloway, 2010). However, the observation that CD00509 increases the sensitivity of *Tdp1*$^{+/+}$ MEFs to CPT over *Tdp1*$^{-/-}$ MEFs suggests that this compound

targets cells expressing the Tdp1 enzyme and thus might be an exception to the PAINS (Pan Assay Interference Compounds) filter which identifies structural features that appear as frequent hitters (promiscuous compounds) in many biochemical high throughput screens. Nonetheless, further studies are required to determine the specificity of CD00509 and its cytotoxicity when combined with CPT.

6.5 Conclusion

In this dissertation, I have advanced the understanding of Tdp1 on two fronts. First, I showed that Tdp1 is a stress-responsive protein capable of translocating between the nucleus and mitochondria, where it maintains the integrity of mtDNA. Second, I showed that Tdp1 is a potential target for cancer treatment beyond its association with topoisomerase I poisons. Through the use of small-molecule inhibitors of Tdp1, one could explore potential synthetic lethal interactions between Tdp1 and other cellular factors. More work needs to be done to establish a functional role for Tdp1 in mitochondria and to explore the intersection of Tdp1 and mitochondria in cancer. The conditions that signal for Tdp1 translocation into the mitochondria should be clearly delineated in an animal model to allow more robust data interpretation. Comparative analyses of mitochondrial function for normal and SCAN1-mutant Tdp1 is necessary to determine whether mitochondrial dysfunction contributes to the pathology of SCAN1.

Bibliography/ References

1. Abou-Sleiman, P.M., Muqit, M.M., and Wood, N.W. (2006). Expanding insights of mitochondrial dysfunction in Parkinson's disease. Nature reviews Neuroscience *7*, 207-219.
2. Adamson, B., Smogorzewska, A., Sigoillot, F.D., King, R.W., and Elledge, S.J. (2012). A genome-wide homologous recombination screen identifies the RNA-binding protein RBMX as a component of the DNA-damage response. Nature cell biology *14*, 318-328.
3. Alagoz, M., Wells, O.S., and El-Khamisy, S.F. (2014). TDP1 deficiency sensitizes human cells to base damage via distinct topoisomerase I and PARP mechanisms with potential applications for cancer therapy. Nucleic acids research *42*, 3089-3103.
4. Alexeyev, M., Shokolenko, I., Wilson, G., and LeDoux, S. (2013). The maintenance of mitochondrial DNA integrity--critical analysis and update. Cold Spring Harbor perspectives in biology *5*, a012641.
5. Aly, A., and Ganesan, S. (2011). BRCA1, PARP, and 53BP1: conditional synthetic lethality and synthetic viability. Journal of molecular cell biology *3*, 66-74.
6. Ames, B.N., Shigenaga, M.K., and Hagen, T.M. (1993). Oxidants, antioxidants, and the degenerative diseases of aging. Proceedings of the National Academy of Sciences of the United States of America *90*, 7915-7922.
7. Aplin, A.E., Stewart, S.A., Assoian, R.K., and Juliano, R.L. (2001). Integrin-mediated adhesion regulates ERK nuclear translocation and phosphorylation of Elk-1. The Journal of cell biology *153*, 273-282.
8. Arndt, C.A., Stoner, J.A., Hawkins, D.S., Rodeberg, D.A., Hayes-Jordan, A.A., Paidas, C.N., Parham, D.M., Teot, L.A., Wharam, M.D., Breneman, J.C.*, et al.* (2009). Vincristine, Actinomycin, and Cyclophosphamide Compared With Vincristine, Actinomycin, and Cyclophosphamide Alternating With Vincristine, Topotecan, and Cyclophosphamide for Intermediate-Risk Rhabdomyosarcoma: Children's Oncology Group Study D9803. J Clin Oncol.
9. Ashley, N., Harris, D., and Poulton, J. (2005). Detection of mitochondrial DNA depletion in living human cells using PicoGreen staining. Experimental cell research *303*, 432-446.
10. Ayala, A., Munoz, M.F., and Arguelles, S. (2014). Lipid peroxidation: production, metabolism, and signaling mechanisms of malondialdehyde and 4-hydroxy-2-nonenal. Oxidative medicine and cellular longevity *2014*, 360438.
11. Ayalon, D., Glaser, T., and Werner, H. (2001). Transcriptional regulation of IGF-I receptor gene expression by the PAX3-FKHR oncoprotein. Growth Horm IGF Res *11*, 289-297.
12. Baell, J.B., and Holloway, G.A. (2010). New substructure filters for removal of pan assay interference compounds (PAINS) from screening libraries and for their exclusion in bioassays. Journal of medicinal chemistry *53*, 2719-2740.
13. Barbosa, M.R., Sampaio, I.H., Teodoro, B.G., Sousa, T.A., Zoppi, C.C., Queiroz, A.L., Passos, M.A., Alberici, L.C., Teixeira, F.R., Manfiolli, A.O.*, et al.* (2013). Hydrogen peroxide production regulates the mitochondrial function in insulin resistant muscle cells: effect of catalase overexpression. Biochimica et biophysica acta *1832*, 1591-1604.
14. Barchiesi, A., Wasilewski, M., Chacinska, A., Tell, G., and Vascotto, C. (2015). Mitochondrial translocation of APE1 relies on the MIA pathway. Nucleic acids research *43*, 5451-5464.

15. Barekati, Z., Radpour, R., Kohler, C., Zhang, B., Toniolo, P., Lenner, P., Lv, Q., Zheng, H., and Zhong, X.Y. (2010). Methylation profile of TP53 regulatory pathway and mtDNA alterations in breast cancer patients lacking TP53 mutations. Human molecular genetics *19*, 2936-2946.
16. Barr, F.G., Galili, N., Holick, J., Biegel, J.A., Rovera, G., and Emanuel, B.S. (1993). Rearrangement of the PAX3 paired box gene in the paediatric solid tumour alveolar rhabdomyosarcoma. Nat Genet *3*, 113-117.
17. Barretina, J., Caponigro, G., Stransky, N., Venkatesan, K., Margolin, A.A., Kim, S., Wilson, C.J., Lehar, J., Kryukov, G.V., Sonkin, D.*, et al.* (2012). The Cancer Cell Line Encyclopedia enables predictive modelling of anticancer drug sensitivity. Nature *483*, 603-607.
18. Bartek, J., Lukas, J., and Bartkova, J. (2007). DNA damage response as an anti-cancer barrier: damage threshold and the concept of 'conditional haploinsufficiency'. Cell Cycle *6*, 2344-2347.
19. Barthelmes, H.U., Habermeyer, M., Christensen, M.O., Mielke, C., Interthal, H., Pouliot, J.J., Boege, F., and Marko, D. (2004). TDP1 overexpression in human cells counteracts DNA damage mediated by topoisomerases I and II. J Biol Chem *279*, 55618-55625.
20. Barzilai, A. (2011). The neuro-glial-vascular interrelations in genomic instability symptoms. Mechanisms of ageing and development *132*, 395-404.
21. Ben-Aroya, S., Coombes, C., Kwok, T., O'Donnell, K.A., Boeke, J.D., and Hieter, P. (2008). Toward a comprehensive temperature-sensitive mutant repository of the essential genes of Saccharomyces cerevisiae. Molecular cell *30*, 248-258.
22. Bender, A., Krishnan, K.J., Morris, C.M., Taylor, G.A., Reeve, A.K., Perry, R.H., Jaros, E., Hersheson, J.S., Betts, J., Klopstock, T.*, et al.* (2006). High levels of mitochondrial DNA deletions in substantia nigra neurons in aging and Parkinson disease. Nature genetics *38*, 515-517.
23. Berman, H.M., Westbrook, J., Feng, Z., Gilliland, G., Bhat, T.N., Weissig, H., Shindyalov, I.N., and Bourne, P.E. (2000). The Protein Data Bank. Nucleic acids research *28*, 235-242.
24. Boerkoel, C.F., Takashima, H., Garcia, C.A., Olney, R.K., Johnson, J., Berry, K., Russo, P., Kennedy, S., Teebi, A.S., Scavina, M.*, et al.* (2002). Charcot-Marie-Tooth disease and related neuropathies: mutation distribution and genotype-phenotype correlation. Annals of neurology *51*, 190-201.
25. Boopathi, E., Srinivasan, S., Fang, J.K., and Avadhani, N.G. (2008). Bimodal protein targeting through activation of cryptic mitochondrial targeting signals by an inducible cytosolic endoprotease. Molecular cell *32*, 32-42.
26. Bouwman, P., Aly, A., Escandell, J.M., Pieterse, M., Bartkova, J., van der Gulden, H., Hiddingh, S., Thanasoula, M., Kulkarni, A., Yang, Q.*, et al.* (2010). 53BP1 loss rescues BRCA1 deficiency and is associated with triple-negative and BRCA-mutated breast cancers. Nature structural & molecular biology *17*, 688-695.
27. Brangi, M., Litman, T., Ciotti, M., Nishiyama, K., Kohlhagen, G., Takimoto, C., Robey, R., Pommier, Y., Fojo, T., and Bates, S.E. (1999). Camptothecin resistance: role of the ATP-binding cassette (ABC), mitoxantrone-resistance half-transporter (MXR), and potential for glucuronidation in MXR-expressing cells. Cancer research *59*, 5938-5946.

28. Brenner, J.C., Feng, F.Y., Han, S., Patel, S., Goyal, S.V., Bou-Maroun, L.M., Liu, M., Lonigro, R., Prensner, J.R., Tomlins, S.A.*, et al.* (2012). PARP-1 inhibition as a targeted strategy to treat Ewing's sarcoma. Cancer research *72*, 1608-1613.
29. Bunting, S.F., Callen, E., Wong, N., Chen, H.T., Polato, F., Gunn, A., Bothmer, A., Feldhahn, N., Fernandez-Capetillo, O., Cao, L.*, et al.* (2010). 53BP1 inhibits homologous recombination in Brca1-deficient cells by blocking resection of DNA breaks. Cell *141*, 243-254.
30. Cahill, D.P., Kinzler, K.W., Vogelstein, B., and Lengauer, C. (1999). Genetic instability and darwinian selection in tumours. Trends Cell Biol *9*, M57-60.
31. Cancer Genome Atlas Research, N., Weinstein, J.N., Collisson, E.A., Mills, G.B., Shaw, K.R., Ozenberger, B.A., Ellrott, K., Shmulevich, I., Sander, C., and Stuart, J.M. (2013). The Cancer Genome Atlas Pan-Cancer analysis project. Nature genetics *45*, 1113-1120.
32. Chen, L.Y., Zhang, Y., Zhang, Q., Li, H., Luo, Z., Fang, H., Kim, S.H., Qin, L., Yotnda, P., Xu, J.*, et al.* (2012). Mitochondrial localization of telomeric protein TIN2 links telomere regulation to metabolic control. Molecular cell *47*, 839-850.
33. Chiang, S.C., Carroll, J., and El-Khamisy, S.F. (2010). TDP1 serine 81 promotes interaction with DNA ligase IIIalpha and facilitates cell survival following DNA damage. Cell cycle *9*, 588-595.
34. Chiarugi, A. (2012). A snapshot of chemoresistance to PARP inhibitors. Trends Pharmacol Sci *33*, 42-48.
35. Ciccia, A., and Elledge, S.J. (2010). The DNA damage response: making it safe to play with knives. Molecular cell *40*, 179-204.
36. Connelly, J.C., and Leach, D.R. (2004). Repair of DNA covalently linked to protein. Molecular cell *13*, 307-316.
37. Cortes Ledesma, F., El Khamisy, S.F., Zuma, M.C., Osborn, K., and Caldecott, K.W. (2009). A human 5'-tyrosyl DNA phosphodiesterase that repairs topoisomerase-mediated DNA damage. Nature *461*, 674-678.
38. Creixell, P., Schoof, E.M., Simpson, C.D., Longden, J., Miller, C.J., Lou, H.J., Perryman, L., Cox, T.R., Zivanovic, N., Palmeri, A.*, et al.* (2015). Kinome-wide decoding of network-attacking mutations rewiring cancer signaling. Cell *163*, 202-217.
39. Dagher, R., and Helman, L. (1999). Rhabdomyosarcoma: an overview. Oncologist *4*, 34-44.
40. Das, B.B., Antony, S., Gupta, S., Dexheimer, T.S., Redon, C.E., Garfield, S., Shiloh, Y., and Pommier, Y. (2009). Optimal function of the DNA repair enzyme TDP1 requires its phosphorylation by ATM and/or DNA-PK. The EMBO journal *28*, 3667-3680.
41. Das, B.B., Dexheimer, T.S., Maddali, K., and Pommier, Y. (2010). Role of tyrosyl-DNA phosphodiesterase (TDP1) in mitochondria. Proceedings of the National Academy of Sciences of the United States of America *107*, 19790-19795.
42. Davis, R.J., D'Cruz, C.M., Lovell, M.A., Biegel, J.A., and Barr, F.G. (1994). Fusion of PAX7 to FKHR by the variant t(1;13)(p36;q14) translocation in alveolar rhabdomyosarcoma. Cancer Res *54*, 2869-2872.
43. de Laat, W.L., Jaspers, N.G., and Hoeijmakers, J.H. (1999). Molecular mechanism of nucleotide excision repair. Genes & development *13*, 768-785.
44. Dean, R., Fam, HK., Shimizu, Y., An, J., Choi, K., Jones, SJ., Boerkoel, CF., Interthal H., Pfeifer T. (2013). Identification of Tdp1 inhibitors by in vitro, in silico and cell-based assays. (Manuscript in preparation).

45. Dean, R.A., Fam, H.K., An, J., Choi, K., Shimizu, Y., Jones, S.J., Boerkoel, C.F., Interthal, H., and Pfeifer, T.A. (2014). Identification of a putative Tdp1 inhibitor (CD00509) by in vitro and cell-based assays. Journal of biomolecular screening *19*, 1372-1382.
46. Debethune, L., Kohlhagen, G., Grandas, A., and Pommier, Y. (2002). Processing of nucleopeptides mimicking the topoisomerase I-DNA covalent complex by tyrosyl-DNA phosphodiesterase. Nucleic acids research *30*, 1198-1204.
47. Dexheimer, T.S., Antony, S., Marchand, C., and Pommier, Y. (2008). Tyrosyl-DNA phosphodiesterase as a target for anticancer therapy. Anti-cancer agents in medicinal chemistry *8*, 381-389.
48. Dexheimer, T.S., Gediya, L.K., Stephen, A.G., Weidlich, I., Antony, S., Marchand, C., Interthal, H., Nicklaus, M., Fisher, R.J., Njar, V.C.*, et al.* (2009). 4-Pregnen-21-ol-3,20-dione-21-(4-bromobenzenesulfonate) (NSC 88915) and related novel steroid derivatives as tyrosyl-DNA phosphodiesterase (Tdp1) inhibitors. J Med Chem *52*, 7122-7131.
49. Dexheimer, T.S., Stephen, A.G., Fivash, M.J., Fisher, R.J., and Pommier, Y. (2010). The DNA binding and 3'-end preferential activity of human tyrosyl-DNA phosphodiesterase. Nucleic acids research *38*, 2444-2452.
50. Di Maio, R., Barrett, P.J., Hoffman, E.K., Barrett, C.W., Zharikov, A., Borah, A., Hu, X., McCoy, J., Chu, C.T., Burton, E.A.*, et al.* (2016). alpha-Synuclein binds to TOM20 and inhibits mitochondrial protein import in Parkinson's disease. Science translational medicine *8*, 342ra378.
51. Dimauro, S. (2011). A history of mitochondrial diseases. Journal of inherited metabolic disease *34*, 261-276.
52. Domagala, P., Huzarski, T., Lubinski, J., Gugala, K., and Domagala, W. (2011). Immunophenotypic predictive profiling of BRCA1-associated breast cancer. Virchows Arch *458*, 55-64.
53. Drew, Y., Ledermann, J., Hall, G., Rea, D., Glasspool, R., Highley, M., Jayson, G., Sludden, J., Murray, J., Jamieson, D.*, et al.* (2016). Phase 2 multicentre trial investigating intermittent and continuous dosing schedules of the poly(ADP-ribose) polymerase inhibitor rucaparib in germline BRCA mutation carriers with advanced ovarian and breast cancer. British journal of cancer *114*, e21.
54. Dunlop, J., Corominas, M., and Serras, F. (2000). The novel gene glaikit, is expressed during neurogenesis in the Drosophila melanogaster embryo. Mechanisms of development *96*, 133-136.
55. Dunlop, J., Morin, X., Corominas, M., Serras, F., and Tear, G. (2004). glaikit is essential for the formation of epithelial polarity and neuronal development. Current biology : CB *14*, 2039-2045.
56. Eaton, S.L., Hurtado, M.L., Oldknow, K.J., Graham, L.C., Marchant, T.W., Gillingwater, T.H., Farquharson, C., and Wishart, T.M. (2014). A guide to modern quantitative fluorescent western blotting with troubleshooting strategies. Journal of visualized experiments : JoVE, e52099.
57. el-Khamisy, S.F., and Caldecott, K.W. (2007). DNA single-strand break repair and spinocerebellar ataxia with axonal neuropathy-1. Neuroscience *145*, 1260-1266.
58. El-Khamisy, S.F., Hartsuiker, E., and Caldecott, K.W. (2007). TDP1 facilitates repair of ionizing radiation-induced DNA single-strand breaks. DNA repair *6*, 1485-1495.

59. El-Khamisy, S.F., Katyal, S., Patel, P., Ju, L., McKinnon, P.J., and Caldecott, K.W. (2009). Synergistic decrease of DNA single-strand break repair rates in mouse neural cells lacking both Tdp1 and aprataxin. DNA repair *8*, 760-766.
60. El-Khamisy, S.F., Masutani, M., Suzuki, H., and Caldecott, K.W. (2003). A requirement for PARP-1 for the assembly or stability of XRCC1 nuclear foci at sites of oxidative DNA damage. Nucleic acids research *31*, 5526-5533.
61. El-Khamisy, S.F., Saifi, G.M., Weinfeld, M., Johansson, F., Helleday, T., Lupski, J.R., and Caldecott, K.W. (2005). Defective DNA single-strand break repair in spinocerebellar ataxia with axonal neuropathy-1. Nature *434*, 108-113.
62. Ellison, L.F., Pogany, L., and Mery, L.S. (2007). Childhood and adolescent cancer survival: a period analysis of data from the Canadian Cancer Registry. Eur J Cancer *43*, 1967-1975.
63. Embirucu, E.K., Martyn, M.L., Schlesinger, D., and Kok, F. (2009). Autosomal recessive ataxias: 20 types, and counting. Arquivos de neuro-psiquiatria *67*, 1143-1156.
64. Fam, A., Chowdhury, M.K., and Boerkoel, C.F. (2012). Spinocerebellar ataxia with axonal neuropathy: a disorder of nuclear and mitochondrial DNA repair. In Spinocerebellar Ataxia (InTech), p. In Press.
65. Fam, H.K., Chowdhury, M.K., Walton, C., Choi, K., Boerkoel, C.F., and Hendson, G. (2013a). Expression profile and mitochondrial colocalization of Tdp1 in peripheral human tissues. Journal of molecular histology.
66. Fam, H.K., Chowdhury, M.K., Walton, C., Choi, K., Boerkoel, C.F., and Hendson, G. (2013b). Expression profile and mitochondrial colocalization of Tdp1 in peripheral human tissues. Journal of molecular histology *44*, 481-494.
67. Fam, H.K., Walton, C., Mitra, S.A., Chowdhury, M., Osborne, N., Choi, K., Sun, G., Wong, P.C., O'Sullivan, M.J., Turashvili, G.*, et al.* (2013c). TDP1 and PARP1 deficiency are cytotoxic to rhabdomyosarcoma cells. Molecular cancer research : MCR *11*, 1179-1192.
68. Fam, H.K., Walton, C., Mitra, S.A., Chowdhury, M., Osborne, N., Choi, K., Sun, G., Wong, P.C., O'Sullivan, M.J., Turashvili, G.*, et al.* (2013d). Tyrosyl-DNA phosphodiesterase 1 (TDP1) and Poly (ADP-Ribose) Polymerase-1 (PARP1) deficiency are cytotoxic to rhabdomyosarcoma cells. Molecular cancer research : MCR.
69. Farmer, H., McCabe, N., Lord, C.J., Tutt, A.N., Johnson, D.A., Richardson, T.B., Santarosa, M., Dillon, K.J., Hickson, I., Knights, C.*, et al.* (2005). Targeting the DNA repair defect in BRCA mutant cells as a therapeutic strategy. Nature *434*, 917-921.
70. Fishel, M.L., Vasko, M.R., and Kelley, M.R. (2007). DNA repair in neurons: so if they don't divide what's to repair? Mutation research *614*, 24-36.
71. Fong, P.C., Boss, D.S., Yap, T.A., Tutt, A., Wu, P., Mergui-Roelvink, M., Mortimer, P., Swaisland, H., Lau, A., O'Connor, M.J.*, et al.* (2009). Inhibition of poly(ADP-ribose) polymerase in tumors from BRCA mutation carriers. The New England journal of medicine *361*, 123-134.
72. Forbes, S.A., Bindal, N., Bamford, S., Cole, C., Kok, C.Y., Beare, D., Jia, M., Shepherd, R., Leung, K., Menzies, A.*, et al.* (2011). COSMIC: mining complete cancer genomes in the Catalogue of Somatic Mutations in Cancer. Nucleic acids research *39*, D945-950.
73. Frosina, G., Fortini, P., Rossi, O., Carrozzino, F., Raspaglio, G., Cox, L.S., Lane, D.P., Abbondandolo, A., and Dogliotti, E. (1996). Two pathways for base excision repair in mammalian cells. The Journal of biological chemistry *271*, 9573-9578.

74. Fukui, H., and Moraes, C.T. (2009). Mechanisms of formation and accumulation of mitochondrial DNA deletions in aging neurons. Human molecular genetics *18*, 1028-1036.
75. Garnett, M.J., Edelman, E.J., Heidorn, S.J., Greenman, C.D., Dastur, A., Lau, K.W., Greninger, P., Thompson, I.R., Luo, X., Soares, J.*, et al.* (2012). Systematic identification of genomic markers of drug sensitivity in cancer cells. Nature *483*, 570-575.
76. Gatenby, R.A., and Gillies, R.J. (2004). Why do cancers have high aerobic glycolysis? Nature reviews Cancer *4*, 891-899.
77. Giovanella, B.C., Stehlin, J.S., Wall, M.E., Wani, M.C., Nicholas, A.W., Liu, L.F., Silber, R., and Potmesil, M. (1989). DNA topoisomerase I--targeted chemotherapy of human colon cancer in xenografts. Science *246*, 1046-1048.
78. Goncalves, A., Finetti, P., Sabatier, R., Gilabert, M., Adelaide, J., Borg, J.P., Chaffanet, M., Viens, P., Birnbaum, D., and Bertucci, F. (2011). Poly(ADP-ribose) polymerase-1 mRNA expression in human breast cancer: a meta-analysis. Breast Cancer Res Treat *127*, 273-281.
79. Gong, X., Ming, X., Deng, P., and Jiang, Y. (2010). Mechanisms regulating the nuclear translocation of p38 MAP kinase. Journal of cellular biochemistry *110*, 1420-1429.
80. Gonzalez-Hunt, C.P., Rooney, J.P., Ryde, I.T., Anbalagan, C., Joglekar, R., and Meyer, J.N. (2016). PCR-Based Analysis of Mitochondrial DNA Copy Number, Mitochondrial DNA Damage, and Nuclear DNA Damage. Current protocols in toxicology *67*, 20 11 21-20 11 25.
81. Gough, D.R., and Cotter, T.G. (2011). Hydrogen peroxide: a Jekyll and Hyde signalling molecule. Cell death & disease *2*, e213.
82. Graham, J., Ford, T., and Rickwood, D. (1994). The preparation of subcellular organelles from mouse liver in self-generated gradients of iodixanol. Anal Biochem *220*, 367-373.
83. Graham, N.A., Tahmasian, M., Kohli, B., Komisopoulou, E., Zhu, M., Vivanco, I., Teitell, M.A., Wu, H., Ribas, A., Lo, R.S.*, et al.* (2012). Glucose deprivation activates a metabolic and signaling amplification loop leading to cell death. Molecular systems biology *8*, 589.
84. Guarente, L. (1993). Synthetic enhancement in gene interaction: a genetic tool come of age. Trends in genetics : TIG *9*, 362-366.
85. Hafezparast, M., Ahmad-Annuar, A., Wood, N.W., Tabrizi, S.J., and Fisher, E.M. (2002). Mouse models for neurological disease. Lancet neurology *1*, 215-224.
86. Hanahan, D., and Weinberg, R.A. (2011). Hallmarks of cancer: the next generation. Cell *144*, 646-674.
87. Harbauer, A.B., Zahedi, R.P., Sickmann, A., Pfanner, N., and Meisinger, C. (2014). The protein import machinery of mitochondria-a regulatory hub in metabolism, stress, and disease. Cell metabolism *19*, 357-372.
88. Harman, D. (1972). The biologic clock: the mitochondria? Journal of the American Geriatrics Society *20*, 145-147.
89. Harman, D. (1981). The aging process. Proceedings of the National Academy of Sciences of the United States of America *78*, 7124-7128.
90. Hawkins, A.J., Subler, M.A., Akopiants, K., Wiley, J.L., Taylor, S.M., Rice, A.C., Windle, J.J., Valerie, K., and Povirk, L.F. (2009). In vitro complementation of Tdp1 deficiency indicates a stabilized enzyme-DNA adduct from tyrosyl but not glycolate lesions as a consequence of the SCAN1 mutation. DNA repair *8*, 654-663.

91. Helleday, T. (2008). Amplifying tumour-specific replication lesions by DNA repair inhibitors - a new era in targeted cancer therapy. Eur J Cancer *44*, 921-927.
92. Hingorani, P., and Kolb, E.A. (2010). Past, present and future of therapies in pediatric sarcomas. Future Oncol *6*, 605-618.
93. Hirano, R., Interthal, H., Huang, C., Nakamura, T., Deguchi, K., Choi, K., Bhattacharjee, M.B., Arimura, K., Umehara, F., Izumo, S.*, et al.* (2007). Spinocerebellar ataxia with axonal neuropathy: consequence of a Tdp1 recessive neomorphic mutation? The EMBO journal *26*, 4732-4743.
94. Hire, R.R., Katrak, S.M., Vaidya, S., Radhakrishnan, K., and Seshadri, M. (2011). Spinocerebellar ataxia type 17 in Indian patients: two rare cases of homozygous expansions. Clinical genetics *80*, 472-477.
95. Holt, I.J., Harding, A.E., and Morgan-Hughes, J.A. (1988). Deletions of muscle mitochondrial DNA in patients with mitochondrial myopathies. Nature *331*, 717-719.
96. Hsiang, Y.H., Lihou, M.G., and Liu, L.F. (1989). Arrest of replication forks by drug-stabilized topoisomerase I-DNA cleavable complexes as a mechanism of cell killing by camptothecin. Cancer research *49*, 5077-5082.
97. Huang, S.Y., Murai, J., Dalla Rosa, I., Dexheimer, T.S., Naumova, A., Gmeiner, W.H., and Pommier, Y. (2013). TDP1 repairs nuclear and mitochondrial DNA damage induced by chain-terminating anticancer and antiviral nucleoside analogs. Nucleic acids research *41*, 7793-7803.
98. Hudson, E.K., Hogue, B.A., Souza-Pinto, N.C., Croteau, D.L., Anson, R.M., Bohr, V.A., and Hansford, R.G. (1998). Age-associated change in mitochondrial DNA damage. Free radical research *29*, 573-579.
99. Hudson, J.J., Chiang, S.C., Wells, O.S., Rookyard, C., and El-Khamisy, S.F. (2012). SUMO modification of the neuroprotective protein TDP1 facilitates chromosomal single-strand break repair. Nature communications *3*, 733.
100. Huh, W.K., Falvo, J.V., Gerke, L.C., Carroll, A.S., Howson, R.W., Weissman, J.S., and O'Shea, E.K. (2003). Global analysis of protein localization in budding yeast. Nature *425*, 686-691.
101. Inamdar, K.V., Pouliot, J.J., Zhou, T., Lees-Miller, S.P., Rasouli-Nia, A., and Povirk, L.F. (2002). Conversion of phosphoglycolate to phosphate termini on 3' overhangs of DNA double strand breaks by the human tyrosyl-DNA phosphodiesterase hTdp1. The Journal of biological chemistry *277*, 27162-27168.
102. Interthal, H., Chen, H.J., and Champoux, J.J. (2005a). Human Tdp1 cleaves a broad spectrum of substrates, including phosphoamide linkages. The Journal of biological chemistry *280*, 36518-36528.
103. Interthal, H., Chen, H.J., Kehl-Fie, T.E., Zotzmann, J., Leppard, J.B., and Champoux, J.J. (2005b). SCAN1 mutant Tdp1 accumulates the enzyme--DNA intermediate and causes camptothecin hypersensitivity. The EMBO journal *24*, 2224-2233.
104. Interthal, H., Pouliot, J.J., and Champoux, J.J. (2001). The tyrosyl-DNA phosphodiesterase Tdp1 is a member of the phospholipase D superfamily. Proceedings of the National Academy of Sciences of the United States of America *98*, 12009-12014.
105. Irwin, J.J., and Shoichet, B.K. (2005). ZINC--a free database of commercially available compounds for virtual screening. Journal of chemical information and modeling *45*, 177-182.

106. Ivashkevich, A., Redon, C.E., Nakamura, A.J., Martin, R.F., and Martin, O.A. (2012). Use of the gamma-H2AX assay to monitor DNA damage and repair in translational cancer research. Cancer letters *327*, 123-133.
107. Izhar, L., Adamson, B., Ciccia, A., Lewis, J., Pontano-Vaites, L., Leng, Y., Liang, A.C., Westbrook, T.F., Harper, J.W., and Elledge, S.J. (2015). A Systematic Analysis of Factors Localized to Damaged Chromatin Reveals PARP-Dependent Recruitment of Transcription Factors. Cell reports *11*, 1486-1500.
108. Jackson, S.P., and Bartek, J. (2009). The DNA-damage response in human biology and disease. Nature *461*, 1071-1078.
109. Jastroch, M., Divakaruni, A.S., Mookerjee, S., Treberg, J.R., and Brand, M.D. (2010). Mitochondrial proton and electron leaks. Essays in biochemistry *47*, 53-67.
110. Jensen, P.W., Falconi, M., Kristoffersen, E.L., Simonsen, A.T., Cifuentes, J.B., Marcussen, L.B., Frohlich, R., Vagner, J., Harmsen, C., Juul, S.*, et al.* (2013). Real-time detection of TDP1 activity using a fluorophore-quencher coupled DNA-biosensor. Biosensors & bioelectronics *48C*, 230-237.
111. Jeppesen, D.K., Bohr, V.A., and Stevnsner, T. (2011). DNA repair deficiency in neurodegeneration. Progress in neurobiology *94*, 166-200.
112. Johns, D.R. (1995). Seminars in medicine of the Beth Israel Hospital, Boston. Mitochondrial DNA and disease. The New England journal of medicine *333*, 638-644.
113. Johnson, G.L., and Lapadat, R. (2002). Mitogen-activated protein kinase pathways mediated by ERK, JNK, and p38 protein kinases. Science *298*, 1911-1912.
114. Kamenisch, Y., Fousteri, M., Knoch, J., von Thaler, A.K., Fehrenbacher, B., Kato, H., Becker, T., Dolle, M.E., Kuiper, R., Majora, M.*, et al.* (2010). Proteins of nucleotide and base excision repair pathways interact in mitochondria to protect from loss of subcutaneous fat, a hallmark of aging. The Journal of experimental medicine *207*, 379-390.
115. Kang, S., Bader, A.G., and Vogt, P.K. (2005). Phosphatidylinositol 3-kinase mutations identified in human cancer are oncogenic. Proceedings of the National Academy of Sciences of the United States of America *102*, 802-807.
116. Katyal, S., el-Khamisy, S.F., Russell, H.R., Li, Y., Ju, L., Caldecott, K.W., and McKinnon, P.J. (2007). TDP1 facilitates chromosomal single-strand break repair in neurons and is neuroprotective in vivo. EMBO J *26*, 4720-4731.
117. Kazak, L., Reyes, A., He, J., Wood, S.R., Brea-Calvo, G., Holen, T.T., and Holt, I.J. (2013). A cryptic targeting signal creates a mitochondrial FEN1 isoform with tailed R-Loop binding properties. PloS one *8*, e62340.
118. Kim, M.Y., Mauro, S., Gevry, N., Lis, J.T., and Kraus, W.L. (2004). NAD+-dependent modulation of chromatin structure and transcription by nucleosome binding properties of PARP-1. Cell *119*, 803-814.
119. Koene, S., and Smeitink, J. (2011). Mitochondrial Medicine: a clinical guideline, 1st edn (Nijmegen, Netherlands: Khondrion).
120. Kolb, E.A., Gorlick, R., Houghton, P.J., Morton, C.L., Lock, R., Carol, H., Reynolds, C.P., Maris, J.M., Keir, S.T., Billups, C.A.*, et al.* (2008). Initial testing (stage 1) of a monoclonal antibody (SCH 717454) against the IGF-1 receptor by the pediatric preclinical testing program. Pediatr Blood Cancer *50*, 1190-1197.

121. Kolch, W., Halasz, M., Granovskaya, M., and Kholodenko, B.N. (2015). The dynamic control of signal transduction networks in cancer cells. Nature reviews Cancer *15*, 515-527.
122. Koopman, M., Antonini, N.F., Douma, J., Wals, J., Honkoop, A.H., Erdkamp, F.L., de Jong, R.S., Rodenburg, C.J., Vreugdenhil, G., Loosveld, O.J.*, et al.* (2007). Sequential versus combination chemotherapy with capecitabine, irinotecan, and oxaliplatin in advanced colorectal cancer (CAIRO): a phase III randomised controlled trial. Lancet *370*, 135-142.
123. Kovtun, I.V., Liu, Y., Bjoras, M., Klungland, A., Wilson, S.H., and McMurray, C.T. (2007). OGG1 initiates age-dependent CAG trinucleotide expansion in somatic cells. Nature *447*, 447-452.
124. Kraemer, K.H., Lee, M.M., and Scotto, J. (1987). Xeroderma pigmentosum. Cutaneous, ocular, and neurologic abnormalities in 830 published cases. Archives of dermatology *123*, 241-250.
125. Krishnakumar, R., and Kraus, W.L. (2010). The PARP side of the nucleus: molecular actions, physiological outcomes, and clinical targets. Molecular cell *39*, 8-24.
126. Krishnan, K.J., Reeve, A.K., Samuels, D.C., Chinnery, P.F., Blackwood, J.K., Taylor, R.W., Wanrooij, S., Spelbrink, J.N., Lightowlers, R.N., and Turnbull, D.M. (2008). What causes mitochondrial DNA deletions in human cells? Nature genetics *40*, 275-279.
127. Kruman, II, Wersto, R.P., Cardozo-Pelaez, F., Smilenov, L., Chan, S.L., Chrest, F.J., Emokpae, R., Jr., Gorospe, M., and Mattson, M.P. (2004). Cell cycle activation linked to neuronal cell death initiated by DNA damage. Neuron *41*, 549-561.
128. Lakshmipathy, U., and Campbell, C. (1999). Double strand break rejoining by mammalian mitochondrial extracts. Nucleic acids research *27*, 1198-1204.
129. Larsen, N.B., Rasmussen, M., and Rasmussen, L.J. (2005). Nuclear and mitochondrial DNA repair: similar pathways? Mitochondrion *5*, 89-108.
130. Lebedeva, N.A., Rechkunova, N.I., Ishchenko, A.A., Saparbaev, M., and Lavrik, O.I. (2013). The mechanism of human tyrosyl-DNA phosphodiesterase 1 in the cleavage of AP site and its synthetic analogs. DNA repair *12*, 1037-1042.
131. Lebedeva, N.A., Rechkunova, N.I., and Lavrik, O.I. (2011). AP-site cleavage activity of tyrosyl-DNA phosphodiesterase 1. FEBS letters *585*, 683-686.
132. Lee, C., Raffaghello, L., Brandhorst, S., Safdie, F.M., Bianchi, G., Martin-Montalvo, A., Pistoia, V., Wei, M., Hwang, S., Merlino, A.*, et al.* (2012a). Fasting cycles retard growth of tumors and sensitize a range of cancer cell types to chemotherapy. Science translational medicine *4*, 124ra127.
133. Lee, M.J., Ye, A.S., Gardino, A.K., Heijink, A.M., Sorger, P.K., MacBeath, G., and Yaffe, M.B. (2012b). Sequential application of anticancer drugs enhances cell death by rewiring apoptotic signaling networks. Cell *149*, 780-794.
134. Lee, S.Y., Kim, H., Hwang, H.J., Jeong, Y.M., Na, S.H., Woo, J.C., and Kim, S.G. (2010). Identification of tyrosyl-DNA phosphodiesterase as a novel DNA damage repair enzyme in Arabidopsis. Plant physiology *154*, 1460-1469.
135. Lehmann, A.R. (2003). DNA repair-deficient diseases, xeroderma pigmentosum, Cockayne syndrome and trichothiodystrophy. Biochimie *85*, 1101-1111.
136. Lennicke, C., Rahn, J., Lichtenfels, R., Wessjohann, L.A., and Seliger, B. (2015). Hydrogen peroxide - production, fate and role in redox signaling of tumor cells. Cell communication and signaling : CCS *13*, 39.

137. Li, F., Wang, Y., Zeller, K.I., Potter, J.J., Wonsey, D.R., O'Donnell, K.A., Kim, J.W., Yustein, J.T., Lee, L.A., and Dang, C.V. (2005). Myc stimulates nuclearly encoded mitochondrial genes and mitochondrial biogenesis. Molecular and cellular biology *25*, 6225-6234.
138. Li, M., and Yu, X. (2013). Function of BRCA1 in the DNA damage response is mediated by ADP-ribosylation. Cancer cell *23*, 693-704.
139. Li, N., Ragheb, K., Lawler, G., Sturgis, J., Rajwa, B., Melendez, J.A., and Robinson, J.P. (2003). Mitochondrial complex I inhibitor rotenone induces apoptosis through enhancing mitochondrial reactive oxygen species production. The Journal of biological chemistry *278*, 8516-8525.
140. Liao, Z., Thibaut, L., Jobson, A., and Pommier, Y. (2006). Inhibition of human tyrosyl-DNA phosphodiesterase by aminoglycoside antibiotics and ribosome inhibitors. Mol Pharmacol *70*, 366-372.
141. Liu, C., Pouliot, J.J., and Nash, H.A. (2002). Repair of topoisomerase I covalent complexes in the absence of the tyrosyl-DNA phosphodiesterase Tdp1. Proceedings of the National Academy of Sciences of the United States of America *99*, 14970-14975.
142. Liu, C., Zhou, S., Begum, S., Sidransky, D., Westra, W.H., Brock, M., and Califano, J.A. (2007). Increased expression and activity of repair genes TDP1 and XPF in non-small cell lung cancer. Lung cancer *55*, 303-311.
143. Lobsiger, C.S., and Cleveland, D.W. (2007). Glial cells as intrinsic components of non-cell-autonomous neurodegenerative disease. Nature neuroscience *10*, 1355-1360.
144. Lopez, J., and Tait, S.W. (2015). Mitochondrial apoptosis: killing cancer using the enemy within. British journal of cancer *112*, 957-962.
145. Lowe, S.W., and Lin, A.W. (2000). Apoptosis in cancer. Carcinogenesis *21*, 485-495.
146. Luo, X., and Kraus, W.L. (2012). On PAR with PARP: cellular stress signaling through poly(ADP-ribose) and PARP-1. Genes & development *26*, 417-432.
147. Macovei, A., Balestrazzi, A., Confalonieri, M., and Carbonera, D. (2010). The tyrosyl-DNA phosphodiesterase gene family in Medicago truncatula Gaertn.: bioinformatic investigation and expression profiles in response to copper- and PEG-mediated stress. Planta *232*, 393-407.
148. Marchand, C., Lea, W.A., Jadhav, A., Dexheimer, T.S., Austin, C.P., Inglese, J., Pommier, Y., and Simeonov, A. (2009). Identification of phosphotyrosine mimetic inhibitors of human tyrosyl-DNA phosphodiesterase I by a novel AlphaScreen high-throughput assay. Molecular cancer therapeutics *8*, 240-248.
149. Marin-Valencia, I., Yang, C., Mashimo, T., Cho, S., Baek, H., Yang, X.L., Rajagopalan, K.N., Maddie, M., Vemireddy, V., Zhao, Z.*, et al.* (2012). Analysis of tumor metabolism reveals mitochondrial glucose oxidation in genetically diverse human glioblastomas in the mouse brain in vivo. Cell Metab *15*, 827-837.
150. Mascarenhas, L., Lyden, E.R., Breitfeld, P.P., Walterhouse, D.O., Donaldson, S.S., Paidas, C.N., Parham, D.M., Anderson, J.R., Meyer, W.H., and Hawkins, D.S. (2010). Randomized phase II window trial of two schedules of irinotecan with vincristine in patients with first relapse or progression of rhabdomyosarcoma: a report from the Children's Oncology Group. Journal of clinical oncology : official journal of the American Society of Clinical Oncology *28*, 4658-4663.
151. Mastrocola, A.S., Kim, S.H., Trinh, A.T., Rodenkirch, L.A., and Tibbetts, R.S. (2013). The RNA-binding protein fused in sarcoma (FUS) functions downstream of poly(ADP-

ribose) polymerase (PARP) in response to DNA damage. The Journal of biological chemistry *288*, 24731-24741.
152. Mathews, M.T., and Berk, B.C. (2008). PARP-1 inhibition prevents oxidative and nitrosative stress-induced endothelial cell death via transactivation of the VEGF receptor 2. Arteriosclerosis, thrombosis, and vascular biology *28*, 711-717.
153. Mecocci, P., MacGarvey, U., Kaufman, A.E., Koontz, D., Shoffner, J.M., Wallace, D.C., and Beal, M.F. (1993). Oxidative damage to mitochondrial DNA shows marked age-dependent increases in human brain. Annals of neurology *34*, 609-616.
154. Meisenberg, C., Gilbert, D.C., Chalmers, A., Haley, V., Gollins, S., Ward, S.E., and El-Khamisy, S.F. (2015). Clinical and cellular roles for TDP1 and TOP1 in modulating colorectal cancer response to irinotecan. Molecular cancer therapeutics *14*, 575-585.
155. Messina, A., Puccinelli, E., Gervasi, P.G., and Longo, V. (2012). Expression and inducibility of CYP1A1, 1A2, 1B1 by beta-naphthoflavone and CYP2B22, CYP3As by rifampicin in heart regions and coronary arteries of pig. Research in veterinary science.
156. Milne, G.W., Nicklaus, M.C., Driscoll, J.S., Wang, S., and Zaharevitz, D. (1994). National Cancer Institute Drug Information System 3D database. Journal of chemical information and computer sciences *34*, 1219-1224.
157. Moreira, P.I., Cardoso, S.M., Santos, M.S., and Oliveira, C.R. (2006). The key role of mitochondria in Alzheimer's disease. Journal of Alzheimer's disease : JAD *9*, 101-110.
158. Morita, M., Gravel, S.P., Hulea, L., Larsson, O., Pollak, M., St-Pierre, J., and Topisirovic, I. (2015). mTOR coordinates protein synthesis, mitochondrial activity and proliferation. Cell cycle *14*, 473-480.
159. Morton, S.W., Lee, M.J., Deng, Z.J., Dreaden, E.C., Siouve, E., Shopsowitz, K.E., Shah, N.J., Yaffe, M.B., and Hammond, P.T. (2014). A nanoparticle-based combination chemotherapy delivery system for enhanced tumor killing by dynamic rewiring of signaling pathways. Science signaling *7*, ra44.
160. Mosesso, P., Piane, M., Palitti, F., Pepe, G., Penna, S., and Chessa, L. (2005). The novel human gene aprataxin is directly involved in DNA single-strand-break repair. Cellular and molecular life sciences : CMLS *62*, 485-491.
161. Mosmann, T. (1983). Rapid colorimetric assay for cellular growth and survival: application to proliferation and cytotoxicity assays. Journal of immunological methods *65*, 55-63.
162. Murai, J., Huang, S.Y., Das, B.B., Dexheimer, T.S., Takeda, S., and Pommier, Y. (2012a). Tyrosyl-DNA phosphodiesterase 1 (TDP1) repairs DNA damage induced by topoisomerases I and II and base alkylation in vertebrate cells. The Journal of biological chemistry *287*, 12848-12857.
163. Murai, J., Huang, S.Y., Das, B.B., Renaud, A., Zhang, Y., Doroshow, J.H., Ji, J., Takeda, S., and Pommier, Y. (2012b). Trapping of PARP1 and PARP2 by Clinical PARP Inhibitors. Cancer research *72*, 5588-5599.
164. Murphy, M.P. (2009). How mitochondria produce reactive oxygen species. The Biochemical journal *417*, 1-13.
165. Nance, M.A., and Berry, S.A. (1992). Cockayne syndrome: review of 140 cases. American journal of medical genetics *42*, 68-84.
166. Negrini, S., Gorgoulis, V.G., and Halazonetis, T.D. (2010). Genomic instability--an evolving hallmark of cancer. Nature reviews Molecular cell biology *11*, 220-228.

167. Nguyen, T.X., Morrell, A., Conda-Sheridan, M., Marchand, C., Agama, K., Bermingham, A., Stephen, A.G., Chergui, A., Naumova, A., Fisher, R.*, et al.* (2012). Synthesis and biological evaluation of the first dual tyrosyl-DNA phosphodiesterase I (Tdp1)-topoisomerase I (Top1) inhibitors. Journal of medicinal chemistry *55*, 4457-4478.
168. Nicholls, D.G., Darley-Usmar, V.M., Wu, M., Jensen, P.B., Rogers, G.W., and Ferrick, D.A. (2010). Bioenergetic profile experiment using C2C12 myoblast cells. Journal of visualized experiments : JoVE.
169. Nitiss, K.C., Malik, M., He, X., White, S.W., and Nitiss, J.L. (2006). Tyrosyl-DNA phosphodiesterase (Tdp1) participates in the repair of Top2-mediated DNA damage. Proceedings of the National Academy of Sciences of the United States of America *103*, 8953-8958.
170. Nosho, K., Yamamoto, H., Mikami, M., Taniguchi, H., Takahashi, T., Adachi, Y., Imamura, A., Imai, K., and Shinomura, Y. (2006). Overexpression of poly(ADP-ribose) polymerase-1 (PARP-1) in the early stage of colorectal carcinogenesis. Eur J Cancer *42*, 2374-2381.
171. Nowell, P.C. (1976). The clonal evolution of tumor cell populations. Science *194*, 23-28.
172. O'Driscoll, M. (2012). Diseases associated with defective responses to DNA damage. Cold Spring Harbor perspectives in biology *4*.
173. Ogata, T., and Yamasaki, Y. (1997). Ultra-high-resolution scanning electron microscopy of mitochondria and sarcoplasmic reticulum arrangement in human red, white, and intermediate muscle fibers. Anat Rec *248*, 214-223.
174. Oh, E.Y., Christensen, S.M., Ghanta, S., Jeong, J.C., Bucur, O., Glass, B., Montaser-Kouhsari, L., Knoblauch, N.W., Bertos, N., Saleh, S.M.*, et al.* (2015). Extensive rewiring of epithelial-stromal co-expression networks in breast cancer. Genome biology *16*, 128.
175. Ohno, M., Sakumi, K., Fukumura, R., Furuichi, M., Iwasaki, Y., Hokama, M., Ikemura, T., Tsuzuki, T., Gondo, Y., and Nakabeppu, Y. (2014). 8-oxoguanine causes spontaneous de novo germline mutations in mice. Scientific reports *4*, 4689.
176. Omura, T. (1998). Mitochondria-targeting sequence, a multi-role sorting sequence recognized at all steps of protein import into mitochondria. Journal of biochemistry *123*, 1010-1016.
177. Owen, B.A., Yang, Z., Lai, M., Gajec, M., Badger, J.D., 2nd, Hayes, J.J., Edelmann, W., Kucherlapati, R., Wilson, T.M., and McMurray, C.T. (2005). (CAG)(n)-hairpin DNA binds to Msh2-Msh3 and changes properties of mismatch recognition. Nature structural & molecular biology *12*, 663-670.
178. Pappo, A.S., Lyden, E., Breitfeld, P., Donaldson, S.S., Wiener, E., Parham, D., Crews, K.R., Houghton, P., and Meyer, W.H. (2007). Two consecutive phase II window trials of irinotecan alone or in combination with vincristine for the treatment of metastatic rhabdomyosarcoma: the Children's Oncology Group. Journal of clinical oncology : official journal of the American Society of Clinical Oncology *25*, 362-369.
179. Pfanner, N. (2000). Protein sorting: recognizing mitochondrial presequences. Current biology : CB *10*, R412-415.
180. Pinilla-Ibarz, J., and Quintas-Cardama, A. (2009). New agents in the treatment of chronic myelogenous leukemia. J Natl Compr Canc Netw *7*, 1028-1037.
181. Plo, I., Liao, Z.Y., Barcelo, J.M., Kohlhagen, G., Caldecott, K.W., Weinfeld, M., and Pommier, Y. (2003). Association of XRCC1 and tyrosyl DNA phosphodiesterase (Tdp1) for the repair of topoisomerase I-mediated DNA lesions. DNA repair *2*, 1087-1100.

182. Pommier, Y., Huang, S.Y., Gao, R., Das, B.B., Murai, J., and Marchand, C. (2014). Tyrosyl-DNA-phosphodiesterases (TDP1 and TDP2). DNA repair *19*, 114-129.
183. Pommier, Y., Pourquier, P., Fan, Y., and Strumberg, D. (1998). Mechanism of action of eukaryotic DNA topoisomerase I and drugs targeted to the enzyme. Biochimica et biophysica acta *1400*, 83-105.
184. Pommier, Y., Redon, C., Rao, V.A., Seiler, J.A., Sordet, O., Takemura, H., Antony, S., Meng, L., Liao, Z., Kohlhagen, G.*, et al.* (2003). Repair of and checkpoint response to topoisomerase I-mediated DNA damage. Mutation research *532*, 173-203.
185. Pouliot, J.J., Yao, K.C., Robertson, C.A., and Nash, H.A. (1999). Yeast gene for a Tyr-DNA phosphodiesterase that repairs topoisomerase I complexes. Science *286*, 552-555.
186. Pourquier, P., and Pommier, Y. (2001). Topoisomerase I-mediated DNA damage. Advances in cancer research *80*, 189-216.
187. Qiu, M., Chen, L., Tan, G., Ke, L., Zhang, S., Chen, H., and Liu, J. (2015). A reactive oxygen species activation mechanism contributes to JS-K-induced apoptosis in human bladder cancer cells. Scientific reports *5*, 15104.
188. Rada, P., Makki, A.R., Zimorski, V., Garg, S., Hampl, V., Hrdy, I., Gould, S.B., and Tachezy, J. (2015). N-Terminal Presequence-Independent Import of Phosphofructokinase into Hydrogenosomes of Trichomonas vaginalis. Eukaryotic cell *14*, 1264-1275.
189. Rando, T.A., and Blau, H.M. (1994). Primary mouse myoblast purification, characterization, and transplantation for cell-mediated gene therapy. The Journal of cell biology *125*, 1275-1287.
190. Ray Chaudhuri, A., Hashimoto, Y., Herrador, R., Neelsen, K.J., Fachinetti, D., Bermejo, R., Cocito, A., Costanzo, V., and Lopes, M. (2012). Topoisomerase I poisoning results in PARP-mediated replication fork reversal. Nature structural & molecular biology *19*, 417-423.
191. Rebrin, I., Kamzalov, S., and Sohal, R.S. (2003). Effects of age and caloric restriction on glutathione redox state in mice. Free Radic Biol Med *35*, 626-635.
192. Reja, R., Venkatakrishnan, A.J., Lee, J., Kim, B.C., Ryu, J.W., Gong, S., Bhak, J., and Park, D. (2009). MitoInteractome: mitochondrial protein interactome database, and its application in 'aging network' analysis. BMC genomics *10 Suppl 3*, S20.
193. Rieder, S.E., and Emr, S.D. (2001). Overview of subcellular fractionation procedures for the yeast Saccharomyces cerevisiae. Current protocols in cell biology *Chapter 3*, Unit 3 7.
194. Rodriguez-Vargas, J.M., Ruiz-Magana, M.J., Ruiz-Ruiz, C., Majuelos-Melguizo, J., Peralta-Leal, A., Rodriguez, M.I., Munoz-Gamez, J.A., de Almodovar, M.R., Siles, E., Rivas, A.L.*, et al.* (2012). ROS-induced DNA damage and PARP-1 are required for optimal induction of starvation-induced autophagy. Cell research *22*, 1181-1198.
195. Rothfuss, O., Gasser, T., and Patenge, N. (2010). Analysis of differential DNA damage in the mitochondrial genome employing a semi-long run real-time PCR approach. Nucleic acids research *38*, e24.
196. Rottenberg, S., Jaspers, J.E., Kersbergen, A., van der Burg, E., Nygren, A.O., Zander, S.A., Derksen, P.W., de Bruin, M., Zevenhoven, J., Lau, A.*, et al.* (2008). High sensitivity of BRCA1-deficient mammary tumors to the PARP inhibitor AZD2281 alone and in combination with platinum drugs. Proceedings of the National Academy of Sciences of the United States of America *105*, 17079-17084.

197. Sahin, E., and Depinho, R.A. (2010). Linking functional decline of telomeres, mitochondria and stem cells during ageing. Nature *464*, 520-528.
198. Salk, J.J., Fox, E.J., and Loeb, L.A. (2010). Mutational heterogeneity in human cancers: origin and consequences. Annual review of pathology *5*, 51-75.
199. Schneider, H., Arretz, M., Wachter, E., and Neupert, W. (1990). Matrix processing peptidase of mitochondria. Structure-function relationships. The Journal of biological chemistry *265*, 9881-9887.
200. Schultz, N., Lopez, E., Saleh-Gohari, N., and Helleday, T. (2003). Poly(ADP-ribose) polymerase (PARP-1) has a controlling role in homologous recombination. Nucleic acids research *31*, 4959-4964.
201. Shoffner, J.M., Lott, M.T., Lezza, A.M., Seibel, P., Ballinger, S.W., and Wallace, D.C. (1990). Myoclonic epilepsy and ragged-red fiber disease (MERRF) is associated with a mitochondrial DNA tRNA(Lys) mutation. Cell *61*, 931-937.
202. Shoffner, J.M., Lott, M.T., Voljavec, A.S., Soueidan, S.A., Costigan, D.A., and Wallace, D.C. (1989). Spontaneous Kearns-Sayre/chronic external ophthalmoplegia plus syndrome associated with a mitochondrial DNA deletion: a slip-replication model and metabolic therapy. Proceedings of the National Academy of Sciences of the United States of America *86*, 7952-7956.
203. Shokolenko, I., Venediktova, N., Bochkareva, A., Wilson, G.L., and Alexeyev, M.F. (2009). Oxidative stress induces degradation of mitochondrial DNA. Nucleic acids research *37*, 2539-2548.
204. Siggens, L., Figg, N., Bennett, M., and Foo, R. (2012). Nutrient deprivation regulates DNA damage repair in cardiomyocytes via loss of the base-excision repair enzyme OGG1. FASEB journal : official publication of the Federation of American Societies for Experimental Biology *26*, 2117-2124.
205. Silhavy, T.J., Benson, S.A., and Emr, S.D. (1983). Mechanisms of protein localization. Microbiological reviews *47*, 313-344.
206. Simon, H.U., Haj-Yehia, A., and Levi-Schaffer, F. (2000). Role of reactive oxygen species (ROS) in apoptosis induction. Apoptosis : an international journal on programmed cell death *5*, 415-418.
207. Smith, D.A., Morgan, B.A., and Quinn, J. (2010). Stress signalling to fungal stress-activated protein kinase pathways. FEMS microbiology letters *306*, 1-8.
208. Spadafora, D., Kozhukhar, N., and Alexeyev, M.F. (2016). Presequence-Independent Mitochondrial Import of DNA Ligase Facilitates Establishment of Cell Lines with Reduced mtDNA Copy Number. PloS one *11*, e0152705.
209. Srivas, R., Shen, J.P., Yang, C.C., Sun, S.M., Li, J., Gross, A.M., Jensen, J., Licon, K., Bojorquez-Gomez, A., Klepper, K.*, et al.* (2016). A Network of Conserved Synthetic Lethal Interactions for Exploration of Precision Cancer Therapy. Molecular cell *63*, 514-525.
210. Stanulla, M., and Schrappe, M. (2009). Treatment of childhood acute lymphoblastic leukemia. Semin Hematol *46*, 52-63.
211. Stegmeier, F., Warmuth, M., Sellers, W.R., and Dorsch, M. (2010). Targeted cancer therapies in the twenty-first century: lessons from imatinib. Clin Pharmacol Ther *87*, 543-552.
212. Stojanovski, D., Bohnert, M., Pfanner, N., and van der Laan, M. (2012). Mechanisms of protein sorting in mitochondria. Cold Spring Harbor perspectives in biology *4*.

213. Stuart, J.A., Hashiguchi, K., Wilson, D.M., 3rd, Copeland, W.C., Souza-Pinto, N.C., and Bohr, V.A. (2004). DNA base excision repair activities and pathway function in mitochondrial and cellular lysates from cells lacking mitochondrial DNA. Nucleic acids research *32*, 2181-2192.
214. Sugimura, K., Takebayashi, S., Taguchi, H., Takeda, S., and Okumura, K. (2008). PARP-1 ensures regulation of replication fork progression by homologous recombination on damaged DNA. The Journal of cell biology *183*, 1203-1212.
215. Taanman, J.W. (1999). The mitochondrial genome: structure, transcription, translation and replication. Biochimica et biophysica acta *1410*, 103-123.
216. Tadi, S.K., Sebastian, R., Dahal, S., Babu, R.K., Choudhary, B., and Raghavan, S.C. (2016). Microhomology-mediated end joining is the principal mediator of double-strand break repair during mitochondrial DNA lesions. Molecular biology of the cell *27*, 223-235.
217. Takashima, H., Boerkoel, C.F., John, J., Saifi, G.M., Salih, M.A., Armstrong, D., Mao, Y., Quiocho, F.A., Roa, B.B., Nakagawa, M.*, et al.* (2002). Mutation of TDP1, encoding a topoisomerase I-dependent DNA damage repair enzyme, in spinocerebellar ataxia with axonal neuropathy. Nature genetics *32*, 267-272.
218. Tanhauser, S.M., and Laipis, P.J. (1995). Multiple deletions are detectable in mitochondrial DNA of aging mice. The Journal of biological chemistry *270*, 24769-24775.
219. Thorburn, D.R., Chow, C.W., and Kirby, D.M. (2004). Respiratory chain enzyme analysis in muscle and liver. Mitochondrion *4*, 363-375.
220. Totrov, M., and Abagyan, R. (1997). Flexible protein-ligand docking by global energy optimization in internal coordinates. Proteins *Suppl 1*, 215-220.
221. Tsao, Y.P., Russo, A., Nyamuswa, G., Silber, R., and Liu, L.F. (1993). Interaction between replication forks and topoisomerase I-DNA cleavable complexes: studies in a cell-free SV40 DNA replication system. Cancer research *53*, 5908-5914.
222. Tutt, A., Robson, M., Garber, J.E., Domchek, S.M., Audeh, M.W., Weitzel, J.N., Friedlander, M., Arun, B., Loman, N., Schmutzler, R.K.*, et al.* (2010). Oral poly(ADP-ribose) polymerase inhibitor olaparib in patients with BRCA1 or BRCA2 mutations and advanced breast cancer: a proof-of-concept trial. Lancet *376*, 235-244.
223. Van Laethem, A., Van Kelst, S., Lippens, S., Declercq, W., Vandenabeele, P., Janssens, S., Vandenheede, J.R., Garmyn, M., and Agostinis, P. (2004). Activation of p38 MAPK is required for Bax translocation to mitochondria, cytochrome c release and apoptosis induced by UVB irradiation in human keratinocytes. FASEB journal : official publication of the Federation of American Societies for Experimental Biology *18*, 1946-1948.
224. Vance, J.R., and Wilson, T.E. (2002). Yeast Tdp1 and Rad1-Rad10 function as redundant pathways for repairing Top1 replicative damage. Proceedings of the National Academy of Sciences of the United States of America *99*, 13669-13674.
225. Vermulst, M., Bielas, J.H., and Loeb, L.A. (2008). Quantification of random mutations in the mitochondrial genome. Methods *46*, 263-268.
226. Walker, S., Meisenberg, C., Bibby, R.A., Askwith, T., Williams, G., Rininsland, F.H., Pearl, L.H., Oliver, A.W., El-Khamisy, S., Ward, S.*, et al.* (2014). Development of an oligonucleotide-based fluorescence assay for the identification of tyrosyl-DNA phosphodiesterase 1 (TDP1) inhibitors. Analytical biochemistry *454*, 17-22.

227. Wallace, D.C. (2005). A mitochondrial paradigm of metabolic and degenerative diseases, aging, and cancer: a dawn for evolutionary medicine. Annual review of genetics *39*, 359-407.
228. Wallace, D.C., Singh, G., Lott, M.T., Hodge, J.A., Schurr, T.G., Lezza, A.M., Elsas, L.J., 2nd, and Nikoskelainen, E.K. (1988). Mitochondrial DNA mutation associated with Leber's hereditary optic neuropathy. Science *242*, 1427-1430.
229. Walterhouse, D.O., Lyden, E.R., Breitfeld, P.P., Qualman, S.J., Wharam, M.D., and Meyer, W.H. (2004). Efficacy of topotecan and cyclophosphamide given in a phase II window trial in children with newly diagnosed metastatic rhabdomyosarcoma: a Children's Oncology Group study. Journal of clinical oncology : official journal of the American Society of Clinical Oncology *22*, 1398-1403.
230. Walton C, Turashvili G, Hirano R, Aparicio S, Boerkoel CF. (2009). Defining the role of Tyrosl-DNA phosphodiesterrase (Tdp1) in human disease. Paper presented at: DNA repair and Mutagenesis: From molecular structure to human disease.
231. Walton, C., Turashvili, G., Hirano, R., Aparicio, S., and Boerkoel, C.F. (2009). Defining the role of Tyrosl-DNA phosphodiesterrase (Tdp1) in human disease. Paper presented at: DNA repair and Mutagenesis: From molecular structure to human disease.
232. Wang, N., Zhu, M., Tsao, S.W., Man, K., Zhang, Z., and Feng, Y. (2013). MiR-23a-mediated inhibition of topoisomerase 1 expression potentiates cell response to etoposide in human hepatocellular carcinoma. Molecular cancer *12*, 119.
233. Wei, Q., Frazier, M.L., and Levin, B. (2000). DNA repair: a double-edged sword. Journal of the National Cancer Institute *92*, 440-441.
234. Wei, Y.H. (1998). Oxidative stress and mitochondrial DNA mutations in human aging. Proceedings of the Society for Experimental Biology and Medicine Society for Experimental Biology and Medicine *217*, 53-63.
235. Wiedemann, N., Frazier, A.E., and Pfanner, N. (2004). The protein import machinery of mitochondria. The Journal of biological chemistry *279*, 14473-14476.
236. Wiedemann, N., Pfanner, N., and Chacinska, A. (2006). Chaperoning through the mitochondrial intermembrane space. Molecular cell *21*, 145-148.
237. Winzeler, E.A., Shoemaker, D.D., Astromoff, A., Liang, H., Anderson, K., Andre, B., Bangham, R., Benito, R., Boeke, J.D., Bussey, H.*, et al.* (1999). Functional characterization of the S. cerevisiae genome by gene deletion and parallel analysis. Science *285*, 901-906.
238. Wu, J., and Liu, L.F. (1997). Processing of topoisomerase I cleavable complexes into DNA damage by transcription. Nucleic acids research *25*, 4181-4186.
239. Yakes, F.M., and Van Houten, B. (1997). Mitochondrial DNA damage is more extensive and persists longer than nuclear DNA damage in human cells following oxidative stress. Proceedings of the National Academy of Sciences of the United States of America *94*, 514-519.
240. Zhan, S., Shapiro, D.N., and Helman, L.J. (1994). Activation of an imprinted allele of the insulin-like growth factor II gene implicated in rhabdomyosarcoma. J Clin Invest *94*, 445-448.
241. Zhang, H., Barcelo, J.M., Lee, B., Kohlhagen, G., Zimonjic, D.B., Popescu, N.C., and Pommier, Y. (2001). Human mitochondrial topoisomerase I. Proc Natl Acad Sci U S A *98*, 10608-10613.

242. Zhang, H.F., Tomida, A., Koshimizu, R., Ogiso, Y., Lei, S., and Tsuruo, T. (2004). Cullin 3 promotes proteasomal degradation of the topoisomerase I-DNA covalent complex. Cancer research *64*, 1114-1121.
243. Zhang, Y.W., Regairaz, M., Seiler, J.A., Agama, K.K., Doroshow, J.H., and Pommier, Y. (2011). Poly(ADP-ribose) polymerase and XPF-ERCC1 participate in distinct pathways for the repair of topoisomerase I-induced DNA damage in mammalian cells. Nucleic acids research.
244. Zhou, T., Akopiants, K., Mohapatra, S., Lin, P.S., Valerie, K., Ramsden, D.A., Lees-Miller, S.P., and Povirk, L.F. (2009). Tyrosyl-DNA phosphodiesterase and the repair of 3'-phosphoglycolate-terminated DNA double-strand breaks. DNA repair *8*, 901-911.
245. Zhou, W., Zhang, Y., Hosch, M.S., Lang, A., Zwacka, R.M., and Engelhardt, J.F. (2001). Subcellular site of superoxide dismutase expression differentially controls AP-1 activity and injury in mouse liver following ischemia/reperfusion. Hepatology *33*, 902-914.

Appendices

Appendix A: Supplementary Tables and Figures for Chapter 2

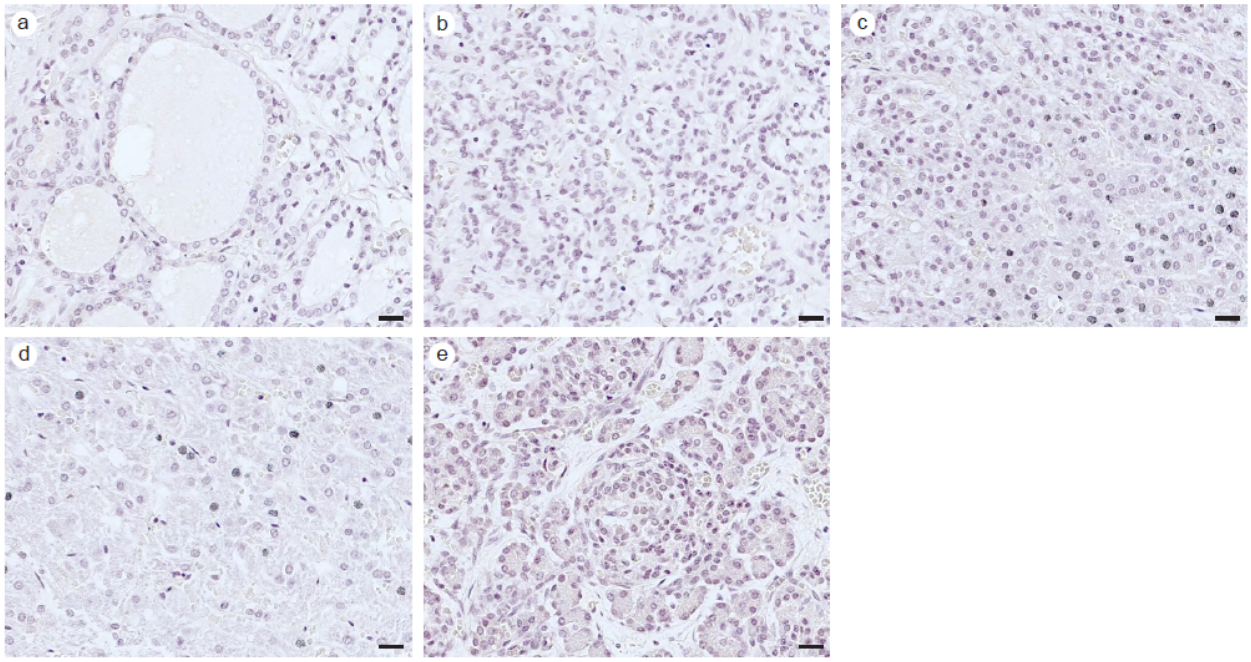

Figure A-1. Photomicrographs of pre-immune staining of Tdp1 in the endocrine system. Pre-immune serum was collected from the same antibody producing rabbit and was used as a negative control. No non-specific staining was detected in **a** thyroid **b** parathyroid **c** adrenal cortex and **d** pancreatic islets. Scale bars = 20 µm

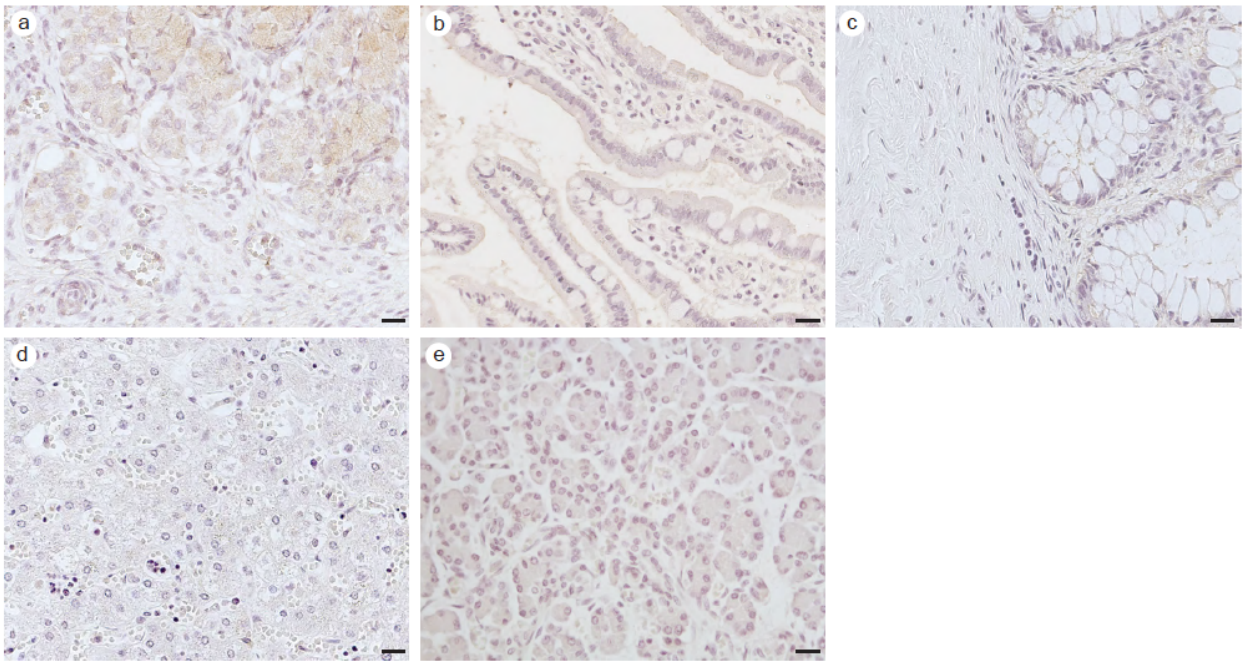

Figure A-2: Photomicrographs of pre-immune staining of Tdp1 in gastrointestinal system. No non-specific staining was detected in **a** stomach **b** small intestine **c** colon **d** liver **e** exocrine pancreas. Scale bars = 20 µm.

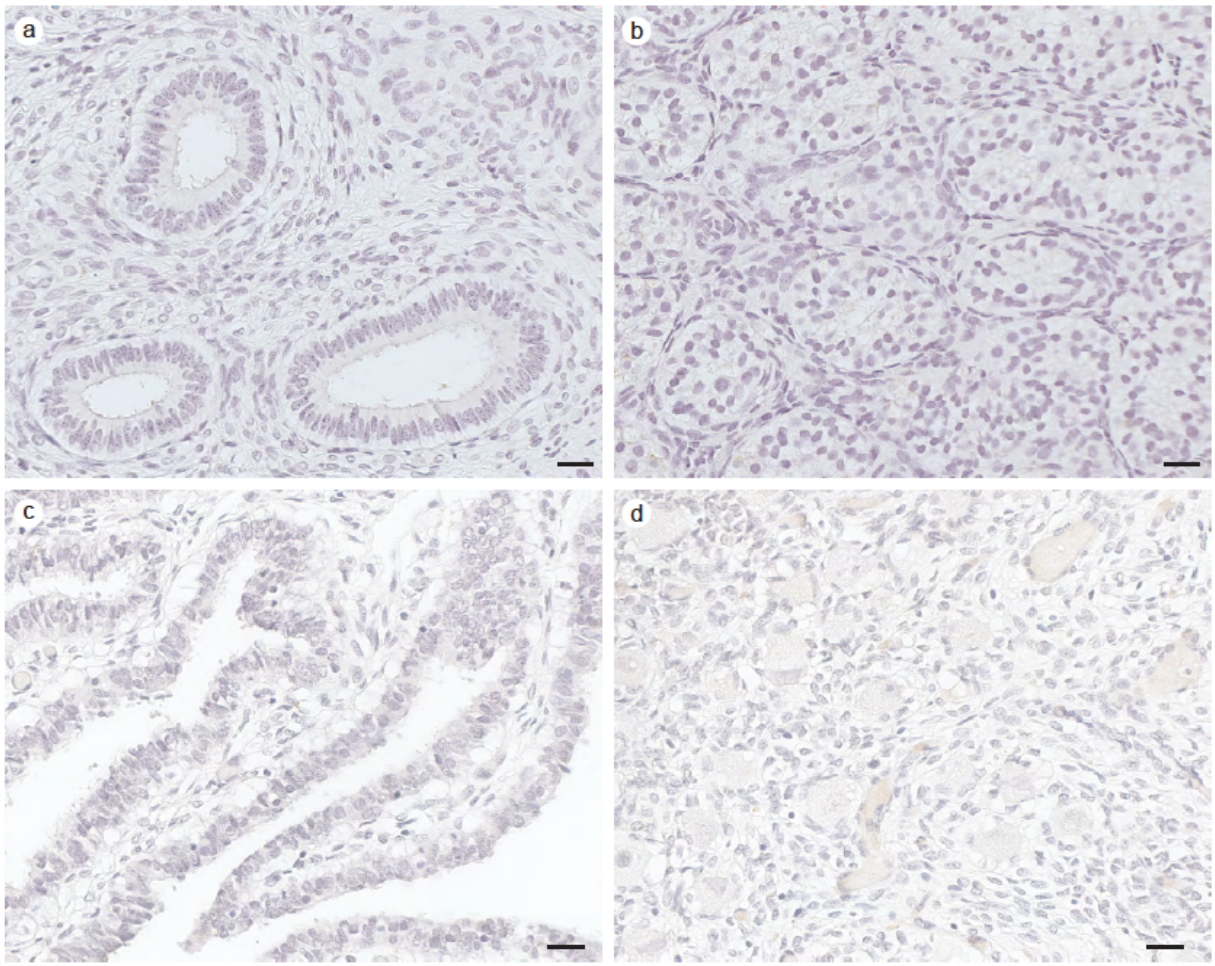

Figure A-3: Photomicrographs of pre-immune staining of Tdp1 in reproductive system. No non-specific staining was detected in **a** epididymis **b** seminiferous tubules **c** oviduct and **d** ovary. Scale bars = 20 μm.

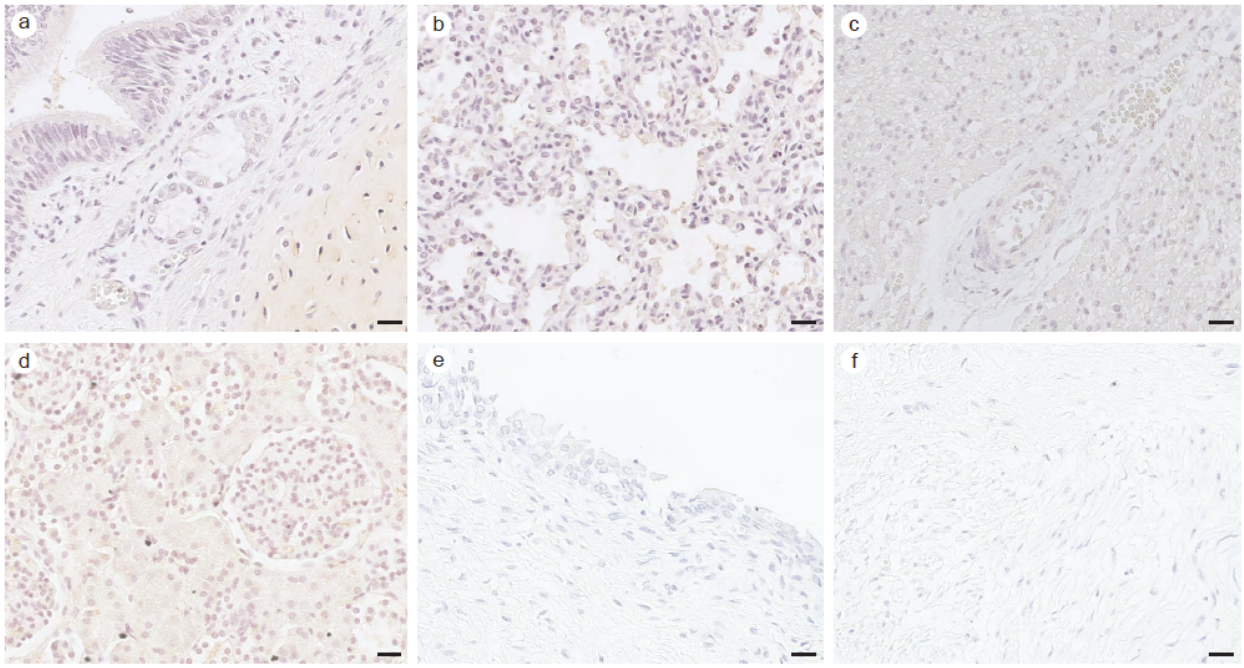

Figure A-4: Photomicrographs of pre-immune staining of Tdp1 in pulmonary, cardiovascular and urinary systems.. No non-specific staining was detected in **a** trachea **b** lung **c** heart **d** kidney **e** epithelium of urinary bladder and **f** muscularis of urinary bladder. Scale bars = 20 μm.

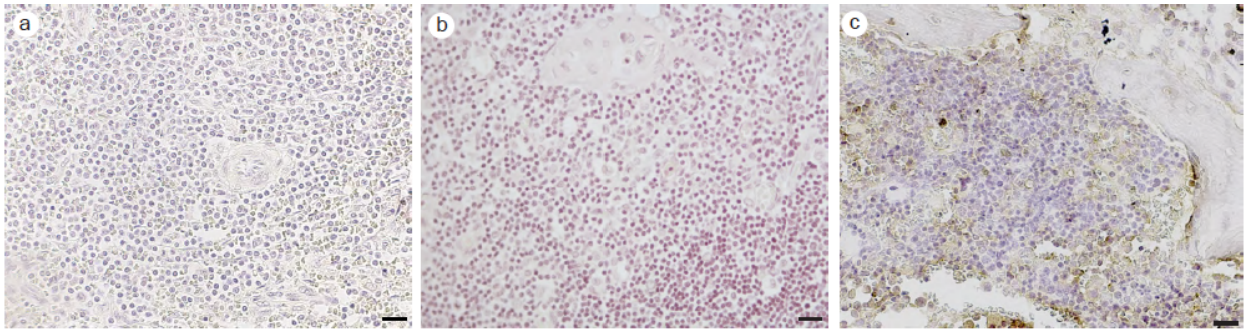

Figure A-5: Photomicrographs of pre-immune staining of Tdp1 in immune system and bone. No non-specific staining was detected in **a** spleen **b** thymus and **c** bone marrow. Scale bars = 20 μm.

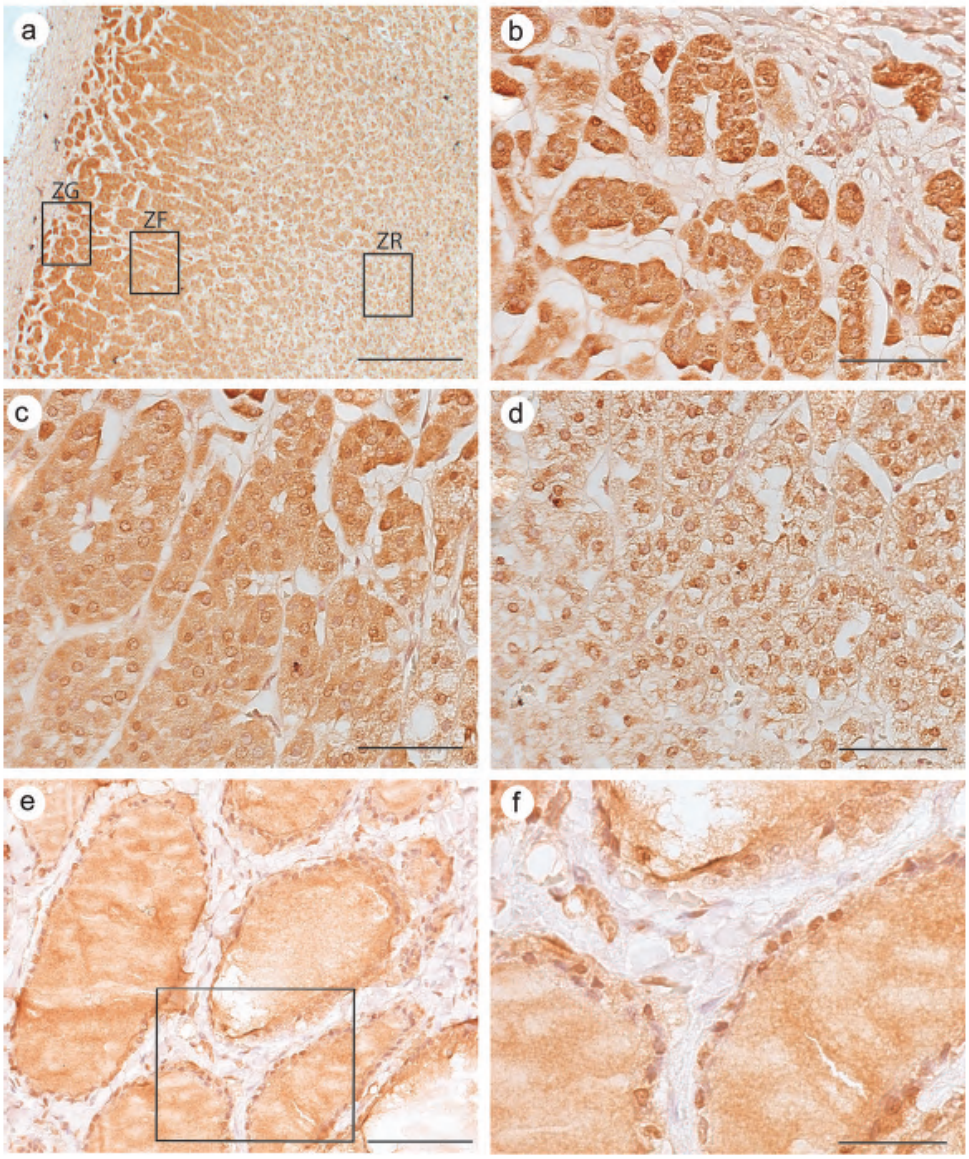

Figure A-6: Photomicrographs of immunohistochemical analysis of Tdp1 in the adolescent endocrine system. **a** overview of the adrenal gland **b** cells of the zona glomerulosa **c** zona fasciculata **d** zona reticularis. **e-f** thyroid. ZG = zona glomerulosa; ZF = zona fasciculata; ZR = zona reticularis; . Boxed regions correspond to higher magnification images. Scale bars: **a** = 2000 µm, **b**, **c**, **d**, **f** = 100µm, **e** = 250µm

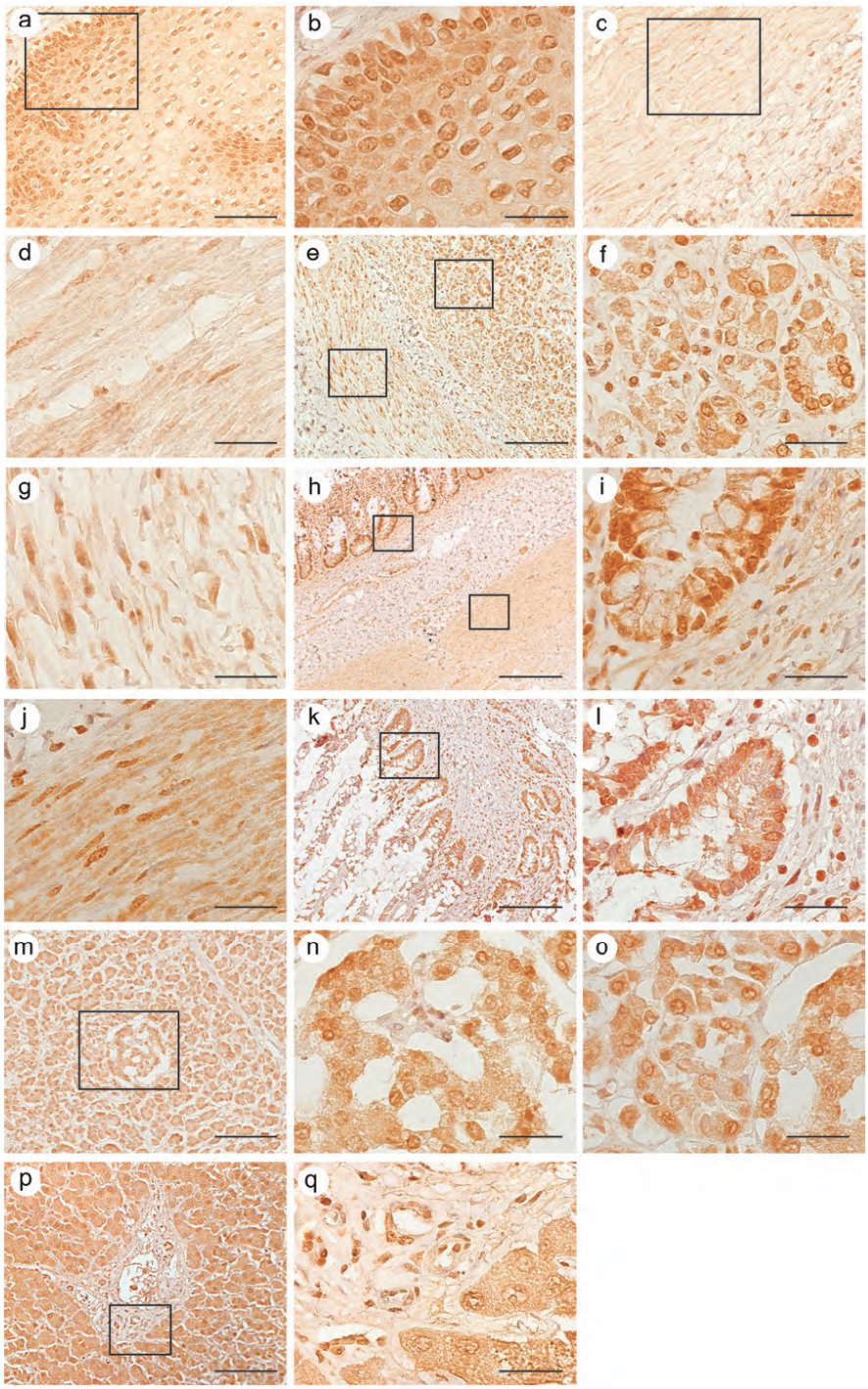

Figure A-7: Photomicrographs of immunohistochemical analysis of human Tdp1 expression in the adolescent gastrointestinal system. **a-b** esophagus – lamina propria **c-d** muscularis **e** stomach overview **f** stomach - gastric pit **g** stomach - muscularis **h** colon overview **i** colonic glands **j** colon – muscularis **k** small intestine overview **l** intestinal villi **m** pancreas overview **n** pancreatic islets **o** exocrine pancreas **p** liver overview **q** hepatic duct and hepatocytes. Boxed regions correspond to higher magnification images. Scale bars: **a,c** = 250 µm, **b, d, f, g, i, j, l, n, o, q** = 100 µm, **e, h** = 1000µm, **k, m, p** = 500 µm

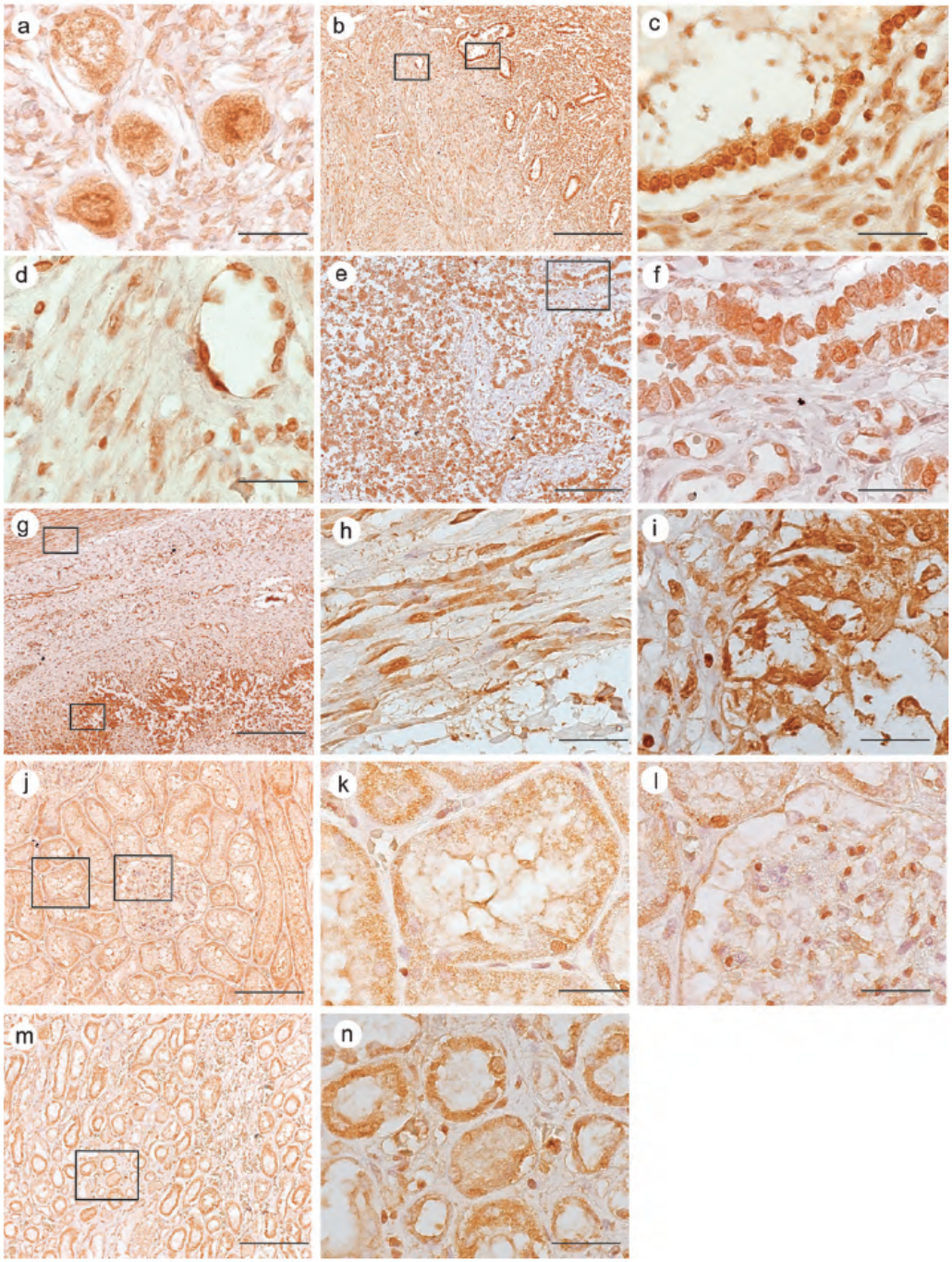

Figure A-8: Photomicrographs of immunohistochemical analysis of human Tdp1 expression in the adolescent genitourinary system. **a** primary oocytes **b** overview of uterus **c** uterine glands **d** endometrium **e** overview of fallopian tube **g** epithelium of fallopian tube **g** overview of urinary bladder **h** muscularis **i** urothelium **j** overview of kidney **k** proximal tubules **l** glomerulus **m-n** distal tubules, collecting ducts and loops of Henle. Boxed regions correspond to higher magnification images. Scale bars: **a, c, d, f, h, i, k, l, n** = 100 µm, **b, g** = 1000 µm, **e, j, m** = 500 µm

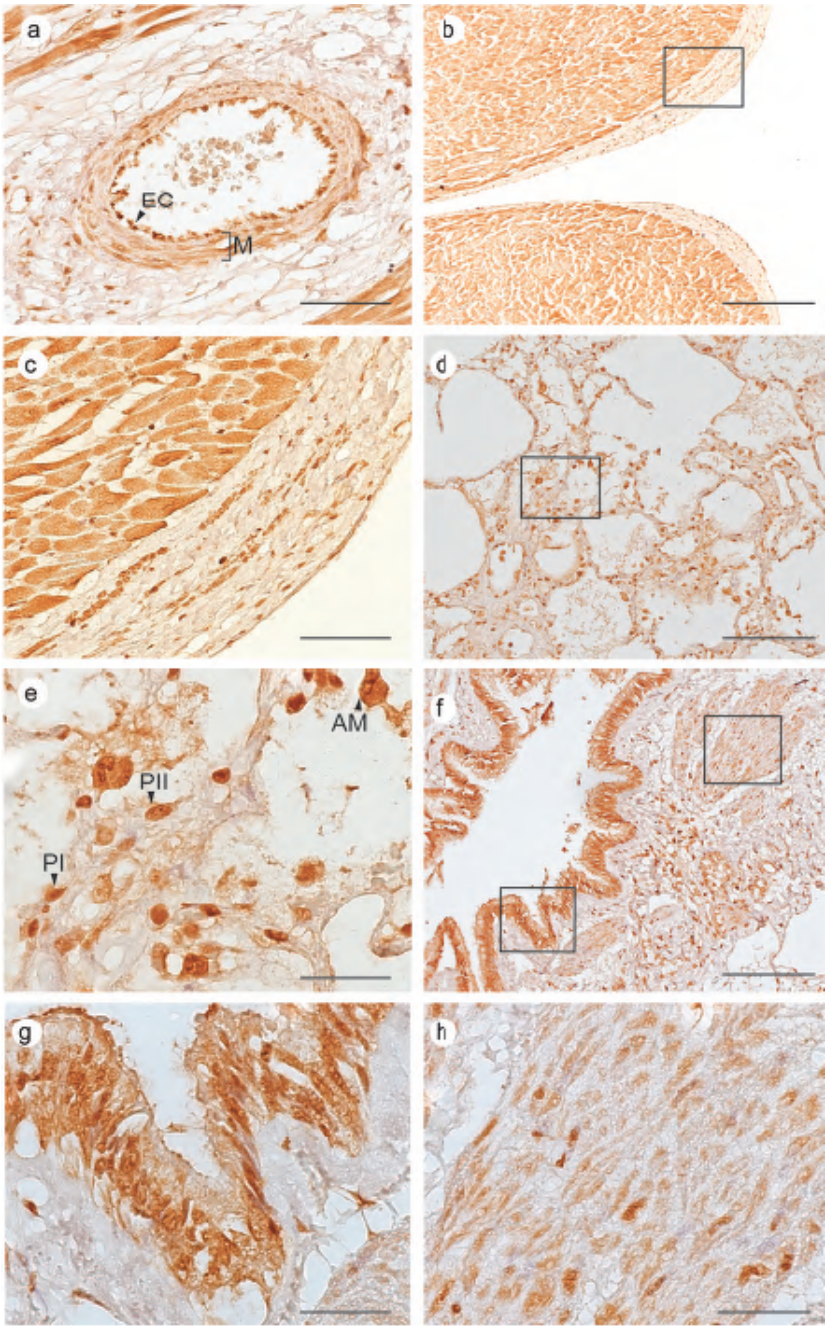

Figure A-9: Photomicrographs of immunohistochemical analysis of human Tdp1 expression in the adolescent cardiovascular and pulmonary system. **a** blood vessel **b-c** endocardium and myocardium **d-e** alveoli **f** overview of trachea and bronchi **g** luminal epithelium **h** bronchial muscularis. Boxed regions correspond to higher magnification images. Arrowheads indicate cells of interest. EC = endothelial cell, M = muscle cell, PI = type I pneumocyte, PII = type II pneumocyte, AM = alveolar macrophage Scale bars: **a** = 250 µm, **b** = 1000 µm, **c, e, g, h** = 100 µm, **d, f** = 500 µm

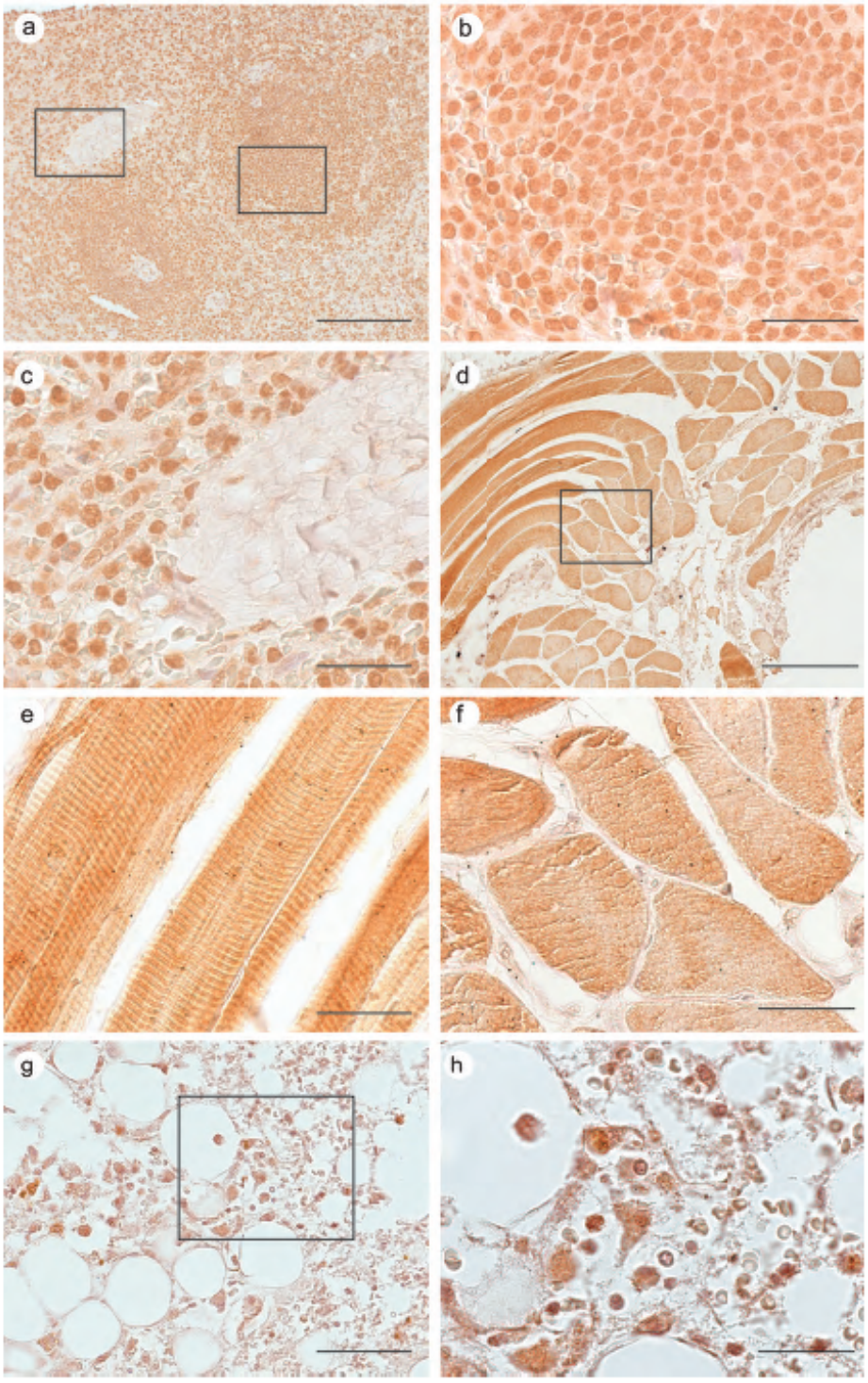

Figure A-10: Photomicrographs of immunohistochemical analysis of human Tdp1 expression in the adolescent immune system and musculoskeletal tissue. **a** overview of spleen **b** white pulp of spleen **c** red pulp of spleen **d-f** skeletal muscle **g-h** bone marrow. Boxed regions correspond to the higher magnification images. Scale bars: **a, d** = 500 µm, **b, c, e, f, h** = 100 µm, **g** = 250 µm

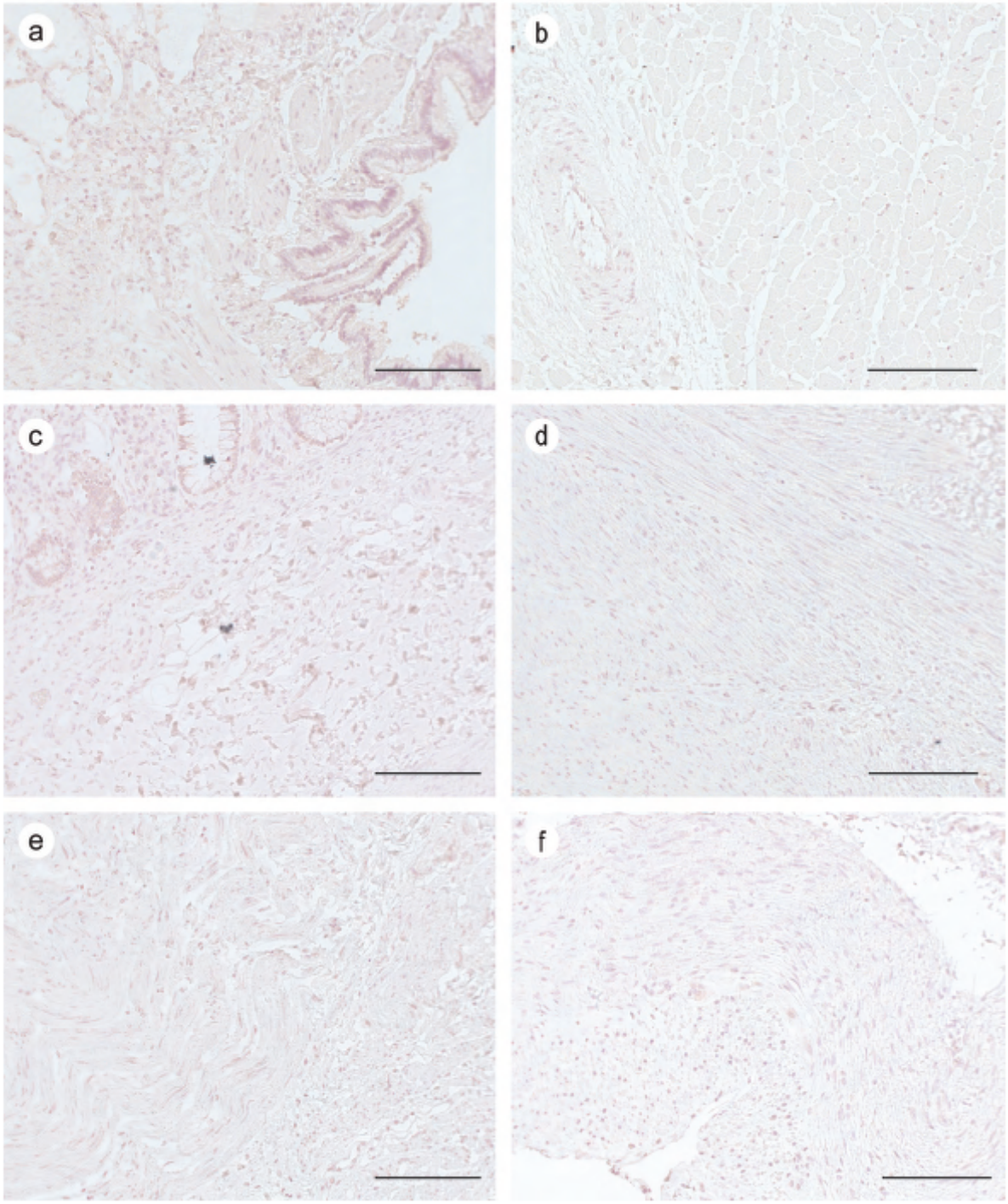

Figure A-11: Photomicrographs of pre-immune staining of Tdp1 in adolescent tissue: 1 of 3. Pre-immune serum was collected from the same antibody producing rabbit and was used as a negative control. **a** lung **b** myocardium and blood vessel **c** colon **d** stomach **e** esophagus **f** small bowel. Scale bars = 500 µm.

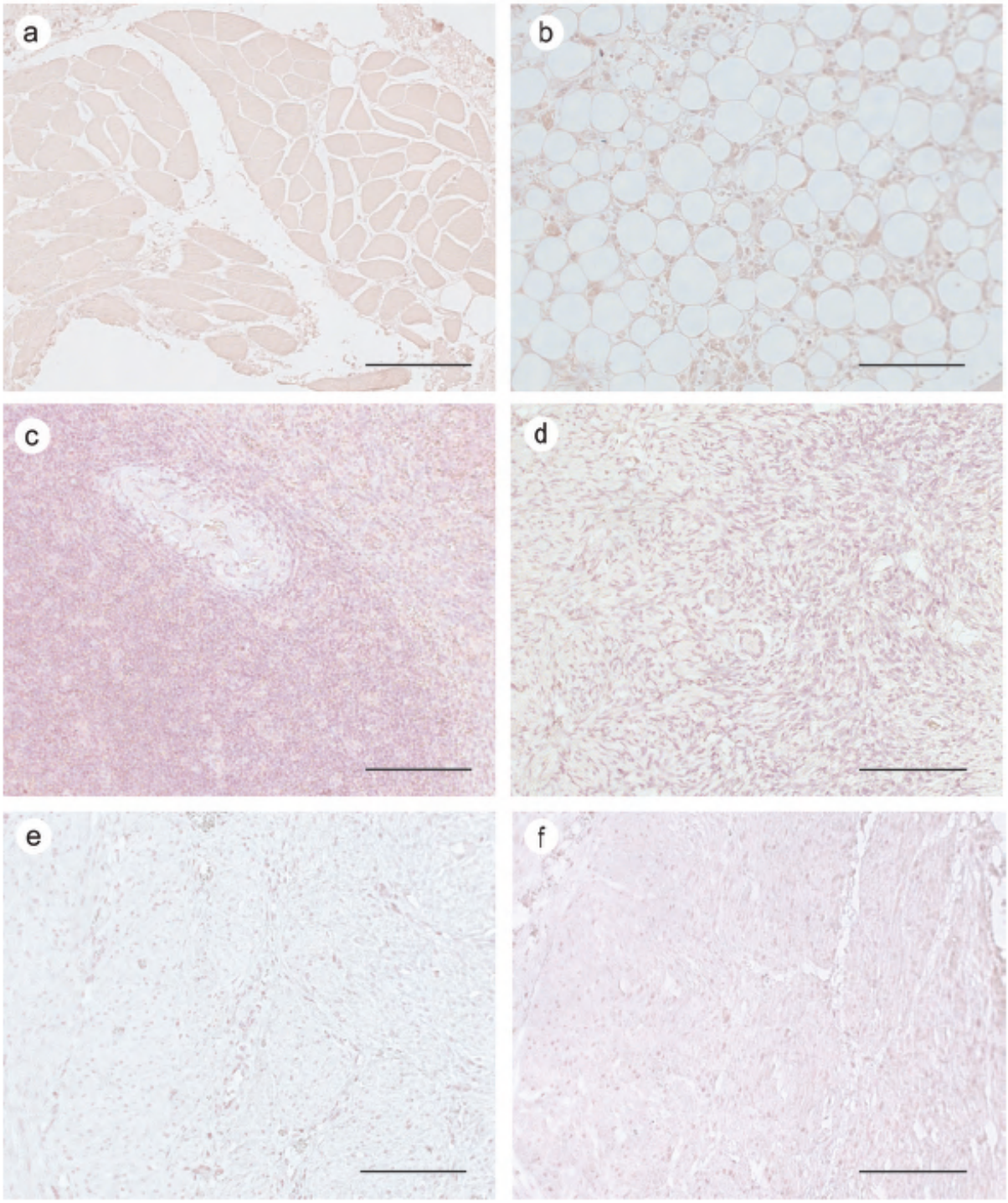

Figure A-12: Photomicrographs of pre-immune staining of Tdp1 in adolescent tissue: 2 of 3. Pre-immune serum was collected from the same antibody producing rabbit and was used as a negative control. **a** skeletal muscle **b** bone **c** spleen **d** ovary **e** uterus **f** urinary bladder. Scale bars = 500 μm

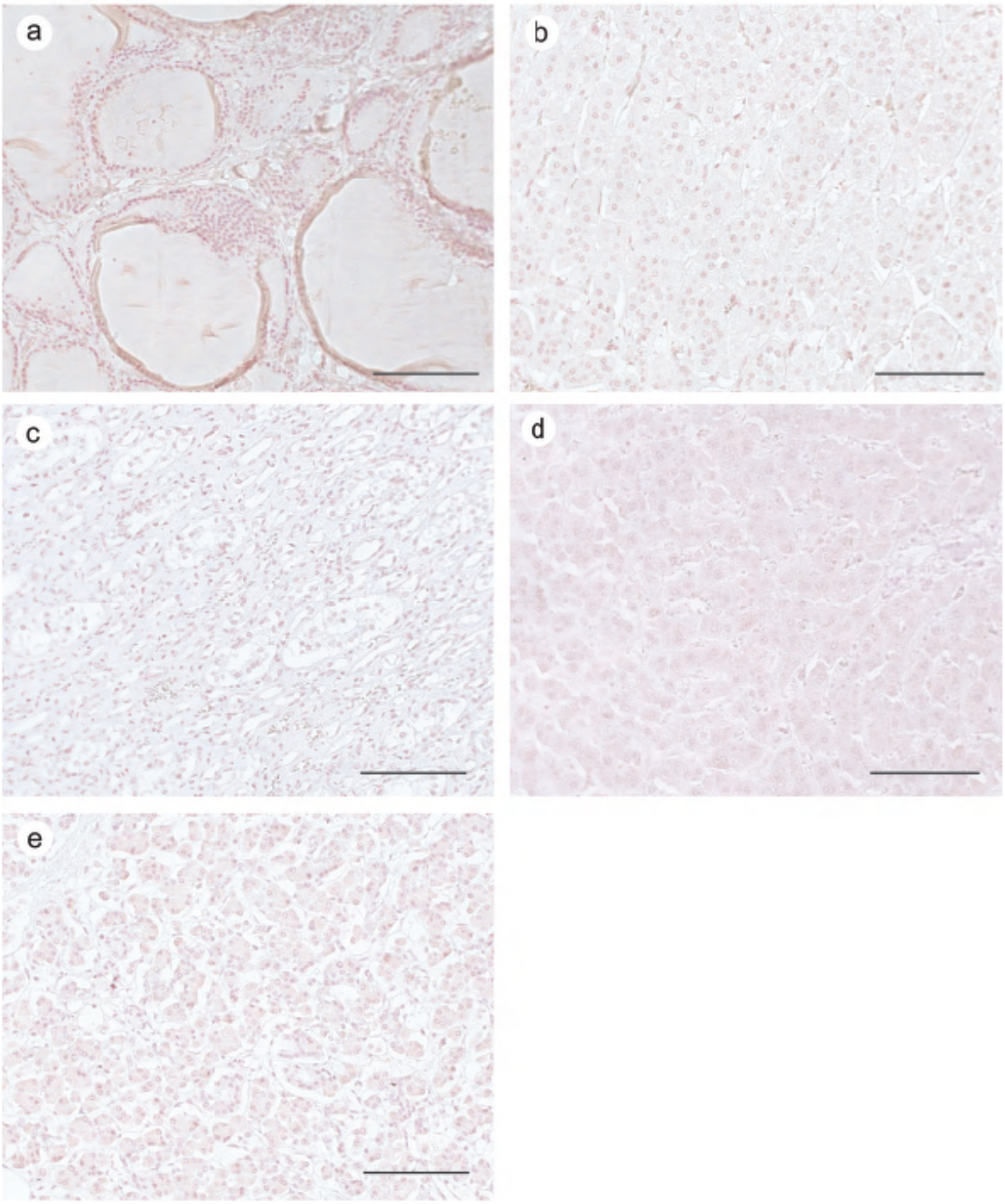

Figure A-13: Photomicrographs of pre-immune staining of Tdp1 in adolescent tissue: 3 of 3. **a** thyroid **b** adrenal gland **c** kidney **d** liver **e** pancreas. Pre-immune serum was collected from the same antibody producing rabbit and was used as a negative control. Scale bars = 500 μm.

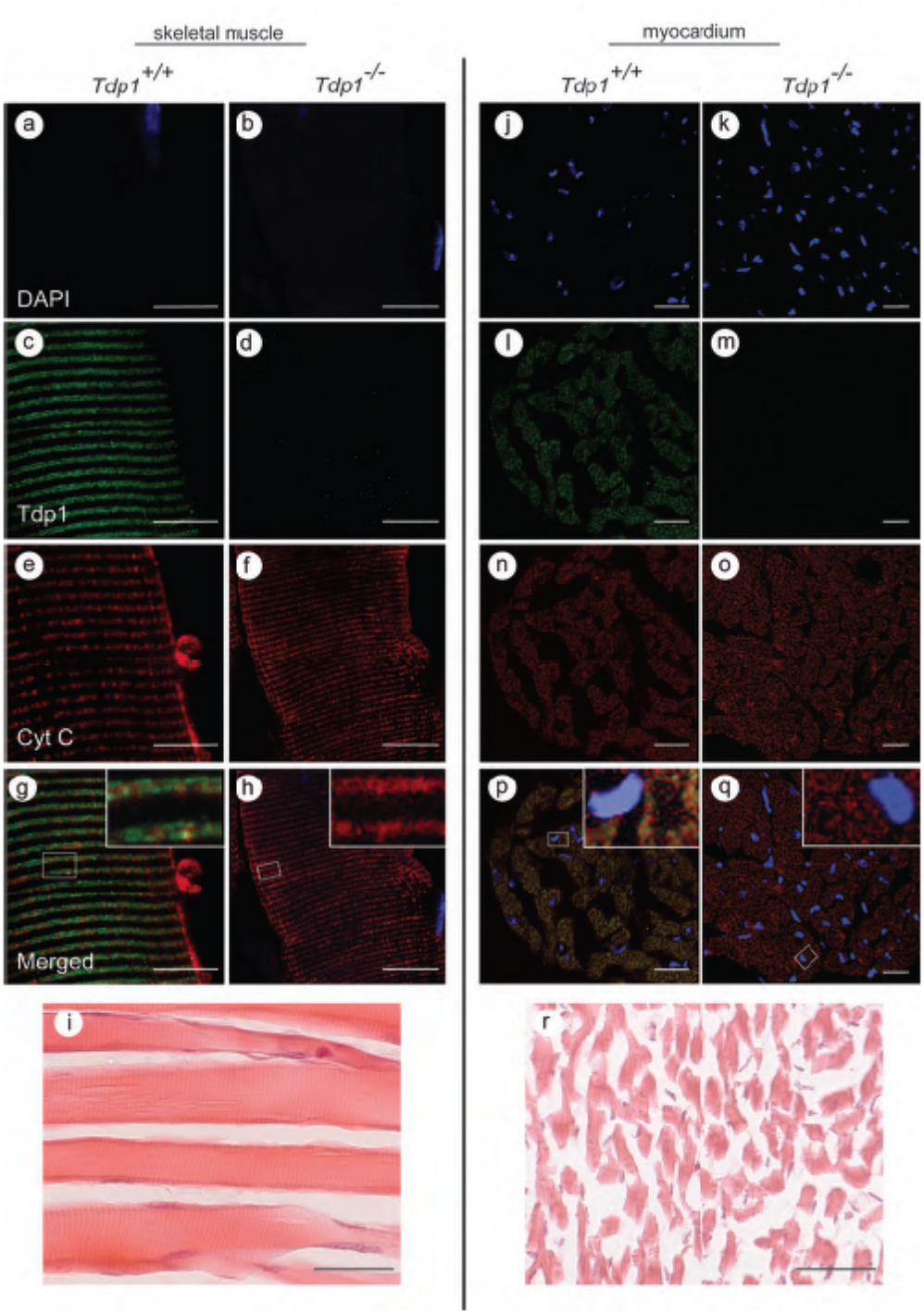

Figure A-14: Photomicrographs of immunofluorescent colocalization of human Tdp1 with the mitochondrial protein cytochrome C in mouse skeletal muscle and myocardium. **a-i** skeletal muscle **j-r** myocardium. Left panels show wild-type mouse tissue. Right panels show *Tdp1*$^{-/-}$ mouse tissue. The boxed regions correspond to higher magnification images. Scale bars for immunofluorescent images = 20 μm. Scale bar for H&E –skeletal muscle = 100 μm, scale bar for H&E – myocardium = 160 μm.

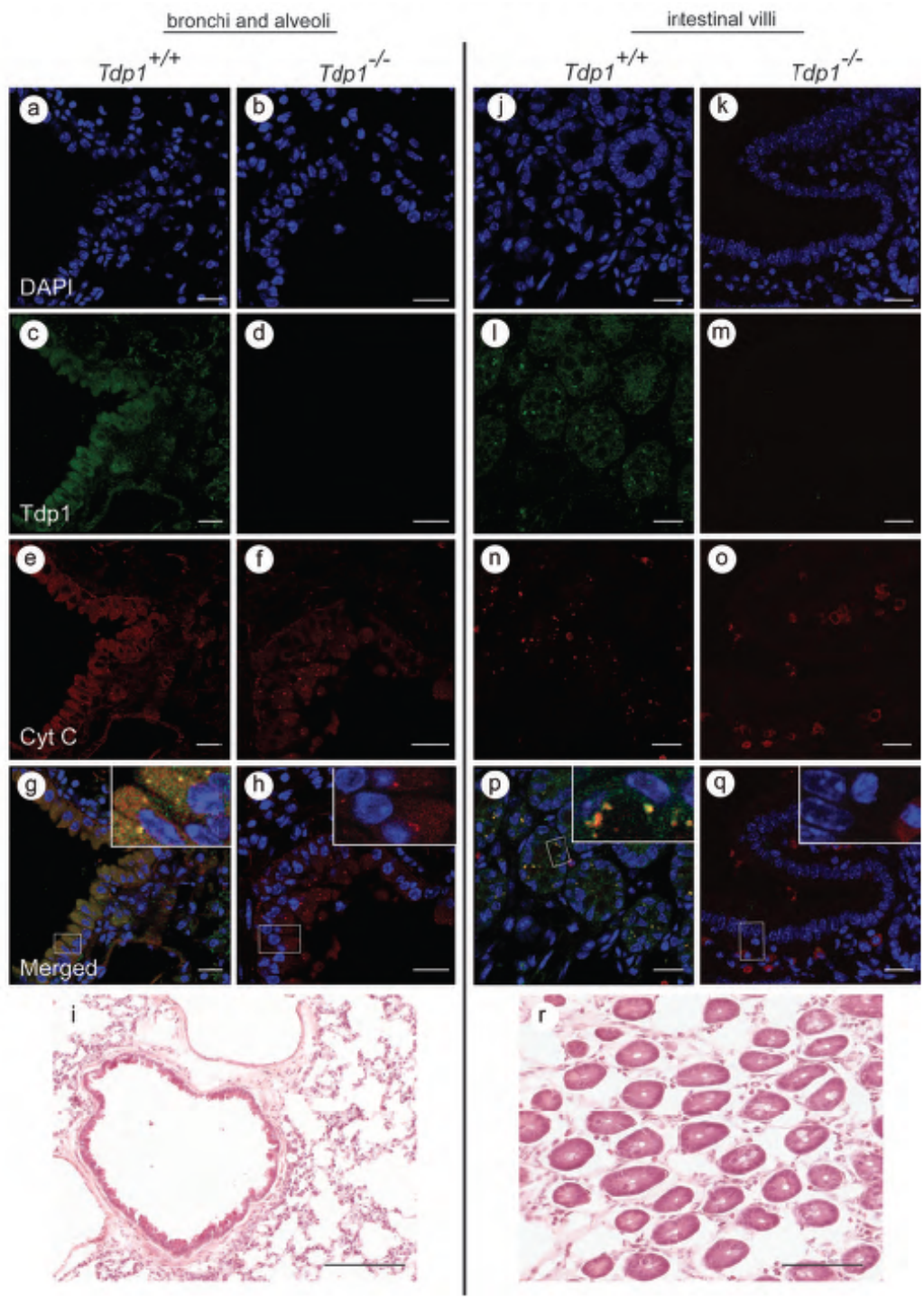

Figure A-15: Photomicrographs of immunofluorescent colocalization of human Tdp1 with the mitochondrial protein cytochrome C in mouse lung and intestine. **a-i** bronchi and alveoli **j-r** intestinal villi. Left panels show wild-type mouse tissue. Right panels show *Tdp1*$^{-/-}$ mouse tissue. The boxed regions correspond to higher magnification images. Scale bars for immunofluorescent images = 20 μm. Scale bar for H&E – lung = 500 μm, scale bar for H&E – intestine = 250 μm.

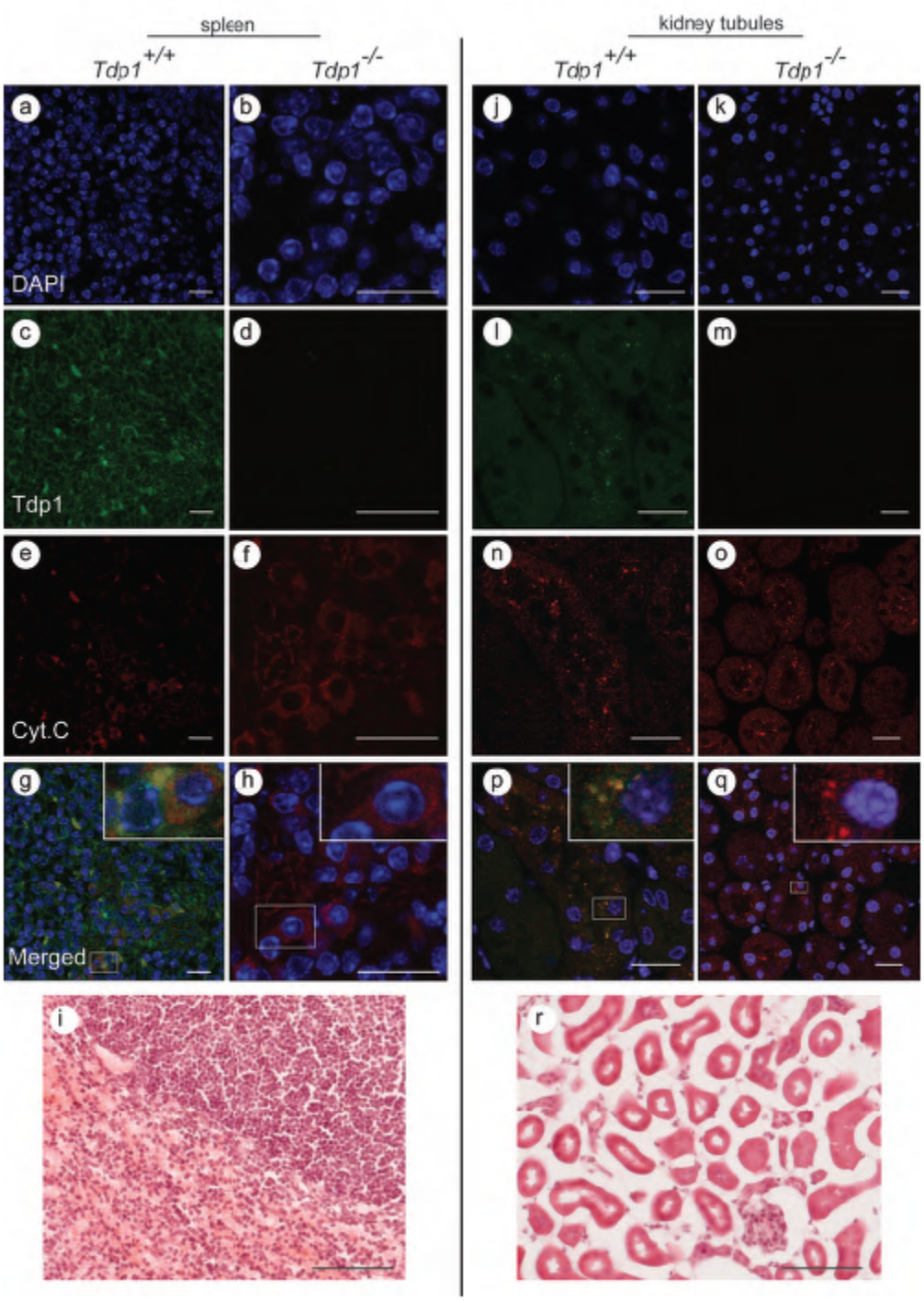

Figure A-16: Photomicrographs of immunofluorescent colocalization of human Tdp1 with the mitochondrial protein cytochrome C in mouse spleen and kidney. **a-i** spleen **j-r** kidney tubules. Left panels show wild-type mouse tissue. Right panels show *Tdp1*$^{-/-}$ mouse tissue. The boxed regions correspond to higher magnification images. Scale bars for immunofluorescent images = 20 μm. Scale bar for H&E – spleen and kidney = 250 μm

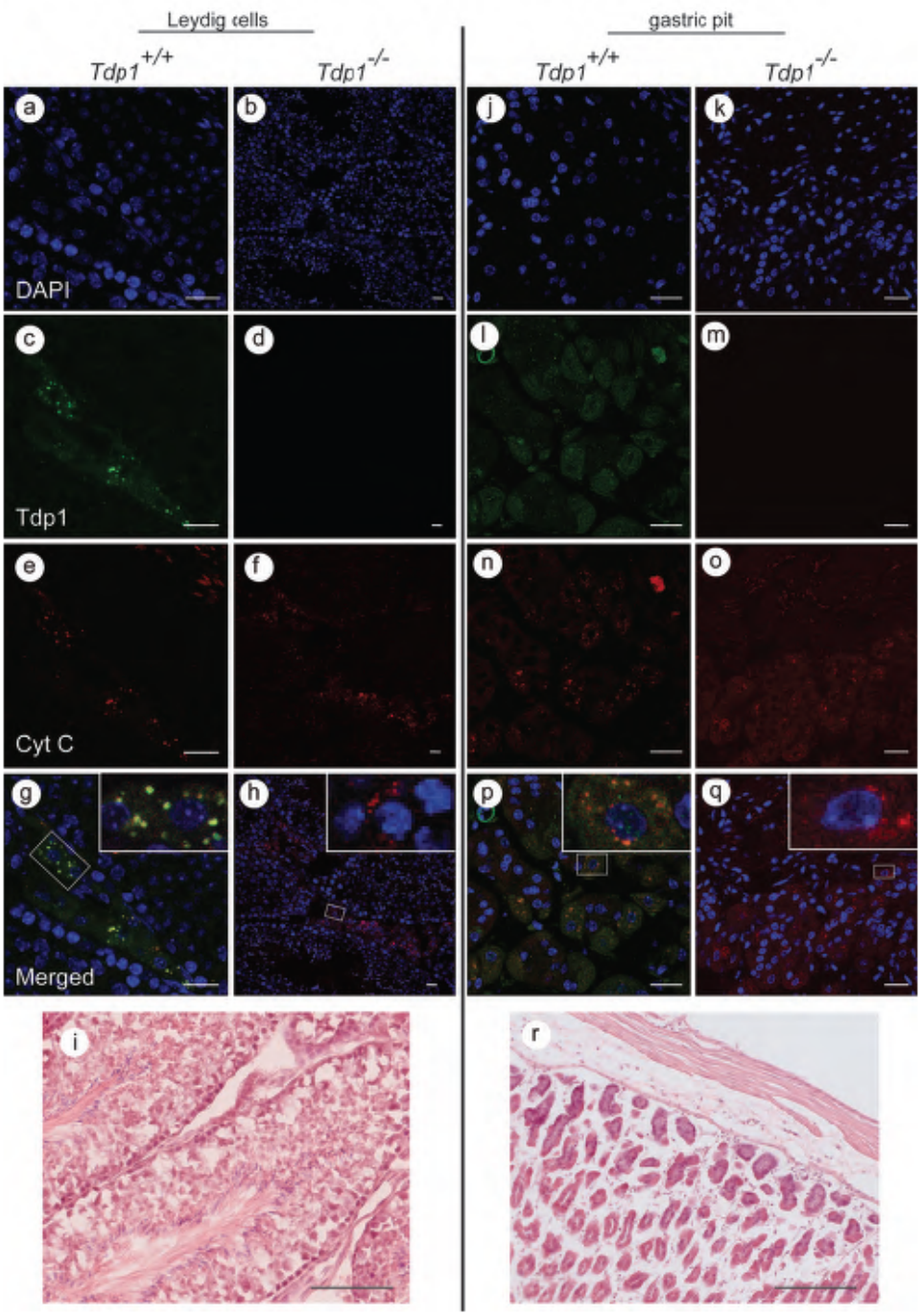

Figure A-17: Photomicrographs of immunofluorescent colocalization of human Tdp1 with the mitochondrial protein cytochrome C in mouse testis and stomach. **a-i** Leydig cells **j-r** gastric pit. Left panels show wild-type mouse tissue. Right panels show *Tdp1*$^{-/-}$ mouse tissue. The boxed regions correspond to higher magnification images. Scale bars for immunofluorescent images = 20 μm. Scale bar for H&E – testis = 250 μm, scale bar for H&E – stomach = 500 μm.

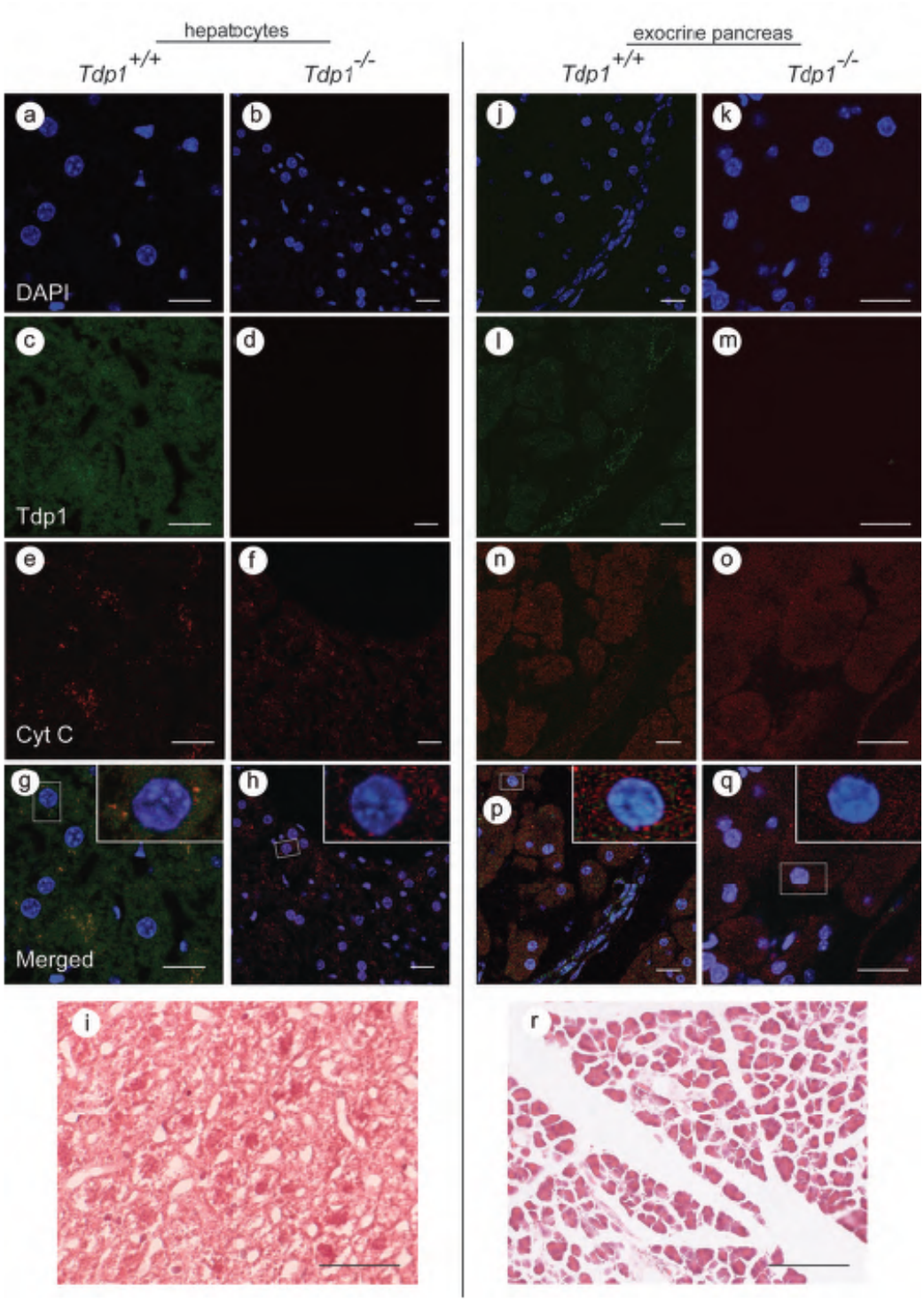

Figure A-18: Photomicrographs of immunofluorescent colocalization of human Tdp1 with the mitochondrial protein cytochrome C in mouse liver and pancreas. **a-i** liver **j-r** exocrine pancreas. Left panels show wild-type mouse tissue. Right panels show *Tdp1*$^{-/-}$ mouse tissue. The boxed regions correspond to higher magnification images. Scale bars for immunofluorescent images = 20 μm. Scale bar for H&E – liver = 160 μm, scale bar for H&E – pancreas = 500 μm.

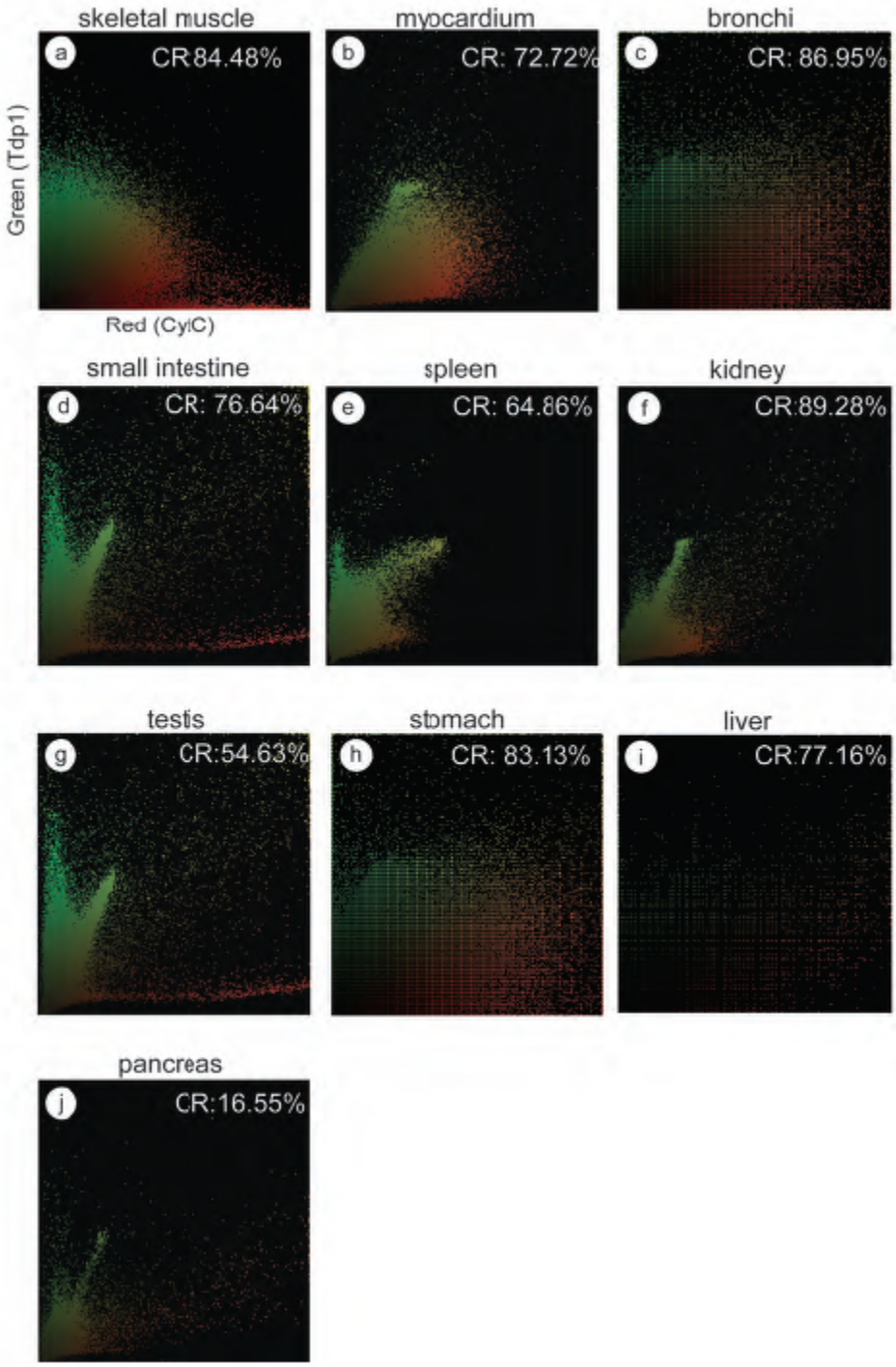

Figure A-19: Scatterplots of Tdp1 and cytochrome C colocalization analysis. **a** skeletal muscle **b** myocardium **c** bronchi **d** small intestine **e** spleen **f** kidney **g** testis **h** stomach **i** liver **j** pancreas. To determine colocalized signals, scatterplot threshold was set at 30%, background at 20%. Colocalization rate [%] = colocalization area/area foreground, and area foreground = area of image − area of background. CR= colocalization rate.

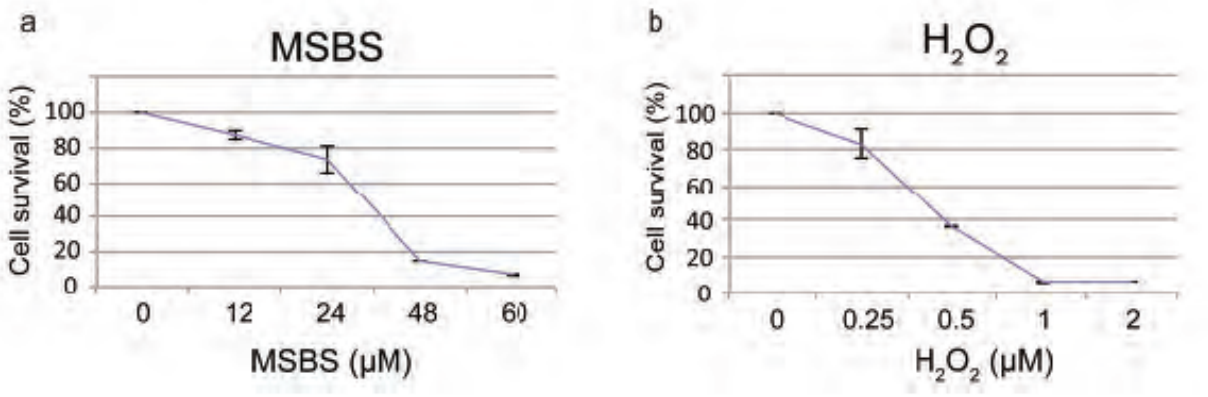

Figure A-20: Determination of lethal oxidant dose in cultured human fibroblasts by MTT assay

Table A-1: Human Tdp1 expression

	Male		Female (2 year old)		Female (16 year old)	
	Cytoplasm	Nucleus	Cytoplasm	Nucleus	Cytoplasm	Nucleus
Thyroid						
Follicular cells	+/-	+/-	+/-	+/-	+	+
Parafollicular cells	+/-	+/-	+/-	+/-	+/-	+/-
Parathyroid						
Chief cells	+	+	+	+	+	++
Pancreatic islets	+	+/-	+	+	+	++
Adrenal cortex						
Zona glomerulosa	+++	+++	+++	+++	+++	+++
Zona fasiculata	++	++	++	+++	++	++
Zona reticularis	+	+	+	++	+	++
Adrenal medulla	+++	+++	+++	++	++	+
Adipose	+++	+/-	+++	+/-	++	+/-
Esophagus						
Strat sq epith	++	+++	+++	+++	++	++
Lamina propria	+/-	+/-	+/-	-	+	+/-
Muscularis	+	++	+	+	+	++
Serosa	+	+++	+	+++	+	+++
Stomach						
Mucosa	+++	+++	+++	+++	+++	+++
Muscularis	+	+/-	+	+/-	+	+
Small intestine						
Mucosa	+++	++	++	+++	++	++
Muscularis	+	++	+	++	+	+
Large intestine						
Mucosa	+++	++	+++	++	++	++
Muscularis	+	++	++	++	+	+
Liver						
Hepatocytes	++	++	++	++	++	++
Kupffer cells	+++	++	+++	++	+++	+++
Bile duct	++	+	++	+	++	+++
Exocrine pancreas						
Acinar cell	+	+/-	++	+/-	++	++
Kidney						
Capsule	+	-	+	+/-	+	+
Glomeruli	+	+/-	+	+/-	+	+/-
Proximal tubules	+++	++	++	++	++	++
Macula densa	++	+/-	++	+	++	++
Distal tubules	++	+	++	+	++	+
Loops of Henle	++	+	++	+	++	+
Collecting ducts	+++	++	+++	++	+++	++
Bladder						
Transitional epith	++	+/-	++	+	++	++
Smooth muscle	++	++	++	+	++	+

	Male		Female (2 year old)		Female (16 year old)	
	Cytoplasm	Nucleus	Cytoplasm	Nucleus	Cytoplasm	Nucleus
Endochondral bone						
Periosteum	+	+	+	++	+	+
Osteoblasts	+	+++	+	+++	++	++
Osteoclasts	+++	+++	+++	++	+	+
Growth plate						
Prolif zone	+++	++	+++	++	N/A	N/A
Hypertr and calcif. zone	++	+	++	+	+++	++
Hyaline cart	++	+++	++	+++	+++	+++
Tendon/CT	++	++	++	++	N/A	N/A
Skeletal muscle						
Myofiber	+	-	+	+/-	+	-
Satellite cell	+	+	+	+	+	+
Fascia	+	+	+	+	+/-	+

Key: +++ = Highly expressed; ++ = Moderately expressed; + = Weakly expressed; - = Not expressed.

Appendix B: Supplementary Tables and Figures for Chapter 3

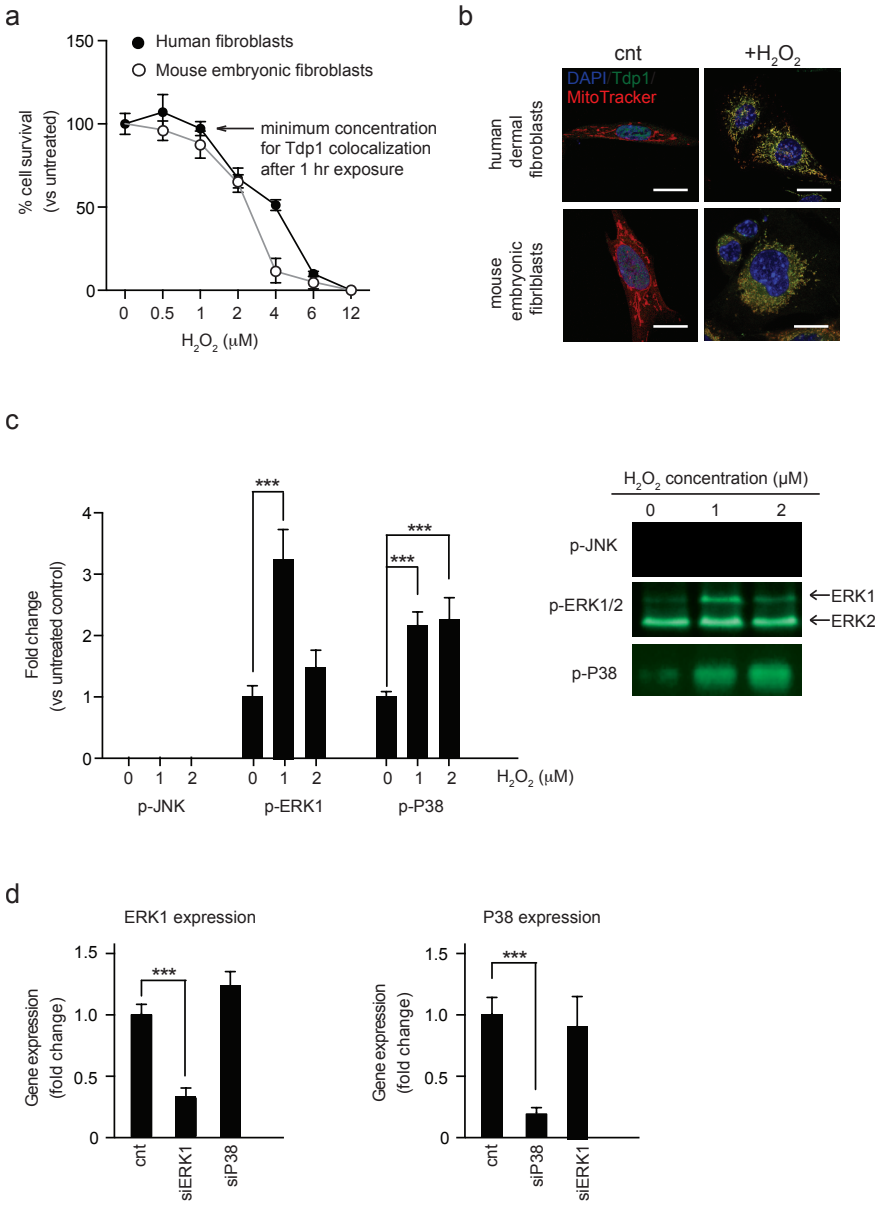

Figure B-1: Effect of H_2O_2 treatment on cultured cells. (a) Graph showing the effect of H_2O_2 treatment on the survival of cultured human dermal fibroblasts and mouse embryonic fibroblasts. Human and mouse cells were treated for 1 hour with varying H_2O_2 concentrations before measuring the level of viable cells using the MTT assay. (b) Representative immunofluorescent images showing colocalization of Tdp1 and the mitochondrial dye MitoTracker® in human dermal fibroblasts and mouse embryonic fibroblasts (MEFs) following treatment with 1 μM H_2O_2 for 1 hour. (c) Activation of MAP kinases in human dermal fibroblasts by H_2O_2 treatment. Left panel: Graph showing the level of JNK, ERK1 and P38 phosphorylation following culture with 0, 1 or 2 μM H_2O_2 for 1 hour.

Right panel: Photograph of an immunoblot of lysates from whole-cell extracts of H_2O_2-treated human fibroblasts probed for p-JNK, p-ERK, and p-P38. ***, $P<0.001$. (d) Graphs showing the expression of ERK1 and P38 after treatment with non-targeting siRNA or siERK1/siP38 for 72 hours. Gene expression was normalized to GAPDH. Error bars represent one standard deviation for three independent experiments.

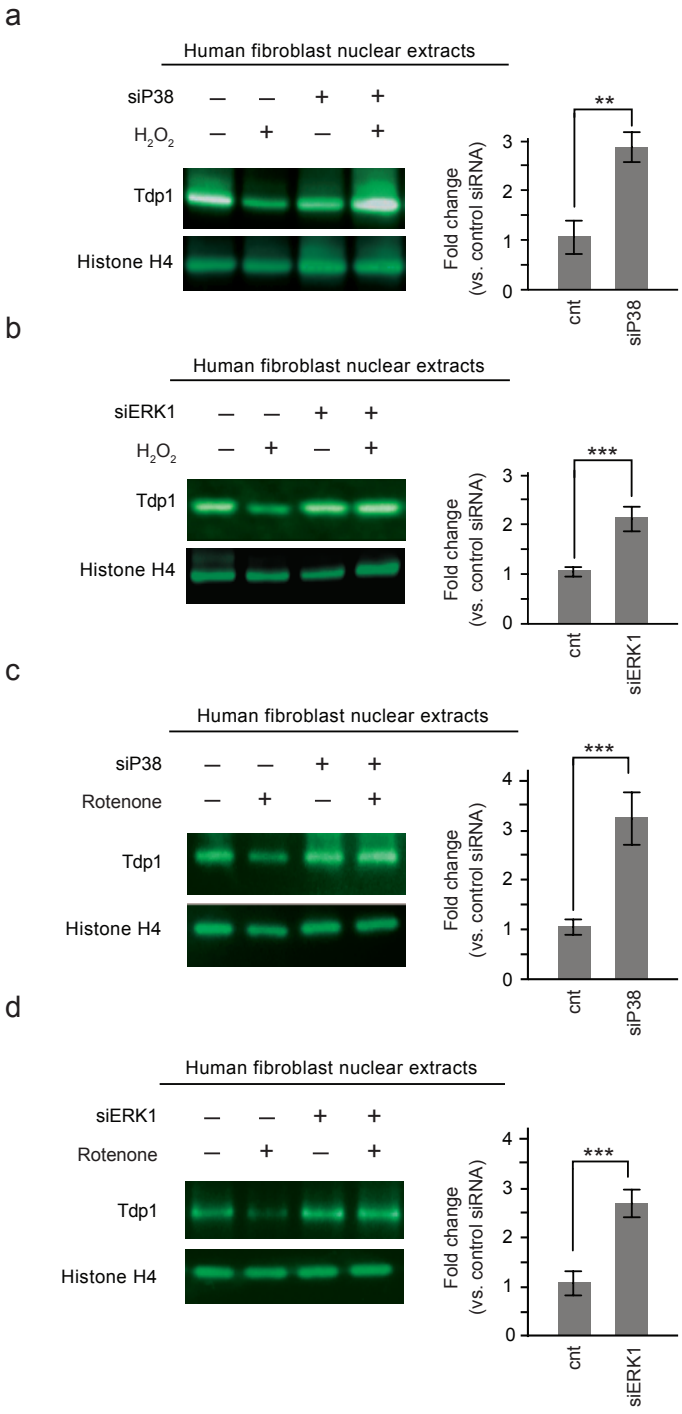

Figure B-2: P38 and ERK1 modulate Tdp1 exit from the nucleus. (a) Dependence of Tdp1 clearance from the nucleus on P38 following H_2O_2 treatment of cultured human fibroblasts. Left panel: Photograph of an immunoblot of lysates from nuclear extracts of cultured human fibroblasts without or with knockdown of P38 and in the absence or presence of H_2O_2 treatment. Histone H4 was used as a loading control. Right panel: Graph showing fold change in nuclear Tdp1 levels across three independent experiments following treatment with 1 μM H_2O_2 for 1 hour and in

the absence or presence of P38 knockdown. Tdp1 levels were normalized to Histone H4 levels and fold changes are shown relative to levels in cells treated with nontargeting siRNA. Error bars represent one standard deviation. (b) Dependence of Tdp1 clearance from the nucleus on ERK1 following H_2O_2 treatment of cultured human fibroblasts. Left panel: Photograph of an immunoblot of lysates from nuclear extracts of cultured human fibroblasts without or with knockdown of ERK1 and in the absence or presence of H_2O_2 treatment. Histone H4 was used as a loading control. Right panel: Graph showing fold change in nuclear Tdp1 levels across three independent experiments following treatment with 1 μM H_2O_2 for 1 hour and in the absence or presence of ERK1 knockdown. Tdp1 levels were normalized to Histone H4 levels and then fold changes are shown relative to levels in cells treated with nontargeting siRNA. Error bars represent one standard deviation. (c) Dependence of Tdp1 clearance from the nucleus on P38 following rotenone treatment of cultured human fibroblasts. Left panel: Photograph of an immunoblot of lysates from nuclear extracts of cultured human fibroblasts without or with knockdown of P38 and in the absence or presence of rotenone treatment. Histone H4 was used as a loading control. Right panel: Graph showing fold change in nuclear Tdp1 levels across three independent experiments following treatment with 200 nM rotenone for 1 hour and in the absence or presence of P38 knockdown. Tdp1 levels were normalized to Histone H4 levels and then fold changes are shown relative to levels in cells treated with nontargeting siRNA. Error bars represent one standard deviation. (d) Dependence of Tdp1 clearance from the nucleus on ERK1 following rotenone treatment of cultured human fibroblasts. Left panel: Photograph of an immunoblot of lysates from nuclear extracts of cultured human fibroblasts without or with knockdown of ERK1 and in the absence or presence of rotenone treatment. Histone H4 was used as a loading control. Right panel: Graph showing fold change in nuclear Tdp1 levels across three independent experiments following treatment with 200 nM rotenone for 1 hour and in the absence or presence of ERK1 knockdown. Tdp1 levels were normalized to Histone H4 levels and then fold changes are shown relative to levels in cells treated with nontargeting siRNA. Error bars represent one standard deviation. **, $P<0.01$; ***, $P<0.001$.

Table B-1. Primary antibodies

Name	Application(s)	Source
Anti-human		
TDP1	WB, IF	Abcam (ab4166)
TIM23	WB, IF	Santa Cruz (sc-13297)
TOM20	WB	Abcam (ab56783)
COMPLEX IV	WB	Abcam (ab14744)
HISTONE 2B	WB	Abcam (ab1790)
HISTONE H4	WB	Cell Signaling Technology (#2592)
UBIQUITIN	WB	Cell Signaling Technology (#3933)
GAPDH	WB	Abcam (ab9485)
HA	WB	Thermo Fisher Scientific (#26183)
DNA LIGASE III	WB	Abcam (ab587)
XRCC1	WB	Abcam (ab1838)
ERK1	WB, IF	Cell Signaling Technology (#4372)
P38	WB, IF	Cell Signaling Technology (#9212)
Phosphorylated ERK1	WB	Cell Signaling Technology (#9101)
Phosphorylated P38	WB	Cell Signaling Technology (#9211)
Phosphorylated JNK1/2	WB	Thermo Fisher Scientific (#44-682G)
Anti-mouse		
TDP1	WB, IF	Abcam (ab4166)
TOM20	WB	Santa Cruz (sc-17764)
HISTONE H4	WB	Cell Signaling Technology (#2592)
DNA LIGASE III	WB	Abcam (ab125434)
HA	WB	Thermo Fisher Scientific (#26183)
XRCC1	WB	Abcam (ab1947)
COMPLEX IV	WB	Abcam (ab14744)
Anti-yeast		
GFP	WB	Abcam (ab290)
NSP1P	WB	Abcam (ab4641)
PORIN	WB	Thermo Fisher Scientific (#459500)

Abbreviations: IF, immunofluorescence; WB, western blot

Table B-2. Oligonucleotide sequences.

Name	Sequence (5′ to 3′)
Quantitative PCR primers	
TDP1 - forward	AGGCTAAGGCTCACCTCCAT
TDP1 - reverse	TTCCTGGAGTCTTGCTTTCC
GAPDH - forward	TTAGCACCCCTGGCCAAGG
GAPDH - reverse	CTTACTCCTTGGAGGCCATG
mtCOXII - forward	GATAACCGAGTCGTTCTGCAA
mtCOXII - reverse	CCTGGTCGGTTTGATGTTACT
S6 ribosomal protein - forward	GTCCGCCAGTATGTTGTCAGGAAG
S6 ribosomal protein - reverse	GCTTTGGTCCTGGGCTTCTTACC
Mutation assay primers	
control - forward	TCGGCGTAAAACGTGTCAAC
control - reverse	CCGCCAAGTCCTTTGAGTTT
Taq634 - forward	ACTCAAAGGACTTGGCGGTA
Taq634 - reverse	AGCCCATTTCTTCCCATTTC
nDNA - forward	ATGGAAAGCCTGCCATCATG
nDNA - reverse	TCCTTGTTGTTCAGCATCAC
mtDNA - forward	CCTATCACCCTTGCCATCAT
mtDNA - reverse	GAGGCTGTTGCTTGTGTGAC
mtDNA lesion assay primers	
long fragment - forward	GCCAGCCTGACCCATAGCCATAATAT
long fragment - reverse	GAGAGATTTTATGGGTGTAATGCGG
short fragment - forward	CCCAGCTACTACCATCATTCAAGT
short fragment - reverse	GATGGTTTGGGAGATTGGTTGATG
mtDNA deletion assay primers	
deletion (D13) - forward	AATTACAGGCTTCCGACACA
deletion (D13) - reverse	TGATGTTGGAGTTATGTTGG
Site-directed mutagenesis primers	
S81A - forward	GGCAGAAAAGCGGTGCCCAGGAGGACCTCGGC
S81A - reverse	GGCGAGGTCCTCCTGGGCACCGCTTTTCTGCC

Appendix C: Supplementary Tables and Figures for Chapter 4

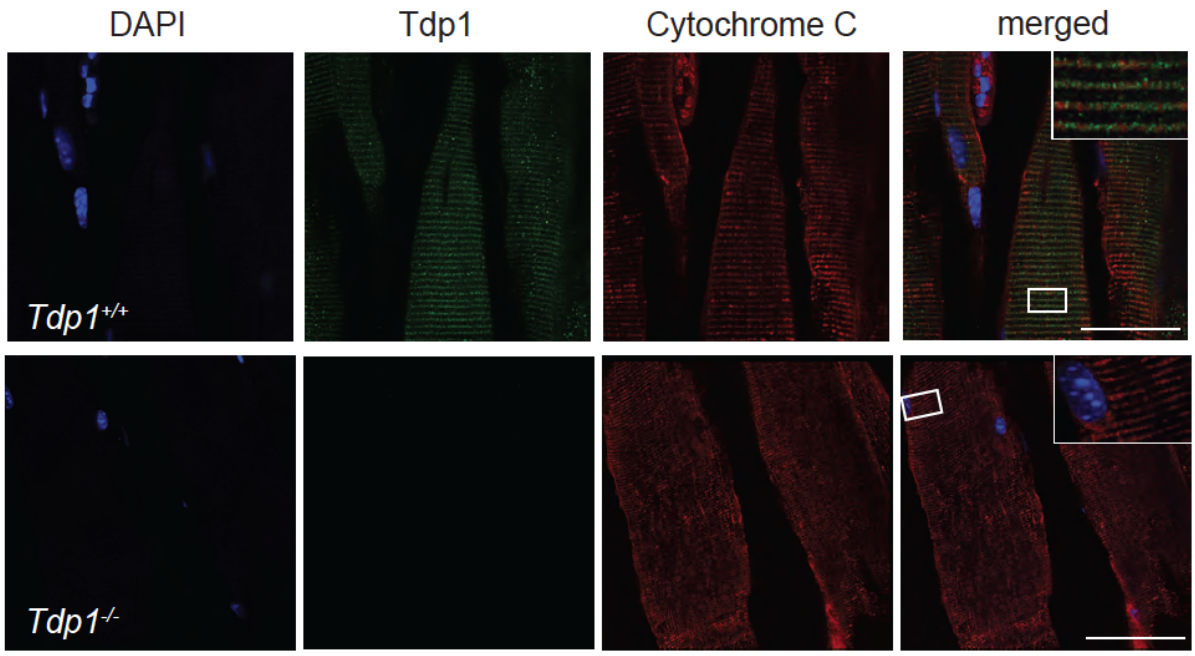

Figure C-1. Specificity of the Tdp1 antiserum. Immunofluorescent photographs illustrating the reactivity of the antiserum in *Tdp1*+/+ and *Tdp1*-/- mouse skeletal muscle tissue. Scale bar = 100 μm.

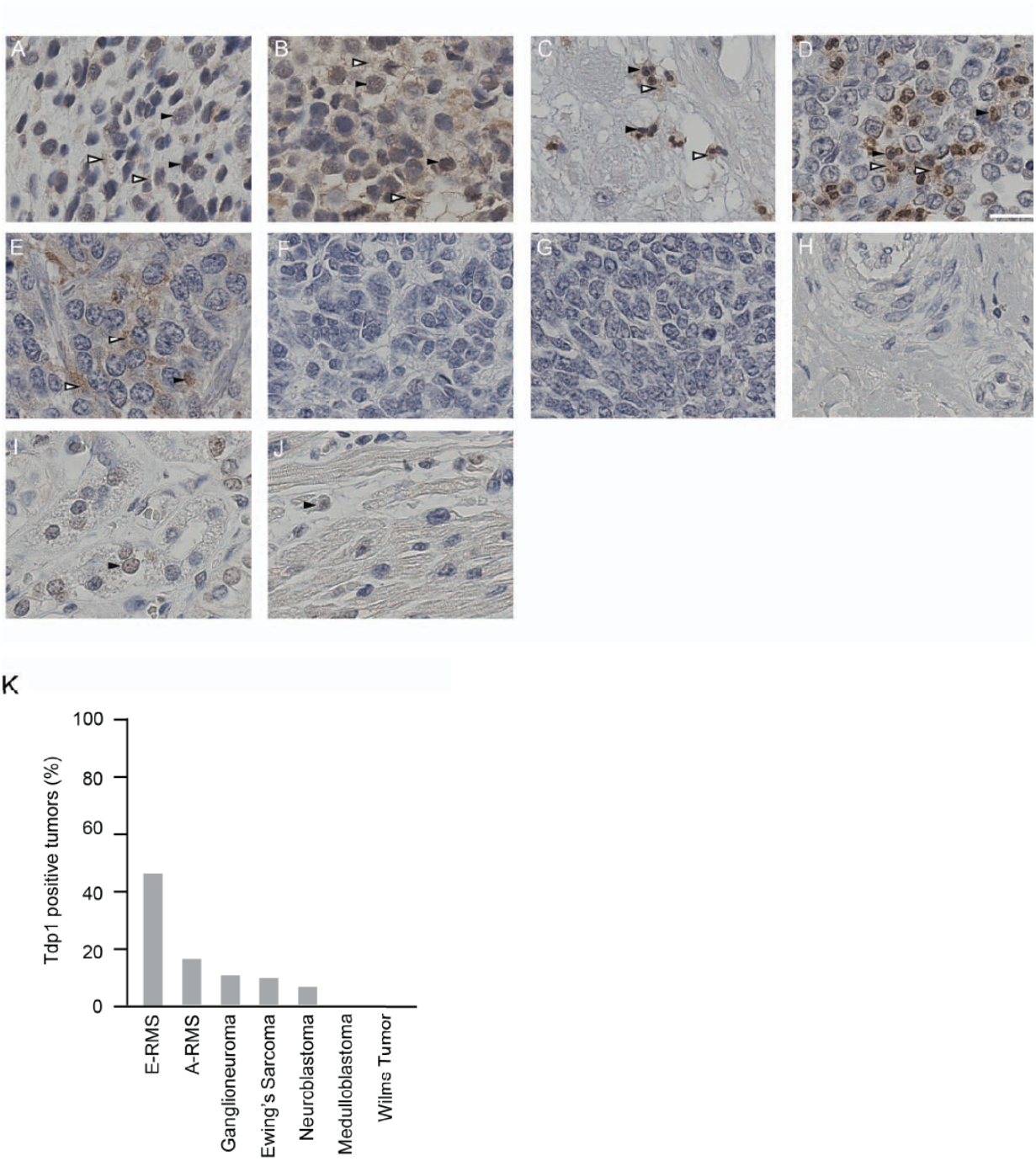

Figure C-2. Tdp1 expression in pediatric solid tumors. Photomicrographs showing immunohistochemical detection of Tdp1 in tumor microarrays of (A) embryonal RMS (B) alveolar RMS (C) ganglioneuroma (D) Ewing's sarcoma (E) neuroblastoma (F) medulloblastoma, (G) Wilm's Tumor, (H) normal pediatric liver, (I) normal pediatric kidney and (J) normal pediatric heart. (K) Graph showing the frequency with which Tdp1 expression was detected in pediatric tumors. Dark arrows indicate nuclear expression and open arrows indicate cytoplasmic expression of Tdp1. Scale bar = 20 μm.

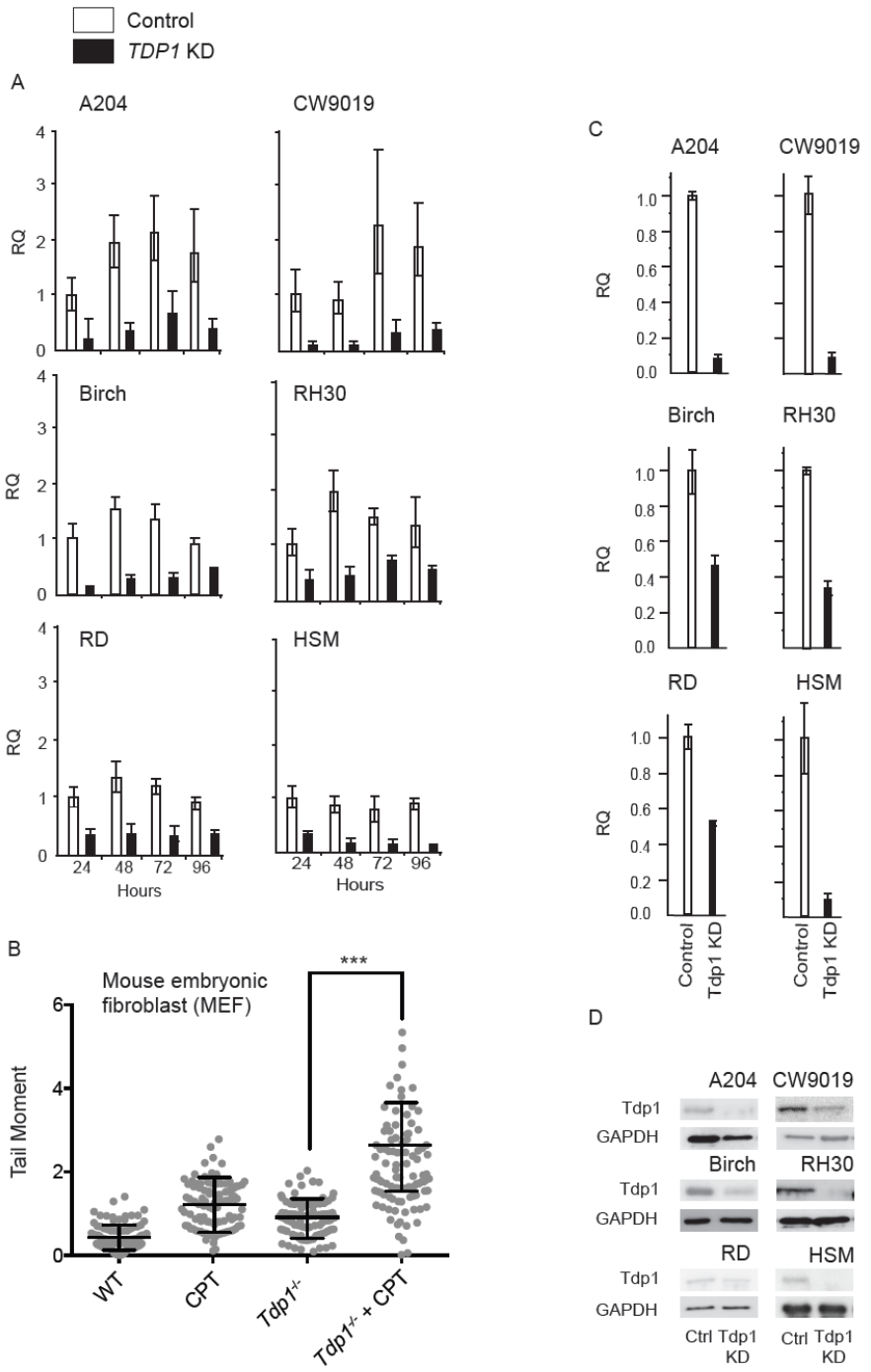

Figure C-3. Generation of transient and constitutive *TDP1* knockdown by treatment with siRNA and shRNA and assay for sensitivity of Tdp1-deficient MEFs to DNA breaks (A) Graphs showing the amount of *TDP1* mRNA in cell lines over 96 hours after treatment with Tdp1 siRNA or non-targeting control (n=3). (B) Graphs showing the result of an alkaline comet assay for DNA breaks in mouse embryonic fibroblasts isolated from *Tdp1+/+* or *Tdp1-/-* mice. Fibroblasts were either cultured without treatment or treated with 1μmol/L CPT 2 hours before the comet assay (n=4) (C) Graphs showing the amount of *TDP1* mRNA in cell lines after treatment with *TDP1* shRNA or non-targeting control (D) photographs of immunoblots showing the amount of Tdp1 protein
posttreatment with *TDP1* shRNA or non-targeting control (n=3). n, number of replicates; error bars, mean ±

s.d. ***, $P<0.001$

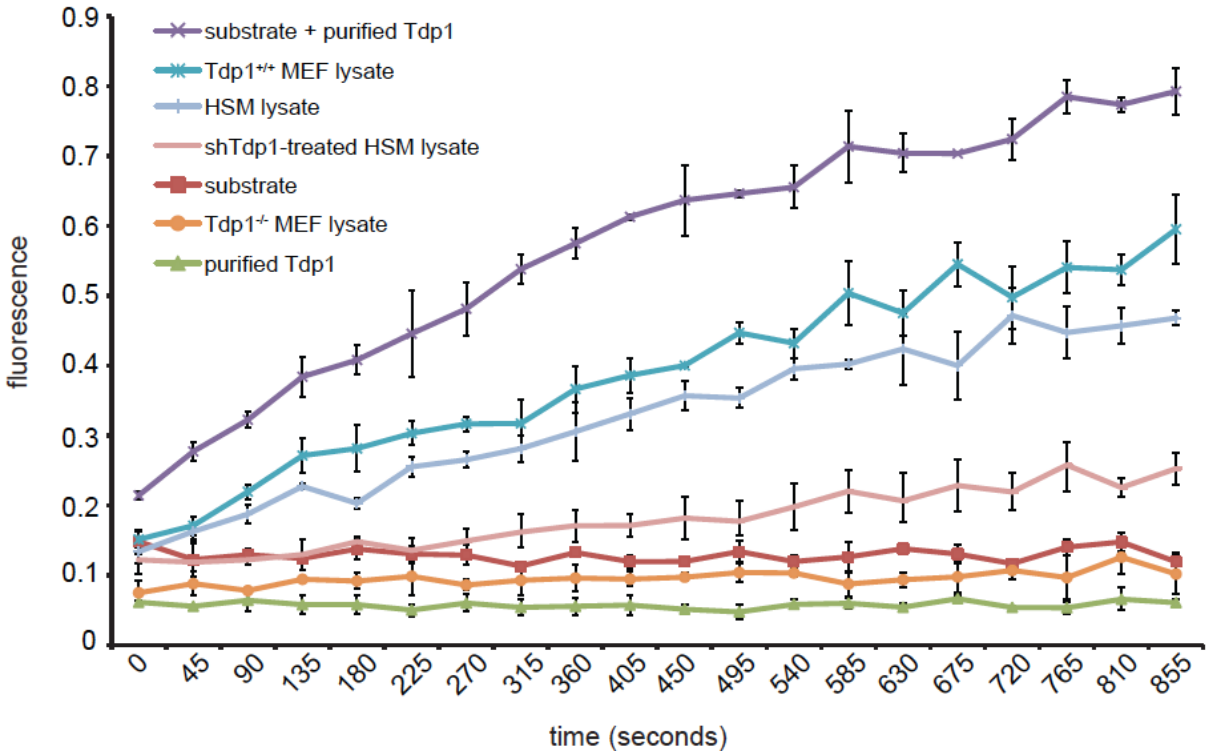

Figure C-4. Detection of Tdp1 cleavage activity in cell lysates by kinetic determination of Tdp1 cleavage activity in nuclear lysates using a real-time fluorophorequencher coupled DNA substrate. Lysates and controls were prepared in a 96-well plate and the substrate was added to the samples immediately before the assay was performed. To establish Tdp1 cleavage activity, fluorescence emission was measured over 20 reads taken at 45-second intervals. Purified Tdp1 enzyme and substrate and *Tdp1*+/+ MEFs were used as positive controls. Negative controls include 1) substrate alone, 2) enzyme alone and 3) *Tdp1*-/- MEFs (n=3). n, number of replicates; error bars, mean ± s.d.

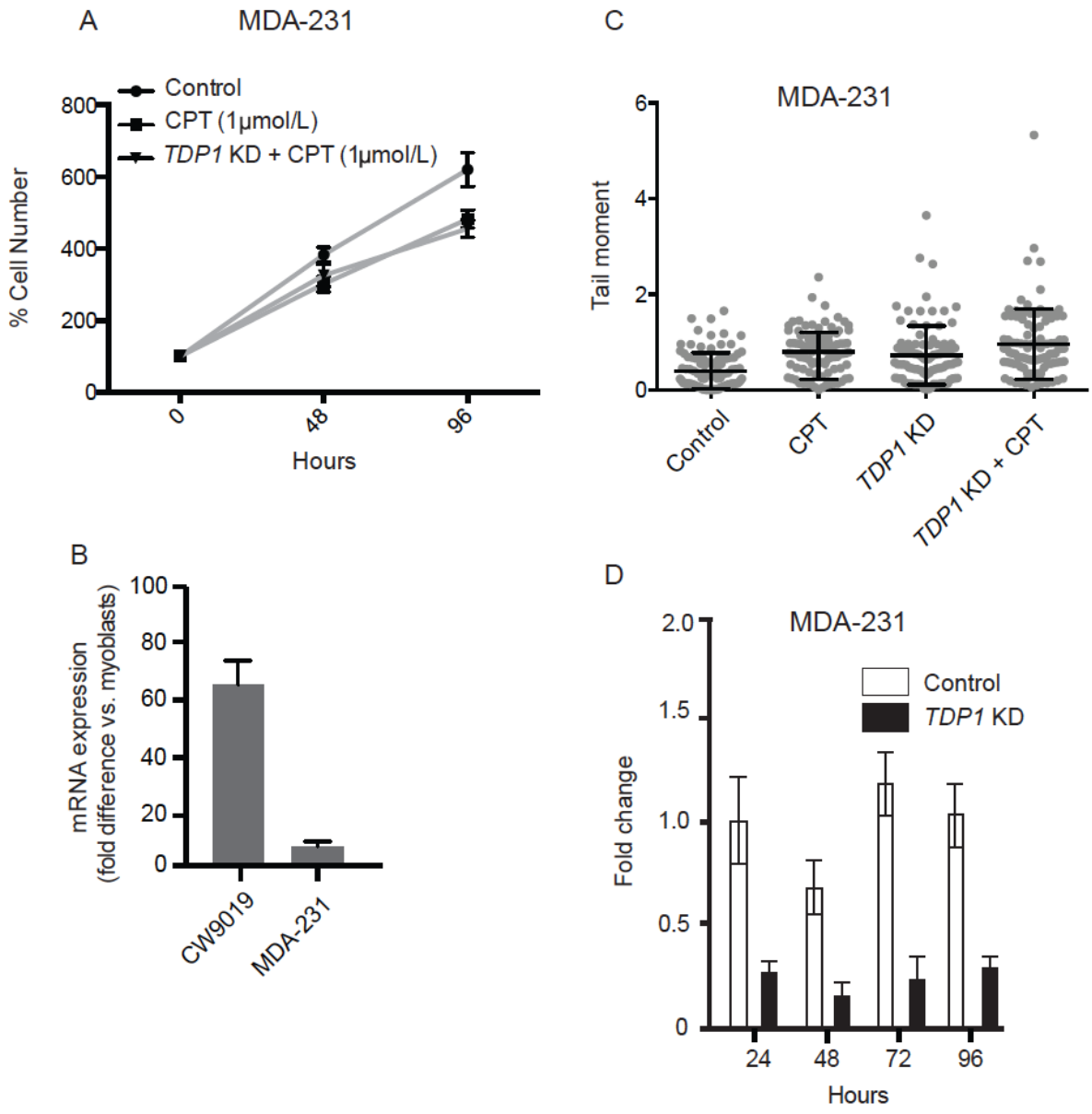

Figure C-5. Effect of cellular growth rate vs. Tdp1 expression on sensitivity to CPT treatment. . A) Growth curve of breast cancer cell line MDA-MB-231 over a 96 hour period during which the cell culture 1) received no CPT, 2) was treated with 1µmol/L CPT or 3) was treated with 1µmol/L CPT after transient *TDP1* knockdown (75%) (n=4). (B) Graph comparing Tdp1 mRNA expression in CW9019 and MDA-231 cells. mRNA expression was normalized to human skeletal myoblasts. (C) Graphs showing the results of an alkaline comet assay showing the number of DNA breaks after 2 hours of culture under the conditions stated above in A (n=4). (D) Graphs showing the amount of *TDP1* mRNA in MDA-231 cells over 96 hours after treatment with *TDP1*
siRNA or non-targeting control (n=3). n, number of replicates; error bars, mean ± s.d.

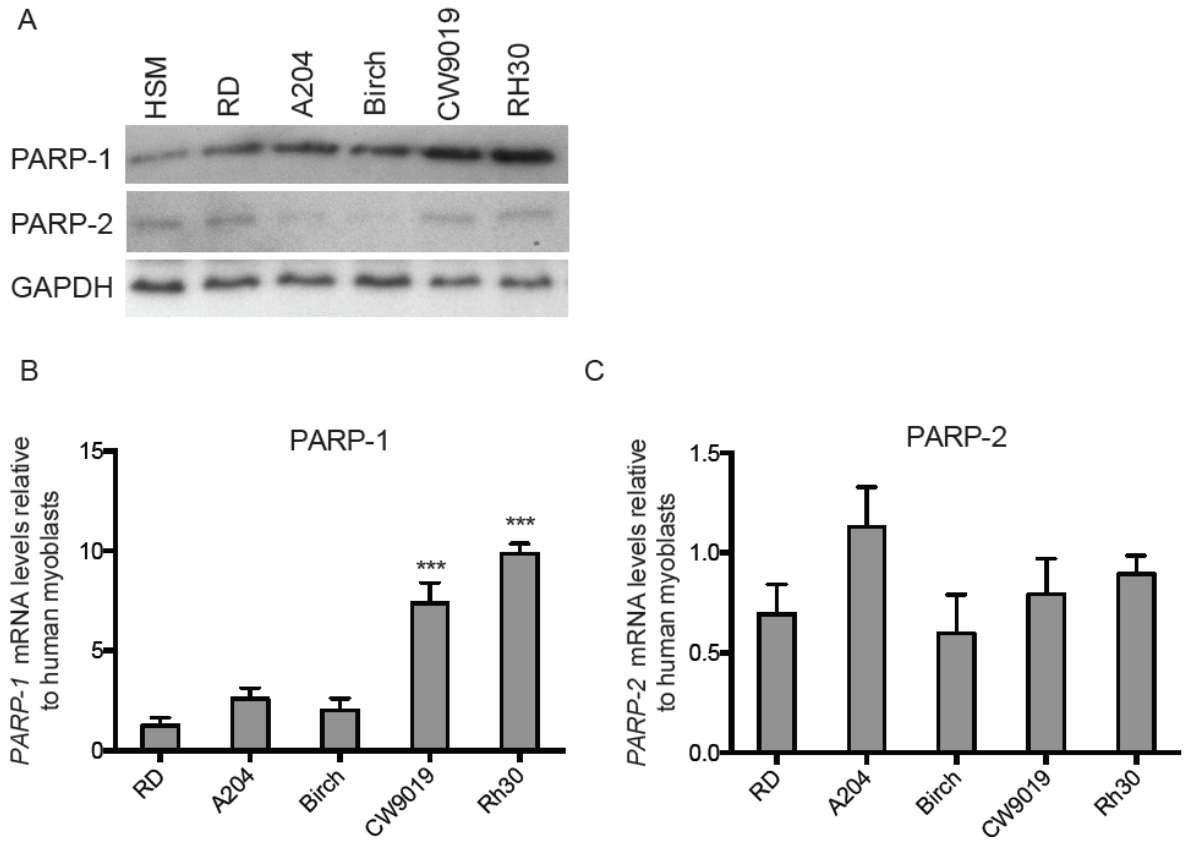

Figure C-6. Analysis of PARP-1 and PARP-2 expression levels in RMS and normal myoblasts. A) Immunoblot showing PARP-1 and PARP-2 protein expression in RMS and normal myoblasts. GAPDH was used as a loading control. B) Graphs indicating the quantity of *PARP-1* and *PARP-2* mRNA in all cell lines relative to control myoblasts (n=3). n, number of replicates, error bars, mean ± s.d. ***, $P<0.001$

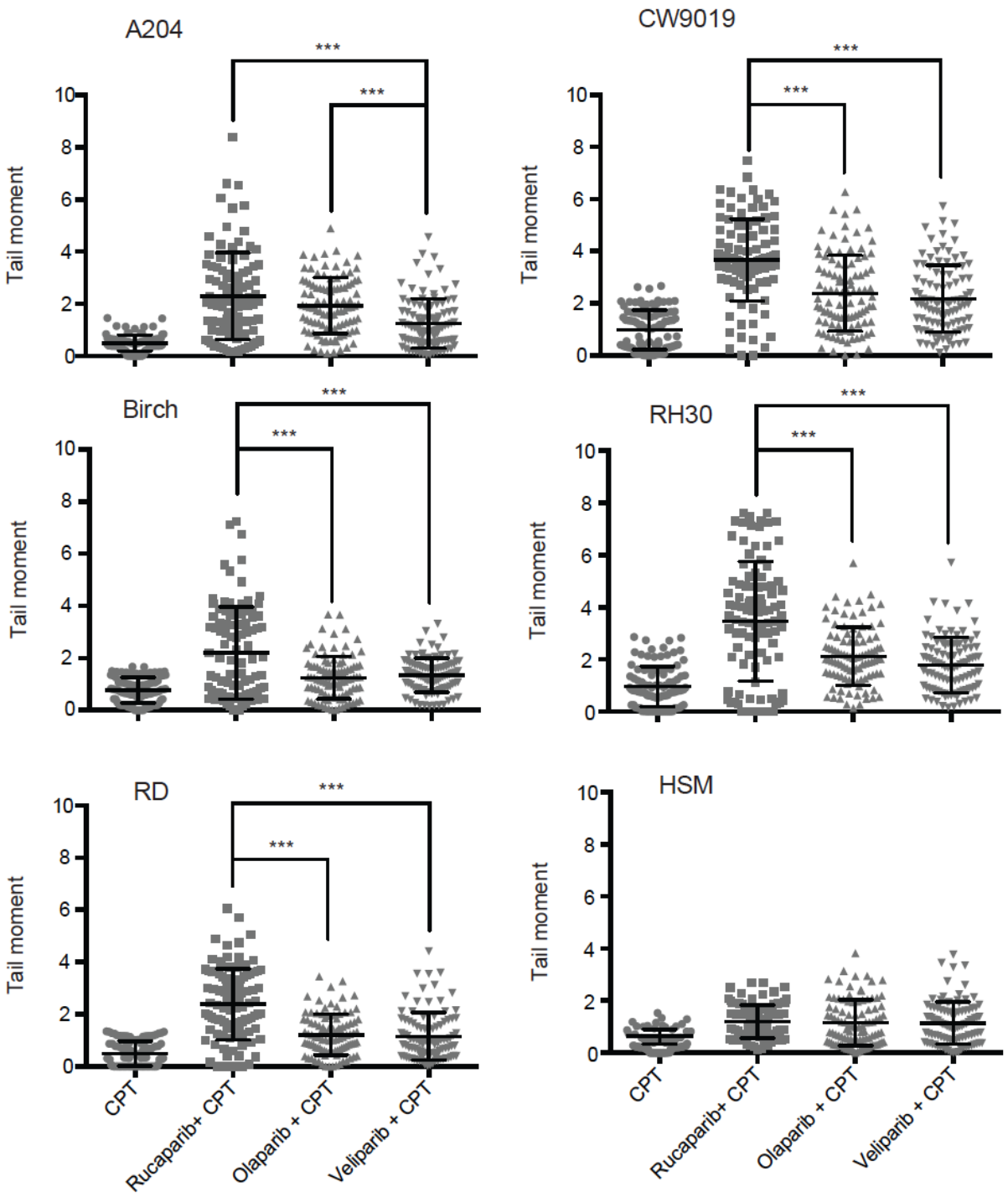

Figure C-7. PARP-1 inhibitor treatment sensitizes RMS cell lines to CPT. Graphs showing the amount of DNA breaks (tail moment) in cell lines post-treatment with 1) 10μmol/L Rucaparib, Olaparib or Veliparib only or 2) 10μmol/L of one of the PARP-1 inhibitors in combination with 1μmol/L CPT (n=4). n, number of replicates; error bars, mean ± s.d. **, $P<0.01$; ***, $P<0.001$

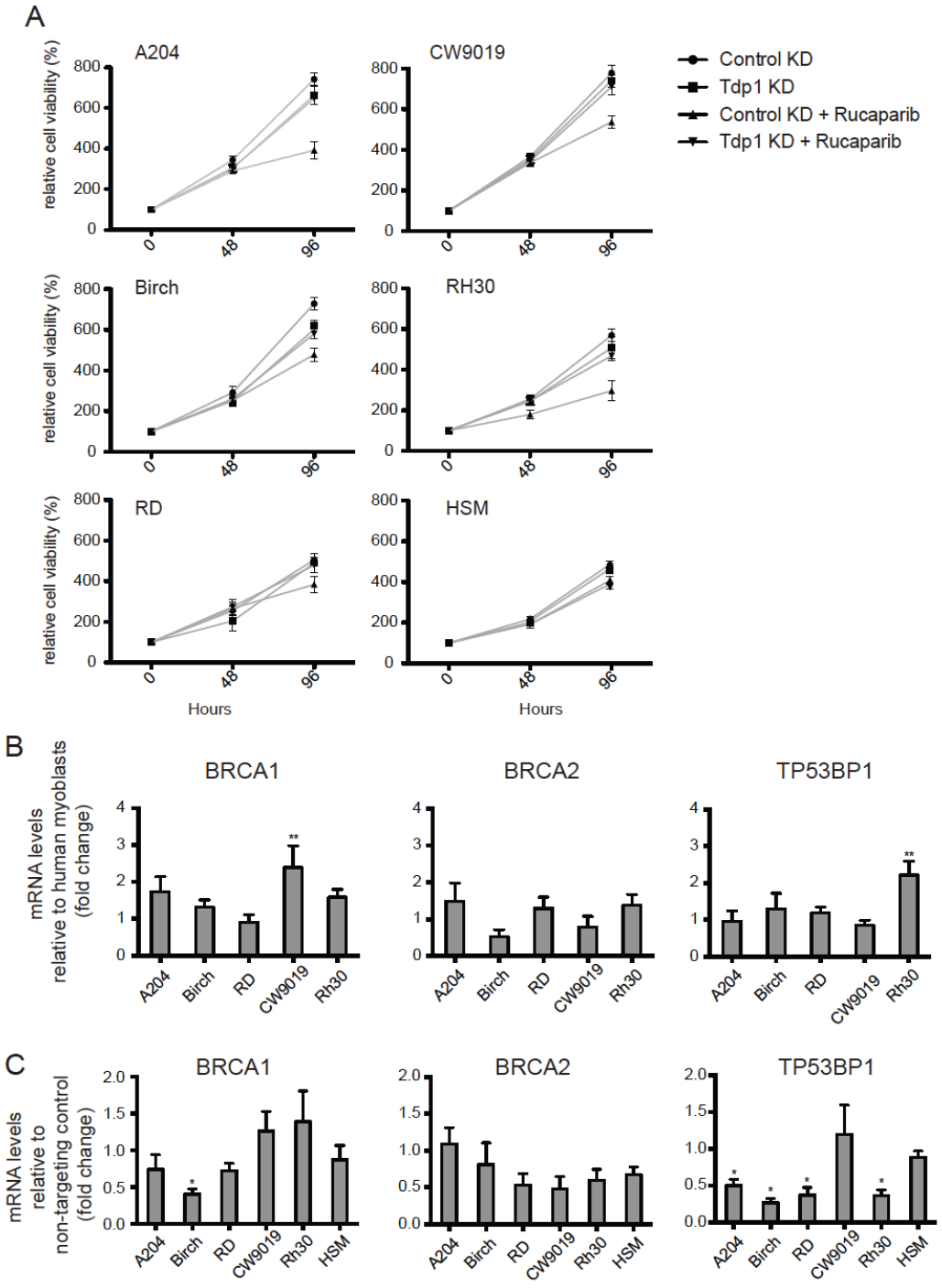

Figure C-8. RMS cells develop resistance to PARP-1 inhibitors posttreatment with *TDP1* shRNA. (A) Graphs showing the number of RMS cells and control myoblasts over a 96 hour period for cells after treatment with 1) non-targeting (control) sRNA, 2) *TDP1* shRNA, 3) a combination of control shRNA and 10µmol/L Rucaparib and 4) a combination of *TDP1* shRNA and 10µmol/L Rucaparib. (n=4) (B) Graphs indicating the quantity of *BRCA1, BRCA2* and *T53BP1* mRNA in all cell lines treated with *TDP1* shRNA relative to control myoblasts (n=3). (C) Graphs indicating fold change of *BRCA1*, *BRCA2* or *TP53BP1* mRNA in all cell lines treated with *TDP1* shRNA relative to cells treated with non-targeting control shRNA (n=3). n, number of replicates, error bars, mean ± s.d.

Table C-1: Nucleotide sequences for oligonucleotides, siRNAs and shRNAs.

Name	Sequence
RT-PCR primers	
TDP1 - forward	AGGCTAAGGCTCACCTCCAT
TDP1 - reverse	TTCCTGGAGTCTTGCTTTCC
GAPDH - forward	TTAGCACCCCTGGCCAAGG
GAPDH - reverse	CTTACTCCTTGGAGGCCATG
BRCA1 - forward	GTATCAGGGTGAAGCAGCATCTGG
BRCA1 -reverse	AGCTGTTAGAAGGCTGGCTCCCA
BRCA2 - forward	TGCAAAAACATCCACTCTGC
BRCA2 - reverse	GCTGTGTCATCCCTTTCCAT
TP53BP1 – forward	TCTGGACTGGCAACCCCGTGAA
TP53BP1 – reverse	GGCTGCACCACCAGTCATGAGG
PARP-1 – forward	GGAAAGGGATCTACTTTGCCG
PARP-1 – reverse	TCGGGTCTCCCTGAGATGTG
PARP-2 – forward	GCCAGCAAAAGGGTCTCTGA
PARP-2 – reverse	GCTGTACACTCTGGGTCCAC
BRCA1 cDNA Sequencing primers	
exon 1 - forward	CGGTAGCCCCTTGGTTTC
exon 1 - reverse	TCCAAACCTGTGTCAAGCTG
exon 2 - forward	GAAAGGGCCTTCACAGTGTC
exon 2 - reverse	TTCATCCCTGGTTCCTTGAG
exon 3 - forward	GCAGCGGATACAACCTCAAA
exon 3 - reverse	TGGGAGTCCGCCTATCATTA
exon 4 - forward	CAGAATGAATGTAGAAAAGGCTGA
exon 4 - reverse	TGGAGTGAACTCTTTCACTTTTACA
exon 5 - forward	TCAAATGCCAAAGTAGCTGATG
exon 5 - reverse	GGGTTAGGATTTTTCTCATTCTGA
exon 6 - forward	AAGCAGATTTGGCAGTTCAAA
exon 6 - reverse	CTCTTCTTGGCTCCAGTTGC
exon 7 - forward	CCCACCTAATTGTACTGAATTGC
exon 7 – reverse	TGGTTCTGTTTTTGCCTTCC
exon 8 - forward	AGGGTTTTGCAAACTGAAAGA
exon 8 – reverse	GACTCATTCTTTCCTTGATTTTCTTC
exon 9 - forward	TGCAGAAGAGGAATGTGCAA
exon 9 – reverse	TTGCTTGAGCTGGCTTCTTT
exon 10 - forward	GGGAAATGAGAACATTCCAAG
exon 10 – reverse	TGCTAAAAACAGCAGAACTTTCC
exon 11 - forward	TGCATCTCAGGTTTGTTCTGA
exon 11 - reverse	TGCACTGTGAAGAAAACAAGC
exon 12 - forward	TGCTACCGAGTGTCTGTCTAAG
exon 12 - reverse	GTTCAGCCATTTCCTGCTG
exon 13 - forward	GCGTCTCTGAAGACTGCTCA
exon 13 - reverse	CTGTTGCTCCTCCACATCAA
exon 14 - forward	GCACAGTTGCTCTGGGAGTC
exon 14 - reverse	GGCAAACTTGTACACGAGCA
exon 15 - forward	AAGTGTGAGCAGGGAGAAGC
exon 15 - reverse	GTTGATCTGTGGGCATGTTG
exon 16 - forward	TGGAAGAAACCACCAAGGTC
exon 16 - reverse	GCCAGGACAGTAGAAGGACTG
exon 17 - forward	AGCCAGCCACAGGTACAGAG
exon 17 - reverse	CACATAATCGATCCCAAGCA
exon 18 - forward	TAGGGCTGGAAGCACAGAGT

Name	Sequence
exon 18 - reverse	CGTGGTATGATCTTGGCTCA
exon 19 - forward	TTAGCCGGTCATGGTGGT
exon 19 - reverse	CAACAGGGAGCAAAGGAAAA
exon 20 - forward	GCTCTGGTATATAATCCATTCCTCTT
exon 20 – reverse	AGTCTTCACTGCCCTTGCAC
TDP1 sequencing primers	
exon 3a – forward	TCTAGGCTGCCCTCCTTGT
exon 3a – reverse	CCAAAACCAGACAAGCCATC
exon 3b – forward	TCCTCCTCTTTGAGCCTGTG
exon 3b – reverse	TTAGGTGGTTCAGCCTCTGG
exon 4 – forward	TCCCCAAACTATGCCTCTCA
exon 4 – reverse	TGAGTCAGATCTTGATTGTCAGTG
exon 5 – forward	AAGATGAGTGGCTTTCACCTG
exon 5 – reverse	ATTGCAGCATAACCCTCCAG
exon 6 – forward	TGCACTAAGTGAGAGGGTGGA
exon 6 – reverse	GCACAACCATGCCTTGTCTA
exon 7 – forward	GGGCCTACCATGCTCAGTCT
exon 7 – reverse	AGGGCTTGCCTGGTAGAGAT
exon 8 – forward	TCTTTTTCTAGGCCATGTGTGTT
exon 8 – reverse	TTAGGCAGACTTTCATCATGG
exon 9 – forward	ATCCCCTCTATCACATCCTGA
exon 9 – reverse	TGGAGATACCGAGAATTCACCT
exon 10 – forward	TTGCCCAGAATTGTGCAG
exon 10 – reverse	TCAAGAAAATGGATTGGCTCTT
exon 11 – forward	GGCAAAGGCAACTTGATTACA
exon 11 – reverse	GGCTTTCCAAGAGCAGAAAA
exon 12 – forward	GTATCATCTGCGGAATGCAG
exon 12 – reverse	AACAGATTTTCATTTCCTTAAAAGC
exon 13 – forward	TTGGTATTAAAAACCTATTCCAAAAA
exon 13 – reverse	TTTTTCCTGTTACCTTCTTGCTG
exon 14 – forward	AGGGATTAGTCATGGGATGC
exon 14 – reverse	CACAGAGTCGTGTAGCCACTG
exon 15 – forward	AAGAGTGCAGGCTCTGGGTA
exon 15 – reverse	TCTTTTCAAAAATGCAGCAA
exon 16 – forward	TGCAAACTTGAGCTTCCAGA
exon 16 – reverse	TTGCCTATGAACATTGAAAATACC
exon 17 – forward	GGAAGTGGACATCCAGTACAAA
exon 17 – reverse	GAAGGGGGAGAATCTTCTGG
BRCA2 sequencing primers	
BRCA2 EXON 2 F	CCAGGAGATGGGACTGAATTAG
BRCA2 EXON 2 R	CGGTGACGTACTGGGTTTTTAGC
BRCA2 EXON 3 F	GATCTTTAACTGTTCTGGGTCACA
BRCA2 EXON 3 R	CCCAGCATGACACAATTAATGA
BRCA2 EXON 4 F	AGAATGCAAATTTATAATCCAGAGAGTA
BRCA2 EXON 4 R	AATCAGATTCATCTTTATAGAACAAA
BRCA2 EXON 5-6 F	TGTGTTGGCATTTTAAACATCA
BRCA2 EXON 5-6 R	CAGGGCAAAGGTATAACGCT
BRCA2 EXON 7 F	CCTTAATGATCAGGGCATTTC
BRCA2 EXON 7 R	CAACCTCATCTGCTCTTTCTTG
BRCA2 EXON 8 F	GCCATATCTTACCACCTTGTGA
BRCA2 EXON 8 R	AGGTTTAGAGACTTTCTCAAAGGC
BRCA2 EXON 9 F	CTAGTGATTTTAAACTATAATTTTTG
BRCA2 EXON 9 R	GTTCAACTAAACAGAGGACT
BRCA2 EXON 10A F	CTATGAGAAAGGTTGTGAG

Name	Sequence
BRCA2 EXON 10A R	CCTAGTCTTGCTAGTTCTT
BRCA2 EXON 10B F	AACAGTTGTAGATACCTCTGAA
BRCA2 EXON 10B R	GACTTTTTGATACCCTGAAATG
BRCA2 EXON 10C F	CAGCATCTTGAATTCTCATACAG
BRCA2 EXON 10C R	CATGTATACAGATGATGCCTAAG
BRCA2 EXON 11A F	AACTTAGTGAAAAATATTTAGTGA
BRCA2 EXON 11A R	ATACATCTTGATTCTTTTCCAT
BRCA2 EXON 11B F	AGAACCAACTTTGTCCTTAA
BRCA2 EXON 11B R	TTAGATTTGTGTTTTGGTTGAA
BRCA2 EXON 11C F	ATGGAAAGAATCAAGATGTAT
BRCA2 EXON 11C R	CCTAATGTTATGTTCAGAGAG
BRCA2 EXON 11D F	GTGTAAAGCAGCATATAAAAAT
BRCA2 EXON 11D R	CTTGCTGCTGTCTACCTG
BRCA2 EXON 11E F	CCATAATTTAACACCTAGCCA
BRCA2 EXON 11E R	CCAAAAAAGTTAAATCTGACA
BRCA2 EXON 11F F	AACGGACTTGCTATTTACTGA
BRCA2 EXON 11F R	AGTACCTTGCTCTTTTTCATC
BRCA2 EXON 11G F	CAGCTAGCGGGAAAAAAGTTA
BRCA2 EXON 11G R	TTCGGAGAGATGATTTTTGTC
BRCA2 EXON 11H F	GCCTTAGCTTTTTACACAA
BRCA2 EXON 11H R	TTTTTGATTATATCTCGTTG
BRCA2 EXON 11I F	CCATTAAATTGTCCATATCTA
BRCA2 EXON 11I R	GACGTAGGTGAATAGTGAAGA
BRCA2 EXON 11J F	GAAGATAGTACCAAGCAAGTC
BRCA2 EXON 11J R	TGAGACTTTGGTTCCTAATAC
BRCA2 EXON 11K F	GTCTTCACTATTCACCTACG
BRCA2 EXON 11K R	CCCCCAAACTGACTACACAA
BRCA2 EXON 12 F	AGTGGTGTTTTAAAGTGGTCAAAA
BRCA2 EXON 12 R	GGATCCACCTGAGGTCAGAATA
BRCA2 EXON 13 F	GCATCCGTTACATTCACTGAAA
BRCA2 EXON 13 R	ACGGGAAGTGTTAACTTCTTAACG
BRCA2 EXON 14A F	ACCATGTAGCAAATGAGGGTCT
BRCA2 EXON 14A R	GCTTTTGTCTGTTTTCCTCCAA
BRCA2 EXON 14B F	CACAGAGTTGAACAGTGTGTTAGG
BRCA2 EXON 14B R	GGGCTTTAAAATTACCACCACC
BRCA2 EXON 15 F	GGCCAGGGGTTGTGCTTTTT
BRCA2 EXON 15 R	AGGATACTAGTTAATGAAATA
BRCA2 EXON 16 F	TTTGGTAAATTCAGTTTTGGTTTG
BRCA2 EXON 16 R	AGCCAACTTTTTAGTTCGAGAG
BRCA2 EXON 17 F	CAGAGAATAGTTGTAGTTGTTGAA
BRCA2 EXON 17 R	AGAAACCTTAACCCATACTGC
BRCA2 EXON 18A F	GATCCACTATTTGGGGATTGC
BRCA2 EXON 18A R	GATCTAACTGGGCCTTAACAGC
BRCA2 EXON 18B F	GCAGATACCCAAAAAGTGGC
BRCA2 EXON 18B R	TCTGGACCTCCCAAAAACTG
BRCA2 EXON 19 F	AAGTGAATATTTTTAAGGCAGTT
BRCA2 EXON 19 R	TATATGGTAAGTTTCAAGAAT
BRCA2 EXON 20 F	CACTGTGCCTGGCCTGATAC
BRCA2 EXON 20 R	ATGTTAAATTCAAAGTCTCTA
BRCA2 EXON 21 F	GGGTGTTTTATGCTTGGTTCT
BRCA2 EXON 21 R	CATTTCAACATATTCCTTCCTG
BRCA2 EXON 22 F	AACCACACCCTTAAGATGAGC
BRCA2 EXON 22 R	GGGCATTAGTAGTGGATTTTGC
BRCA2 EXON 23 F	ACTTCTTCCATTGCATCTTTCTCA
BRCA2 EXON 23 R	AAAACAAAACAAAAATTCAACATA
BRCA2 EXON 24 F	GCAGCGACAAAAAAAAACTCA

Name	Sequence
BRCA2 EXON 24 R	ATTTGCCAACTGGTAGCTCC
BRCA2 EXON 25 F	GCTTTCGCCAAATTCAGCTA
BRCA2 EXON 25 R	TACCAAAATGTGTGGTGATGC
BRCA2 EXON 26 F	GTCCCAAACTTTTCATTTCTGC
BRCA2 EXON 26 R	GGAGCCACATAACAACCACA
BRCA2 EXON 27A F	CTGTGTGTAATATTTGCGTGCT
BRCA2 EXON 27A R	GCAAGTTCTTCGTCACTATTG
BRCA2 EXON 27B F	GAATTCTCCTCAGATGACTCCA
BRCA2 EXON 27B R	TCTTTGCTCATTGTGCAACA
Tdp1 siRNAs	
siRNA 1	GGAGUUAAGCCAAAGUAUA
siRNA 2	UCAGUUACUUGAUGGCUUA
siRNA 3	GACCAUAUCUAGUAGUGAU
siRNA 4	CUAGACAGUUUCAAAGUGA
Tdp1 shRNAs	
shRNA 1	GTATGGAAGTAAAGATCGG
shRNA 2	TCAAAGCACCGGATACGCA
shRNA 3	TTGGAACACACCACACGAA
Control	GTGTGAACCATGAGAAGTA

Table C-2: Comparison of Tdp1 expression between noncancerous skeletal muscle and RMS subtypes

Tissue	***n***	**Tdp1 expression (mean ± SD)**	***p****
Normal Skeletal Muscle	7	130.7 ± 19.4	
Primary RMS	147	209.2 ± 62.6	<0.001
Alveolar RMS	70	226.8 ± 74.5	<0.001
Fusion-positive	61	233.1 ± 76.3	<0.001
PAX3-FOXO1	44	231.0 ± 83.9	<0.001
PAX7-FOXO1	17	238.5 ± 53.8	<0.001
Fusion-negative	9	183.6 ± 42.3	0.016
Embryonal RMS	69	194.6 ± 44.9	<0.001
Spindle RMS	8	179.3 ± 36.1	0.009

* Based on Mann-Whitney U test when compared to normal skeletal muscle.

Abbreviations - SD, standard deviation; RMS, rhabdomyosarcoma.

Table C-3: Effect of 96-hour PARP inhibitor treatment on the proliferation of RMS cell lines.

PARP inhibitor (µmol/L)	Cell line (% cell number)					
Rucaparib	A204	Birch	RD	CW9019	RH30	HSM
0	100	100	100	100	100	100
10	35	45	50	59	49	90
20	22	33	45	24	25	72
50	14	15	8	12	14	39
100	11	7	6	5	5	18
Olaparib						
0	100	100	100	100	100	100
10	37	51	85	89	52	94
20	34	40	61	52	26	74
50	26	30	32	52	13	37
100	13	14	7	26	8	17
Veliparib						
0	100	100	100	100	100	100
10	45	58	88	74	75	97
20	42	39	67	64	65	84
50	30	12	44	43	24	47
100	9	10	14	18	8	23

Table C-4: Summary of BRCA1 sequnce variants in RMS cell lines

Cell line	mutation	aa variant	Exon	dbSNP (freq)	HGMD entry?
RD					
	c.-25_-20GTAAAG>del		alt. splice donor of exon 1	No	
	c.442_444CAG>del	p.Q148del	alt. splice isoform 6	No	No
	c.2082C>T	p.S694S	Exon 10	Yes-SNP (31%)	
	c.2311T>C	p.L771L	Exon 10	Yes-SNP (29%)	
	c.2612C>T	p.P871L	Exon 10	Yes-SNP (50%)	
	c.3113A>G	p.E1038G	Exon 10	Yes-SNP (29%)	
	c.3548A>G	p.K1183R	Exon 10	Yes-SNP (31%)	
	c.4308C>T	p.S1436S	Exon 10	Yes-SNP (29%)	
	c.4357_4359GCA>del	p.A1453del	alt. splice-in isoforms 4 &5	No	No
	c.4837A>G	p.S1613G	Exon 15	Yes-SNP (31%)	
A204					
	c.442_444CAG>del	p.Q148del	alt. splice isoform 6	No	No
	c.1067A>G	p.Q356R	Exon 10	Yes-SNP (3%)	
	c.2082C>T	p.S694S	Exon 10	Yes-SNP (31%)	
	c.2311T>C	p.L771L	Exon 10	Yes-SNP (29%)	
	c.2612C>T	p.P871L	Exon 10	Yes-SNP (50%)	
	c.3113A>G	p.E1038G	Exon 10	Yes-SNP (29%)	
	c.3548A>G	p.K1183R	Exon 10	Yes-SNP (31%)	
	c.4308C>T	p.S1436S	Exon 10	Yes-SNP (29%)	
	c.4357_4359GCA>del	p.A1453del	alt. splice-in	No	No
CW					
	c.135_212ATTTTGCATGCTGAA ACTTCTCAACCAGAAGAAAGG GCCTTCACAGTGTCCTTTATGT AAGAATGATATAACCAAAAG>del	p.46_71del	Skipping of exon 4	No	No
	c.4357_4359GCA>del	p.A1453del	alt splice-in isoforms 4 & 5	No	No
Birch					
	c.1067A>G	p.Q356R	Confirmed - het	Yes-SNP	

Cell line	mutation	aa variant	Exon	dbSNP (freq)	HGMD entry?
				(3%)	
	c.2082C>T	p.S694S	Exon 10	Yes-SNP (31%)	
	c.2311T>C	p.L771L	Exon 10	Yes-SNP (29%)	
	c.2612C>T	p.P871L	Exon 10	Yes-SNP (50%)	
	c.3113A>G	p.E1038G	Exon 10	Yes-SNP (29%)	
	c.4308C>T	p.S1436S	Confirmed - het	Yes-SNP (29%)	
	c.4357_4359GCA>del	p.A1453del	alt. splice-in	No	No
RH30					
	c.-25_-20GTAAAG>del		alt. splice donor of exon 1		
	c.1067A>G	p.Q356R	confirmed	Yes-SNP (3%)	
	c.4357_4359GCA>del	p.A1453del	alt. splice-in isoforms 4 & 5	No	No
HSM					
	c.2167A>G	p.N723D	Exon 10	Yes-SNP (2%)	
	c.2311T>C	p.L771L	Exon 10	Yes-SNP (29%)	
	c.2612C>T	p.P871L	Exon 10	Yes-SNP (50%)	
	c.3418A>G	p.S1140G	Exon 10	Yes-SNP (11%)	
	c.4357_4359GCA>del	p.A1453del	Alt splice-in isoforms 4 & 5	No	No
	c.4900A>G	p.S1634G	Exon 16	Yes-SNP (33%)	

Table C-5: Summary of BRCA2 sequence variants in RMS cell lines

Cell line	mutation	aa variant	Exon	dbSNP (freq)	HGMD entry?
RD	c.8182G>A	p.V2728I	Exon 18	Yes-SNP (3%)	
A204	c.2254_2256GAC>del	p.D752del	alt. splice-in	No	No
	c.3396A>C	p.K1132N	Exon 11	Yes-SNP (28%)	
	c.7242A>G	p.S2414S	Exon 14	Yes-SNP (25%)	
CW	c.2350A>G	p.M784V	Exon 11	Yes-SNP (8%)	
Birch	c.3396A>C	p.K1132N	Exon 11	Yes-SNP (28%)	
	c.8246_8251AGAAGA>del	p.2749_2751del	alt. splice acceptor of exon 18	No	No
RH30	c.4133_4141CTCAGATTA>del	P.1378_1380del	alt. splice acceptor of exon 11	No	No
HSM	c.1365_A>G	p.S455S	Exon 10	Yes-SNP (7%)	

Appendix D: Supplementary Tables and Figures for Chapter 5

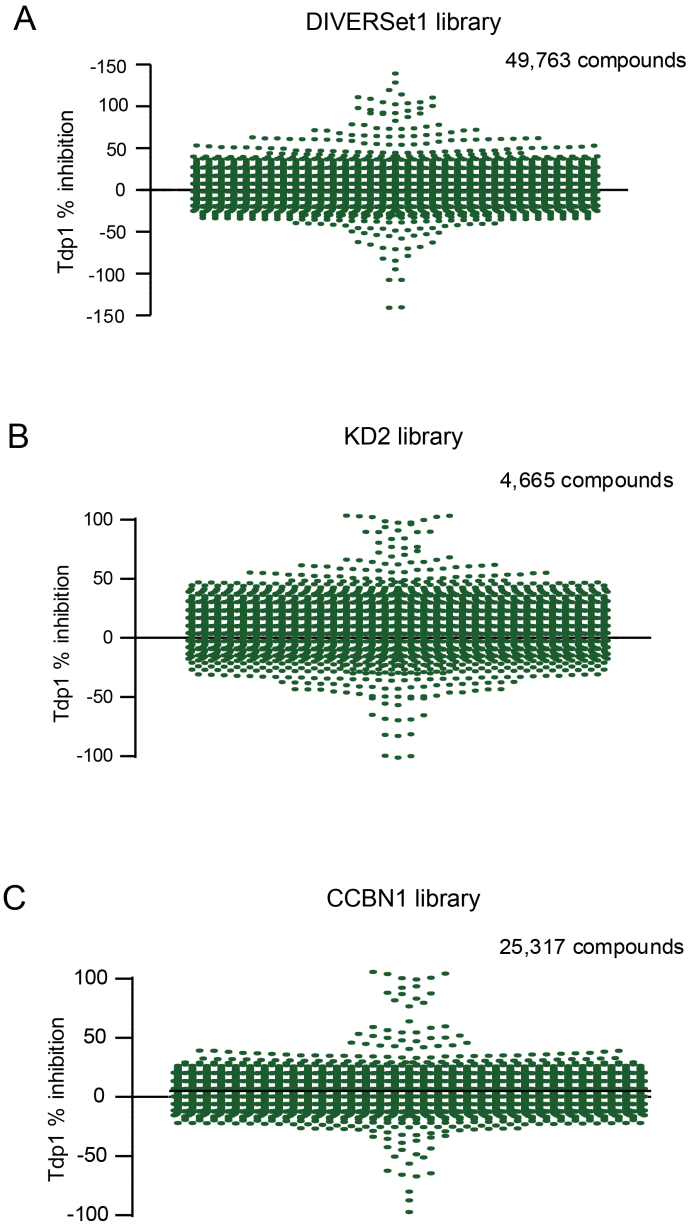

Figure D-1. High throughput screening results for three separate libraries. The KD2 library was used in the pilot, and the CCBN and DIVERset libraries were used for the primary *in vitro* screen. Some compounds had additional quenching properties and decreased the background fluorescence, which would show as greater than 100% inhibition.

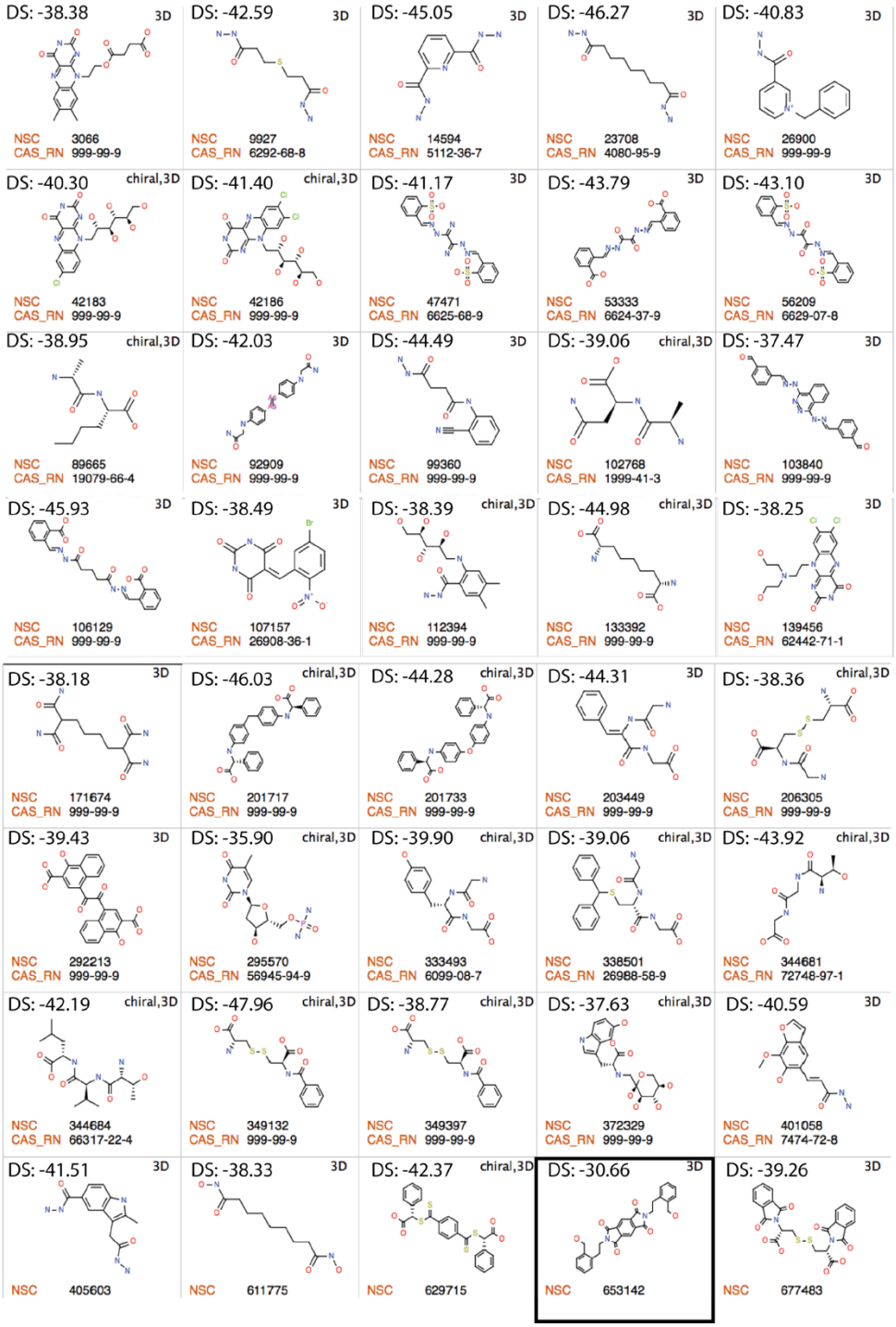

Figure D-2. Chemical structures and docking scores of the top 40 compounds from the *in silico* screen. Boxed compound (NSC# 653142) indicates potential Tdp1 inhibitor with an IC_{50} of 3.5µM. Compounds are identified by their NSC and CAS numbers. DS: Docking score. Higher scores indicate better fit.

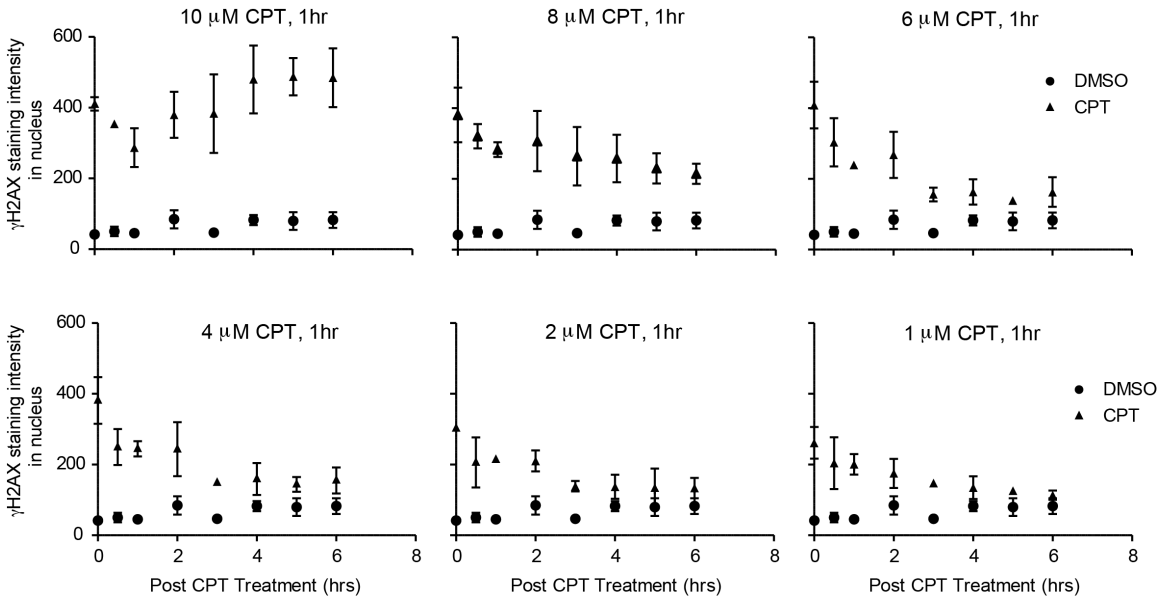

Figure D-3. Sensitivity of MCF-7 cells to CPT. MCF-7 cells were treated with varying concentrations of CPT for 1 hour and allowed to recover for 8 hours post-treatment. γH2AX staining of MCF-7 cells was used as a measure of DNA damage.

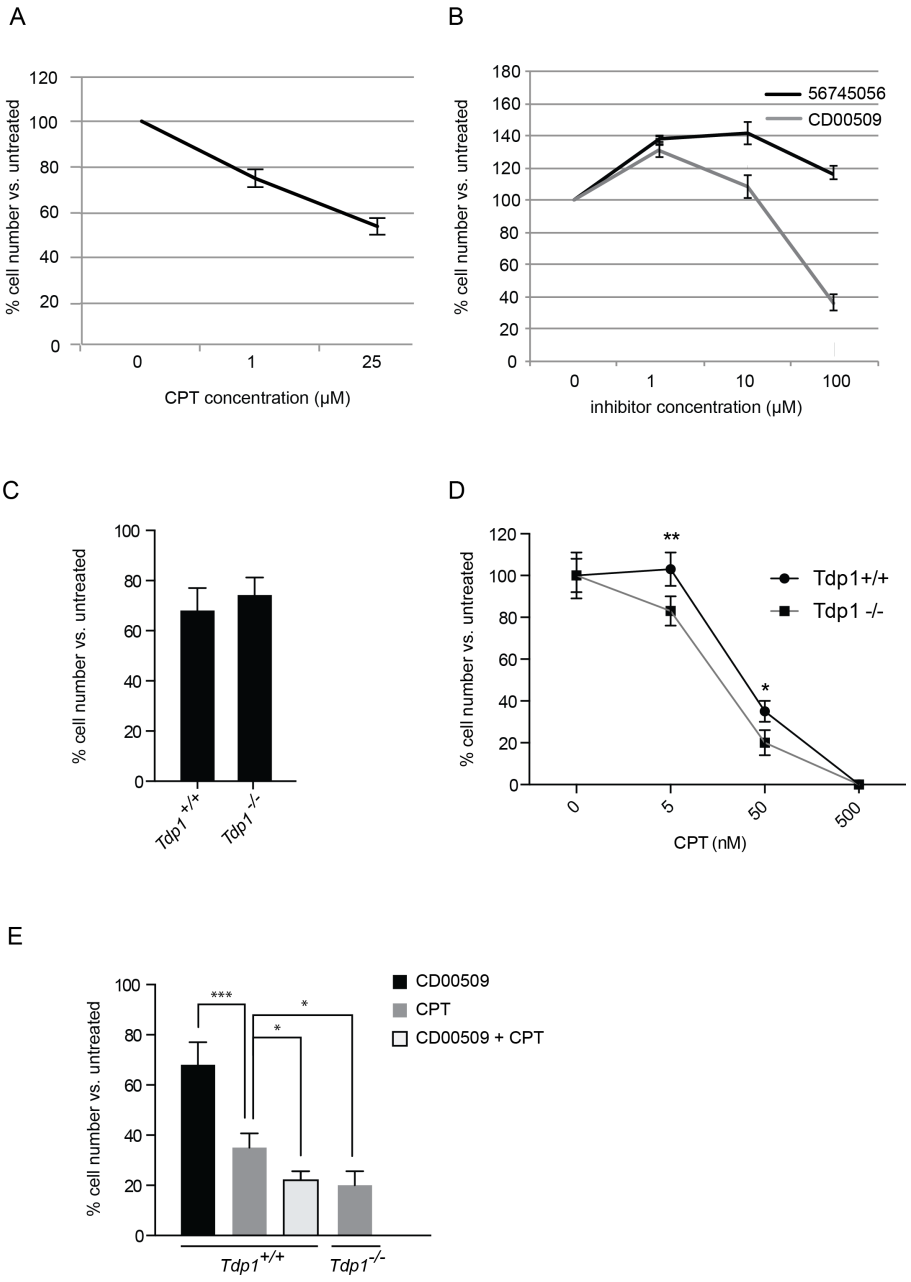

Figure D-4. Sensitivity of human mammary epithelial cells and mouse embryonic fibroblasts (MEFs) to CPT and Tdp1 inhibitor treatment **A.** Determination of LD_{50} of CPT over the course of 96 hours in human mammary epithelial cells. **B.** Determination of LD_{50} of 5675056 and CD00509 over the course of 96 hours in human mammary epithelial cells. **C.** Relative number of *Tdp1*$^{+/+}$ and *Tdp1*$^{-/-}$ MEFs treated with 10μM CD00509 for 96 hours versus untreated *Tdp1*$^{+/+}$ and *Tdp1*$^{-/-}$ MEFs. **D.** Determination of LD_{50} of CPT in *Tdp1*$^{+/+}$ and *Tdp1*$^{-/-}$ MEFs following 96 hours of treatment. **E.** Relative number of treated *Tdp1*$^{+/+}$ and *Tdp1*$^{-/-}$ MEFs versus untreated *Tdp1*$^{+/+}$ and *Tdp1*$^{-/-}$ MEFs. The MEFs were treated with 10μM CD00509 and/or 50nM CPT . (n=3) n, number of replicates; error bars, mean ± s.d. *, P<0.05, **, P<0.01 . ***, P<0.001

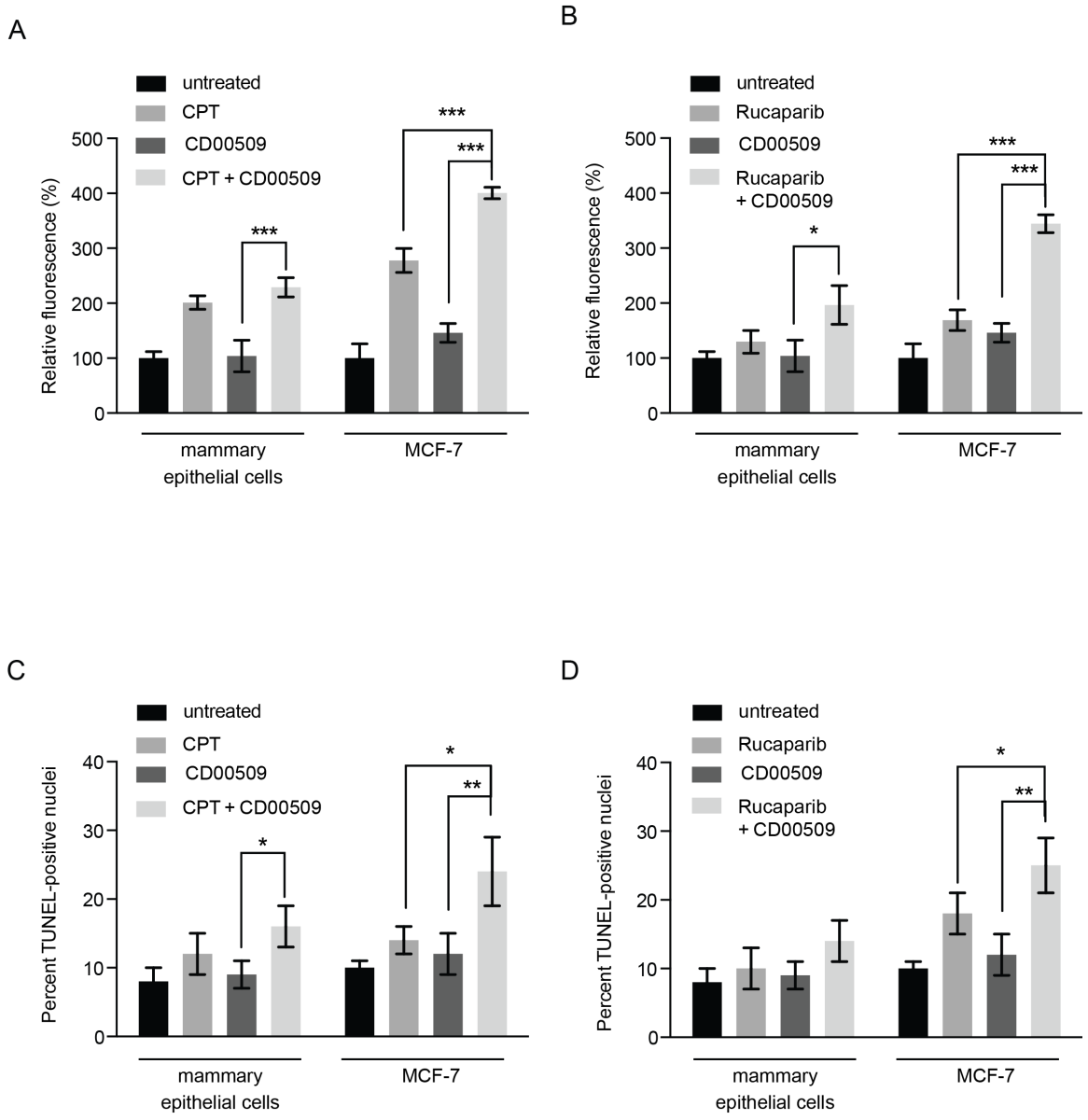

Figure D-5. Tdp1 inhbition is cytotoxic to MCF-7 cells and increases the cytotoxicity of CPT and Rucaparib. **A-B.** Graphs of caspase-3/7 activity as measured by fluorescence of cleaved caspase-3/7 substrates at 96 hours following treatment with the indicated compounds. Fluorescence units have been converted to percentages by normalizing to untreated controls within each cell line. **C-D.** Graphs showing the percentage of TUNEL-stained nuclei following 96 hours of treatment with the indicated compounds. Concentrations of compounds used were 1 μM CPT, 10 μM CD00509 and 10 μM Rucaparib. (n=3) n, number of replicates; error bars, mean ± s.d. *, $P<0.05$, **, $P<0.01$. ***, $P<0.001$

Table D-1. Oligonucleotide and siRNAsequences.

Name	Sequence
RT-PCR primers (5'-3')	
TDP1 - forward	AGGCTAAGGCTCACCTCCAT
TDP1 - reverse	TTCCTGGAGTCTTGCTTTCC
GAPDH - forward	TTAGCACCCCTGGCCAAGG
GAPDH - reverse	CTTACTCCTTGGAGGCCATG
Tdp1 siRNAs (5'-3')	
siRNA 1	GGAGUUAAGCCAAAGUAUA
siRNA 2	UCAGUUACUUGAUGGCUUA
siRNA 3	GACCAUAUCUAGUAGUGAU
siRNA 4	CUAGACAGUUUCAAAGUGA